N d'ordre: 40095

Université Lille1
Sciences et Technologies

Université des sciences et technologies de Lille

Thèse

pour obtenir le grade de

Docteur de l'Université des sciences et technologies de Lille

Spécialité Microondes et Microtechnologies

Présentée par

Fuli ZHANG

TECHNOLOGIES DES METAMATERIAUX ELECTROMAGNETIQUES EN VOLUME : APPLICATION AUX ELEMENTS DE GUIDAGE ET DE RAYONNEMENT

Soutenance prévue le 20 Novembre 2009

M. J. P. Parneix	**Président**
M. D. Lippens	**Directeur de thèse**
M. P. Ferrari	**Rapporteur**
M. P. Queffelec	**Rapporteur**
Mme. A. C. Hladky	**Examinateur**
M. J. P. Ganne	**Examinateur**

Abstract

Recently, metamaterial has attracted much attention due to unique property such as negative index. This thesis is devoted to various aspects of this field: left and right handed balanced structure, low loss, tunability and Mie resonance based metamaterial.

An omega-like left and right handed balanced metamaterial was proposed following the guideline of equality of magnetic and electric plasma frequency. It is shown that this metamaterial exhibits a broad passband from 8.0 - 16.0 GHz with a transition frequency at 13.6 GHz between negative and positive index branches.

Then, an omega-type left handed metamaterial (LHM) operating at millimeter wavelengths was fabricated. The left handed passband centered around 80 GHz was observed. The low insertion loss of -0.5 dB/cell may meet requirement of practical application.

We studied tunable metamaterial based on nematic liquid crystal. Magnetically tunable split ring resonator shows a resonance dip shift of 300 MHz under external magnetic field. Then a tunable LHM was fabricated. Effective index variation of 0.25 arising from liquid crystal reorientation was found.

Finally, we investigated Mie resonance based dielectric resonator and its related application. $Ba_{0.5}Sr_{0.5}TiO_3$ (BST) cube exhibits isotropic magnetic resonance for tilted incidence. Besides, a thin layer of BST cubes can perform as an artificial magnetic conductor (AMC) due to in-phase reflection around magnetic resonance. Such an AMC enhances directivity of antenna more than two times. In addition, a full dielectric cloak was also demonstrated numerically by radically positioning BST rectangular bricks.

Key words: metamaterial, Split ring resonator, Negative index, Tunability, Mie resonance, artificial magnetic resonator.

Acknowledgements

It has been three years that since the first time of leaving my motherland, China, to this far, romantic, great European country, France. Since being here, I have interacted so many people who have offered generous assistances on both emotional and academic states. I would like to sincerely thank each one of them.

It is my pleasure to express my deepest gratitude and respect to Prof. Dr. Didier Lippens for his invaluable guidance, helpful suggestions and endless support. His personal and academic virtue shaped my academic personality and changed my approach to scientific study. I am grateful to him for allowing me some freedom to pursue research topics of my own interest. Without his generous help and guidance, I cannot finish my PhD study. I really feel lucky to have the chance to carry out PhD study under his supervision.

I am also indebted to Prof. Xiaopeng Zhao who opens the door to metamaterial field for me.

Many thanks to my office partner, Mr. Gregroy Houzet, for giving a lot of helps and suggestions not only for academic research but also for life business especially at the beginning of my study in France.

I would like to thank former and currents members in Prof. D. Lippens'group, Dr. Davy Paul Gaillot, Mr. Charles Croënne, Dr. Alejandro Lucas Borja, Dr. Nathalie Fabre, Assoc. Prof. Dr. Eric Lheurette, Assoc. Prof. Dr. Xavier Melique, Prof. Olivier Vanbesien for various successful collaborations and valuable technical discussions.

I would like to thank Mdm. Marie-Benedicte Dernoncourt and Mdm. Anne-Marie Gregis for generous helps on life issues.

I would like to give my special grateful acknowledgement to Dr. Qian Zhao, and Mr. Lei Kang for their fruitful supports and friendship.

Many thanks to Prof. Dr. Ji Zhou for the assistance on the experimental demonstration on liquid crystal based metamaterial.

I am sincerely thankful to my close friends, Tao Jiang, Liang Huang, Hong Zhong, Jing Li, Tao Chang, Jie Xu, and Fengying Zhang for friendship and continuous support.

I also thank to Tao Xu, Zhenkun Chen, Wenxing Zhang, Lei Qiu, Qi Zhang, and Sunyan Liu, who I met during my study in France. Your friendship is invaluable to me. Moreover, I would like to thank all my other friends, no matter whether old or new, far away or nearby, to offer various helps to me. Thank you all.

Importantly, I would like to thank my family, my mother, father, elder brother and younger sister for their endless love, unwavering encouragement and care.

Finally, special acknowledgements to my girlfriend, Qian Lu, for her eternal love, endless trust and boundless encouragement. I cannot imagine finishing all my works without her endless moral support.

Contents

Abstract ..... **i**

Acknowledgements ..... **iii**

Contents **1**

List of Figures **3**

List of Tables **12**

Chapter 1 Theoretical background research development of metamaterial **13**

1.1 Introduction 13
1.2 Background 14
1.2.1 Negative permittivity ($\varepsilon < 0$) 17
1.2.2 Negative permeability ($\mu < 0$) 19
1.3 Experimental demonstration of LHMs and its development 21
References 24

Chapter 2 Balanced Metamaterial Structure **29**

2.1 Introduction 29
2.2 Balanced Metamaterial 30
2.2.1 Mode Analysis 30
2.2.2 Balanced condition 34
2.2.3 Tunability of balanced structure 36
2.3 Transmission measurement of slab sample 38
2.4 Angle resolved measurement of the prism like device 40
2.4.2 Microstructured and homogenous Prisms 47
2.4.3 Prism Experiment 53
2.6 Summary 58
References 59

Chapter 3 Low loss metamaterial at millimeter waves **61**

3.1 Introduction 61
3.2 Simulation 63
3.3 Fabrication 68
3.3.1 Mask preparation 68
3.3.2 Wafer 70
3.3.3 First omega layer 72
3.3.4 BCB layer 73

3.3.5 Second omega layer 74
3.4 Characterization 75
3.4.1 Transmission spectrum 75
3.4.2 Phase offset 76
3.4.3 Tilted incidence response 77
3.5 Summary 78
References 79

Chapter 4 Tunable metamaterial via liquid crystal molecular reorientation 81

4.1 Introduction 81
4.2 Numerical analysis on tunable metamaterial based on LC technology 82
4.2.1 S-type tunable metamaterial 83
4.2.2 Influence on the magnetic response 86
4.2.3 Influence on the electric response 90
4.3 Tunable negative permeability metamaterial 93
4.3.1 Tunable SRR prototype 93
4.3.2 Simulation 95
4.3.3 Sample fabrication and experiment 97
4.4 Tunable double negative metamaterial 100
4.4.1. Tunable omega-like LHM prototype 101
4.4.2. Birefringence of LC mixture at microwave frequency 102
4.4.3. Transmission measurement of LHM 105
4.4.4. Effective index variation 108
4.5. Summary 113
References 115

Chapter 5 Full dielectric metamaterial and its application 118

5.1 Introduction 118
5.2 Dielectric negative permeability metamaterial 119
5.2.1 Mie resonance in BST cubes 120
5.2.2 Loss tangent influence 125
5.2.3 Periodicity influence 126
5.2.4 Experimental demonstration of Mie resonance metamaterial 127
5.2.5 Isotropic property of BST cube via tilted transmission 131
5.3 Application of dielectric artificial magnetic resonator (AMC) 142
5.3.1 Dielectric AMC application on dipole antenna 143
5.3.2 Full dielectric cloak. 158
5.4 Summary 164
References 166

Chapter 6 Conclusions and future direction 170

List of Publications 173

List of Figures

Fig. 1.1 The material types definition based on permittivity and permeability sign. 14
Fig. 1.2 Negative and positive refractions between different types of materials. For the refracted beam inside LHM, it is noted that wave vector *k* and pointing vectors **S** are antiparallel.....17
Fig. 1.3 Wire array used to generate negative effective permittivity at microwave frequency 18
Fig. 1.4 (a) Split ring resonator used to generate negative permeability. (b) Lorentz-like effective permeability of SRR around its magnetic resonance frequency [4].....20
Fig. 1.5 (a) Schematic of LHM elementary cell that is composed of metallic rod and SRR to provide negative permittivity and negative permeability, respectively. (b) Equivalent circuit for transmission line based LHM. 21
Fig. 2.1 Characteristics of an edge-coupled SRR /wire (basic cell is shown in inset). (a) Real parts of permeability (solid) and permittivity (dash). (b) Frequency dependence of the transmission of an array. The bandgap (grey region) ranging from ω_p and ω_{mp} is caused by single negative permittivity.....31
Fig. 2.2 Schematic view of (a) omega unit cell and (b) omega pattern array with an edge illumination by a plane wave. 32
Fig. 2.3 Dispersion characteristics of the negative-zero-positive index structure depicted in Fig. 2.2 (b).....35
Fig. 2.4 Effective parameters of negative-zero-positive structure retrieved from the scattering parameters of one unit cell. (a) Refractive index. (b) Impedance. (c) Permittivity. (d) Permeability.....36
Fig. 2.5 Propagation phase constant as a function of the substrate permittivity.....37
Fig. 2.6 Photograph of slab sample fabricated for transmission measurements.....38
Fig. 2.7 Photograph of the transmission coefficient measurement setup. The upper aluminum plate was removed for clarity. 39
Fig. 2.8 Transmission coefficient of the metamaterial slab. The experimental and simulated results are denoted by black circular and grey line, respectively. .39
Fig. 2.9 The basic unit cell is bounded by the PMC and PEC boundaries along *x* and *y* directions, respectively. An incident beam is illuminated along *z* direction to retrieve the permittivity and permeability tensors ε_y and μ_x. 40
Fig. 2.10 The transmission and reflection for the basic unit cell of omega-based metamaterial under the incident beam electric field polarized along *y* and

magnetic field along *x* axes, as shown in Fig. 2.8 41
Fig. 2.11 Characteristic parameters for the unit cell of omega pattern as shown in Fig. 2.8. (a) Index; (b) Impedance; (c) permittivity tensor element ε_y, (d) permeability tensor element μ_x . The real and imaginary parts of the each effective parameters are represented by solid black and red dashed lines, respectively. 42
Fig. 2.12 The basic unit cell is assumed to be illuminated along the *y* direction. Periodic boundaries with two pairs of Master and Slave were employed transversal to the propagation direction. The thickness of unit cell along propagation direction is 1.66mm. An incident beam with electric polarized along *x* direction and magnetic polarized along *z* direction was propagated.43
Fig. 2.13 The magnitude of transmission and reflection for omega pattern under the normal incidence shown in Fig. 2.9. 43
Fig. 2.14 Effective parameters of omega pattern retrieved from the scattering parameters of one unit cell under normal incidence. (a) Refractive index. (b)Impedance. (c) Permittivity tensor element μ_z. (d) Permeability tensor element ε_y. The real and imaginary parts of the each effective parameters are represented by solid black and red dashed lines, respectively. 44
Fig. 2.15 The basic unit cell is assumed to be illuminated along *y* direction. Periodic boundaries with two pairs of Master and Slave definition were employed transversal to the propagation direction. The thickness of unit cell along propagation direction is 1.66mm. An incident beam is electrically polarized along *z* direction and magnetically polarized along *x* direction. 45
Fig. 2.16 The scattering parameters of the omega pattern under the normal incidence with proper polarization as shown in Fig. 2.14. 45
Fig. 2.17 Effective parameters of omega pattern retrieved from the scattering parameters of one unit cell under normal incidence. (a) Refractive index. (b) Impedance. (c) Permittivity. (d) Permeability. The real and imaginary parts of the each effective parameter are represented by solid black and red dashed lines, respectively. 46
Fig. 2.18 Illustration of the prism configuration for refraction simulation. (a) 3D view of the prism model which consists of eight stairs; (b) Close up view of one step which consists of four cells along *y* direction and one cell along *x* direction; (c) Top view of the prism model indicating the boundaries. 48
Fig. 2.19 Numerical evidence of negative refraction at 10.9 GHz. Electric field intensity of (a) homogenous and (b) microstructed prisms at the same input phase; refractive angle plotted in far field for (c) homogenous and (d) microstructed prisms. 51

Fig. 2.20 Numerical evidence of zero-index refraction at 12.8 GHz. Electric field intensity of (a) homogenous and (b) microstructed prisms at the same input phase; refractive angle plotted in far field for (c) homogenous and (d) microstructed prisms.....52
Fig. 2.21 Numerical evidence of positive refraction at 15.0 GHz. Electric field intensity of (a) homogenous and (b) microstructed prisms at the same input phase; refractive angle plotted in far field for (c) homogenous and (d) microstructed prisms.....53
Fig. 2.22 Photograph of a prism–type sample. 54
Fig. 2.23 Photo of the angle resolved measurement setup (the upper metal aluminium plate was removed for clarity).....55
Fig. 2.24 Angle dependence of the detected signal at three characteristic frequencies: at the negative index band at 12.0 GHz (dashed line), zero index at 13.6 GHz (solid line) and positive index at 15 GHz (dotted line). 56
Fig. 2.25 Simulated and measured refractive indices *n* as a function of frequency. The solid and dotted lines represent the real parts while the dashed and short dotted lines show the imaginary parts of *n* when the substrate is assumed to have relative permittivity of 4.0 and 3.6, respectively. The square symbol denotes the experimental refractive index, which was plotted from 10.2 to 15.0 GHz with a step of 0.1 GHz.....57
Fig. 2.26 Frequency dependence of the group velocity. 58
Fig. 3.1 (a) Schematic diagram of the basic unit cell. The dimensions of the basic unit cell are as follows: R = 90, g = 27.5, w = 42.0 (unit: μm). The periodicities along the x and z directions are 350 μm and 500 μm, respectively. (b) Schematic of the bulk metamaterial.....63
Fig. 3.2 CST model for elementary unit cell of metamaterial in W band. Omega pattern is made of gold with a thickness of 0.4 μm. BCB is defined with relative permittivity of 2.6 (tan δ=0.001) [24] while fused quartz has a relative permittivity of 3.794 (tan δ=0.0003) [25].....65
Fig. 3.3 Dielectric property of BCB as a function of frequency [24]. 65
Fig. 3.4 The propagation constant versus frequency. 66
Fig. 3.5 The effective parameters of omega cell at W band. (a) impedance (z), (b) index(n), (c) permeability (μ), (d) permittivity (ε). The real and imaginary parts are represented by solid (black) and dashed (red) lines, respectively...67
Fig. 3.6 (a) CST model and (b) scattering coefficient for 10 omega cells stacked along the propagation directions.....68
Fig. 3.7 Masks for fabrication of metamaterial at W band. (a) Mask for the first layer of omega pattern; (b) Zoom view of the first layer of mask; (c) Mask used for

dicing; (d) Mask for second layer of omega pattern; (e) Zoom view of double omegas when the two masks of omega pattern overlaps 69
Fig. 3.8 Schematic view for simplified illustration of the fabrication process. 70
Fig. 3.9 RC8 spin coater (a), hotplate (b), and mask aligner MA/BA6 (Suss MicroTec) 72
Fig. 3.10 Optical photograph of portion of first omega layer. 73
Fig. 3.11 Two metamaterial slices having 10 (a) and 14 cells (b), respectively. (c) Optical photograph of omega metamaterial at W band. 74
Fig. 3.12 (Left axis) Experimental (solid black) and simulation (dashed black) transmission spectra of the metamaterial with 10 cells stacked along the propagation direction. (Right axis) The real (dotted red) and imaginary parts (dashed red) of the effective index are also represented. 76
Fig. 3.13 The phase delay for the metamaterials with 10 (solid black) and 14 cells (dashed red) stacked along the propagation direction, respectively. 77
Fig. 3.14 Oblique transmission spectra of the 10-cell prototype for incident angle values ranging from 10° to 30°. Inset: The incident polarization orientation. 78
Fig. 4. 1 Tunable metamaterial based on anisotropic LC in the microwave frequency. (a) 3D view and (b) Side view of the basic unit cell and (c) the schematic of LC director reorientation. The geometrical parameters of the unit cell are as follows: $l1$ =3.0, $l2$ = 2.15, w = 0.4, $t_{Rogers\ Duriod}$=0.8, t_{LC} = 0.8, p = 5.0 (unit: millimeter). Rogers RT/Duriod 5880 (εr = 2.2, tan δ= 0.0004) was chosen as the host medium. 85
Fig. 4.2 The dependence of the real part of the effective permeability μ' of the metamaterial to the director angle of LC obtained from (a) isotropic and (b) anisotropic treatments. Inset: the magnetic resonance frequency ω_m as a function of the reorientation angle of LC. 87
Fig. 4.3 Surface currents (a) and electric field distribution (b) for metamaterials incorporating LC with a director angle of 0° at magnetic resonance frequency (8.20 GHz) obtained under an isotropic treatment. 88
Fig. 4.4 Electric field distribution in different magnetic resonators at frequencies corresponding to a negative permeability. (a) Single SRR with the gap parallel to the incident. electric field, (b) single SRR with the gap perpendicular to the incident electric field, (c) double SRR, (d) short wire pair. In all cases, the electric fields in the *x*-*z* plane are shown, which have been normalized by the respective maximum values. The incident beam is illuminated with its electric field polarized along the *x* axis. 89
Fig. 4.5 The dependence of the real part of the effective permittivity ε' of the

metamaterial to the LC reorientation obtained from (a) an isotropic and (b) an anisotropic treatment. Inset: the plasma frequency ω_p as a function of the reorientation angle of LC. 90

Fig. 4.6 Surface currents (a) and electric field distribution (b) for metamaterial incorporating LC with a director angle of 0º at plasma frequency of 14.9 GHz, which is predicted with an isotropic treatment. 92

Fig. 4.7 Tunable broadside coupled SRR metamaterial based on anisotropic LC. (a) Schematic diagrams of basic unit cell. (b) Side view of unit cell and reorientation of LC molecule in *x-y* plane. The geometrical parameters of unit cell are as follows: r = 0.5, w = 1.0, $t_{Teflon\ fiberglass}$ = 1.0, t_{LC} = 0.5, a = 6.0, b = 10.0 (unit: mm). Teflon fiberglass (ε_r=2.65, tanδ=0.001) was chosen as host medium. 94

Fig. 4.8 (a) The transmission spectra and (b) magnetic resonance frequency of the basic unit cell as a function of the reorientation angle of the LC molecules. (c) Electric field distribution of SRR in the *x-y* plane when it is magnetically resonated. 96

Fig. 4.9 (a) Schematic of assembly process of metamaterial. (b) Close-up view of the resulting SRR metamaterial. 97

Fig. 4.10 Schematic front (a), top (b), and side (c) views of SRR metamaterial infiltrated by LC. 98

Fig. 4.11 Schematic diagram of the studied LC orientation obtained with a pair of permanent magnets (a) θ=0° and (b) θ=90°. (c) Digital magnetometer used to measure magnetic field intensity. 99

Fig. 4.12 Demonstration of the magnetically tunable negative permeability metamaterial. (a) Experimental results, (b) Simulations including the loss of LC (tanδ = 0.05). 100

Fig. 4.13 (a) Schematic of the basic unit cell of the tunable negative index metamaterial as well as the reorientation of the LC molecule in the *x-y* plane. The geometry dimensions are as follows: R = 0.5, g = 0.4, w =1.0, t_{teflon} = 1.0, t_{LC} = 0.5 (unit: mm). The unit cell is stacked along the x and z directions with periodicities of 10.0 and 6.0 mm, respectively. (b) Close-up view of the mid-plane of the sample with the other part was removed to clarify the configuration of the voids. 102

Fig. 4.14 Schematic of LC inside a waveguide. 104

Fig. 4.15 (a) Extraordinary (black triangular) and ordinary (red circle) refractive indexes measured at room temperature as a function of frequency. (b) Birefringence of the nematic compound was deduced in the 10-12 GHz frequency band. 105

Fig. 4. 16 The experimental (a), (c) and simulation (b), (d) transmission responses of the metamaterial with infiltrated by LC under different molecules orientations: $\theta = 0°$ (solid black line) and 90° (dashed red line), respectively. The transmission spectra are plotted in dB ((a), (b)) and linear scale ((c), (d)), respectively. 106
Fig. 4.17 The local electric field distribution is plotted in the *x-y* plane at the magnetic resonance of omega pattern. Teflon fiberglass boards were invisible for clarity. 108
Fig. 4.18 (a) The real parts of retrieval indexes for metamaterial infiltrated by LC under different LC molecular reorientations: θ = 0° (solid black line) and 90° (dashed red line). (b) Index variation of metamaterial between LC molecular reorientation. 109
Fig. 4.19 (a) Phase delays for metamaterial under orientations of LC. (b)The measured phase shift for a nine-cell prototype when the LC molecules are reorientated from θ = 0° to 90°. 111
Fig. 4.20 (a) Optimized tunable omega metamaterial model. The geometrical parameters are nearly the same as the original one except for the periodicity along *x* direction reduces to 6.0 mm. (b) simulated transmission spectra of tunable omega metamaterial under LC reorientation. 112
Fig. 5.1 (a) The schematic diagram of the basic unit cell of BST-based metamaterial. The geometry parameters are as follows: $l = 0.9$ $a = 2.5$ (unit: mm). (b) Zoom view of displacement currents inside BST cube excited by the incident magnetic field are shown in the *x-z* plane. 121
Fig. 5.2 (a) Scattering parameters of dielectric metamaterial based on BST. (b) Reflection phase of dielectric metamaterial based on BST. 122
Fig. 5.3 Dispersion diagram of BST cube whose geometry dimensions are shown in Fig. 5.1. 123
Fig. 5.4 The effective parameters of BST based dielectric metamaterial. (a) Index n; (b) Impedance Zc; (c) Permeability μ; (d) Permittivity ε. The real and imaginary parts are presented by solid black and dashed red line, respectively. Another dotted line is added to distinguish the positive and negative values of effective parameters. 124
Fig. 5.5 The local magnetic field component H*y* in the *y-z* plane. 125
Fig. 5.6 The influence on the scattering parameters of Mie resonance based metamaterial. The geometrical dimension as well as the relative permittivity is used the same as stated above (l=0.9 a=2.5, ε=850). 126
Fig. 5.7 The influence of periodicity of elementary cell for dielectric metamaterial on the Mie resonance. The size as well as dielectric property of BST is fixed

as constant.....127
Fig. 5.8 (Close-up view of BST cubes arranged periodically (a) and randomly (b) inside a Teflon template, which is placed into an X band waveguide flange. 127
Fig. 5.9 The experimental (solid line) and simulated (dashed line) results of transmission spectra (a) and reflection phase (b) of BST cubes. The BST cube has a side length of 0.9mm and is arranged in square array of periodicity of 2.5 mm. The simulation is performed by presuming BST with a relative permittivity ε = 850, tanδ = 0.03.....128
Fig. 5.10 Experimental and simulated retrieval effective permeability of BST cube based metamaterial. The dimension and periodicity are the same as shown in Fig. 5.1. 129
Fig. 5.11 Transmission spectra comparison between periodically and randomly arranged BST cubes. The photographs for these two prototype are shown in Fig. 5.8. 130
Fig. 5.12 Simulated (a) and experimental (b) transmission spectra of BST cubes with various periodicity. The side length of BST cube is 0.9 mm. Three cubes are stacked along the propagation direction. 131
Fig. 5.13 Schematic diagram of oblique incidence on one thin layer of BST cube array. 132
Fig. 5.14 (a) HFSS model of dielectric metamaterial consisting of BST cube under oblique incidence. The geometry dimensions of the elementary cell are: l = 0.9, a = 1.25 mm. Teflon (ε = 2.1 tan δ = 0.001) was chosen to support the BST dielectric cube. Two pairs of Master and Slave periodic boundaries are used to vary phase shift so as to control the incident angle. (b) Schematic of HFSS model for the homogenous dielectric metamaterial, whose dielectric and magnetic material properties are defined by using effective permittivity and permeability depicted in Fig. 5.15. 133
Fig. 5.15 Effective constitutive parameters (a) permeability and (b) permittivity of the dielectric metamaterial under normal incidence. 134
Fig. 5.16 Transmission spectra for a single layer of dielectric negative permeability metamaterial under various incidences angles (θ, Φ) and modes (TE and TM). 135
Fig. 5.17 Transmission spectra comparison for microstructured and homogenous single layer of dielectric negative permeability metamaterial under various incidence angles θ ($\phi = 45°$) and modes (TE and TM).....136
Fig. 5.18 Transmission spectra for a layer of dielectric negative permeability metamaterial along three principal directions [*x, y, z*] of a cube cell by

considering TE and TM (b) modes with lattice a = 1.25 (a, b) and a = 2.0 mm (c, d), respectively. 138
Fig. 5.19 The front view of dielectric metamaterial sample consisting of BST resonator in a dense arrangement. The single layer is rotated around the x and y axes to measure the transmittance for TE (a) and TM (b) modes with various incidence angles, respectively. 139
Fig. 5.20 Schematic parallel plate system used for oblique incidence measurement of thin layer of BST cubes. 140
Fig. 5.21 Parallel plate step used for oblique incidence measurement of thin layer of BST cubes. 140
Fig. 5.22 The simulated ((a), (b)) and experimental ((c), (d)) oblique transmission spectra for the single layer of dielectric metamaterial with TE and TM modes. 142
Fig. 5.23 (a) The schematic diagram of the basic unit cell of BST-based AMC. The geometry parameters are as follows: l = 0.8 a =1.5 (unit: mm). (b) The displacement currents excited by the incident magnetic field are shown in the x-z plane. 144
Fig. 5.24 (Left axis) The phase of reflection S_{11} (dotted red line). The magnitude of the S_{21} (solid red line) and S_{11} (dashed red line). The bandwidth of dielectric AMC is colored in grey. 145
Fig. 5.25 The effective parameters of the BST-based AMC. (a) Impedance, (b) index, (c) permeability, and (d) permittivity. The real and imaginary parts are presented by solid black and dashed red lines, respectively. 146
Fig. 5.26 (a) Close-up and (b) side views of the model for AMC based on dielectric metamaterial working as reflector for electrically small antenna. 147
Fig. 5.27 The frequency dependent front-to-back ratio of far field pattern of the dipole working with dielectric metamaterial layer. 148
Fig. 5.28 The far field pattern of the dipole antenna alone in the free space and with AMC based on dielectric metamaterial layer at 10.612 GHz: (a) Normalized E plane; (b) Normalized H plane. 149
Fig. 5.29 The electric field distribution in the near field for the dipole antenna working with dielectric metamaterial: (a) the x-z plane; (b) the y-z plane. .150
Fig. 5.30 Scattering parameters of BST cube array. The permittivity of BST: ε=196, tan δ = 0.005, The side length and cubic periodicity are 1.75 and 3.0 mm, respectively. 151
Fig. 5.31 Effective impedance (a) and index of BST cube array. 152
Fig. 5.32 Printed dipole antenna: (a) 3d and (b) top view of antenna model in HFSS. Dipole antenna geometry dimensions are as follows: L_{sub} = 10.5 w_{sub} = 11.25

w_{tl} = 0.1, l = 5.1 w = 0.508 the gap between transmission lines is g = 0.0015 (unit: mm). Roger 5080(ε_r =2.2 tan δ=0.0004) is chosen for the substrate and the thickness of each substrate is t_{sub} =0.508. The dipole and transmission line are made of copper whose thickness is 0.030 mm.....153
Fig. 5.33 Return loss of printed dipole antenna.....154
Fig. 5.34 Directivity pattern of printed dipole antenna 154
Fig. 5.35 HFSS model for printed dipole antenna integrated with BST based dielectric AMC array.....155
Fig. 5.36 The comparison of return loss for dipole antenna alone and dipole antenna interacted with dielectric AMC.....156
Fig. 5.37 The far field pattern comparison between dipole antenna alone and dipole antenna along with dielectric AMC at 9.97 GHz.....157
Fig. 5.38 (a) 3d view and (b) *x-z* plane of far field radiation pattern at 9.97 GHz. .157
Fig. 5.39 Far field pattern for dipole and dipole along with AMC at 10.14 GHz. ..158
Fig. 5.40 (a) Schematic view of homogenous cloak. (b) HFSS Mode for elementary cell used for cloak. The fixed dimension of elementary are as follows: w_θ =2.0, h_{bst} = 1.0 , a_r = 3.32, a_θ=4.14, a_z = 3.4 mm. w_z is varied to tailor the magnetic permeability. BST has a relative dielectric ε = 194, tan δ= 0.005. 159
Fig. 5.41 Effective parameters of elementary cell for cloak at 10.554 GHz. μ_θ, μ_r, and ε_z are represented by square, circular and triangular symbols, respectively. The theoretical value for μ_r is also plotted by dashed dotted line.....162
Fig. 5.42 Field mapping for homogenous cloak with effective parameters of BST elementary cell with varied sidelength. 163
Fig. 5.43 Top view (a) and close-up view of full dielectric cloak consisting of BST rectangular bricks.....163
Fig. 5.44 Electric field mapping for micro-structure cloak surrounding a radius 30 mm metallic rod at 10.60 GHz (a) Maximum magnitude 2000 (b) 250 for field intensity. 164

List of Tables

TABLE 2-1 Anisotropic effective parameters of omega pattern at specified frequencies.....49

TABLE 3-1 Full steps of omega metamaterial fabrication.....71

TABLE 5-1 Effective parameters of elementary cloak cell.....161

Chapter 1 Theoretical background research development of metamaterial

1.1 Introduction

In recent few years, there has been an increasing interest in the field of metamaterial. Metamaterial is one type of material who possesses abnormal property that can not be found in natural occurring materials. Instead of constructing materials at the chemical level, as is ordinarily done, these are constructed with two or more materials at the macroscopic level. One of their defining characteristics is that the electromagnetic response results from combining two or more distinct materials in a specified way which extends the range of electromagnetic patterns.

Specially, people are more interested in the metamaterial with both simultaneously negative effective permittivity and permeability. This type of metamaterial was firstly studied by Veselago [1], who named this metamaterial as left-handed material (LHM) due to the fact that electric field **E**, magnetic field **H** and pointing vector *k* formed left handed rule rather than right handed case for electromagnetic wave propagated inside common material. Due to double negative effective parameters, LHM exhibits unique properties such as negative index, backward wave phenomena, as well as reversal Doppler shift and Cerenkov radiation. However, this type of material does not exists in nature such that this theoretical investigation has been laid dormant for long times. Until recent few years, D. R. Smith *et al*.experimentally realized LHM [2, 3] by stacking periodically split ring resonator and wire which were proposed by J. B. Pendry [4, 5], a renewed interests emerges on this topics. With numerous efforts of scientists from various fields, researches of metamaterial, from basic investigation to practical application, have been developed rapidly these few years.

In this chapter, we give a brief overview of theoretical background of LHM such as negative permeability, negative permittivity, negative index and so on. Then, latest research advances of LHMs are also outlined. Finally, we would like to give a summary of the organization of this thesis.

1.2 Background

The dielectric and magnetic response of material to incident electromagnetic waves are determined by dielectric permittivity and magnetic permeability. Figure 1.1 shows material type divided by the sign of permittivity and permeability. For common materials, both permittivity and permeability are positive. Obviously, most of natural occurring materials belong to this case. In addition, there are also another three types of material according to the sign of permittivity and permeability, as shown in Fig. 1.1. These are so called single negative permittivity, single negative permeability and double negative (negative permittivity and negative permeability) materials.

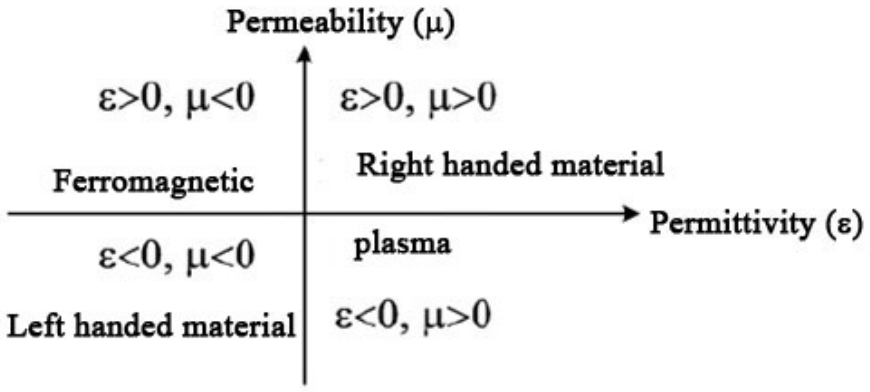

Fig. 1.1 The material types definition based on permittivity and permeability sign.

For a monochromatic wave propagated inside a homogenous medium, Maxwell formula can be written as follows [1]:

$$\nabla \times \mathbf{E} = -\frac{\partial \mathbf{B}}{\partial t}, \quad \nabla \times \mathbf{H} = \frac{\partial \mathbf{D}}{\partial t} \tag{1.1}$$

$$\mathbf{B} = \mu\mu_0\mathbf{H}, \quad \mathbf{D} = \varepsilon\varepsilon_0\mathbf{E} \tag{1.2}$$

where **E** and **H** represent the electric and magnetic field, respectively. For a plane wave propagated along *z* direction, **E** and **H** can be transformed by time varying vactor

$$\mathbf{E} = \mathbf{E}_0 e^{i(k\cdot z-\omega t)}, \quad \mathbf{H} = \mathbf{H}_0 e^{i(k\cdot z-\omega t)} \tag{1.3}$$

where *k* and ω represent wave vector and angular frequency, respectively.

Then, Eqs. 1.1 and 1.2 can be rewritten

$$k \times \mathbf{E} = \frac{\omega}{c} \mu \mathbf{H} \qquad (1.4)$$

$$k \times \mathbf{H} = -\frac{\omega}{c} \varepsilon \mathbf{E} \qquad (1.5)$$

For a common material with both positive permittivity and permeability, it is clear that incident electric field **E**, magnetic field **H** and wave vector *k* form a right-handed triplet, so this type material is also termed as right-handed material (RHM). However, for a double negative material ($\varepsilon < 0$ and $\mu < 0$), these three components of incident wave, **E**, **H** and *k* follow a left-handed triad, so that this type of material is also referred to as left handed material (LHM).

Actually, metal can perform as negative permittivity medium ($\varepsilon < 0$) when an incident electromagnetic waves is working below plasma frequency of metal. In very recent investigations on metamaterial, negative permeability ($\mu < 0$) is found to exist in dielectric ceramic particles with high permittivity due to Mie resonance [6-13] and ferromagnetic ceramic around ferromagnetic resonance [14-16]. However, LHM with simultaneous effective permittivity, ε_{eff} and permeability, μ_{eff} possessing negative values is not available in nature. In previous analysis from Veselago [1], one thing to be noted is that propagated wave inside LHM is still supported due to the fact that permittivity and permeability have the same algebraic sign, whereas it is prohibited for a material with different sign of permittivity and permeability, single negative permittivity or single negative permeability material, because wave vector as well as the refractive index is imaginary in single negative material such that an incident signal is evanescent exponentially along the propagation direction.

In addition to left-handed triad of **E**, **H** and *k* inside LHM, the time-average energy flow still forms right-handed triplet as energy flow **S** is independent of the algebraic sign of permittivity and permeability.

$$\mathbf{S} = \frac{1}{2} \mathrm{Re}(\mathbf{E} \times \mathbf{H}) \qquad (1.6)$$

Therefore, incident wave inside LHM is still directed away from the point source as that of common double positive material, whereas wave vector *k*, which is anti-parallel to energy flow **S**, is pointed towards source. Due to reversed directions of wave vector and energy flow **S**, LHM is also termed as backward wave (BW)

media [1, 17, 18].

For the refractive index of LHM with simultaneous negative permittivity and permeability, let us consider the refraction phenomena occurring when an incident beam transits from one medium into another. Suppose that the initial has a positive refractive index, therefore $\varepsilon_1 > 0$ and $\mu_1 > 0$. If $\varepsilon_2 > 0$ and $\mu_2 > 0$, we shall have an positive refraction between two materials interface, i.e., incident and refractive beams lay on both side of interface normal. For the case of RHM and LHM possessing $\varepsilon_2 < 0$ and $\mu_2 < 0$, we have a beam transition from an ordinary medium into a material II with negative ε and μ. However, in each case the boundary conditions should be satisfied. Remember that boundary conditions require tangential components of **E** and **H,** and normal components of **D** and **B** to be continuous at the interface.

$$E_{t1} = E_{t2}, \quad H_{t1} = H_{t2} \tag{1.8}$$

$$\varepsilon_1 E_{n1} = \varepsilon_2 E_{n2}, \quad \mu_1 E_{n1} = \mu_2 E_{n2} \tag{1.9}$$

Evidently, the tangential components of incident wave do not change during the transition from material 1 to 2, no matter the sign of ε and μ. However, for the normal components of the field (denoted by subscript n), they preserve their directions if ε and μ preserve their signs, otherwise they will change if two media have different signs of ε and μ [1]. As depicted in Fig. 1.2, the direction of magnetic field **H** changes such that the energy will flow along the "negative" direction, according the relation between **S**, **E**, and **H** (Eq.1.6), whereas the wave vector is directed towards the interface between RHM and LHM (Eqs.1.4 and 1.5), i.e., opposite to the direction of Poynting vector **S**. This means one beam goes from an ordinary material into the one with negative ε and μ, the refraction is symmetrical to the case with positive ε and μ.

In Fig. 1.2, as a TE wave is incident with an angle i off to the surface normal of the interface between RHM and LHM, it is bent to the same side of surface normal with a refractive angle of r. Using the Snell's law, the refractive index of LHM can be determined by

$$n_1 \sin i = n_2 \sin r \tag{1.10}$$

As refractive angle $r < 0$, thus the refractive index of LHM is also negative, as pointed by Veselago [1].

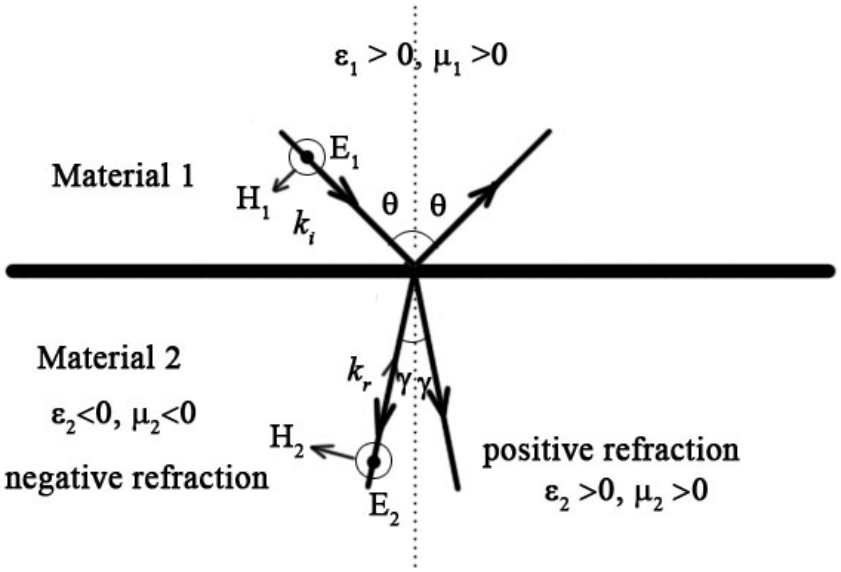

Fig. 1.2 Negative and positive refractions between different types of materials. For the refracted beam inside LHM, it is noted that wave vector *k* and pointing vectors **S** are antiparallel.

A material with negative index has promising applications on optics. For instances, one can use one LHM based flat lens to focus radiation of one point source to the other side. In addition, we can focus plane wave by using a concave lens with negative index rather than common convex lens. Although LHM is intriguing, for a long time, however, Veselago's work was not explored further due to the fact the people do not know any natural material has negative index. This standstill situation is not break until Pendry and his colleagues' works on artificial material composed of metallic elements characterized by effective permittivity and permeability [4, 5]. These works are outlined in following sections.

1.2.1 Negative permittivity (ε < 0)

In physics, a plasmon is a collective oscillation of electron density. In a solid, the negative charges of the conduction electrons are balanced by an equal concentration of positive charge of the nuclear. The corresponding dielectric constant can be given by a Drude model [5, 19]

$$\varepsilon(\omega) = 1 - \frac{\omega_p^2}{\omega(\omega + i\gamma)} \tag{1.11}$$

where ω_p is electric plasma frequency, γ is the damping factor. From Eq. 1.11, it can be seen that the real part of effective permittivity is essentially negative below the plasma frequency. The plasma frequency is as follows,

$$\omega_p^{\,2} = \frac{n_{eff} e^2}{\varepsilon_0 m_{eff}} \tag{1.11}$$

where n_{eff}, m_{eff}, and e are the effective electron density, effective electron mass, and electron charge, respectively.

In general, the plasma frequency of metal is around visible or ultraviolet frequencies. For instance, aluminum has plasmas frequency ω_p = 15 eV. The electromagnetic response of metal is dominated by negative permittivity concept near plasma frequencies. However, at lower frequencies beginning from near infrared and downwards, dissipation factor γ asserts itself, therefore dielectric function becomes imaginary. To achieve negative permittivity values at lower frequencies notably at microwave range, Pendry and his partner proposed the thin metallic wire array whose collective behavior is similar to the dielectric response of a low density, neutral, low loss plasma but at Gigahertz frequency [4, 20, 21].

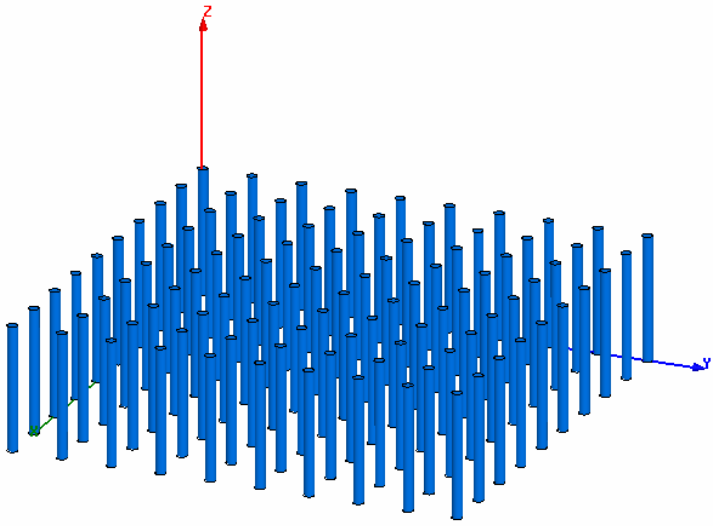

Fig. 1.3 Wire array used to generate negative effective permittivity at microwave frequency .

As depicted in Fig. 1.3, 1D thin wires were arranged in square array with a lattice of a to form a periodic medium. In this type of artificial medium, negative permittivity can be achieved at microwave frequencies. The corresponding plasma frequency of for metallic wires is rewritten by [5],

$$\omega_p^{\,2} = \frac{n_{eff} e^2}{\varepsilon_0 m_{eff}} = \frac{2\pi c_0^{\,2}}{a^2 \ln(a/r)} \tag{1.12}$$

where c_0 is the speed of light in free space, r is the radius of the wires. From a rigorous theoretical analysis [5], the plasma frequency for metallic wire array is only expressed by periodic structure parameters, providing more convenient method to tailor plasma frequency. On the other hand, unlike common photonic crystal structure, wire type negative permittivity medium is constructed with a periodicity much smaller than that of incident wave, which allows us to consider it as a homogenous material from a point view of effective medium theory

$$a << \lambda = 2\pi c / \omega \tag{1.13}$$

1.2.2 Negative permeability (μ < 0)

Electric charge is responsible for large electric response in dielectric materials. However, because of the lack of magnetic charge analogous to an electric charge caused by the fact that natural materials are limited to spin systems, it is more difficult to obtain a material with negative magnetic permeability. The challenge is much higher as frequency moves beyond the gigahertz range of frequency where the magnetic response of most materials begins to die away. Up to microwave frequencies, a large permeability is common in ferromagnetic and ferrite materials. Certain insulating ferromagnets [22] and antiferromagnetic compounds such as MgF_2 and FeF_2 [23] can exhibit a negative permeability. However, these materials often have undesirable mechanical properties, such as large weight and high losses. Therefore, the possibility of creating non-magnetic media with a magnetic response is very attractive notably for the construction of left handed metamaterial.

In 1999, Pendry *et al.* [4] introduced non-magnetic a double concentric split rings resonators (SRR) motif to produce negative permeability around its resonance frequency, as depicted in Fig. 1.4(a). This work is even more critical for the progress of LHM research. As shown in Fig. 1.4(a), for an incident electromagnetic wave with magnetic field perpendicular to SRR plane, SRR unit can resonate at wavelengths much larger than the diameter of the rings because of the existence of split. From an electrical engineering point of view, SRR can be considered as inductive-capacitive resonator, in which arms of ring offers inductance whereas the gap between two rings is to generate a large capacitance enabling induced current to flow.

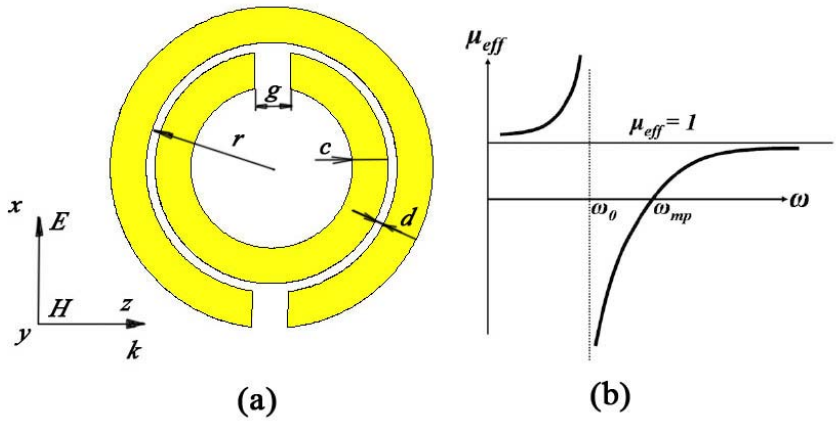

Fig. 1.4 (a) Split ring resonator used to generate negative permeability. (b) Lorentz-like effective permeability of SRR around its magnetic resonance frequency [4].

From detailed analysis described in Ref. 4, the generic effective permeability of SRR based medium is given by

$$\mu_{eff}(\omega) = 1 - \frac{F\omega_0^2}{\omega^2 - \omega_0^2 + i\omega\Gamma} \tag{1.14}$$

where ω_0 is the resonance frequency of SRR, Γ is the dissipation factor and $F = \pi r^2 / a^2$ is the fractional volume of elementary cell occupied by SRR. The resonant frequency of SRR is expressed by

$$\omega_0^{\ 2} = \frac{3lc_0^{\ 2}}{\pi r^3 \ln(2c/d)} \tag{1.15}$$

where c_0 is light velocity in vacuum, c is the width of ring, d is the gap between two rings (Fig. 1.4).

From Eq. 1.14, we see that the propagating modes occur up until the frequency ω_0, followed by a gap where no propagating modes exist, followed by propagating modes starting from the frequency, $1/\sqrt{1-F}\ \omega_0$. The schematic diagram of generic form for effective permeability of SRR is depicted in Fig. 1.4(b). The real part of the permeability of SRR shows a Lorentz-like resonance around the magnetic resonance frequency, ie., increases from unity to a large positive values near $\omega = \omega_0$, where it then abruptly passes to a large negative value, crossing $\mu = 0$ at the so-called magnetic plasma frequency, $\omega = \omega_{mp}$. The relation between ω_0 and ω_{mp} can be given by

$$\omega_{mp} = \frac{1}{\sqrt{1-F}}\omega_0 \tag{1.16}$$

Above magnetic plasma frequency, the real part of permeability for SRR returns positive value and reach unity at high frequency. Clearly, SRR exhibits negative permeability in a frequency regime ranging from $\omega_0 < \omega < \omega_{mp}$.

1.3 Experimental demonstration of LHMs and its development

Up to now, there are mainly two approaches to realize LHM. For the first case, inspired by Pendry's pioneering work on negative permittivity and negative permeability models, D. R. Smith *et al.* fabricated periodic structure consists of metallic wire and SRR schemes (Fig. 1.5(a)). It was experimentally demonstrated a stop band occurs either for SRR or wire array alone, whereas a combination structure of SRR and wire supports the propagation mode at specific microwave regime where the effective permittivity and permeability are simultaneously negative [3]. Please note that the incident wave should be electric polarized along the wire axis and magnetic polarized perpendicular to SRR plane such that metallic elements can be excited properly.

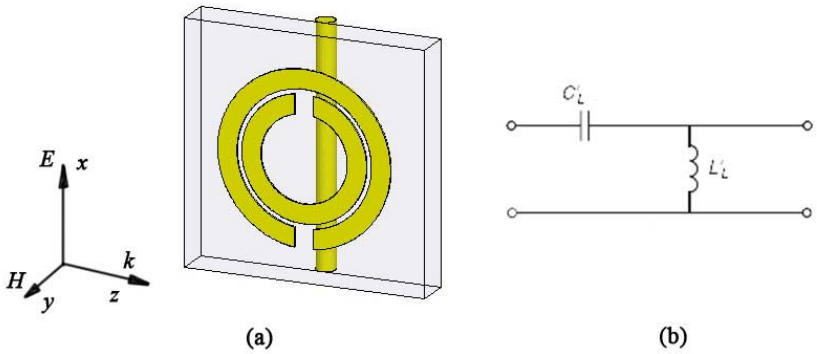

Fig. 1.5 (a) Schematic of LHM elementary cell that is composed of metallic rod and SRR to provide negative permittivity and negative permeability, respectively. (b) Equivalent circuit for transmission line based LHM.

After this proof-of-principle experiments of LHM, Shelby *et al.* assembled a 2D orthogonal arranged LHM prism and experimentally demonstrated negative refraction around the LHM pass band, which was considered as one of milestones for development of LHM [2]. Since then, greatly interest was aroused. The corresponding publications number was increased exponentially these years. In fact, there are still some doubts on LHM notably on the validity of negative refraction proof as it was carried out in near field [24]. In order to eliminate this criticism, Boeing Phantom Works group carried out transmission and refraction measurements

in a free space configuration and confirmed the left-handed passband characteristics and negative refraction again [25, 26], which helped to refute argument of original measurement was only due to near field effect.

SRR/wire-type LHM opens a new field of electromagnetic response with matter. However, there are still some drawbacks such as high losses and limited bandwidth, anisotropic property preventing its further development. These issues prompted researchers to investigate on the loss mechanism [27], as well as exploring new designs such as omega pattern [28-33], S-type [34, 35], fishnet [36-38] and so on. On the other hand, dentritic [10] and 2D [40] and 3D SRR/wire structure [41] were also proposed to overcome anisotropic property of original configuration.

Since both SRR and wire possess resonant characteristic, leading to high loss and limited bandwidth as stated above, some researcher are devoted to another approach to realize LHM property by making use of transmission line (TL) approach. Unlike conventional transmission line which is also named as Right handed transmission line, a serial capacitance and shunt inductance elements were introduced to form negative parameters of transmission line [42-50], as depicted in Fig. 1.5(b). The advantage of this approach is TL can exhibit left-handed property in a relative broad frequency band while not suffering from high insertion loss as SRR/wire design, showing more promising in potential applications notably for planar configuration [51].

Even though, compared to TL approach, SRR/wire design shows advantage of applications in the other fields requiring bulk materials, which are under rapid advances. S. Enoch e*t al.* experimentally shown that surrounding a dipole antenna by wire array based zero index medium, an extremely high directivity can be achieved [52]. MIT group reported a controllable steerable antenna which is integrated with an active radome based on S-type LHM [53]. A. Erentok *et al.* investigated a compact AMC with high impedance arising from the extremely large permeability along with a zero permittivity at the resonance frequency of SRR [54, 55]. Very recently, an electric and magnetic resonance based perfect absorber was proposed and attracted much attention in metamaterial research [56-58]. By radically positioned electrically/ magnetically resonant elements, a cloak can be formed and used to make objects inside cloak invisible, becoming one of metamaterial focus [59-62].

In addition to transfer basic research to industrial application, there are also many efforts devoted to pushing forwards the working frequency of metamaterial

from initial microwave to higher frequencies notably visible regime. By scaling the unit size, the working frequency of metamaterial can be enhanced considerably. Following this guidance, magnetic metamaterial towards working at 1 THz [63] and 100 THz [64] by using photolithography were fabricated. Moreover, rod pair [65], fishnet [36-38, 66] and subwavelength hole array [67-70] are also proposed to simplify the fabrication process at infrared or even visible frequencies.

As one of the goals in proposed thesis is to investigate metamaterial which can be applied on antenna as well as cloak, we chose SRR/wire and its related configurations as the main metamaterial structure in this thesis. Therefore, all the works are devoted to solve some problems on the advance of SRR/wire type LHM such as limited bandwidth, composite left-handed and right-handed balanced structure, tunability as well as isotropic metamaterial based on Mie resonance. All these works will be described in details in following parts of this thesis.

References

[1]. V. G. Veselago, Sov. Phys. Usp. **10**, 509 (1968).

[2]. R. Shelby, D. R. Smith, and S.Schultz, Science **292**, 77 (2001).

[3]. D. R. Smith, W. J. Padila, D. C. Vier, S. C. Nemat-Nasser, and S. Schultz, Phys. Rev. Lett. **84**, 4184 (2000).

[4]. J. B. Pendry, A. J. Holden, D. J. Ribbins, and W. J. Stewart, IEEE Trans. Microwave Theory Tech. **47**, 2075 (1999).

[5]. J. B. Pendry, A. J. Holden, W. J. Stewart and I. Youngs, Phys. Rev. Lett. **76**, 4773 (1996).

[6]. S. O'Brien, and J. B.Pendry, J. Phys.: Condens. Matter **14**, 4035 (2002).

[7]. C. L. Holloway, E. F. Kuester, J. Baker-Jarvis, and P. Kabos , IEEE Trans. Antennas Propag. **51**, 2596 (2003).

[8]. L. Peng, L. Ran, H. Chen, H. Zhang, J. A. Kong, and T. M. Grzegorczyk, Phys. Rev. Lett. **98**, 157403 (2007).

[9]. B.-I. Popa, and S. A. Cummer, Phys. Rev. Lett. **100**, 207401 (2008).

[10]. Q. Zhao, L. Kang, B. Du, H. Zhao, Q. Xie, X. Huang, B. Li, J. Zhou, and L. Li, Phys. Rev. Lett. **101,** 027402 (2008).

[11]. C. Rockstuhl, F. Lederer, C. Etrich, T. Pertsch, and T. Scharf, Phys. Rev. Lett. **99**, 017401 (2007).

[12]. W. Park, and Q. Wu, Solid State Commun. **146**, 221 (2008).

[13]. J. H. Lee, Q. Wu, and W. Park, Opt. Lett. **34**, 443 (2009).

[14]. H. Zhao, J. Zhou, Q. Zhao, B. Li, L. Kang, and Y. Bai, Appl. Phys. Lett. **91**, 131107 (2007).

[15]. Y. He, P. He, S. D. Yoon, P.V. Parimic, F. J. Rachfordd, V.G. Harris, C. Vittoria, J. Magn. Magn. Mater. **313**, 187 (2007).

[16]. R. X. Wu, J. Appl. Phys. **97**, 076105 (2005).

[17]. A. Gribic, and G. V. Eleftheriades, J. Appl. Phys. **92**, 5930 (2002).

[18]. T. M. Grzegorczyk, C. D. Moss, J. Lu, X. Chen, J. Jr. Pacheco, J. A. Kong, IEEE Trans. Microw. Theory Tech. **53**, 2956 (2005).

[19]. P. B. Johnson and R. W. Christy, Phys. Rev. B **6**, 4370 (1972).

[20]. J. B. Pendry, A. J. Holden, D. J. Robbins, and W. J. Stewart, J. Phys.Condens Matt. **10**, 4785 (1998).

[21]. D. R. Smith, D. C. Vier, Willie Padilla, S. C. Nemat-Nasser, and S. Schultz, Appl. Phys. Lett. **75**, 1425 (1999).

[22]. A Hartstein, E Burstein, A A Maradudin, R Brewer, and R F Wallis, J. Phys. C, **6**, 1266 (1973).

[23]. R. E. Camley and D. L. Mills. Phys. Rev. B **26**,1280 (1982).

[24]. P. M. Valanju, R. M. Walser, and A. P. Valanju, Phys. Rev. Lett. **88**, 187401 (2002).

[25]. K. Li, J. Mclean, R. B. Greegor, C. G. Parazzoli, and M. Tanielian, Appl. Phys. Lett. **82**, 2535 (2003).

[26]. C. G. Parazzoli, R. B. Greegor, K. Li, B. E. C. Koltenbah, and M. Tanielian, Phys. Rev. Lett. **90**, 107401 (2003)

[27]. C. G. Parazzoli, R. B. Greegor, J. A. Nielsen, M. A. Thompson, K. Li, A. M. Vetter, M. H. Tanielian, and D. C. Vier, Appl. Phys. Lett. **84**, 3232 (2004).

[28]. C. R. Simovski and S. He, Phys. Lett. A **311**, 254 (2003).

[29]. J. Huangfu, L. Ran, H. Chen, X. Zhang, K. Chen, T. M. Grzegorczyk, and J. A. Kong, Appl. Phys. Lett. **84**, 1537 (2004).

[30]. L. Ran, J. Huangfu, H. Chen, Y. Li, X. Zhang, K. Chen, and J. A. Kong, Phys. Rev. B **70,** 073102 (2004).

[31]. L. Ran, J. Huangfu, H. Chen, X. Zhang, K. Cheng, T. M. Grzegorczyk, and J. A. Kong, Prog. Electromagn. Res. **51**, 249 (2005).

[32]. E. Lheurette, O. Vanbésien, and D. Lippens, Microwave Opt. Tech. Lett. **49**, 84 (2007).

[33]. F. Zhang, G. Houzet, E. Lheurette, D. Lippens, M. Chaubet, and X. Zhao, J. Appl. Phys. **103**, 084312 (2008).

[34]. H. Chen, L. Ran, J. Huangfu, X. Zhang, K. Chen, T. M. Grzegorczyk, and J. A. Kong, Phys. Rev. E **70**, 057605 (2004).

[35]. H. Chen, L. Ran, J. Huangfu, X. Zhang, K. Chen, T. M. Grzegorczyk, and J. A. Kong, Appl. Phys. Lett. **86**, 151909 (2005).

[36]. G. Dolling, C. Enkrich, M. Wegener, C. M. Soukoulis, and S. Linden, Science

312, 892 (2006).

[37]. M. Kafesaki, I. Tsiapa, N. Katsarakis, Th. Koschny, C. M. Soukoulis, and E. N. Economou, Phys. Rev. B **75**, 235114 (2007).

[38]. A. Mary, Sergio G. Rodrigo, F. J. Garcia-Vidal, and L. Martin-Moreno, Phys. Rev. Lett. **101**, 103902 (2009).

[39]. X. Zhou, Q. H. Fu, J. Zhao, Y. Yang, and X. P. Zhao, Opt. Express **14**, 7188 (2006).

[40]. R. A. Shelby, D. R. Smith, S. C. Nemat-Nasser, and S. Schultz, Appl. Phys. Lett. **78**, 489 (2001).

[41]. T. Koschny, P. Markosm E. N. Economou, D. R. Smith, D. C. Vier, and C. M. Soukoulis, Phys. Rev. B **71**, 245105 (2005).

[42]. A. Grbic and G. V. Eleftheriades, Appl. Phys. Lett. **82**, 1815 (2003).

[43]. A. Grbic and G. V. Eleftheriades, J. Appl. Phys. **92**, 5930 (2002).

[44]. G. V. Eleftheriades, A. K. Iyer, and P. C. Kremer, IEEE Trans. Microwave Theory Tech. **50**, 2702 (2002).

[45]. A. Lai, C. Caloz, and T. Itoh, IEEE Microwave Mag. **5**, 34 (2004).

[46]. S. Lim, C. Caloz, and T. Itoh, IEEE Trans. Microwave Theory Tech. **53**, 161 (2004).

[47]. A. Lai, C. Caloz, and T. Itoh, IEEE Microwave Wireless Components Lett. **14**, 68 (2004).

[48]. A. Grbic and G. V. Eleftheriades, Phys. Rev. Lett. **92**, 117403 (2004).

[49]. A. Lai, C. Caloz, and T. Itoh, IEEE Microwave Mag. **5**, 34 (2004).

[50]. T. Crépin, J. F. Lampin, T. Decoopman, X. Mélique, L. Desplanque, and D. Lippens, Appl. Phys. Lett. **87**, 104105 (2005).

[51]. L. Liu, C. Caloz, and T. Itoh, Electron. Lett. **38**, 1414 (2000).

[52]. S. Enoch, G. Tayeb, P. Sabouroux, N. Guerin, and P. Vincent, Phys. Rev. Lett. **89**, 213902 (2002).

[53]. H. Chen, B. –I. Wu, L. Ran, T. M. Grzegorczyk, and J. A. Kong, Appl. Phys. Lett. **89**, 053509 (2005).

[54]. A. Erentok, P. Luljak, and R. W. Ziolkowski, IEEE Trans. Antennas Prog. **53**, 160 (2005).

[55]. A. Erentok, D. Lee, and R. W. Ziolkowski, IEEE Antennas Wirel. Propag. Lett. **6**, 134 (2007).

[56]. N. I. Landy, S. Sajuyigbe, J. J. Mock, D. R. Smith, and W. J. Padilla, Phys. Rev. Lett. **100**, 207402 (2008).

[57]. H. Tao, C. M. Bingham, A. C. Strikwerda, D. Pilon, D. Shrekenhamer, N. I. Landy, K. Fan, X. Zhang, W. J. Padilla, and R. D. Averitt, Phys. Rev. B **78**, 241103 (2008).

[58]. N. I. Landy, C. M. Bingham, T. Tyler, N. Jokerst, D. R. Smith, and W. J. Padilla, Opt. Express **79**, 125104 (2009).

[59]. J. B. Pendry, D. Shurig, and D. R. Smith, Science **312**, 1780 (2006).

[60]. D. Schurig, J. J. Mock, B. J. Justice, S. A. Cummer, J. B. Pendry, A. F. Starr, and D. R. Smith, Science 314, 977 (2006).

[61]. J. Valentine, J. Li, T. Zentgraf, G. Bartal, and X. Zhang, Nature Mater. **8**, 568 (2009).

[62]. R. Liu, C. Ji, J. J. Mock, J. Y. Chin, T. J. Cui, and D. R. Smith, Science **323**, 366 (2009).

[63]. T. J. Yen, W. J. Padilla, N. Fang, D. C. Vier, D. R. Smith, J. B. Pendry, D. N. Basov, and X. Zhang, Science **303**,1494 (2004).

[64]. S. Linden, C. Enkrich, M. Wegener, J. Zhou, T. Koschny, and C. M. Soukoulis, Science **306**, 1351 (2004)

[65]. V. M. Shalaev, W. Cai, U. K. Chettiar, H.-K. Yuan, A. K. Sarychev, V. P. Drachev, and A. V. Kildishev, Opt. Lett. **30**, 3356 (2005).

[66]. J. Valentine, S. Zhang, T. Zentgraf, E. Ulin-Avila, D. A. Genov, G. Bartal, X. Zhang, Nature **455**, 376 (2009).

[67]. C. Croenne, F. Garet, E. Lheurette, J.-L. Coutaz, and D. Lippens, Appl. Phys. Lett. **94**, 133112 (2009).

[68]. J. Rivas, C. Schotsch, P. H. Bolivar, and H. Kurz, Phys. Rev. B **68**, 201306 (2003).

[69]. M. Beruete, M. Sorolla, I. Campillo, J. S. Dolado, L. Martin Moreno, J. Bravo-Abad, and F. J. Garcia-Vidal, Opt. Lett. **29**, 2500 (2004).

[70]. A. Mary, S. G. Rodrigo, F. J. Garcia-Vidal, and L. Martin-Moreno, Phys. Rev. Lett. **101**, 103902 (2008).

Chapter 2 Balanced Metamaterial Structure

2.1 Introduction

Left Handed Metamaterials (LHMS) [1] can be synthesized either by introducing Split Ring Resonator (SRR)/wire structures [2-5] or by other related particles such as omega-type arrays [6-10] or by periodically loaded phase advance transmission lines [11-16] as it was proposed in the pioneered book of Brillouin [17]. For most of LHMs, left-handed (LH) passband is separated from the Right-handed (RH) one by a bandgap. At the edges of this passband, the group velocity vanishes. It was recently shown that a zero-gap dispersion characteristic can be achieved in LH transmission lines [12-14] so that an infinite wavelength condition can be met at the wave vector k=0 with a non-vanishing group velocity. Such a structure was termed Composite Right and Left Handed (CRLH) Material with an equality criterion between the series and parallel resonant frequencies of the lumped circuit elements. CRLH waveguides were used successfully at microwaves for sub-wavelength resonators and leaky wave antennas notably. However, in view of physical investigation as well as the potential application of metamaterial, such as perfect lens and antenna radome [18] requiring volumetric structure rather than transmission line based metamaterial, it is also of interest to develop SRR/wire based metamaterial possessing the balanced composite left and right handed dispersion property.

In this chapter, we investigate how the SRR/wire technology, which exhibits a narrow LH band separated by a forbidden gap from the RH one, can be used to realize a negative-zero-positive index material. To this aim, we based our analysis on an omega-type metal inclusion which can be considered as a related compound of broadside coupled SRR/wire arrays so that the electric and magnetic responses can be treated as a whole. Firstly, we will show that under the condition of interconnecting the omega-shaped particles, a broader band can be achieved as demonstrated before [7-9]. In a second stage, we identify the key geometrical parameters to balance the dielectric and magnetic plasma frequencies and demonstrate the balanced composite character of the structure by the retrieval of the effective permittivity and permeability. These conclusions are then assessed

experimentally by carrying out frequency and angle resolved transmission measurements on slab and wedge-type prototypes operating at centimeter wavelengths. We find a seamless transition between negative and positive index frequency ranges. It is also shown that a rather good agreement between the experiment and simulation results of both the transmission and the angle-resolve demonstrations.

2.2 Balanced Metamaterial

2.2.1 Mode Analysis

Figure 2.1 illustrates the typical dispersion of the effective permittivity and permeability of common used LHM unit cell, an edge coupled SRR/wire [2], and transmission response of one array whose basic cell is shown in inset. In fact, an infinite wire array yields a quasi Drude-like dependence for the dispersion of the effective permittivity. The effective permittivity is negative below the electric plasma frequency ω_p [19]. However, the effective permittivity of SRRs exhibits a Lorentz type resonant dispersion characteristic, in which the permeability becomes negative ranging from the magnetic resonant frequency ω_m and magnetic plasma frequency ω_{mp} [4]. It can be concluded that the material behaves as a single negative medium in the grayed frequency band between the magnetic plasma frequency ω_{mp} and the electric plasma frequency $\omega_{p.}$ within which the wave are evanescent. In contrast, the propagation is backward between the resonance frequency ω_0 (the magnetic resonance frequency of SRR's) and ω_{mp} and forward above ω_p.

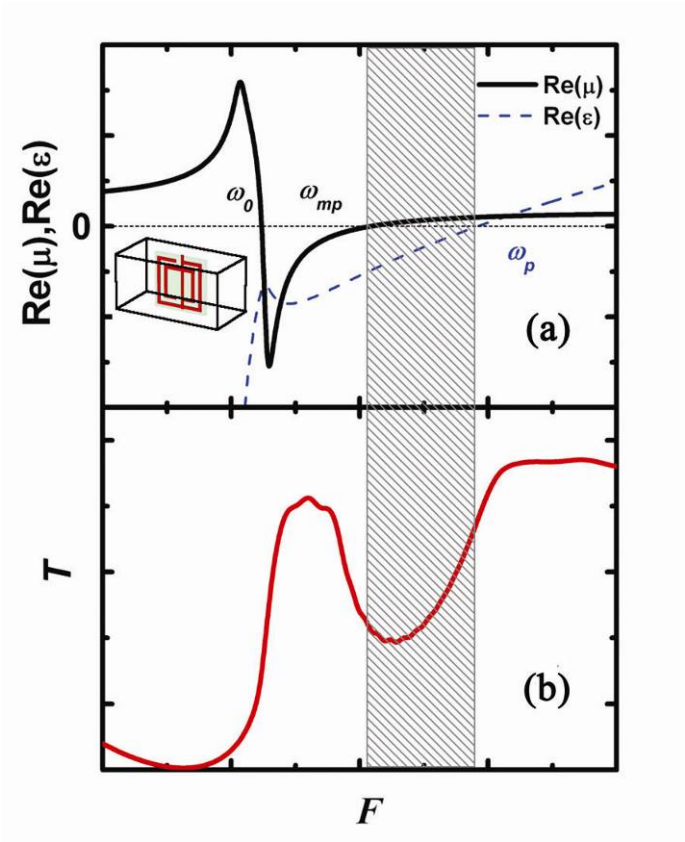

Fig. 2.1 Characteristics of an edge-coupled SRR /wire (basic cell is shown in inset). (a) Real parts of permeability (solid) and permittivity (dash). (b) Frequency dependence of the transmission of an array. The bandgap (grey region) ranging from ω_p and ω_{mp} is caused by single negative permittivity.

Let us now consider an omega-type metal inclusion as depicted in Fig. 2. The basic unit cell (Fig. 2.2(a)) is composed of two Ω-patterns in a back-to-back configuration to avoid chiral effects as well as the magnetoelectric effect [6, 20]. For pure magnetic excitation, namely for a magnetic dipole induced by the incident magnetic field (**H**), the polarization of **H** has to be along a direction normal to the surface on which the current loops (the C shape of the Omega inclusion) are implemented. In addition, in order to induce an electrical activity, the **E** field polarization has to be oriented parallel to the arms of the omega patterns. Under these polarization considerations, the array was implemented according to the scheme shown in Fig. 2.2(b). A volumetric prototype is achieved by stacking several substrates with omega-shaped metal inclusions printed on one side of each layer. In order to alleviate a resonant characteristic in the dielectric response (quasi Drude–like dispersion), the omega arms are interconnected along the direction of the E-field. As seen above, the plasma frequency ω_p is usually higher than the magnetic plasma frequency ω_{mp} for an unbalanced metamaterial. As a consequence, the condition of a balanced composite structure, achieved when $\omega_p = \omega_{mp}$, requires an

increase of ω_{mp} or a decrease of ω_p.

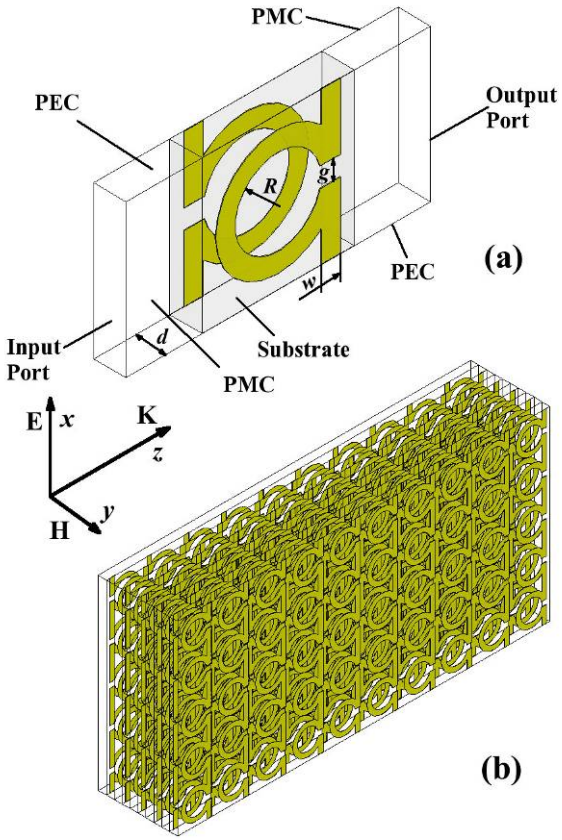

Fig. 2.2 Schematic view of (a) omega unit cell and (b) omega pattern array with an edge illumination by a plane wave.

In order to satisfy this criterion for omega type arrays, we first considered a lumped-element circuit description of the magnetic response of the current loops [9, 10, 19] and focused on some guidelines to achieve a balanced structure with negative-zero-positive behavior. For the current loops, the magnetic angular resonance frequency ω_0 can be described by the equation:

$$\omega_0 = \frac{1}{\sqrt{LC}} \tag{2.1}$$

where L is the inductance of the current loops and C is the total capacitances between the broadside coupled split ring resonators. Using a parallel-plate model, the total capacitance C (the fringing effect is not considered) is approximated by

$$C = \frac{1}{2} C_g = \frac{1}{2} \frac{\varepsilon_0 \varepsilon_r w}{d} (\pi \frac{2R + w}{2} - \frac{g}{2}) \tag{2.2}$$

where C_g is the capacitance between two half circular rings of current loops, ε_0 ,ε_r are the effective permittivity of vacuum and substrate, respectively. w is the wire width, R is the inner radius, g is the gap of omega pattern and d is the thickness of substrate. The inductance L of omega pattern is given by

$$L = \mu_0 \pi R^2 / d \tag{2.3}$$

The relation between the magnetic plasma frequency ω_{mp} and the resonant frequency ω_0 can be expressed as

$$\omega_{mp} = \frac{\omega_0}{\sqrt{1-F}} \tag{2.4}$$

where $F = \frac{\pi R^2}{\mathrm{S}}$ is the fraction occupied by the interior ring of the omega pattern in the xz plane, S is the area of the basic unit cell in the xz plane. On the other hand, the electric plasma frequency ω_p can be described in a first approximation by Pendry's formula as follows [19]

$$\omega_p^{\ 2} = \frac{2\pi c_0^2}{a^2 \ln(a/r)} \tag{2.5}$$

where a and r are the periodicity of the wire array and wire radius, respectively. It can be seen that the plasma frequency ω_p increases with the wire radius r. The cross section of wire considered here is rectangular, different from the original circular shape in Pendry's model, but the plasma frequency has an analogous function, i.e., increasing with the wire width w [21]. Therefore, we see that reducing the strip width will cause an increase of ω_{mp} and a decrease of ω_p simultaneously, which could be employed as a rather simple method to achieve a balanced condition.

The aforementioned arguments can be used not only as a first estimate of the relevant geometry of the omega inclusions but also as guidelines to tune ω_{mp} and ω_p. However, as the magnetic and electric responses are not strictly separated, a finer optimization has to be conducted by means of a full wave analysis. In practice, this procedure was performed with High Frequency Structure Simulator (HFSS) by Ansoft, a finite element commercial software package. The dimensions of the basic unit cell were chosen as follows: R = 1.1, w = g = 0.5 (unit: mm). For these simulations, we assumed a substrate with the following dielectric characteristics at centimeter wavelength (ε = 4.0, $tan\delta$ = 0.02) and a thickness of 0.8mm for the model

(Fig. 2.2). The basic cell dimensions are 3.9mm along *x* and *z* directions. My colleague Mr. G.regory HOUZET initially performed the geometrical dimensions calculation.

2.2.2 Balanced condition

The first clue for a zero gap CRLH metamaterial is a broad transmission window, which is assessed by the magnitude of the scattering parameter S_{21}. It is however difficult to conclude on the left-handedness or right-handedness of the dispersion characteristics. Consequently, we calculated in the second stage the dispersion characteristics according to the method we used in [22, 23] based on the Bloch Floquet theorem. Note that this approach is similar to the retrieval method reported in references [24, 25]. For this calculation, only one cell was considered along the propagation direction whereas an infinitely long periodic array was mimicked along the transverse directions with proper boundary conditions (see Fig. 2.2 (a)). Perfect **E** conditions were applied for the surfaces normal to the omega arms and perfect **H** boundaries to the surface parallels to the omega plane. In short, the solved scattering matrix is converted into the corresponding transfer matrix M which is also termed ABCD or chain matrix. On the other hand, the chain matrix of a homogeneous propagation medium can also be written as a function of a complex propagation constant $\gamma=\alpha + j\beta$ where α and β depict the evanescence of the wave and the phase constant. *z* is the reduced impedance of the propagation medium with respect to its surrounding environment.

$$M = \begin{bmatrix} A & B \\ C & D \end{bmatrix} = \begin{bmatrix} ch(\gamma a) & z \cdot sh(\gamma a) \\ \frac{1}{z} \cdot sh(\gamma a) & ch(\gamma a) \end{bmatrix} \tag{2.6}$$

By equating term by term the various matrix elements of the microstructured and homogeneous media it can be shown that

$$\alpha = \frac{1}{a} \ln \left| A \pm \sqrt{A^2 - 1} \right| \tag{2.7}$$

$$\beta a = \angle \left(A \pm \sqrt{A^2 - 1} \right) + 2k\pi, k \in Z \tag{2.8}$$

$$z = \pm \sqrt{\frac{B}{C}} \tag{2.9}$$

The information about the index is implicitly presented in the complex propagation

constant since

$$n = \frac{c\gamma}{i\omega} \tag{2.10}$$

The dispersion characteristics of the real and imaginary parts of the propagation constant are displayed as a function of $\alpha.a$ and $\beta.a$ (a is the periodicity along the propagation direction; Fig. 2.2). It can be noted that the phase constant β is negative in the frequency domain in the 8.0~12.8 GHz frequency domain with a positive group velocity v_g ($\partial\omega/\partial\beta$). Hence, the group velocity and phase velocities of the propagating wave are antiparallel and therefore it supports a backward wave (LH mode). On the other hand, it supports a forward wave (RH mode) above 12.8 GHz. The corner frequency between the two modes is at 12.8 GHz where the phase constant is zero (infinite wavelength). In contrast with conventional Split Ring Resonator array (see Fig. 2.1), here the group velocity ($\partial\omega/\partial\beta$) does not vanish and presents a value close to 5.5x10 ^{7} m.s^{-1} by taking an estimate of the slope at k=0. Below the resonant frequency of the current loops, corresponding to a forbidden gap, the evanescence of the waves is directly related to the decay length α^{-1}.

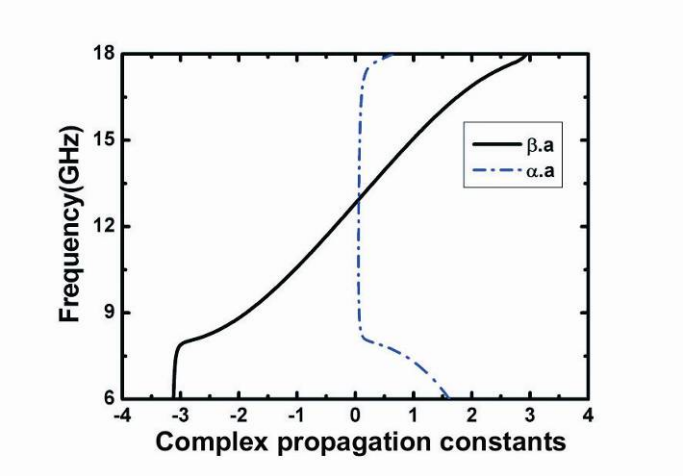

Fig. 2.3 Dispersion characteristics of the negative-zero-positive index structure depicted in Fig. 2.2 (b).

The variations of the Bloch impedance and of the refractive index, which can be determined from Eq. 9 and Eq. 10, are plotted in Fig. 2.4. The physical meaning of n below ω_0 (grey region) is doubtful since the incident wave is evanescent. Just above ω_0, a spike can be seen in the impedance resulting from the resonance effect. The refractive index exhibits a smooth transition between the negative band (8.0 ~ 12.8GHz) and the positive band (12.8 GHz~16.0 GHz), hence, a transition frequency

at 12.8 GHz where the refractive index value is zero. A Drude model (continuous increase of the negative permittivity up to the electric plasma frequency) can describe the frequency dependence of the effective permittivity. Although a slight resonant feature is superimposed at 8.1 GHz, the value of the effective permittivity is always negative. The effective permeability shows a well-defined negative peak at the resonance frequency with an increase in the losses. Importantly, the effective permittivity and permeability becomes zero at 12.8 GHz, indicating the electric and magnetic plasma frequencies ω_p and ω_{mp} are equal to each other. Strictly speaking, there is still small discrepancy between the real part values of permittivity and permeability since the impedance z does not reach unity at 12.8 GHz. Even though, this does not influence the realization of the balanced condition for metamaterial.

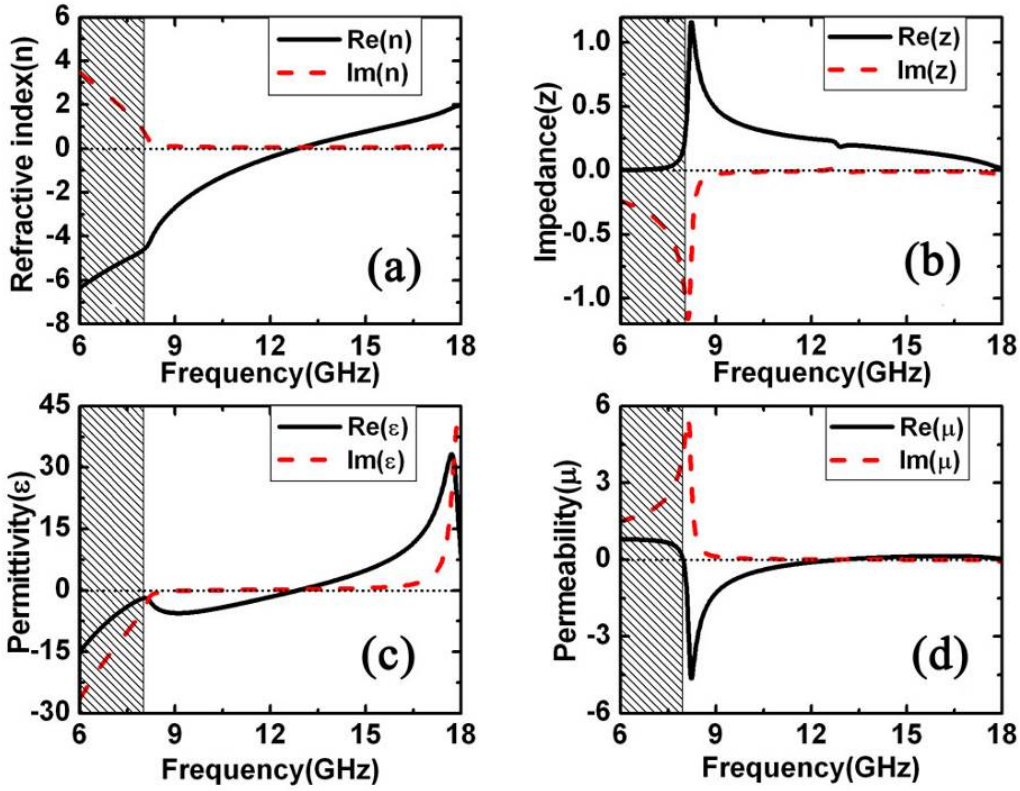

Fig. 2.4 Effective parameters of negative-zero-positive structure retrieved from the scattering parameters of one unit cell. (a) Refractive index. (b) Impedance. (c) Permittivity. (d) Permeability.

2.2.3 Tunability of balanced structure

As the balanced structures enable smoothly switch from LH branch to the RH one, this opens the possibility to fabricate tunable balanced composite metamaterials. However, when some tunability is introduced, the magnetic plasma frequency ω_{mp}

should always be equal to the plasma frequency ω_p in order to maintain the balanced condition, which considerably increases the difficulties. Basically, tunability can be introduced by changing the value of the capacitance C given by Eq. 2.2 via the modification of the unit cell geometry for fixed tuning or by varying the permittivity of the substrate. Such a tuning of ω_0 yields a concomitant shift of the magnetic plasma frequency ω_{mp} which varies as the inverse of the square root of the permittivity of the substrate according to Eq. 2.4.

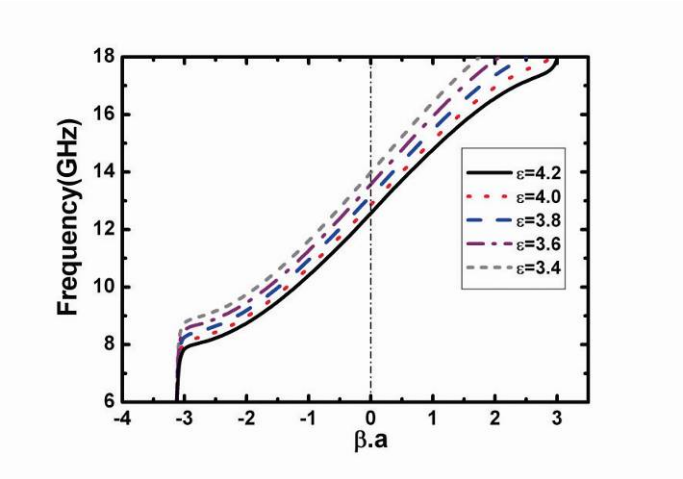

Fig. 2.5 Propagation phase constant as a function of the substrate permittivity.

For the frequency dependence of this artificial permittivity, the plasma frequency ω_p can also be described as the cutoff frequency of a metal wire array given by [26, 27]

$$\omega_p = C_{light} / 2a\sqrt{\varepsilon_r} \tag{2.11}$$

where a is the periodicity of the wire array. From Eq. (2.4) and Eq. (2.11), we see that both ω_{mp} and ω_p are proportional to $1/\sqrt{\varepsilon_r}$. Therefore, the balanced condition will be independent on the permittivity of the substrate. In order to check this analysis, the influence of the substrate permittivity on the balanced condition was studied numerically. The results of this study in terms of dispersion characteristics are shown in Fig. 2.5. It is important to note that the balanced criterion is maintained when the permittivity of substrate varies. The transition frequency increases gradually from 12.5 GHz to 14.0 GHz as the relative permittivity of substrate is decreased from 4.2 to 3.4 with a step of 0.2. In summary, by incorporating some materials which exhibit a tunable permittivity such as liquid crystals and ferroelectrics, it is possible to realize a reconfigurable balanced composite omega-based metamaterial.

2.3 Transmission measurement of slab sample

In order to confirm experimentally the main conclusions of the previous theoretical analysis, we carried out two complementary studies. We firstly performed transmission measurements of a metamaterial slab in order to check the absence of a band gap between the LH and RH transmission window. The second type transmission experiment was carried out on a prism-like prototype under angle-resolved conditions in order to determine the refractive index via the Snell-Descarte's law.

In practice, the metamaterial slab (Fig. 2.6(a)) consists of 100 layers of epoxy glass with omega patterns printed on one side by the standard Print Circuit Board (PCB) technology. Each layer consists of 10 unit cells along the *z*-direction and 18 unit cells along *x* with the same periodicity of 3.9 mm. Two horizontal strips were printed at the top and bottom edges of each layer to further increase the electrical length of the omega arms in order to avoid the influence of the wire finite length [28].

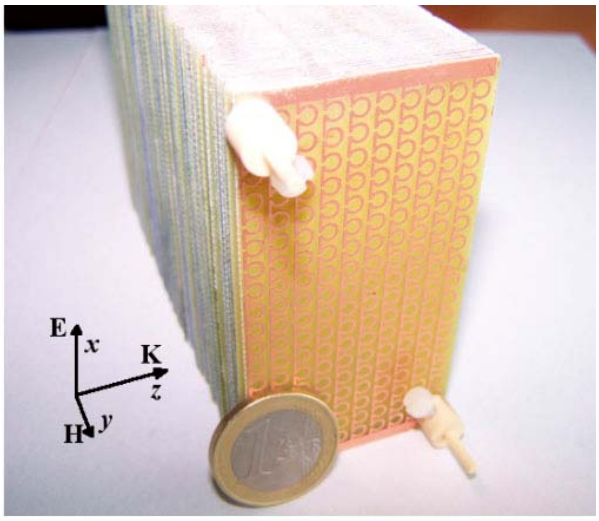

Fig. 2.6 Photograph of slab sample fabricated for transmission measurements

For transmission experiment, the metamaterial slab was placed between two aluminum plates with microwave absorbers (Eccosorb AN-75) on the sidewalls as shown in Fig. 2.7. This parallel plate wave guiding set up is similar to the one described in Ref. [29]. The spacing between the aluminum plates supported by several PolyvinylChloride (PVC) cylinders fits the horn apertures equal to 7.5 cm,. Two pairs of horns were used to initiate a Gaussian shaped electromagnetic excitation at the input and for probing the transmitted signal at the output for X band and for Ku bands respectively. The incident wave was set to propagate along the

z-direction with the electric field along the *x*-direction and the magnetic field along *y*. The transmission spectrum was measured by a HP 85107A Vector Network Analyzer.

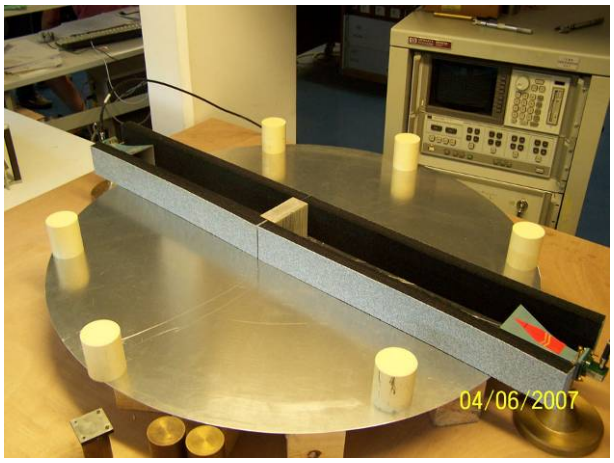

Fig. 2.7 Photograph of the transmission coefficient measurement setup. The upper aluminum plate was removed for clarity.

Figure 2.8 compares the experimental and simulation transmission results. It can be seen that the slab exhibits a broad pass-band from 8.3 ~ 16.0 GHz with a good agreement with the simulated transmission window. Despite the ripple resulting from the truncation of the structure, no band gap is evidenced in the pass-band, which is consistent with the analysis of the dispersion curve of Fig. 2.2. The transmission level of pass band is -8 dB, which means maximum insertion loss of metamaterial is 0.8 dB/cell, nearly fitting the real application requirement. This low loss property of omega based metamaterial is similar to the conclusion reported by Refs [7-9].

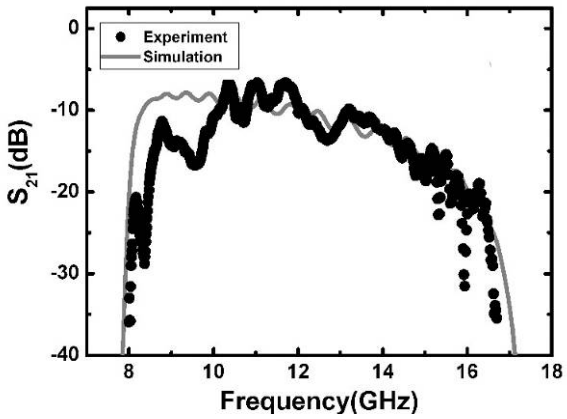

Fig. 2.8 Transmission coefficient of the metamaterial slab. The experimental and simulated results are denoted by black circular and grey line, respectively.

2.4 Angle resolved measurement of the prism like device

2.4.1 Anisotropic properties of Omega pattern

It is well known that most conventional metamaterials exhibit intrinsically anisotropic properties, i.e., showing the negative effective parameter only in one or two directions but still positive value in other directions. The omega based metamaterial cell used in this chapter cannot be the exception. In order to fully describe the property of omega pattern elementary cell, we will try to retrieve all the effective parameters tensors. As the reverse orientation of the face-to-face omega patterns, the magnetoelectric effect arising from asymmetry of the current loops gap is not considered [20]. The complex permittivity and permeability components can be diagonalizable

$$\varepsilon = \begin{Bmatrix} \varepsilon_x & 0 & 0 \\ 0 & \varepsilon_y & 0 \\ 0 & 0 & \varepsilon_z \end{Bmatrix} \qquad \mu = \begin{Bmatrix} \mu_x & 0 & 0 \\ 0 & \mu_y & 0 \\ 0 & 0 & \mu_z \end{Bmatrix} \tag{2.12}$$

In the previous sections, the permittivity and permeability components ε_x and μ_y have been retrieved by calculating the electric field and magnetic field polarized along x and y axes, respectively (Fig. 2.2). In the following parts, the other four principal elements of permittivity and permeability tensors are retrieved using the same method, i.e., calculating the scattering parameters. As a consequence, the incident wave with different polarizations as well as the various orientation of the structure is considered in following parts.

2.4.1.1. ε_y and μ_x

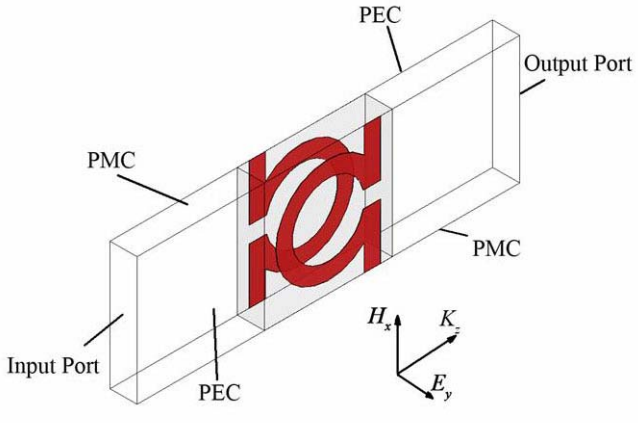

Fig. 2.9 The basic unit cell is bounded by the PMC and PEC boundaries along x and y directions, respectively. An incident beam is illuminated along z direction to retrieve the permittivity and

permeability tensors ε_y and μ_x.

In this section, we would like to retrieve the permittivity and permeability tensors ε_y and μ_x. Contrary to the configuration of the basic unit of omega pattern shown aforementioned (Fig. 2.2(a)), PEC and PMC periodic boundaries are applied along y and x directions, respectively. Using HFSS Ansoft commercial package, we calculate the scattering parameters of incident beam with electric field in the x and magnetic field in the y axes, hence, the permittivity and permeability elements ε_y and μ_x can be retrieved.

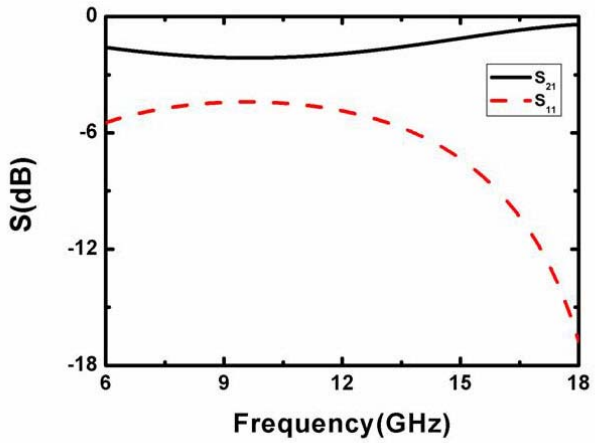

Fig. 2.10 The transmission and reflection for the basic unit cell of omega-based metamaterial under the incident beam electric field polarized along y and magnetic field along x axes, as shown in Fig. 2.8

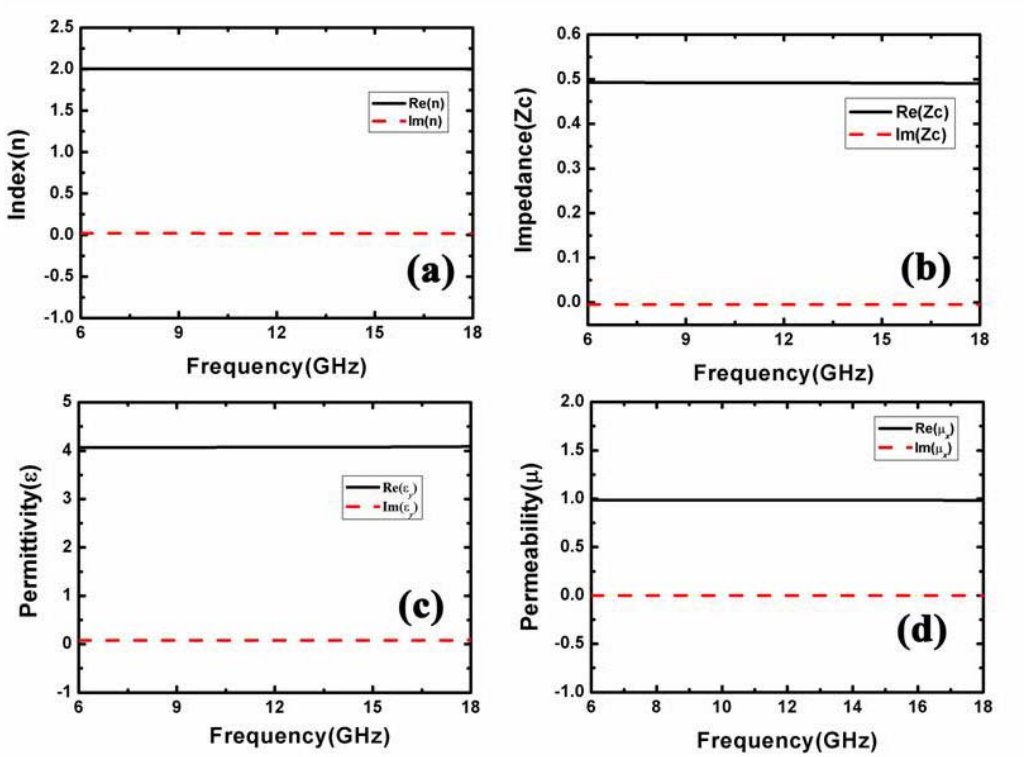

Fig. 2.11 Characteristic parameters for the unit cell of omega pattern as shown in Fig. 2.8. (a) Index; (b) Impedance; (c) permittivity tensor element ε_y, (d) permeability tensor element μ_x . The real and imaginary parts of the each effective parameters are represented by solid black and red dashed lines, respectively.

Fig. 2.10 shows the magnitude of transmission and reflection for the omega pattern cell with the specified orientation (See Fig. 2.9). The basic cell for metamaterial under this configuration shows a high pass band except for some loss, which is similar to a transparent substrate. As the incident magnetic field is perpendicular to the omega cell axis, the induced circular current can no longer be excited by external magnetic field, hence, magnetic resonance does not exit. As omega pattern has no response to the incident beam, the whole unit cell is somewhat like a pure dielectric substrate, which is confirmed by the consequent retrieval of effective parameters. As shown in Fig. 2.11, both ε_y and μ_x are remained constant as 4.07 and 0.99, respectively in a relative large band, which are very close to the corresponding effective parameters values of pure epoxy glass.

2.4.1.2 μ_z

In this section, we would like to obtain permeability tensor elements μ_z. In order to set the incident magnetic field polarized along z direction, an incident beam was

propagated normal to the surface of omega pattern. Two pairs of the Master and Slave periodic boundaries were employed along the lateral directions. As it is not possible to connect Master or Slave boundary to waveport directly in HFSS model setup, we employ two waveguides bounded by PEC and PMC boundarries to guide a plane wave to transmit through omega pattern cell layer (Fig. 2.12). The unit cell has a thickness of 1.66 mm along the transmitted direction.

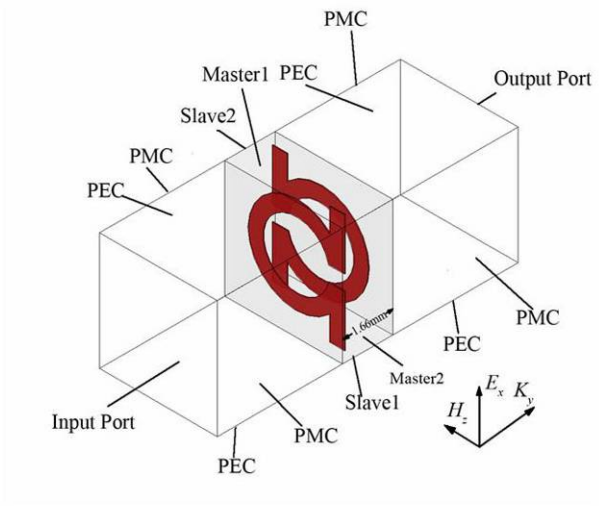

Fig. 2.12 The basic unit cell is assumed to be illuminated along the *y* direction. Periodic boundaries with two pairs of Master and Slave were employed transversal to the propagation direction. The thickness of unit cell along propagation direction is 1.66mm. An incident beam with electric polarized along *x* direction and magnetic polarized along *z* direction was propagated.

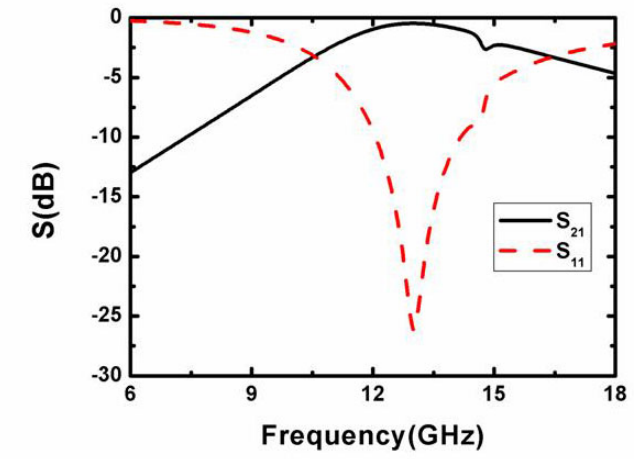

Fig. 2.13 The magnitude of transmission and reflection for omega pattern under the normal incidence shown in Fig. 2.9.

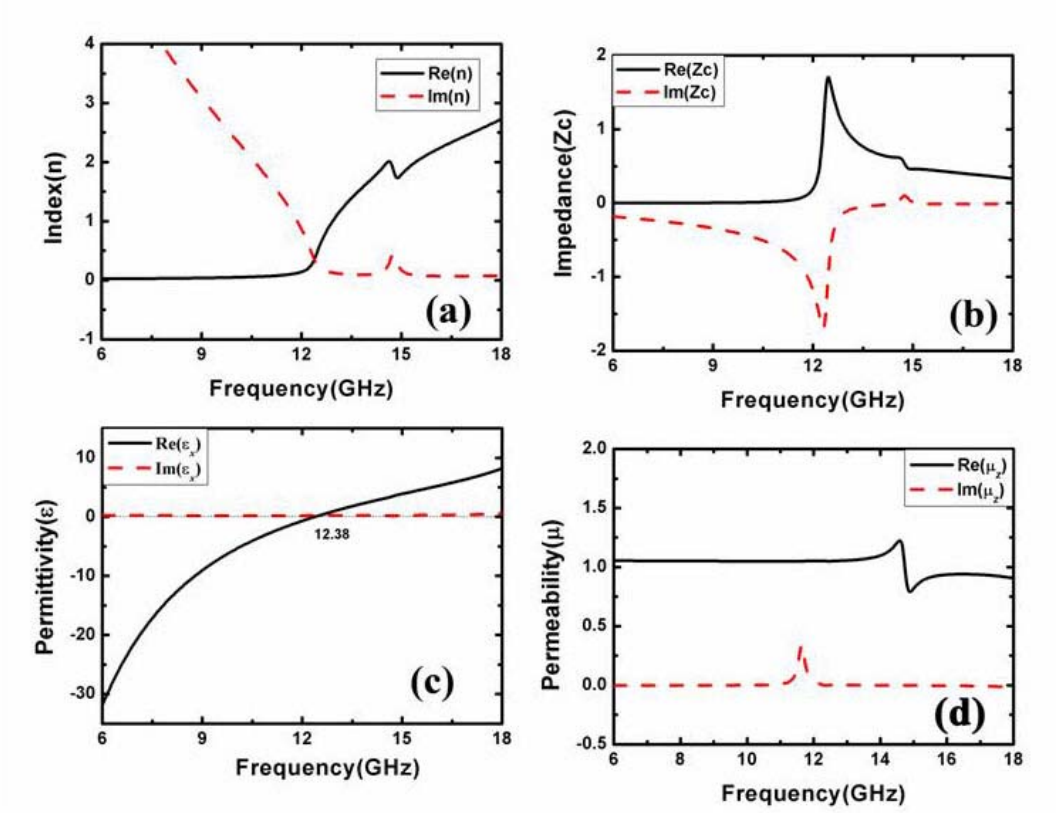

Fig. 2.14 Effective parameters of omega pattern retrieved from the scattering parameters of one unit cell under normal incidence. (a) Refractive index. (b)Impedance. (c) Permittivity tensor element μ_z. (d) Permeability tensor element ε_y. The real and imaginary parts of the each effective parameters are represented by solid black and red dashed lines, respectively.

Fig. 2.13 shows the magnitude of transmission and reflection for omega cell under normal incidence. It exhibits a high-pass property with a transmittance peak around 12.38 GHz. From the effective parameters plotted in Fig. 2.14, the effective permittivity tensor element ε_x is always negative up to 12.38GHz, corresponding to the small transmittance at low frequency band. As the incident beam is electrically polarized parallel to the omega arms, the electric resonance can still be excited as the configuration in previous section. In comparison to electric resonance of the unit cell under the grazing incidence (See Fig. 2), electric plasma frequency ω_p has shifted a little lower, which is due to the varied periodicity for continuous wires (omega arms) along the y and z directions in the y-z plane. Fig. 2.14(d) shows the frequency dependent permeability. We can see the permeability component along μ_y remains constant as 1.05 for the most the frequency range except for a weak resonant around 14.68 GHz.

2.4.1.3 ε_z

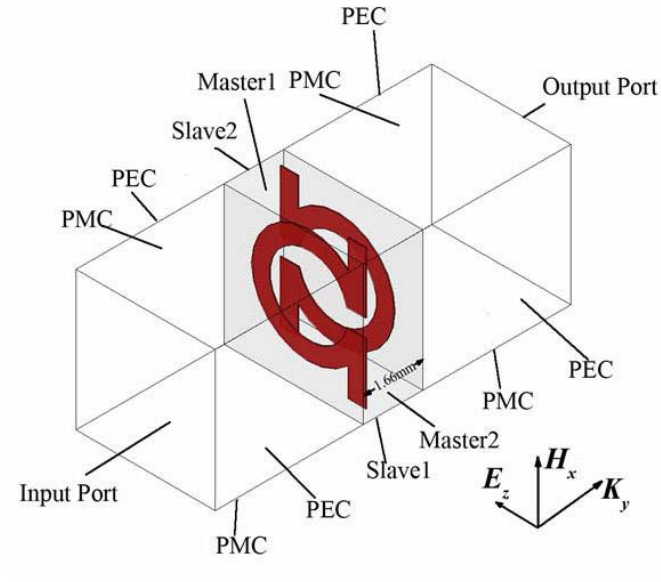

Fig. 2.15 The basic unit cell is assumed to be illuminated along *y* direction. Periodic boundaries with two pairs of Master and Slave definition were employed transversal to the propagation direction. The thickness of unit cell along propagation direction is 1.66mm. An incident beam is electrically polarized along *z* direction and magnetically polarized along *x* direction.

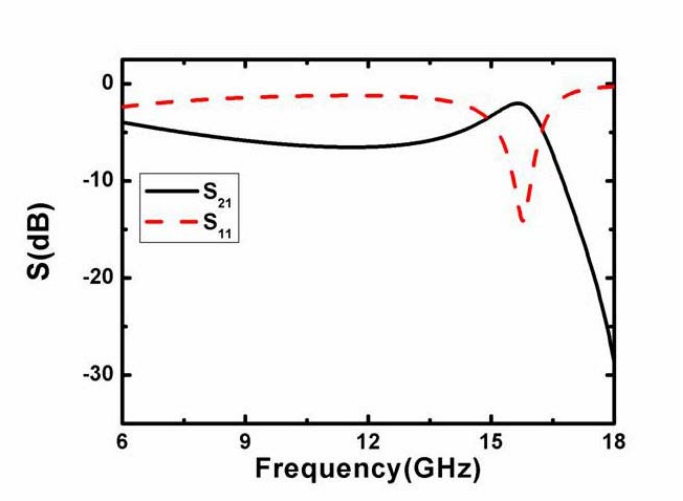

Fig. 2.16 The scattering parameters of the omega pattern under the normal incidence with proper polarization as shown in Fig. 2.14.

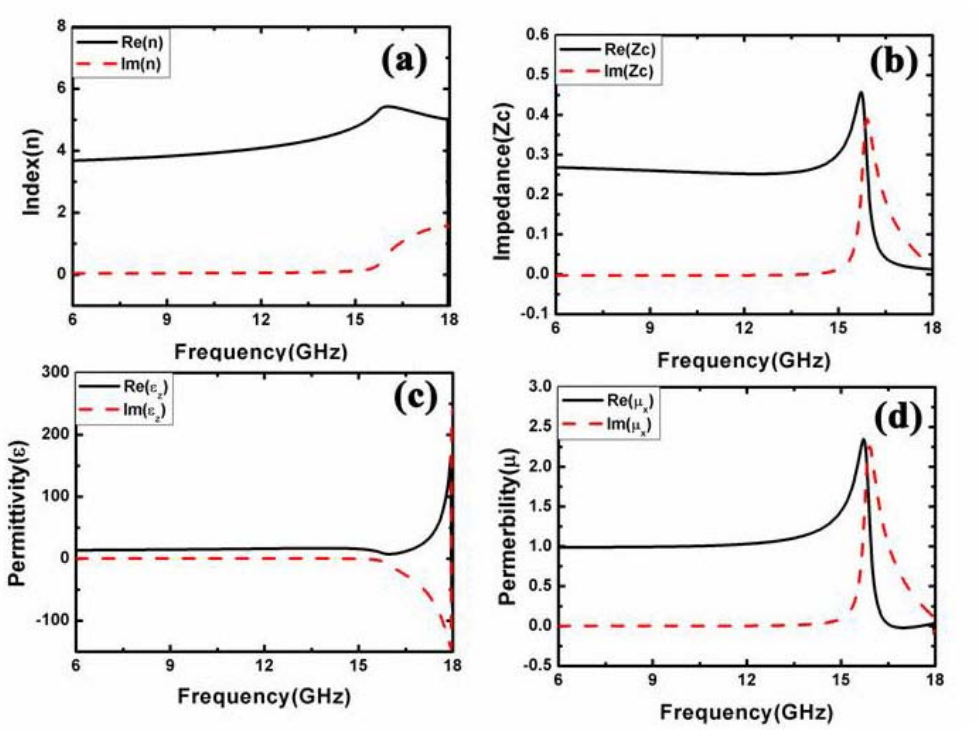

Fig. 2.17 Effective parameters of omega pattern retrieved from the scattering parameters of one unit cell under normal incidence. (a) Refractive index. (b) Impedance. (c) Permittivity. (d) Permeability. The real and imaginary parts of the each effective parameter are represented by solid black and red dashed lines, respectively.

In order to retrieve the permittivity elements $\varepsilon_{z,}$ we set a plane wave, having electric field polarized along z and magnetic field polarzied along the *x*, to transit normal to surface of the unit cell. Peiodic bounaries Master and Slave are also used along the tranverse direction of unit cell, whereas PEC and PMC are bound to the *z* and *x* direction of two waveguides so as to lauch to required polarized wave. Fig. 2.16 shows the scattering parameters of unit cell. It can be seen that a tranmittance dip occurs above 15.3 GHz. Fig. 2.17 shows the effective parameters retrieved from the scattering parameters. As shown in Fig. 2.17(c), the permittivity component ε_z keeps constant as 16.0 from 6.0 to15.0 GHz, followed by the resonant regime above 15.0 GHz with a peak value as high as 300. This electric resonance arising from the dipole resonance of the omega ring is responsible for the transmittance dip. On the other hand, due to the electric resonance, the permittivity tensor component ε_z is much larger than that of the pure substrate of 4.0 at the lower frequencies, similar to the results of the broadside coupling SRR reported by Prof. J. A. Kong's group [30]. Fig. 2.17(d) shows the frequency dependent permeability tensor element $\mu_{x.}$ We can see the permeability remains unity below 15.0 GHz, which is the same as that

retrieval from the case of ε_y and μ_x. However, above 15.0GHz, μ_x exhibits a slight resonant behavior with a peak of 2.3 at 15.7GHz, and then decreases sharply to zero.

2.4.2 Microstructured and homogenous Prisms

Over the past investigations of the metamaterial prism, a homogenous model was often used to look into the behavior of metamaterial prism refractions [31-34]. However, this simplicity neglects the local field distribution especially for the field around unit cells. Furthermore, the effective permittivity and permeability tensors rather than isotropic assumption are rarely used for a full description of metamaterial property

While the refracted index and characteristic impedance were plotted under Bloch wave condition (unit cell of an infinite medium), the demonstration of negative-zero-positive index requires designing a prototype where n can be assessed by the Snell-Descartes law. To this aim, the slab schematically described in Fig. 2.1(b) cannot be used for inducing a double refraction under tilted incidence and subsequent measurement of the beam shift at it was performed in [12]. Indeed, the artificial medium made of a stacked omega array is highly anisotropic with a negative value of n only in the propagation direction. Such a difficulty can be alleviated by using a prism-type prototype as illustrated in Fig. 2.18.

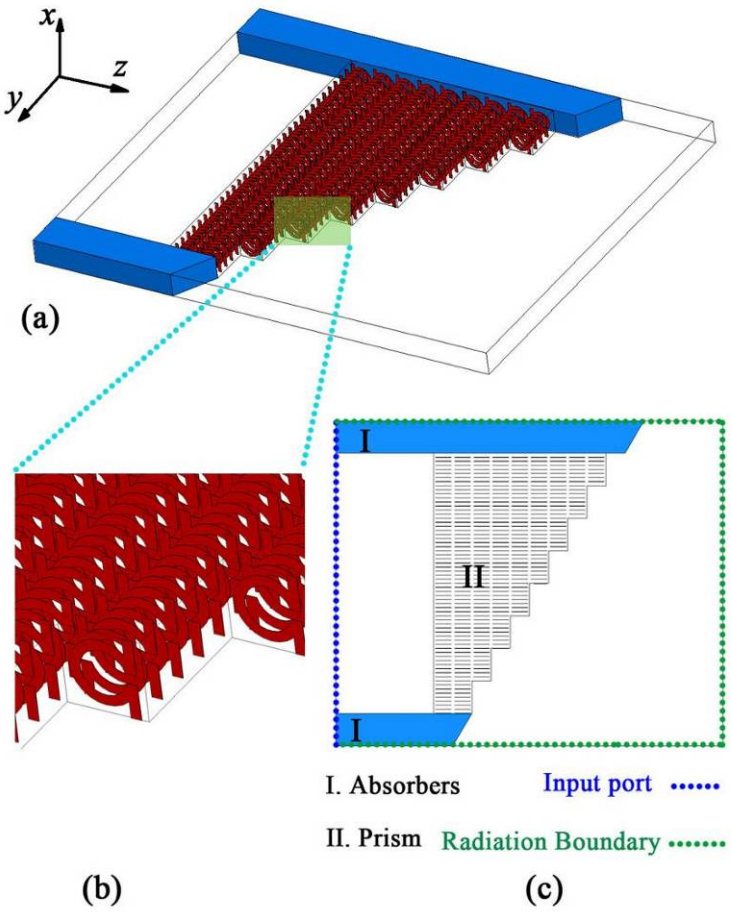

Fig. 2.18 Illustration of the prism configuration for refraction simulation. (a) 3D view of the prism model which consists of eight stairs; (b) Close up view of one step which consists of four cells along *y* direction and one cell along *x* direction; (c) Top view of the prism model indicating the boundaries.

The model of the prism sample is depicted in Fig. 2.18. The incident beam impinges onto the sample at normal incidence with a Gaussian intensity profile tailored by side absorbers. For this condition of excitation, the electromagnetic wave undergoes refraction at the second tilted interface. Let us note that the prism model, which exhibits a stair-like pattern with four-unit-cells (eight omega patterns) step along the *y*-direction and one-unit-cell along *z*, can be considered as a wedge of 30.5°. Eight stairs along the *y*-direction was found as good tradeoff between computer resources, accuracy and reasonable calculation time. The prism was positioned between two PECs, which sandwiched a unit cell in the *x* direction so that the structure can be considered as infinite along this direction. We performed ab-initio calculations by a proper representation of the microstructure.

In addition, we also performed a comparative analysis of the refraction by

treating the prism as a homogenous medium. To this aim, we used a permittivity and permeability tensor approach, which is much more rigorous compared to the isotropic homogenous analysis used in several previous publications [30, 31], to define the prism constitutive dielectric and magnetic properties. The homogenous model has the same size and boundaries setup as the microstructured one except for the metallic inclusions. Table 2-1 shows the permittivity and permeability tensor components at three specified frequencies, which are retrieved in the previous section.

TABLE 2-1 Anisotropic effective parameters of omega pattern at specified frequencies

Frequency (GHz)		10.9	12.8	15.0
n		-1.0052	-0.038	0.777
ε	ε_x ($\tan \varepsilon_x$)	-3.49+0.13i (-0.036)	-0.17+0.04i (-0.234)	4.90+0.57i (0.117)
	ε_y ($\tan \varepsilon_y$)	4.07+0.08i (0.02)	4.07+0.08i (0.02)	4.07+0.08i (0.02)
	ε_z ($\tan \varepsilon_z$)	15.56+0.36i (0.023)	16.66+0.38i (0.02)	15.74+0.24i (0.0153)
μ	μ_x ($\tan \mu_x$)	0.99+0.00034i (0.0003)	0.9858+0.0003i (0.0003)	0.9850+0.0003i (0.0003)
	μ_y ($\tan \mu_y$)	-0.28+0.03i (-0.091)	-0.0082+0.0002i (-0.022)	0.1232+0.005i (0.04)
	μ_z ($\tan \mu_z$)	1.050+0.007i (0.007)	1.055+0.002i (0.002)	0.818+0.002i (0.002)
θ_r (°) (Retrieval value)		-30.6°	-1.10°	23.2°
θ_r (°) Homogenous prism		-28.6°	-2.6°	21.5°
θ_r (°) Microstructured prism		-25.6°	-0.4°	25.4°

Figure 2.19 shows the magnitude map of the electric field component along the *x* axis at the mid-plane between the top and bottom perfect electric conductors at 10.9 GHz with an index value extremely close to -1. The structure is illuminated from the left side according to the layout displayed in Fig. 2.18(a). In Figs. 2.19(a)

and (b), the arrow and dotted lines represent the direction of refracted wave and the surface normal, respectively. For the homogenous prism (Fig. 2.19(a)), it can be noticed that the wave is not diffracted when impinging on the first interface so that a quasi plane wave is preserved within the negative index medium. This wave interacts with the second interface where it experiences a negative refraction as it can be pointed by tracing the direction of the transmitted beam with respect to the surface normal. The field distribution inside the microstructured prism is comparable to that of the homogenous one at the same phase (Fig. 2.19(b)). Some high field regions inside the microstructured prism can also be noticed, which gives an insight into the local field in the vicinity of the omega patterns. Furthermore, it can be interesting to confirm the direction of refraction by calculating the far field patterns in the *y*-*z* plane, which is displayed in Figs. 2.19(c) and (d) for the homogenous and microstructured prisms, respectively. The far field pattern is plotted with the angle calculated with respect to the -*y* axis. For the frequency of interest, the refractive angles are -28.6° and -25.6° for the homogenous and microstructured prisms, respectively. These values are in a relative good agreement with that calculated based on the effective parameters listed in Table 2-1. It is believed that the slight discrepancy is mainly due to the stair-case interface rather than a smooth one. The small side lobe which occurs at the positive direction with respect to the surface normal is due to the diffraction effect investigated by Smith *et al.* [32].

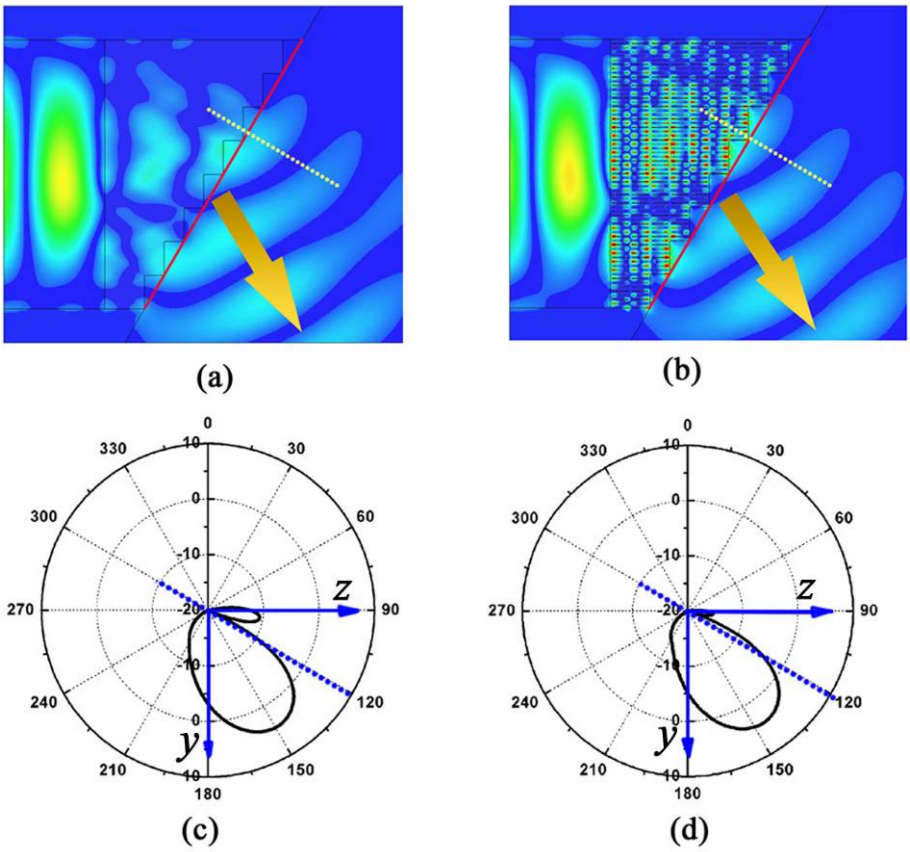

Fig. 2.19 Numerical evidence of negative refraction at 10.9 GHz. Electric field intensity of (a) homogenous and (b) microstructed prisms at the same input phase; refractive angle plotted in far field for (c) homogenous and (d) microstructed prisms.

The same kind of numerical refraction experiment was conducted at a frequency of 12.8 GHz, which is expected to be near-zero index condition. At Table 2-1, the effective index of -0.038 was calculated at 12.8 GHz. The map of the magnitude of the E_x component is displayed in Fig. 2.20. As shown in Figs. 2.20(a) and (b), the refracted beam is oriented parallel to the surface normal, indicating that the refraction index is extremely close to zero. This is confirmed by the refractive angles of -2.6° and -0.4° retrieved from the far field pattern (Figs. 2.20(c) and (d)) for the homogenous and microstructured prisms. The wavelength inside the prism is seen extremely huge, which is consistent with the zero-index properties. Furthermore, the magnitude of the refracted beam at 12.8 GHz is comparable to that of 10.9 GHz, indicating high transmission level with a non vanishing group velocity. At last, Fig. 2.21 shows the results of the calculation performed for a frequency of 15.0 GHz. It can be seen that the transmitted beam is refracted positively with respect to the surface normal, as it is confirmed by the far field angle-resolved transmissivity.

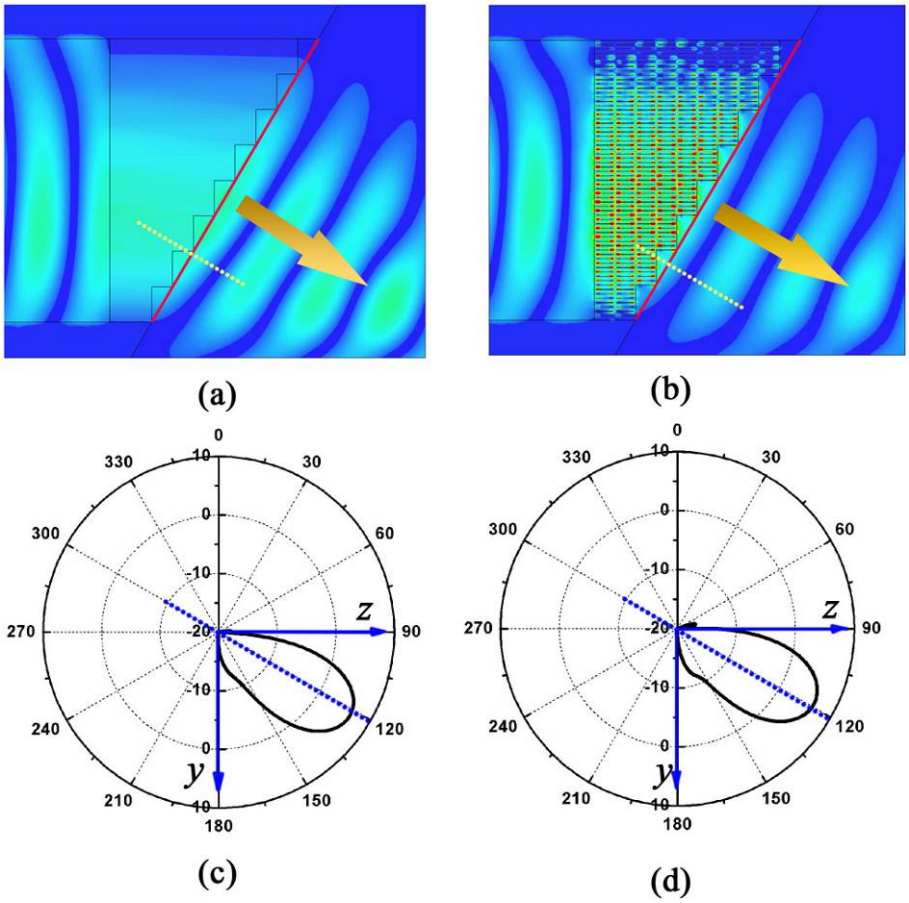

Fig. 2.20 Numerical evidence of zero-index refraction at 12.8 GHz. Electric field intensity of (a) homogenous and (b) microstructed prisms at the same input phase; refractive angle plotted in far field for (c) homogenous and (d) microstructed prisms.

From the comparison between the homogenous and microstructured prisms shown in Figs 2.19, 2.20 and 2.21, good agreements can be observed not only for the electric field distribution but also for the far field pattern. A satisfactory agreement of the refractive angle is also achieved between the retrieved values and those deduced from the far field pattern.

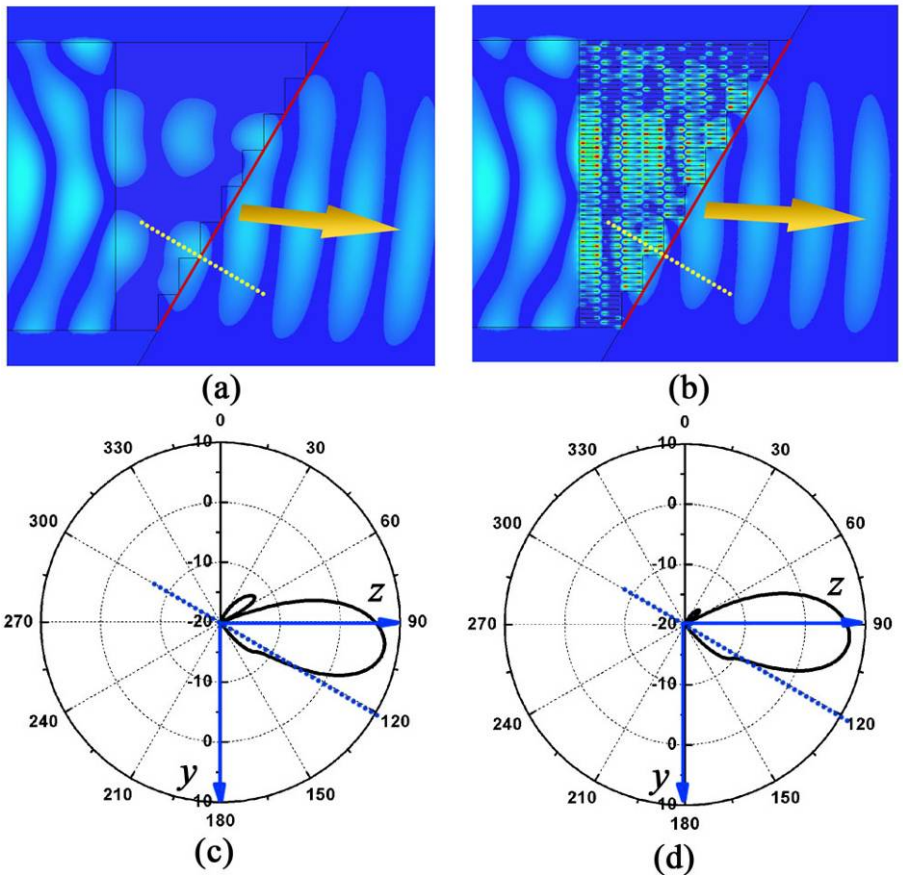

Fig. 2.21 Numerical evidence of positive refraction at 15.0 GHz. Electric field intensity of (a) homogenous and (b) microstructed prisms at the same input phase; refractive angle plotted in far field for (c) homogenous and (d) microstructed prisms.

2.4.3 Prism Experiment

The prism sample, composed of eleven stairs rather than eight for the simulation prototype, is shown in Fig. 2.22. The prism sample slice was also fabricated using a printed circuit board technology. The number of unit cells of each layer along the propagation direction at the first and last stairs were increased to five and fifteen, respectively. Each layer consists of 18 unit cells along *x*-direction with a periodicity of 3.9 mm.

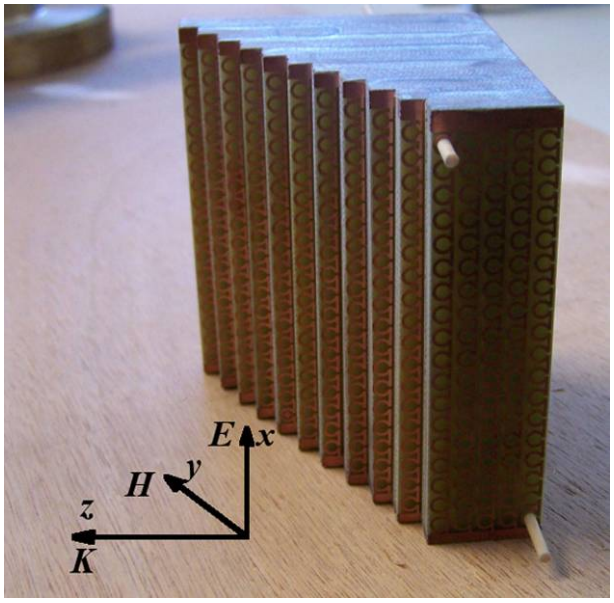

Fig. 2.22 Photograph of a prism–type sample.

The prism refraction experimental setup is shown in Fig. 2.23. Two absorbing layers (Eccosorb AN-75) are used in the input section for shaping the incident beam with a quasi-plane phase front. Absorber layers were also placed around the prototype for avoiding cavity effects which could result from the reflected beams. The angle resolved measurements of the transmitted field are carried out by means of a rotating detector whose angular position is recorded via a homemade large scale circular protractor with a step of 1.25°, as shown in Fig. 2.23. In comparison to the similar scattering chamber which can be found in the literature notably in [13], the emission as well as the detection of electromagnetic wave was performed via two horn antennas rather than by using waveguides flanges. For covering all the bands, two sets of horn pairs were used. The two horns were placed at the periphery of the 96-cm-diameter aluminium plates in order to satisfy the far field condition. The refraction measurement was performed by a HP 85107A Vector Network Analyzer.

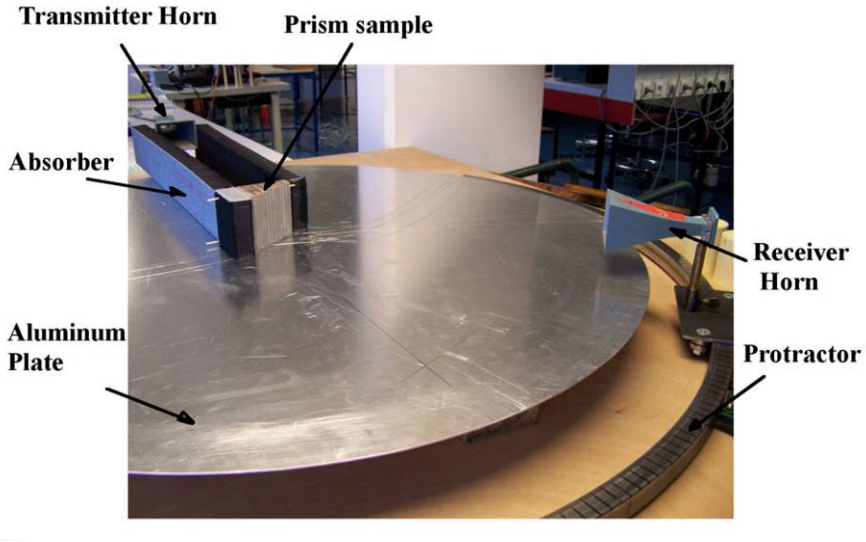

Fig. 2.23 Photo of the angle resolved measurement setup (the upper metal aluminium plate was removed for clarity).

Fig. 2.24 shows the intensity of the refracted beam as a function of angular position of the probing horn antenna for three characteristics frequencies 12.0, 13.605 and 15.0 GHz. The calibration was performed when the prism sample was removed. By taking the central angle at the half wave bandwidth, the refraction beam peak was found to occur at -22.0°, 0° and 13.0°, at 12.0 GHz, 13.605 GHz and 15.0 GHz, respectively. As the incident angle at the interface between the prism and air is 30.5°, the corresponding index can be calculated as -0.72, 0 and 0.46. More importantly, the refracted beam intensity at 13.605 GHz is comparable to that of 12.0 GHz, confirming that refracted beam though this type of zero-index is no vanishing.

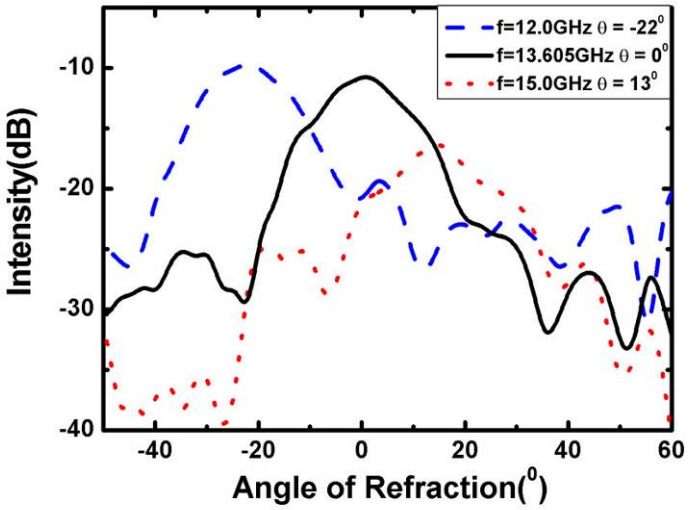

Fig. 2.24 Angle dependence of the detected signal at three characteristic frequencies: at the negative index band at 12.0 GHz (dashed line), zero index at 13.6 GHz (solid line) and positive index at 15 GHz (dotted line).

The experimental and simulated index as a function of frequency are plotted in Fig. 2.25. It can be seen the refractive index is negative from 10.2 GHz to 13.605 GHz with a minimum value of -1.7. Above 13.6 GHz, *n* becomes positive with values ranging from 0 to 0.5. Clearly, the experimental result demonstrates that the proposed structure indeed exhibits a balanced property with a negative-zero-positive behavior. The frequencies shift of the transition frequency between experimental and simulated retrieval results is mainly due to a smaller permittivity value of the substrate than that employed in simulation. To verify this assumption, we performed an extra calculation for the effective index of the proposed omega structure but with decreasing permittivity of the substrate. As seen in Fig. 2.25, an excellent agreement between the simulation and experimental results can be obtained when the permittivity of epoxy glass is assumed to be 3.6. It is noted that the balanced condition is also achieved when the permittivity of the substrate is lowered from 4.0 to 3.6, because it does not depend on the substrate permittivity as shown in Fig. 2.5.

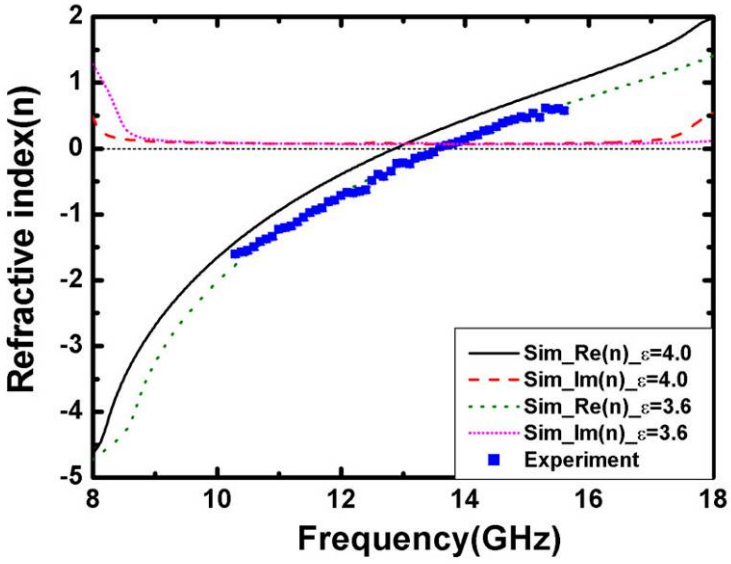

Fig. 2.25 Simulated and measured refractive indices n as a function of frequency. The solid and dotted lines represent the real parts while the dashed and short dotted lines show the imaginary parts of n when the substrate is assumed to have relative permittivity of 4.0 and 3.6, respectively. The square symbol denotes the experimental refractive index, which was plotted from 10.2 to 15.0 GHz with a step of 0.1 GHz.

2.5 Group velocity

From the measured value of index for omega pattern, the group velocity v_g of this metamaterial can also be obtained from as follows [17, 35]

$$v_g = \frac{c}{\mathrm{Re}(n) + \omega \dfrac{\partial \mathrm{Re}(n)}{\partial \omega}} \tag{12}$$

As shown in Fig. 2.26, the group velocity continuously decreases as the frequency is increased, indicating that the proposed structure is highly dispersive. For the transition frequency of 13.6 GHz, the group velocity is 4.8 x 10^7 m.s^{-1}, which clearly shows that energy can be transmitted through the device and offers possibility to make use of the desired frequency point of zero refractive index.

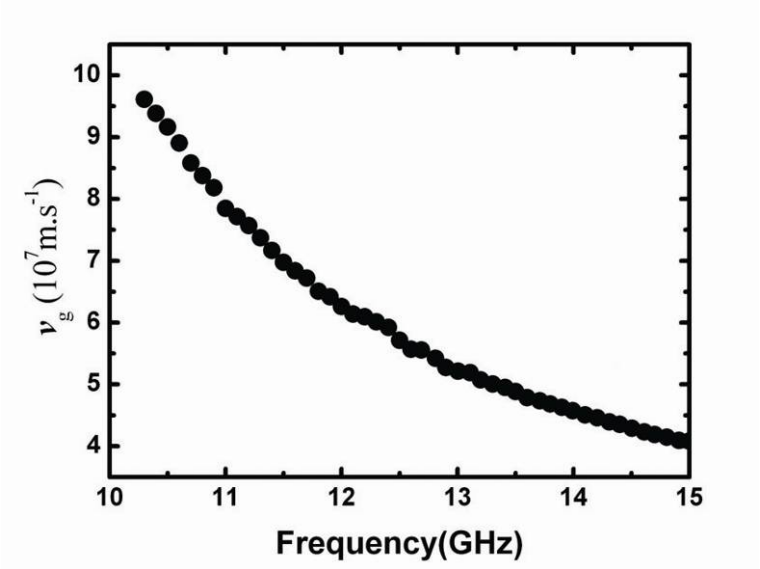

Fig. 2.26 Frequency dependence of the group velocity.

2.6 Summary

In summary, we have proposed, built and demonstrated a balanced composite LH/RH metamaterial based on omega-type structures. This bulk balanced metamaterial was designed to achieve the equality between the electric and magnetic plasma frequencies, which are the characteristic frequencies to distinguish the negative permittivity and permeability to the positive ones, respectively. We firstly assess the balanced condition on the basis of the calculation of the dispersion characteristics and subsequent retrieval of the effective parameters. Then, we experimentally and numerically demonstrated that this structure exhibits a broad transmission window from 8.3 GHz to 16.0 GHz without any gap in between. From the angle-resolved measurement of a prism-like sample, it was found that the proposed structure shows a negative-zero-positive property with a seamless transition frequency at 13.605 GHz. The group velocity exhibits continuous frequency dependence notably at k = 0 with a non-vanishing group velocity. Furthermore, the insensitiveness of the balanced frequency to the tuning of the substrate permittivity makes the proposed architecture an interesting platform for steerable antennas at microwave frequencies.

References

[1]. V. G. Veselago, Sov. Phys. Usp. **10**, 509 (1968).

[2]. R. Shelby, D. R. Smith, and S.Schultz, Science **292**, 77 (2001).

[3]. D. R. Smith, W. J. Padila, D. C. Vier, S. C. Nemat-Nasser, and S. Schultz, Phys. Rev. Lett. **84**, 4184 (2000).

[4]. J. B. Pendry, A. J. Holden, D. J. Ribbins, and W. J. Stewart, IEEE Trans. Microwave Theory Tech. **47**, 2075 (1999).

[5]. F. Zhang, Q. Zhao, Y. Liu, C. Luo, and X. Zhao, Chin. Phys. Lett. **21**, 1330 (2004).

[6]. C. R. Simovski and S. He, Phys. Lett. A **311**, 254 (2003).

[7]. J. Huangfu, L. Ran, H. Chen, X. Zhang, K. Chen, T. M. Grzegorczyk, and J. A. Kong, Appl. Phys. Lett. **84**, 1537 (2004).

[8]. L. Ran, J. Huangfu, H. Chen, Y. Li, X. Zhang, K. Chen, and J. A. Kong, Phys. Rev. B **70,** 073102 (2004).

[9]. L. Ran, J. Huangfu, H. Chen, X. Zhang, K. Cheng, T. M. Grzegorczyk, and J. A. Kong, Prog. Electromagn. Res. **51**, 249 (2005).

[10]. E. Lheurette, O. Vanbésien, and D. Lippens, Microwave Opt. Tech. Lett. **49**, 84 (2007).

[11]. A. Grbic and G. V. Eleftheriades, Phys. Rev. Lett. **92**, 117403 (2004).

[12]. A. Lai, C. Caloz, and T. Itoh, IEEE Microwave Mag. **5**, 34 (2004).

[13]. S. Lim, C. Caloz, and T. Itoh, IEEE Trans. Microwave Theory Tech. **53**, 161 (2004).

[14]. A. Lai, C. Caloz, and T. Itoh, IEEE Microwave Wireless Components Lett. **14**, 68 (2004).

[15]. T. Crepin, J. F. Lampin, T. Decoopman, X. Mélique, L. Desplanque, and D. Lippens, Appl. Phys. Lett. **87**, 104105 (2005).

[16]. A. Grbic and G. V. Eleftheriades, J. Appl. Phys. **98**, 043106(2005).

[17]. L. Brillouin, Wave Propagation and Group Velocity (Academic, New York, 1960).

[18]. H. Chen, B.-I. Wu, L.Ran, T. M. Grzegorczyk, and J. A. Kong, Appl. Phys. Lett., 89, 053509 (2006).

[19]. J. B. Pendry, A. J. Holden, W. J. Stewart and I. Youngs, Phys. Rev. Lett. **76**, 4773 (1996).

[20]. R. Marques, F. Mesa, J. Martel and F. Medina, IEEE Trans. Antennas Propag. **51**, 2572 (2003).

[21]. I. Bulu, H. Caglayan and E. Ozbay, Microwave Opt. Tech. Lett. **48**, 2611(2006).

[22]. T. Decoopman, O. Vanbesien, D. Lippens, IEEE Microwave Wireless Components Lett. **14**, 507 (2004).

[23]. C. Croënne, B. Fabre, D. Gaillot, O. Vanbésien, and D. Lippens, Phys. Rev. B, **77**, 125333 (2008).

[24]. D. R. Smith, D. C. Vier, T. Koschny, and C M. Soukoulis, Phys. Rev. E **71**, 036617 (2004).

[25]. X. Chen, T. M. Grzegorczyk, B.-I. Wu, J. Pacheco, and J. A. Kong, Phys. Rev. E **70**, 016608 (2004).

[26]. P. Markos and C. M. Soukoulis, Phys. Rev. B **65**, 033401 (2001).

[27]. X. Xu, Y. Xi; D. Han;, X. Liu, J. Zi, and Z. Zhu, Appl. Phys. Lett. **86**, 091112 (2005).

[28]. T. Koschny, M. Kafesaki, E. N. Economou, and C. M. Soukoulis, Phys. Rev. Lett. **93**, 107402 (2004).

[29]. R. A. Shelby, D. R. Smith, S. C. Nemat-Nasser, and S. Schultz, Appl. Phys. Lett. **78**, 489 (2001).

[30]. H. Chen, J. Zhang, Y. Bai, Y. Luo, L. Ran, Q. Jiang, and J. A. Kong, Opt. Express **14**, 12944 (2006).

[31]. D. R. Smith, P. M. Rye, J. J. Mock, D. C. Vier, and A. F. Starr, Phys. Rev. Lett. **93**,137405 (2004).

[32]. P. Kolinko and D. R. Smith, Opt. Express, **11**, 640 (2003).

[33]. R. B. Greegor, C. G. Parazzoli, K. Li, B. E .C. Koltenbah, and M. Tanielian, Opt. Express, **11**, 688 (2003).

[34]. C.G. Parazzoli, R. B. Greegor, K. Li, B. E.C. Koltenbah, and M. Tanielian, Phys. Rev. Lett. **90**, 107401 (2003).

[35]. J. F. Woodley and M. Mojahedi, Phys. Rev. E **70**, 046603 (2004).

Chapter 3 Low loss metamaterial at millimeter waves

3.1 Introduction

Millimeter wave, the highest radio frequency band ranging from 30 to 300 GHz, is considered as “bridge” from the microwave frequency band to the low infrared light that is also referred as “terahertz frequency”. Compared to lower bands, the wavelength of millimeter is much shorter, which allows for small and compact devices working at this frequency band. Besides, it is also made use in the field of remote sensing because signals in the 57 – 64 GHz region are subject to a resonance of the oxygen molecule and are severely attenuated [1]. A recent development has been imagers for security applications as clothing and other organic materials are translucent in some millimeter wave atmospheric windows. Therefore, the importance of devices of millimeter wave has increased in commercial and military communication, scanner and navigation technologies.

Recently, there has been considerable effort to construct engineered electromagnetic metamaterials [2] operating in a relative large spectrum [3-18] which includes the work devoted to millimeter wave as well [18]. Split ring resonator (SRR) arrays as proposed in the seminal work of Pendry [3] have been successfully used for designing and fabricating single negative magnetic media, along with double negative media [4, 5] when they are associated with wire arrays [6]. At centimeter wavelengths, successful experimental demonstrations were reported in the literature with first-principle proof experiments but also with practical applications such as negative refractive index lens [7] and artificial magnetic conductors [8]. The extension of such studies to higher frequencies notably at millimeter wave and sub-millimeter wavelengths (THz frequencies) was

addressed by several groups [9-14]. Notably, the group of Los Alamos reported on an efficient control of the transmission of electromagnetic waves through frequency selective surfaces (FSS) [9, 10]. For all of these studies, the main difficulty of realizing metamaterial at higher frequencies stems from the requirement of **H**-field polarization normal to the SRR planar pattern or consequent some variation types of magnetic cells [6, 17], a necessary condition for inducing a significant artificial magnetic polarization. On the other hand, as operation frequencies increases away from microwave frequency, elementary cell scale of metamaterial becomes smaller, bringing difficulty of the assembly for bulk sample having enough size along lateral direction to the incident beam, which is a necessary requirement for actual measurement. As a consequence, many of these studies take benefit of the electric polarization of the magnetic resonant particles [11-13] or employing of wires-pairs [6, 17], in a single layer arrangement and a front illumination.

However, the problem of extending the concept of artificial magnetism with an edge-illumination (grazing incidence) at millimeter frequencies was addressed by Prof. E. Ozbay's group [15]. In this work, one SRR plus three wires comprises elementary cell. The difficulty to blue shift the electrical plasma frequency was solved by a proper design of the wire array. Indeed, the plasma frequency $\omega_p \sim (\frac{n_{eff}}{m_{eff}})^{1/2}$ (effective electron density, n_{eff}, and electron mass, m_{eff}) was engineered by keeping thin wire arrays in order to take benefit of the increase of the effective mass while the effective electron density was adjusted via the metal filling factor. Promising results were reported on this basis of the comparison between closed and split ring patterns. Thus, an experimental evidence of the LH behavior of the transmission window was experimentally pointed out around 100 GHz. However, a direct application of this proof-of-principle experiment appears problematic at this stage, because the loss per cell is as high as 2.5 dB/cell. Under this condition, it seems difficult to envisage real applications with a sizable thickness of metamaterials such as those required for the fabrication of prism or lens devices. Besides, the fact to combine multiple arrays with one substrate patterned with SRRs clad by two other dielectric layers printed with metal wires increases the complexity of the assembling. Hence, the prototype is more sensitive to the fabrication imperfections, which influences the total performance of metamaterial [18].

In this chapter, we considered the problem of the fabrication of low-loss left handed metamaterial aimed at operating at W band (75-110 GHz). With respect to the previous works in this field, notably those aforementioned, the originality stems

from an omega type approach with a broad-side coupling scheme. In addition, the omega patterns are coupled via their arms along the direction transverse to the propagation [19-22]. This permits one to decrease the loaded quality factor of the micro-resonator array and, hence, to broaden their operating band while maintaining low intrinsic losses per basic unit cell. The experimental verification of the left-handedness will be carried out by three different approaches (i) normal incidence measurement and the retrieval of the effective parameters from the theoretical side (ii) the measurements of the phase offset between two prototypes of different lengths and (iii) the transmittance measurements by varying incidence angle.

3.2 Simulation

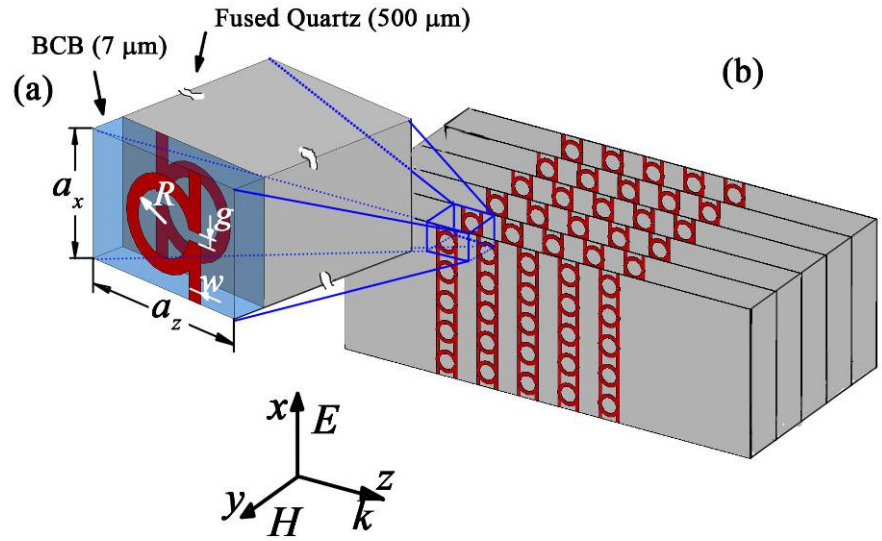

Fig. 3.1 (a) Schematic diagram of the basic unit cell. The dimensions of the basic unit cell are as follows: R = 90, g = 27.5, w = 42.0 (unit: μm). The periodicities along the x and z directions are 350 μm and 500 μm, respectively. (b) Schematic of the bulk metamaterial.

Figure 3.1(a) shows the basic unit cell, which consists of two reversed omega patterns on fused quartz substrates. Here, a thin dielectric film is sandwiched between omega patterns with standard photolithography techniques. This is different from the previous fabrication approaches such as the standard printed circuit board technology employed in the microwave frequencies, where we can pattern directly omega cells on both sides of dielectric substrate [19-22]. In fact, by increasing the operation frequency the relevant dimensions have to be shrunk whereas the thickness of common material of wafer such as quartz or GaAs can not be reduced accordingly due to proper rigidity required, hence, it is no longer possible to sustain

the desired effects with the omegas printed on both faces of a thick substrate. Clearly, wafer substrate with a thickness of 500 μm is only used to support elementary cells rather than the magnetic resonator substrate. In previous work mainly involved in the dissipation loss of left handed metamaterials (LHMs) [23], it is found that loss tangent of dielectric substrate plays an important role in the determination of total insertion loss of bulk metamaterial. Follow this guidance, we select benzocyclobutene (BCB) as dielectric substrate owing to its moderate dielectric constant and low loss-tangent in the millimeter waves and terahertz range along with its planarizing properties [24]. Besides, electric resonance arising from omega arms suffer strong from surrounding material, which means the higher dielectric permittivity, the lower electric plasma frequency. To make sure electric plasma frequency is high enough, we choose fused quartz rather than GaAs due to its lower dielectric constant [25].

The geometrical dimensions of omega cell are depicted in the caption of Fig. 3.1. BCB has a thickness of 7 um, is a good tradeoff between the desired simulation results and actual difficulty for the fabrication. The periodicity along *z* direction is 500 um, approximately one seventh of the wavelength of central frequency of interest, enable elementary cells to be considered as homogeneous medium.

The simulation is performed by using commercial software package CST MICROWAVE STUDIO (CST MWS) [26], which uses the finite integration technique (FIT). The combination of the proprietary PERFECT BOUNDARY APPROXIMATION (PBA) and the unbeatable efficiency of (FIT) is the basis for CST MICROWAVE STUDIO success. In time domain, the numerical effort of FIT increases more slowly with the problem size than other commonly employed methods. Fig. 3.2 illustrates the CST model for the elementary omega unit. In order to mimic bulk metamaterial array as shown in Fig. 3.1, we impose perfect electric conductor (PEC) and perfect magnetic conductor (PMC) boundaries along the transverse directions to the propagation direction of incident beam. The incident beam has electric and magnetic polarizations along the *x* and *y* directions, respectively.

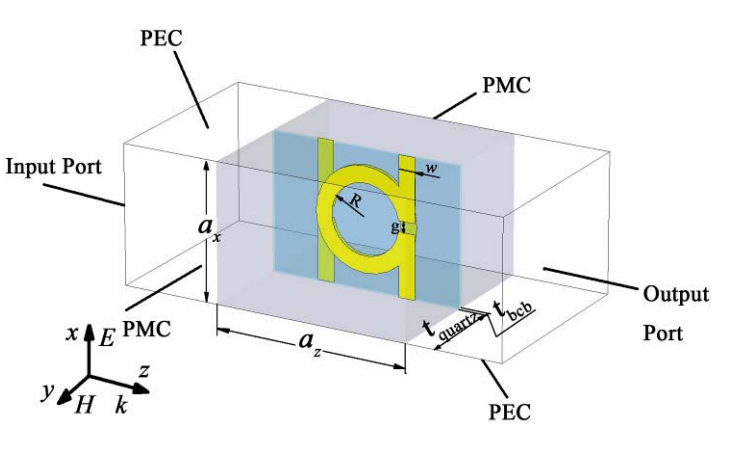

Fig. 3.2 CST model for elementary unit cell of metamaterial in W band. Omega pattern is made of gold with a thickness of 0.4 μm. BCB is defined with relative permittivity of 2.6 (tan δ=0.001) [24] while fused quartz has a relative permittivity of 3.794 (tan δ=0.0003) [25].

Figure 3.3 shows the dielectric constant of BCB versus frequency [24], in which we see both dielectric constant and loss tangent of BCB is rather small at few hundreds gigahertz. Although the datasheet has not show exact dielectric property for BCB around *W* band, we induced as the trend of dielectric property v.s. frequency. Here we set BCB has a relative permittivity $\varepsilon_{(BCB)}$=2.6+0.002i. The dielectric constants of fused quartz $\varepsilon_{Fused\ Quartz}$ = 3.794+0.003i can be readily found in the literature [25].

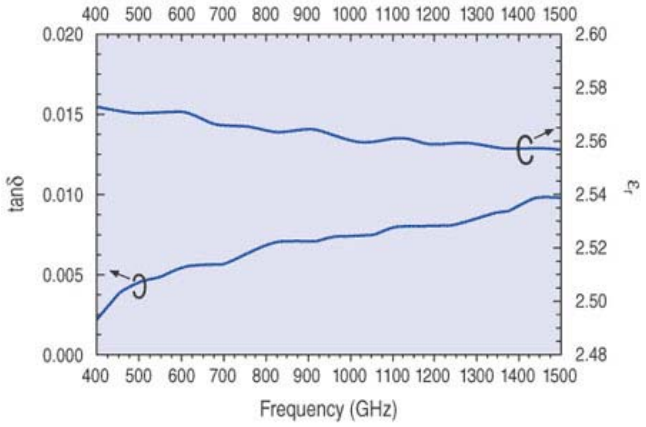

Fig. 3.3 Dielectric property of BCB as a function of frequency [24].

For the simulation setup, we use time domain solver of CST MWS which is more efficient than frequency solver. In this case, only quadrangular mesh can be used for time domain. As local field is concentrated between reversed omega patterns, mesh intensity for BCB layer is optimized by increases mesh number to 10 along the *y* direction. After obtaining the scattering parameters for elementary cell,

we can retrieve the dispersive diagram as well as the effective electromagnetic parameters by using common retrieval methods [27-29]. Figure 3.4 depicts propagation complex constant of elementary cell. As shown in Fig. 3.4, propagation phase $\beta. a$ (a is the periodicity along propagation direction) is negative from 76 to 87 GHz, whereas the slope $\partial\omega/\partial\beta$ is positive, revealing the phase velocity is antiparallel to the group velocity. Thus, the proposed omega pattern exhibits left handed dispersion in this band.

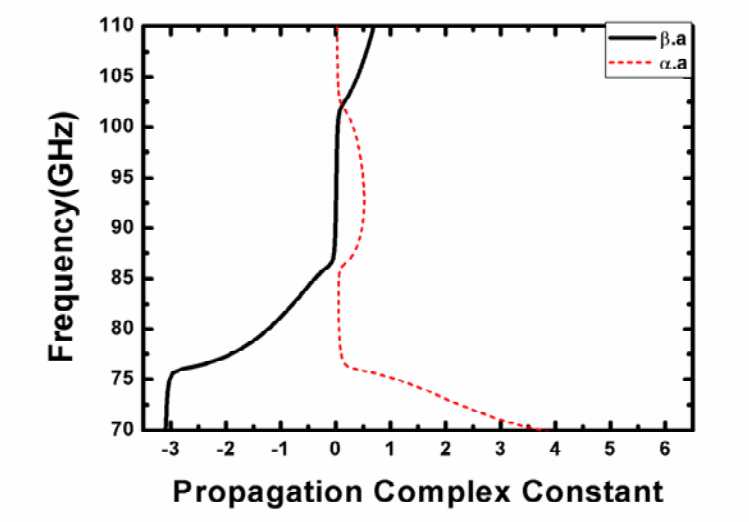

Fig. 3.4 The propagation constant versus frequency.

Figure 3.5 shows the effective parameters of omega type metamaterial at W band. The real part of effective index shows negative value from 76.1 to 87.0 GHz, whereas imaginary parts are close to zero, indicating this is a true negative index band where energy can be transmitted. From Fig. 3.5 (c) and (d), we see there is a Lorenetz-like magnetic resonance around 76.0 GHz, while the effective permittivity is always negative until 102.5 GHz, demonstrating the negative index is arising from the simultaneous negative permittivity and permeability. The negative value of index accompanied with high imaginary parts below 75.0 GHz is doubtful, as the wavelength is comparable to the periodicity [29].

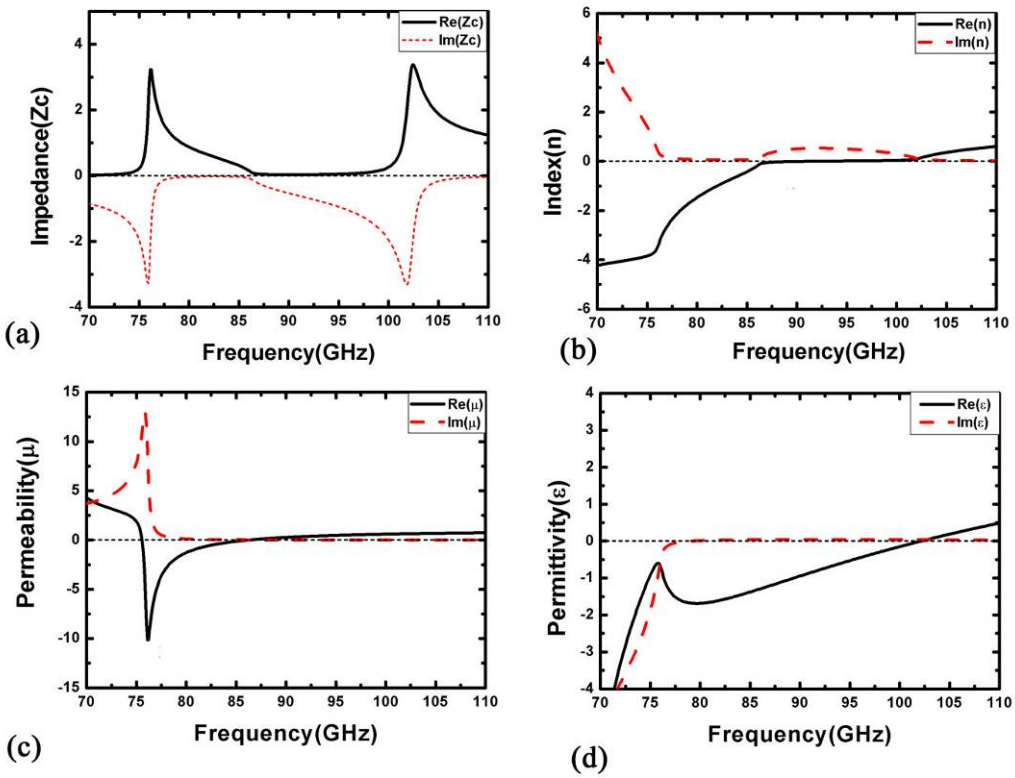

Fig. 3.5 The effective parameters of omega cell at W band. (a) impedance (z), (b) index(n), (c) permeability (μ), (d) permittivity (ε). The real and imaginary parts are represented by solid (black) and dashed (red) lines, respectively.

The transmission and reflection spectrum for 10 omega cells stacked along the propagation direction is also calculated and plotted in Fig. 3.6. It can seen that there are two passbands, one is from 75.0 to 90.0 GHz and the other one begins above 103.3 GHz, separated by a bandgap in between. From effective index shown in Fig. 3.5, we can conclude that the first passband is a LH band whereas the second is a true right-handed (RH) band where both permittivity and permeability are positive. It is noted that transmittance for LH passband is around -5.2 dB, corresponding to a maximum insertion loss of 0.52 dB/cell. This low insertion loss enables possibility for metamaterial application requirement at millimeter wave.

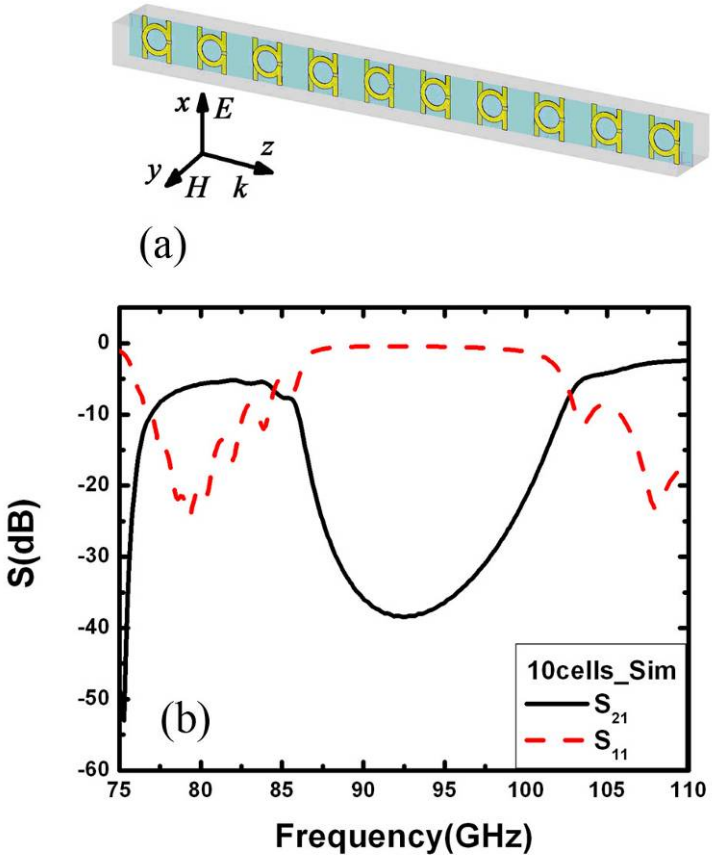

Fig. 3.6 (a) CST model and (b) scattering coefficient for 10 omega cells stacked along the propagation directions.

3.3 Fabrication

As the dimensions for omega unit cell operating at this frequency is much smaller than that at microwave frequencies, optical lithography technology is employed to fabricate the sample. Photo lithography, is a process used in micro fabrication to selectively remove parts of a thin film or the bulk of a substrate. It uses light to transfer a geometric pattern from a photo mask to a light-sensitive chemical photo resist, or simply "resist" on the substrate. A series of chemical treatments then engraves the exposure pattern into the material underneath the photo resist. For omega pattern, the whole process consists of following five steps, mask preparation, wafer, first omega layer, BCB layer, and second omega layer.

3.3.1 Mask preparation

In our actual fabrication process, a 2” 500-thick double-side polished fused quartz wafer is used. To be more efficient fabrication, on each of the wafers 6

individual layers (15.0 mm ×20.0 mm × 0.5 mm) were fabricated with 42 omega cells along the *x* direction. Three of them have 10 cells along the *z* direction and the other three 14 cells with a view to measuring the phase offset. As shown in Fig. 3.7, three layers masks are prepared, two masks for omega pattern and one for wafer and omega layer dicing, for full fabrication steps.

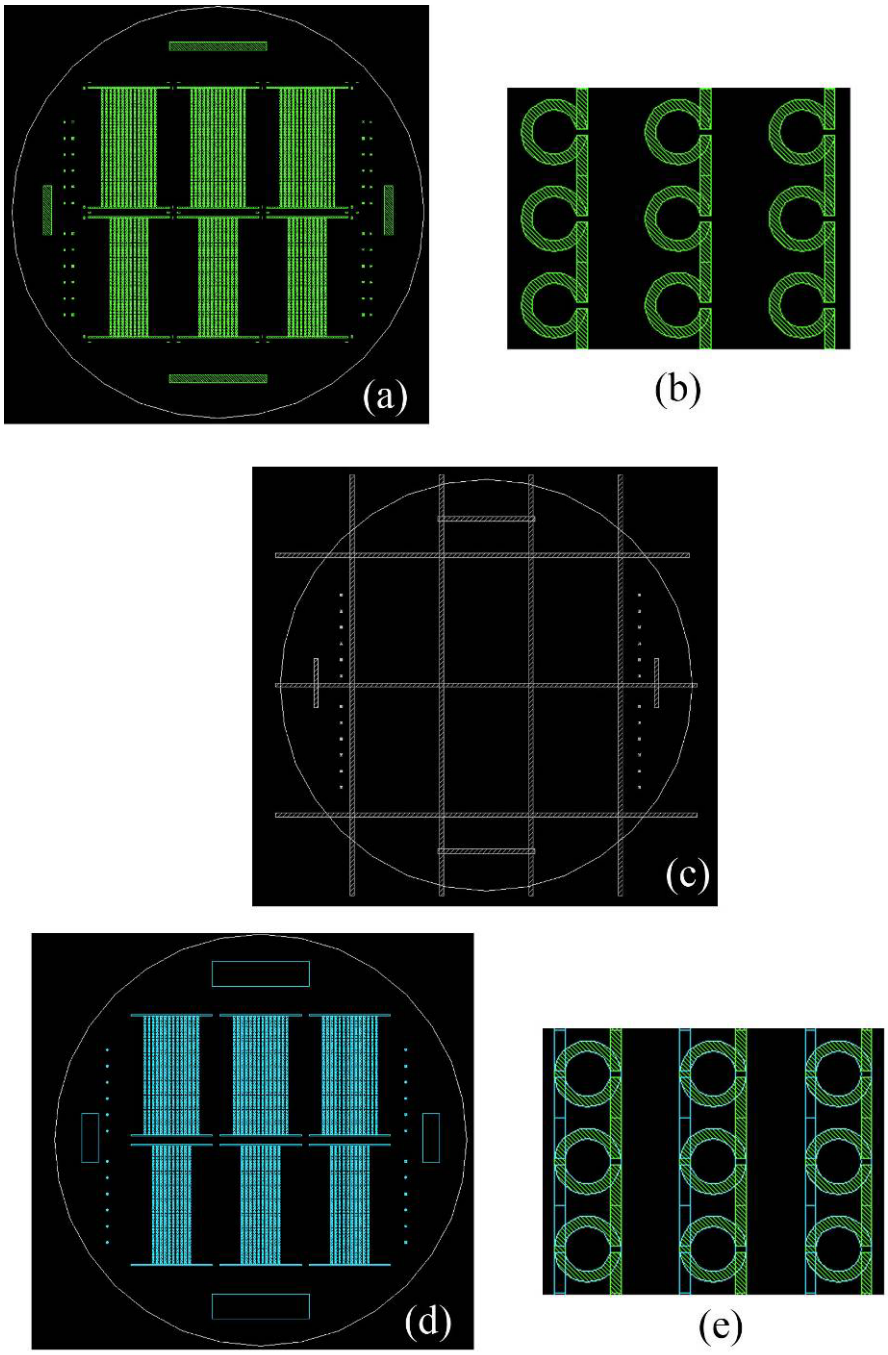

Fig. 3.7 Masks for fabrication of metamaterial at W band. (a) Mask for the first layer of omega pattern; (b) Zoom view of the first layer of mask; (c) Mask used for dicing; (d) Mask for second layer of omega pattern; (e) Zoom view of double omegas when the two masks of omega pattern overlaps

3.3.2 Wafer

We fabricated omega-like metamaterial (Fig. 3.1) using a surface micromachining process as shown in Fig. 3.8. The full fabrication process is composed of four steps: wafer preparation, first omega layer deposition, BCB layer, and the second omega layer. In the pre-process for each full process, one slice fused quartz wafer having a thickness of 500 μm was cleaned with two sides abolished. In total, 10 slices of quartz wafers were used such that we have enough slice of omega material to assembly a bulk structure. The wafer was initially heated to a temperature sufficient to drive off any moisture that may be present on the wafer surface. The subsequent fabrication process and relative parameters are summarized in Table 3-1 and described in detail in following parts.

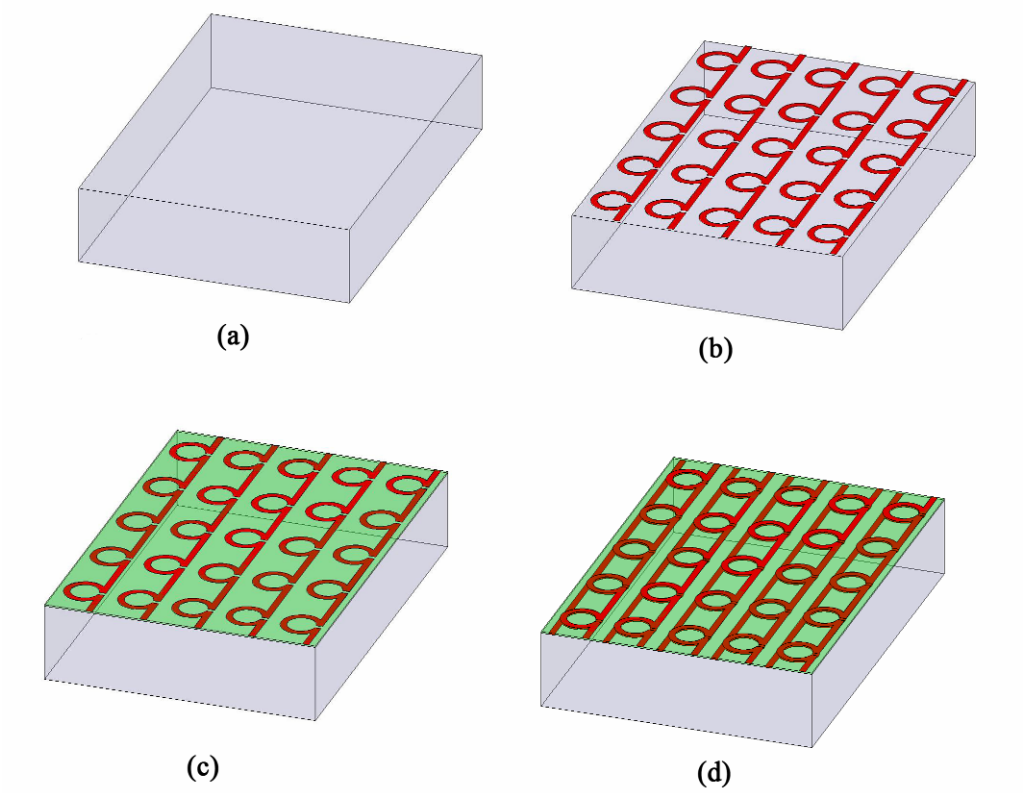

Fig. 3.8 Schematic view for simplified illustration of the fabrication process.

TABLE 3-1 Full steps of omega metamaterial fabrication

Stage I	**Deposite AZ1518 via spin coater RC8** Speed 4000 rpm– acceleration 5000 m/s^2 – 10s Prebaked at 110°C for 1mn Immersed into surfactant AZ326 for 35s, then rinsed by EDI water for 15s
	Exposure via mask aligner MA/BA6 Variable: Hard – Contact – 5.5s exposition time – 30µm gap Baked 125°C for 1mn
	Development Developer : mixture of 50 ml AZ400 / 150 ml EDI for 1 mn - then rinsed by EDI
	Metalization Plasma Ar / 500Å Ti / 4000 Å Au
	Lift-off by using acetone
Stage II	**Deposite adhensive promoter AP4000** Spin coater variable : 1500trs/mn – Acceleration 3 – 30s
	Deposite BCB Photosensible 4024-46 Depose 1.5ml BCB by pipette Variable of spin coater : i) 500 rpm - Acceleration 1 – 30s ii) 2500rpm – Acceleration 5 – 30s Prebaked at 80°C for 30mn
	Isolation via mask aligner MA/BA6 Variable: Soft – Contact / Spacer – 40s exposition – 30µm gap Baked at 125°C for 1mn
	Development on spin coater DeposeDS21000 on water by pipette Variable of spin coater : i)500 rpm – Acceleration 1 – 15s ii)2500 rpm – Accélération 5 – 20s
	Baked at Sawatec hotplate for 13 hours
Stage III	**Deposited AZ1518 via spin coater RC8** Speed 4000 rpm– acceleration 5000 m/s^2 – 10s Prebaked at 110°C for 1mn Immersed into surfactant AZ326 for 35s, then rinsed by EDI water for 15s
	Isolation via mask aligner MA/BA6 Variable: Hard – Contact – 5.5s exposition time – 30µm gap 125°C pendant 1mn
	Development Developer : mixture of 50 ml AZ400 / 150 ml EDI for 1 mn - then rinsed by EDI
	Metallization Plasma Ar / 500Å Ti / 4000 Å Au
	Lift-off acetone

3.3.3 First omega layer

In the first stage, a 1.2-μm thick AZ1518 positive image photoresist liquid was spin-coated on the surface of quartz wafer using RC8 spin coater (Suss MicroTec, Germany, shown in Fig. 3.9) with 4000 rpm and acceleration speed 5000 m/s^2 for 10 second. The photoresist covered water was then prebaked to drive off excess via a hot plate at 110 °C for one minute

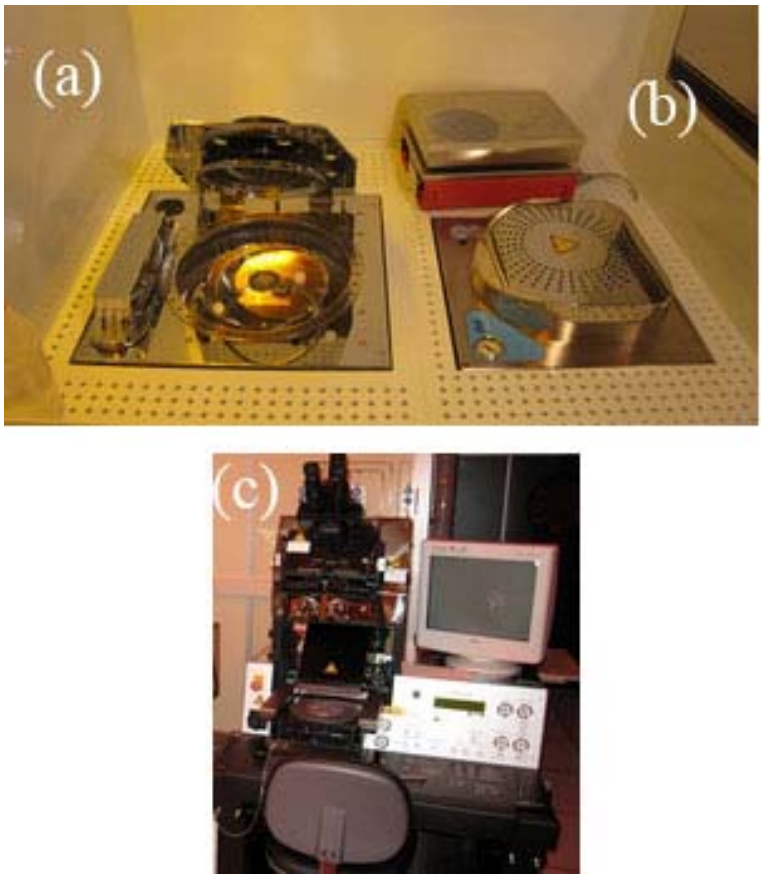

Fig. 3.9 RC8 spin coater (a), hotplate (b), and mask aligner MA/BA6 (Suss MicroTec)

After prebaking, the photoresist was exposed to a pattern of intense light. Using mask aligner MA/BA6 (Suss MicroTec), the first omega pattern on the top layer mask (Fig. 3.7(a)) was transferred on the photoresist via ultraviolet (UV) exposure process. A PEB (post-exposure bake), 125 °C for one minute, was carried out before developing, to help reduce standing wave phenomena caused by the destructive and constructive interference patterns of the incident light. Later, photoresist was developed by immersing wafer into 200 ml developer composed of AZ400 and (Electrodeionization) EDI water with volume ratio of 1:3 for one minute, followed by being rinsed by EDI water. The quality of the developing was checked

empirically whether photoresist was fully open or not through an optical microscopy. If it looks fine for requirement, we can turn to the metallization process of 400 nm Au/Ti (50nm) film. Otherwise, we need to repeat the photoresist process as stated above. Finally, photoresist was lifted-off by rinsing in acetone for several minutes. The photograph of resulting omega layer is shown in Fig. 3.10, where we can see the quality is rather good.

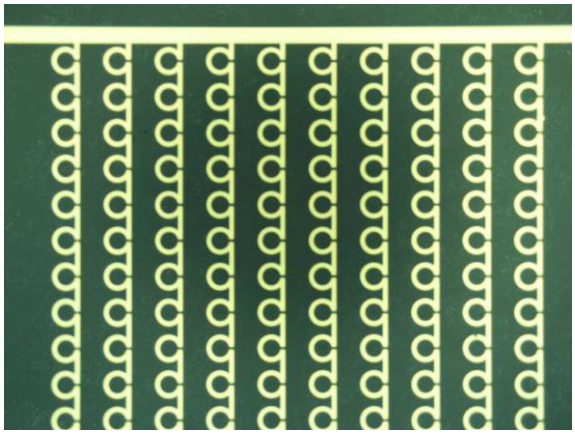

Fig. 3.10 Optical photograph of portion of first omega layer.

3.3.4 BCB layer

In this section, our purpose is to spin 7 μm thick BCB as well as the dicing line. A liquid adhesion promoter, AP4000, is applied to promote adhesion of BCB to wafer via using spin coater. 1.5 ml BCB photosensible 4024-46 liquid was then covered and spin-coated on water surface evenly. It is noted that the uniformity of resulting BCB layer is very sensitive to any bubble inside BCB liquid, which has to be removed by pipe before starting spin coating. Wafer was then prebaked in a hotplate at 80 °C for 30 minutes. With the second mask for dicing (Fig. 3.7(c)), some specified regions of BCB were exposed to UV light using mask aligner MA/BA6(Suss MicroTec) and then removed by adding DS21000. Finally, water was heated in oven (Sawatec) for 13 hours.

Scanning profile variation of dicing lines regions on BCB, the thickness of resulting BCB can be measured. If the thickness did not reach requirement, we had to remove and redo it again. BCB layer can be dissolved inside a mixture of H_2SO_4 and H_2O_2 with a volume ratio (5:1).

3.3.5 Second omega layer

The fabrication process for second omega layer is nearly the same as that of the first omega pattern: photoresist application, exposure, metallization and lift off. One thing to be noted is that perfect overlap of two omega layers is essential for mask alignment in the UV exposure process. Fig. 3.11(c) shows close-up view of omega-like metamaterial. We can see that fabrication quality and alignment between two omega layers are excellement.

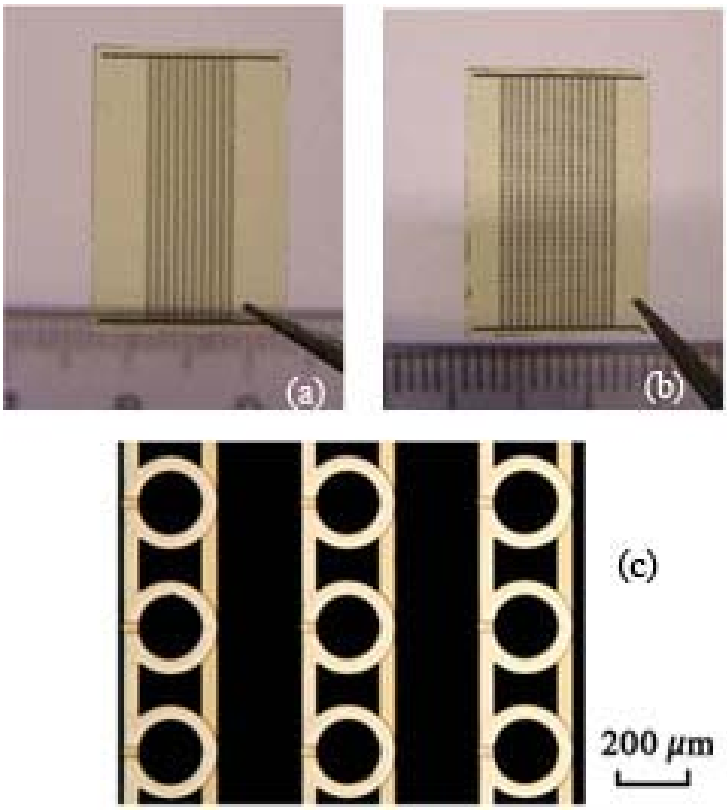

Fig. 3.11 Two metamaterial slices having 10 (a) and 14 cells (b), respectively. (c) Optical photograph of omega metamaterial at W band.

The resulting wafer was divided into six pieces of omega metamaterial, three of which have 10 cells whereas the other three have 14 cells along the propagation direction (Fig. 3.11). There are 10 quartz wafers used for omega-like metamaterial preparation, which means we have 30 slices to assembly bulk structure.

3.4 Characterization

3.4.1 Transmission spectrum

As illustrated in Fig. 3.1(b), a bulk metamaterial was assembled with 30 layers stacked via the edge alignment, leaving no air-gap between the layers. Thus, the metamaterial bulk has a width (y) of about 15 mm and height (x) of 20 mm. metamaterial sample inside the aperture of an absorbing was measured in free space, which is similar to the method used in Ref. [27].

In a first stage, ten-cell long sample was illuminated under normal incidence with polarization for the electric field along the x direction and magnetic field along the y direction. The measurements of the S parameters as a function of frequency were performed by using an Agilent 8510C vector network analyzer. Figure 3.12 shows the transmission spectra of the 10-cell-long device. As seen in Fig. 3.12, the metamaterial structure exhibits two clear pass-bands with high transmission levels, one is from 75.0 to 87.0 GHz and the other one occurs above 100 GHz, with a band gap in between. In order to distinguish the properties of these two pass-bands, we also reproduced simulation results such as transmission (Fig. 3.6) and effective index (Fig. 3.5). From Fig. 3.12, it can be seen that the simulation transmission spectrum shows a good agreement with the experimental result. Furthermore, the real part of the retrieved effective index exhibits negative values for the first pass-band below 87.0 GHz, indicating a left handed dispersion characteristic. For this pass-band, it is noticed a transmission peak as high as - 4.6 dB at 81.6 GHz for a ten-cell prototype. To the best of our knowledge, this is the lowest loss level for SRR-based metamaterials in this frequency range. The experimental results confirmed that low dielectric loss of substrate and omega pattern are the key issues to realize low insertion loss metamaterial, as mentioned before.

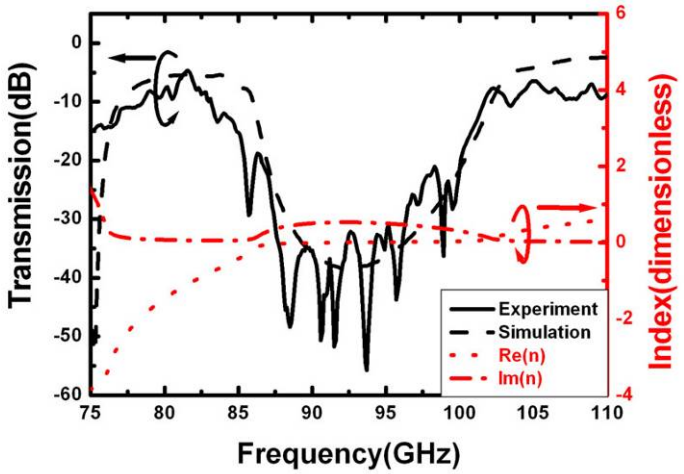

Fig. 3.12 (Left axis) Experimental (solid black) and simulation (dashed black) transmission spectra of the metamaterial with 10 cells stacked along the propagation direction. (Right axis) The real (dotted red) and imaginary parts (dashed red) of the effective index are also represented.

3.4.2 Phase offset

When an electromagnetic (EM) wave passing through a given material with finite length, there is phase delay Φ between the incident and output interfaces

$$\phi = -nk_0 d \tag{3.1}$$

where n is effective index of material, k_0 is wave number in free space and d is the material length that EM passes. From Eq.3.1, it is easy to find that phase delay depends on the material length d. There is phase difference once the length d varies. For two prototypes of same material but with various lengths d_1 and d_2 ($d_1 > d_2$), the phase differences can be written

$$\Delta\phi = \phi_1 - \phi_2 = -nk_0(d_1 - d_2) = -nk_0\Delta d \tag{3.2}$$

As Δd is positive, the phase difference ΔΦ has a negative correlation with n. Thus, we can deduce the sign of index via that of ΔΦ. For example, if ΔΦ is larger than zero, then n will be negative, which offers a direct demonstration route for distinguish the sign of material index.

In order to further confirm the left-handed properties of the first pass-band, we measured the frequency dependence of the phase delay for the 10- and 14-cell prototypes, as presented in Fig. 3.13. The distances between emitter and receiver are fixed during phase measurement for two prototypes. As shown in Fig. 3.13, the

phase offset $\Delta\Phi = \Phi_{14}-\Phi_{10}$ is positive below 89 GHz corresponding to a negative refractive index, whereas it becomes negative above 95 GHz, indicating a positive index material.

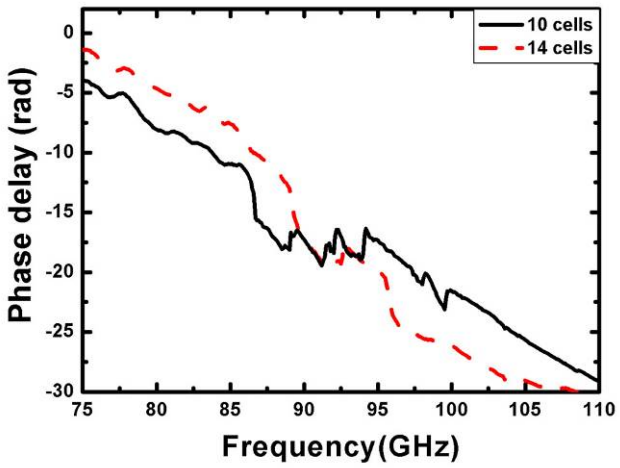

Fig. 3.13 The phase delay for the metamaterials with 10 (solid black) and 14 cells (dashed red) stacked along the propagation direction, respectively.

3.4.3 Tilted incidence response

Figure 3.14 shows the oblique transmission response of the 10-cell-long metamaterial structure. As shown in the inset of Fig. 3.14, the incidence direction is rotated around the *x* axis by an angle of θ with respect to the initial incident route along the *z* direction. This results in a changing magnetic field polarization while the electric field polarization remains the same. In Fig. 3.14, when the oblique incidence angle is increased from 0° to 30°, the transmission peak of the first pass-band decreases down from -4.6 to -21.9 dB, with a narrower bandwidth. By contrast, the second transmission window is much less sensitive to the angle of incidence. As incidence angle is increased, the magnetic field component perpendicular to the omega pattern plane decreases and the artificial magnetic resonance strength is weakened [10, 14]. As a consequence, the transmission level, which corresponds to a left-handed dispersion branch, decreases accordingly. On the other hand, the electric plasma frequency is hardly affected by the oblique incidence since the electric field remains polarized along the same direction. This sensitivity to an oblique incidence permits us to conclude about the left-handed behavior of the first transmission window.

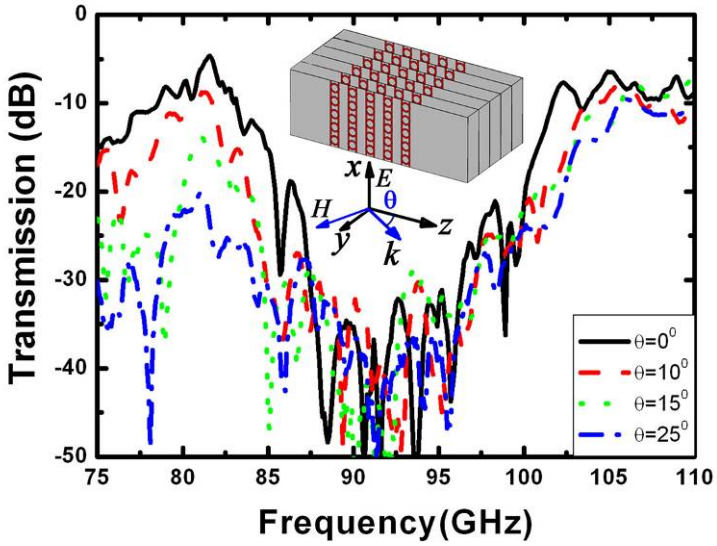

Fig. 3.14 Oblique transmission spectra of the 10-cell prototype for incident angle values ranging from 10° to 30°. Inset: The incident polarization orientation.

3.5 Summary

In summary, a low-loss omega-like metamaterial was successfully fabricated on BCB substrate via optical photolithography technology at millimeter waves. Low loss of metamaterial was realized by using low dielectric constant as well as omega pattern. The left-handedness of the transmission window was confirmed by phase delay measurement under normal incidence and by the sensitivity of transmission levels of oblique incidence. An insertion loss below -0.5 dB per unit cell was observed which becomes comparable to that reported for a non-resonant transmission line approach at THz frequency [31], allowing the possibility for real application.

References

[1]. C. Elachi, Introduction to the Physics and Techniques of Remote Sensing, New York, NY: John Wiley & Sons, (1987).

[2]. V. G. Veselago, Sov. Phys. Usp. **10**, 509 (1968).

[3]. J. B. Pendry, A. J. Holden, D. J. Robbins, and W. J. Stewart, IEEE Trans. Micro. Theory Tech. **47**, 2075 (1999).

[4]. R. A. Shelby, D. R. Smith, and S. Schultz, Science **292**, 77 (2001).

[5]. J. B. Pendry, A. J. Holden, W. J. Stewart, and I. Youngs, Phys. Rev. Lett. **76**, 4773 (1996).

[6]. J. Zhou, L. Zhang, G. Tuttle, T. Koschny, and C. M. Soukoulis, Phys. Rev. B **73**, 041101 (2006).

[7]. C. G. Parazzoli, R. B. Greegor, J. A. Nielsen, M. A. Thompson, K. Li, A. M. Vetter, M. H. Tanielian, and D. C. Vier, Appl. Phys. Lett. **84**, 3232 (2004).

[8]. A. Erentok, P. L. Luljak, and R. W. Ziolkowski, IEEE Trans. Antennas propag. **53**, 160 (2005).

[9]. H.-T.Chen, J. F. O'harai , A. K. Azadi, A J. Taylor, R. D. Averitt, D. B. Shrekenhamer, and W. J. Padilla, Nat. Photonics **2**, 295 (2008).

[10]. W. J. Padilla, A. J. Taylor, C. Highstrete, M. Lee, and R. D. Averitt, Phys. Rev. Lett. **96**, 107401 (2006).

[11]. C. Croenne, F. Garet, E. Lheurette, J.-L. Coutaz, and D. Lippens, Appl. Phys. Lett. **94**, 133112 (2009).

[12]. T. Driscoll, G. O. Andreev, D. N. Basov, S. Palit, Tong Ren, J. Mock, S.-Y. Cho, N. M. Jokerst, and D. R. Smith, Appl. Phys. Lett. **90**, 092508 (2007).

[13]. S. Linden, C. Enkrich, M. Wegener, J. Zhou, T. Koschny, and C. M. Soukoulis, Science, **306**, 1351 (2004).

[14]. T. F. Gundogdu, I.Tsiapa, A. Kostopoulos, G. Konstantinidis, N. Katsarakis, R. S. Penciu, M. Kafesaki, E. N. Economou, Th. Koschny, and C. M. Soukoulis, Appl. Phys. Lett. **89**, 084103 (2006)

[15]. M. Gokkavas, K. Guven, I. Bulu, K. Aydin, R. S. Penciu, M. Kafesaki, C. M. Soukoulis, and E. Ozbay, Phys. Rev. B **73**, 193103 (2006).

[16]. J. Valentine, S. Zhang, T. Zentgraf, E. Ulin-Avila, D. A. Genov, G. Bartal, X. Zhang, Nature **455**, 369 (2008).

[17]. G. Dolling, C. Enkrich, M. Wegener, J. F. Zhou, and C. M. Soukoulis, Opt. Lett. **30** 3198 (2005).

[18]. K. Aydin, Kaan Guven, Nikos Katsarakis, Costas M. Soukoulis, and Ekmel Ozbay, Opt. Express **12**, 5896 (2004).

[19]. J. Huangfu, L. Ran, H. Chen, X. Zhang, K. Chen, T. M. Grzegorczyk, and J. A. Kong, Appl. Phys. Lett. **84**, 1537 (2004).

[20]. F. Zhang, G. Houzet, E. Lheurette, D. Lippens, M. Chaubet, and X. Zhao, J. Appl. Phys. **103**, 084312 (2008).

[21]. L. Ran, J. Huangfu, H. Chen, Y. Li, X. Zhang, K. Chen, and J. A. Kong, Phys. Rev. B **70**, 073102 (2004).

[22]. E. Lheurette, O. Vanbésien, and D. Lippens, Microwave Opt. Tech. Lett. **49**, 84 (2007).

[23]. R. B. Greegor, C. G. Parazzoli, K. Li, and M. H. Tanielian, Appl. Phys. Lett. **82**, 2356 (2003).

[24]. Dow Chemicals Product datasheet http: //www.dow.com/cyclotene/solution/highfreq. htm

[25]. M. N. Afsar and H. Ding, IEEE Trans. Instrum. Meas. **50**, 402 (2001).

[26]. CST Studio Suite ® 2006B Microwave Studio

[27]. D. Vier, D. R. Fredkin, A. Simic, S. Schultz, and M. Tanielian, Appl. Phys. Lett. **86**, 241908 (2005).

[28]. C. Croënne, B. Fabre, D. Gaillot, O. Vanbésien, and D. Lippens, Phys. Rev. B **77**, 125333 (2008).

[29]. D. R. Smith, S. Schultz, P. Markoš, and C. M. Soukoulis, Phys. Rev. B **65**, 195104 (2002).

[30]. X. Chen, T. M. Grzegorczyk, B.-I. Wu, J. Pacheco, and J. A. Kong, Phys. Rev. E **70**, 016608 (2004).

[31]. T. Crépin, J. F. Lampin, T. Decoopman, X. Mélique, L. Desplanque, and D. Lippens, Appl. Phys. Lett. **87**, 104105 (2005).

Chapter 4 Tunable metamaterial via liquid crystal molecular reorientation

4.1 Introduction

To date, Split Ring Resonators (SRRs)/wire arrays can be considered as a generic electromagnetic (EM) metamaterial [1-3], in which SRR array exhibits negative permeability above the magnetic resonance frequency whereas wire array behaves as a negative permittivity medium below the electric plasma frequency. Although various related structures such as S-type [4, 5], omega-type [6-8], fishnet [9] and quasi-periodic arrays [10] have also been developed, in most of these cases, their magnetic and electric resonance frequencies are fixed by the geometrical parameters. In view of many applications which are developed with the prospect of increasing bandwidth and smart EM properties, it is highly desirable to dynamically tune their characteristics. Changing the conductivity and permittivity conditions of the substrate were shown as efficient methods to modulate the properties of SRR-like structures according to recent studies [11-15]. There have been some efforts to realize tunable metamaterial by the judicious incorporation of active devices or materials, such as varactor diode [16-18], semiconductors [12-15], ferroelectics [19] and more generally anisotropic materials [20-25], as a part of the metamaterial elements to change the resonance condition. On the other hand, it also demonstrated that by introducing some active magnetic material such as yttrium iron garnet (YIG) rods so as to tune surrounding effective medium inductance, it is possible to tune

resonance frequency of SRR as well as left handed (LH) passband [26-28]. On the contrary, research on the tunability of wire array is relatively rare [29], which is due to the fact that wire array exhibits negative permittivity in a large frequency regime.

Liquid crystal (LC), which has been widely employed to realize tunable photonic crystals at optical frequencies [30-33], phase shifters at millimeter and microwave frequencies [34-37], is considered as a promising candidate for tunable metamaterial substrate. Recently, Khoo *et al.* reported a theoretical analysis on tunable metamaterial based on core-shell nanosphere randomly dispersed in LC [21]. Werner *et al.* presented a reconfigurable metamaterial by sandwiching LC layers as a substrate into the conventional negative index metamaterial [22]. Wang *et al.* numerically investigated reconfiguration of metamaterials on LC director reorientation or by using temperature dependent LC [23]. Q. Zhao *et al.* reported a negative permeability uniplanar SRR array infiltrated with LC can be reversibly controlled by an external electric field [24]. However, most of these works are concentrated on the numerical analysis whereas experimental demonstration is scare.

In this chapter, we firstly focus on numerical analysis method of the tunability of metamaterial based on LC molecular reorientation by a comparative analysis of anisotropic and isotropic treatments of LC. Then, a magnetically tunable negative permeability metamaterial of broadside couple SRR is shown experimentally and numerically. On the basis of successful realized tunable SRR, we present dynamic property of omega-like left handed metamaterial (LHM) via LC. The variation of left handed (LH) passband as well as negative index is observed and used to demonstrate the feasibility of LC technology.

4.2 Numerical analysis on tunable metamaterial based on LC technology

LC is a typical anisotropic material possessing different permittivity tensor along three principal axes, however, it can be considered as isotropic medium as only one polarized direction is considered. As aforementioned in introduction, in most of numerical works [21, 22] on tunable metamaterial based on LC, an isotropic treatment of nematic LC was employed as an approximate method to describe the permittivity properties of LC in comparison with a more rigorous anisotropic treatment reported by Wang *et al* [23]. An isotropic treatment is valid provided that the EM fields exhibit isotropic field distributions as it is the case for non resonant

structures such as photonic crystals and phase shifters. When metamaterial emerges, it seems reasonable to analyze LC on the same way in the new field as a matter of course. However, as a resonant structure arising from the electric or magnetic resonance, a metamaterial is completely different from the structures mentioned above. It is of interest to give a comprehensive description of LC molecular reorientation in metamaterial.

In this section, we present a comprehensive investigation of the influence of LC on the dispersion characteristics of LHMs. Both an approximate isotropic approach and a rigorous anisotropic treatment were employed in order to obtain a comparative analysis on the dependences of magnetic and electric resonances to the reorientation of LC molecules. The operating regime was scaled down to the microwave frequencies because most of the tunable metamaterial microstructure are today realized and characterized in the gigahertz spectral region. However, it is believed that the conclusions drawn in the present work are still valid at higher frequencies and notably in the infrared spectral region.

In following numerical investigation, we describe in details the configuration of tunable LHMs infiltrated with LC as well as the isotropic and anisotropic methods, then a comparison between the isotropic and anisotropic treatments is presented by investigating the dependences of the magnetic and electric resonance frequencies of LHMs to the reorientation of LC molecules. The results are explained via the mapping of the local electric field and the surface currents.

4.2.1 S-type tunable metamaterial

In order to simplify the analysis, we employed an S-type LHM whose parallel plate capacitance is derived from the broadside coupling between the facing strips rather than SRR-type motifs with more complicated capacitance distribution [24]. The basic unit cell is composed of double S strips in a reversed configuration, as depicted in Fig. 4.1. As seen from Figs. 4.1(a) and (b), double S strips are printed on the surface of two dielectric slabs with a typical relative permittivity around two in the present case and with voids in between infiltrated by LC compounds. For the sake of modeling purpose, the basic unit cell is only modeled as one third of the real S-type structure [4, 5] with perfect electric and perfect magnetic conductors imposed along the x and y directions, respectively. Thus, the unit cell is periodically repeated in a mirror way along the directions transverse to the propagation direction, in accordance with the image theory, i.e., the side boundaries act indeed as mirrors. Under this condition the finite height prototype appears as though it was infinite

along the *x* and *y* directions. An incident beam with the electric field polarized along the *x* direction and the magnetic field polarized along the *y* direction is assumed to illuminate the structure along the *z* direction. The S-type strips bounded with perfect electric condutors at the top and bottom sides can be considered as current loops in the *x*-*z* plane. With an external time-varying incident magnetic field impinging along the *z* direction, currents flow within the loops, driven by the parallel-plate capacitances formed by the horizontal strips of the reversed S strips. A negative effective permeability effect originates from these resonant currents. It is worthwhile mentioning that in the present broadside coupling of the current loops, the LC slabs can be considered as a tunable substrate for the magnetic resonators whereas the dielectric slabs are only used to hold the metal strips. On the other hand, the vertical continuous strips provide a negative effective permittivity effect when the surface currents are induced by the electric field component of the incident beam.

Let us suppose the director of the anisotropic LC molecules lies in the *x*-*y* plane (Fig. 4.1(b)). For a LC slab with a director (**n**) initially aligned along the *x* axis, the director can be oriented in the *x*-*y* plane and take any values $\mathbf{n} = \{\cos\theta, \sin\theta, 0\}$, where θ denotes the reorientation angle of molecular director with respect to the *x* axis. This reorientation can be achieved by applying an electro-static or a magneto-static field based on the Fréedericksz effect.

To date, nematic compounds with a large birefringence $\Delta n = 0.37$ at microwave frequencies have been synthesized by Weil *et al*. [35]. In the following analysis on this basis, the permittivity characteristics of LC were chosen as $\varepsilon_{//} = 3.94$ and $\varepsilon_{\perp} = 2.62$, where $\varepsilon_{//}$ and $\varepsilon_{\perp}$ are the permittivity for the beam polarized parallel and perpendicular to the director axis **n**, respectively. Using the finite element code Ansoft's High Frequency Structure Simulator (HFSS), a full-wave analysis was performed to determine the scattering parameters of the basic unit cell. On this basis, the effective permittivity and permeability frequency dependences could be unambiguously determined from the well-established inversion procedures [41-43].

At the first stage, LC was treated as a homogenous isotropic material with respect to the linearly polarized incident beam. The effective index of the aligned nematic LC is given by [44]

$$n_{eff} = \frac{n_e n_0}{\sqrt{n_e^2 \sin^2\theta + n_0^2 \cos^2\theta}} \tag{4.1}$$

where n_0 and n_e present the ordinary and extraordinary indices, respectively. As the

LC is non-magnetic material, Eq. (1) can be rewritten

$$\varepsilon = \frac{\varepsilon_{//}\varepsilon_{\perp}}{\varepsilon_{//}\sin^2\theta + \varepsilon_{\perp}\cos^2\theta} \tag{4.2}$$

From Eq. (2), it can be seen that the incident beam experiences a LC permittivity equal to $\varepsilon_{//}$ for the initial case (θ = 0°) and equal to $\varepsilon_{\perp}$ when the director of LC molecule is parallel to the y axis (θ=90°), respectively.

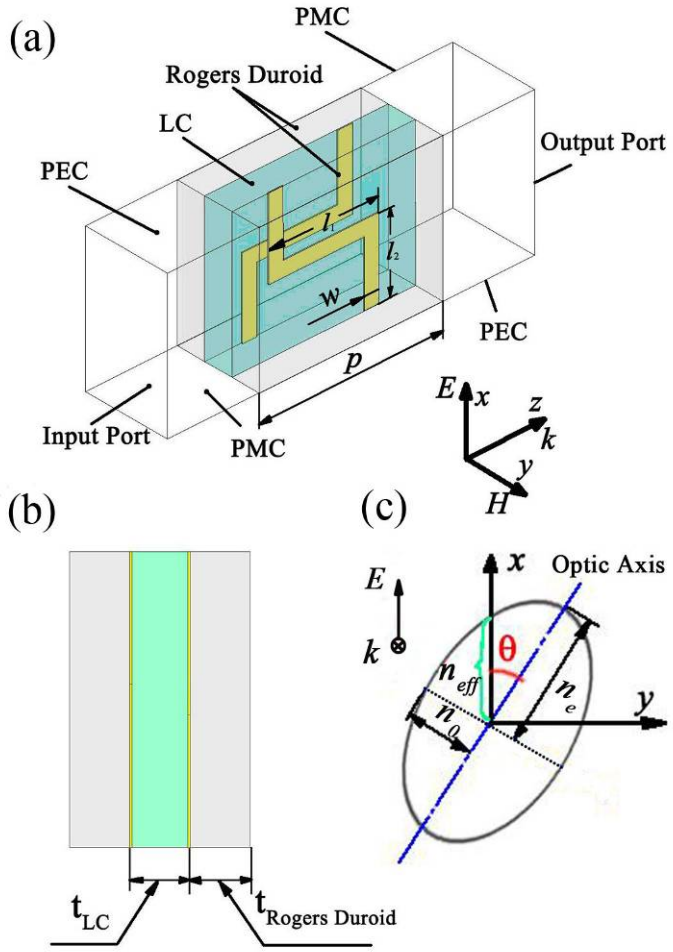

Fig. 4. 1 Tunable metamaterial based on anisotropic LC in the microwave frequency. (a) 3D view and (b) Side view of the basic unit cell and (c) the schematic of LC director reorientation. The geometrical parameters of the unit cell are as follows: $l1$ =3.0, $l2$ = 2.15, w = 0.4, $t_{Rogers\ Duriod}$=0.8, t_{LC} = 0.8, p = 5.0 (unit: millimeter). Rogers RT/Duriod 5880 (εr = 2.2, tan δ= 0.0004) was chosen as the host medium.

In a second stage, influence of LC on the metamaterial was investigated more rigorously by characterizing the LC compound with a permittivity tensor $\{\varepsilon_x, \varepsilon_y, \varepsilon_z\}$.

For the initial case (θ = 0°), the LC permittivity can be described by $\{\varepsilon_{//}, \varepsilon_{\perp}, \varepsilon_{\perp}\}$. Once LC molecules are oriented in the *x*-*y* plane by an external field, the permittivity components ε_x and ε_y change while ε_z remains constant as $\varepsilon\perp$. In order to describe the reorientation of LC molecules, we rotated the whole system including both the metamaterial model and the boundaries around the *z* axis while maintaining the LC permittivity tensor as the initial case, which is equivalent to alter the LC permittivity tensor.

4.2.2 Influence on the magnetic response

Figure 4.2 shows the frequency dependence of the real part of the effective permeability μ′for the LC director angle values θ = 0°, 30°, 45°, 60°, and 90°. For the LC influence on the magnetic resonance, analyzed by the isotropic treatment (Fig. 4.2(a)), the metamaterial exhibits negative permeability values in the frequency band ranging from 8.15 GHz to 10.75 GHz for the initial case (θ = 0°). By increasing the director angle from 0° to 90°, a clear blueshift of the frequency band with negative permeability from the 8.15-10.75 GHz up to 9.5-12.6 GHz can be observed. As shown in the inset of Fig. 4.2(a), the magnetic resonance frequency ω_m, at which the permeability changes abruptly, is gradually increased with the LC director angle. In contrast, Fig. 2(b) presents the frequency dependence of the permeability μ′ on the LC reorientation based on an anisotropic LC treatment. For the initial case, it can be seen that the metamaterial exhibits negative permeability from 9.15 GHz to 12.25 GHz, and thus in a quite different frequency band in comparison with the result obtained with the isotropic treatment Furthermore, the magnetic resonance frequency ω*m* shifts about 0.6 GHz towards lower frequencies from 9.15 GHz to 8.55 GHz as the LC director angle is increased from 0° to 90° (Inset of Fig. 4.2(b)). This tuning behavior is completely reversed compared to the frequency shift calculated for the isotropic treatment case.

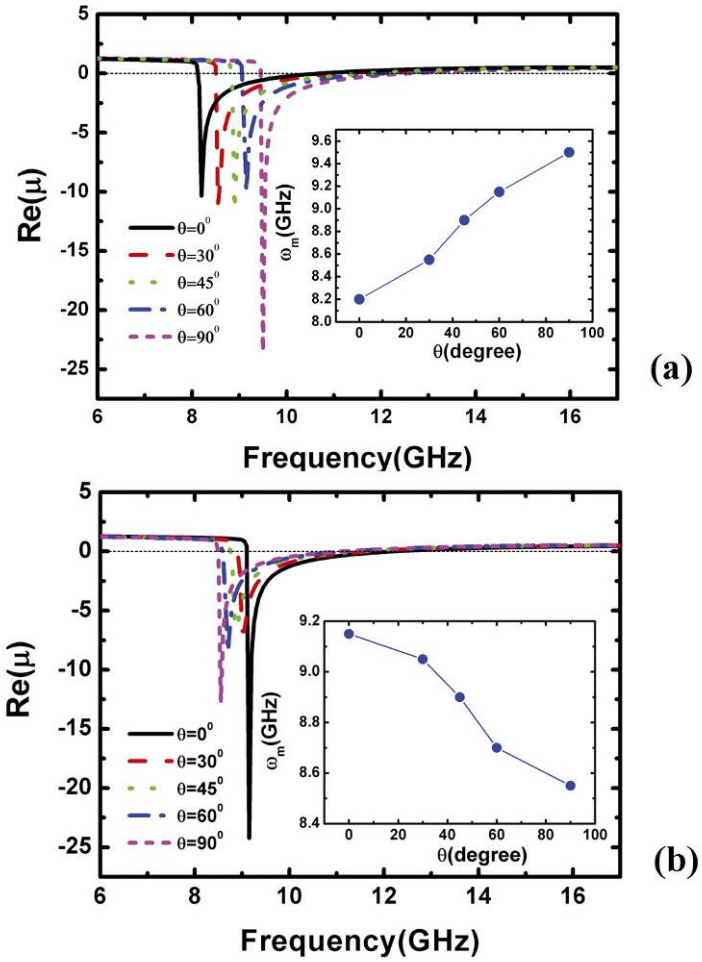

Fig. 4.2 The dependence of the real part of the effective permeability μ′ of the metamaterial to the director angle of LC obtained from (a) isotropic and (b) anisotropic treatments. Inset: the magnetic resonance frequency ω_m as a function of the reorientation angle of LC.

It is known that all the magnetic resonances based on metallic structures, arising from an *LC* . Tuning is consequently introduced by changing the capacitance or the inductance. Here, the reorientation of the LC molecules only varies the permittivity values and hence the capacitance of the structure. For the results obtained with an isotropic treatment, the average LC permittivity, given by Eq. 2, decreases when the director angle is increased. This yields a decrease of the capacitance and an increase of the magnetic resonance frequency. In contrast, the opposite magnetic resonance shift between the isotropic and anisotropic treatment of LC has to be interpreted as a different change of the permittivity as a function of the LC molecule orientation. As the isotropic treatment of LC is equal to the anisotropic method on condition that the scattering field is unchanged during the propagating path, this difference is explained hereafter by field and surface current mapping.

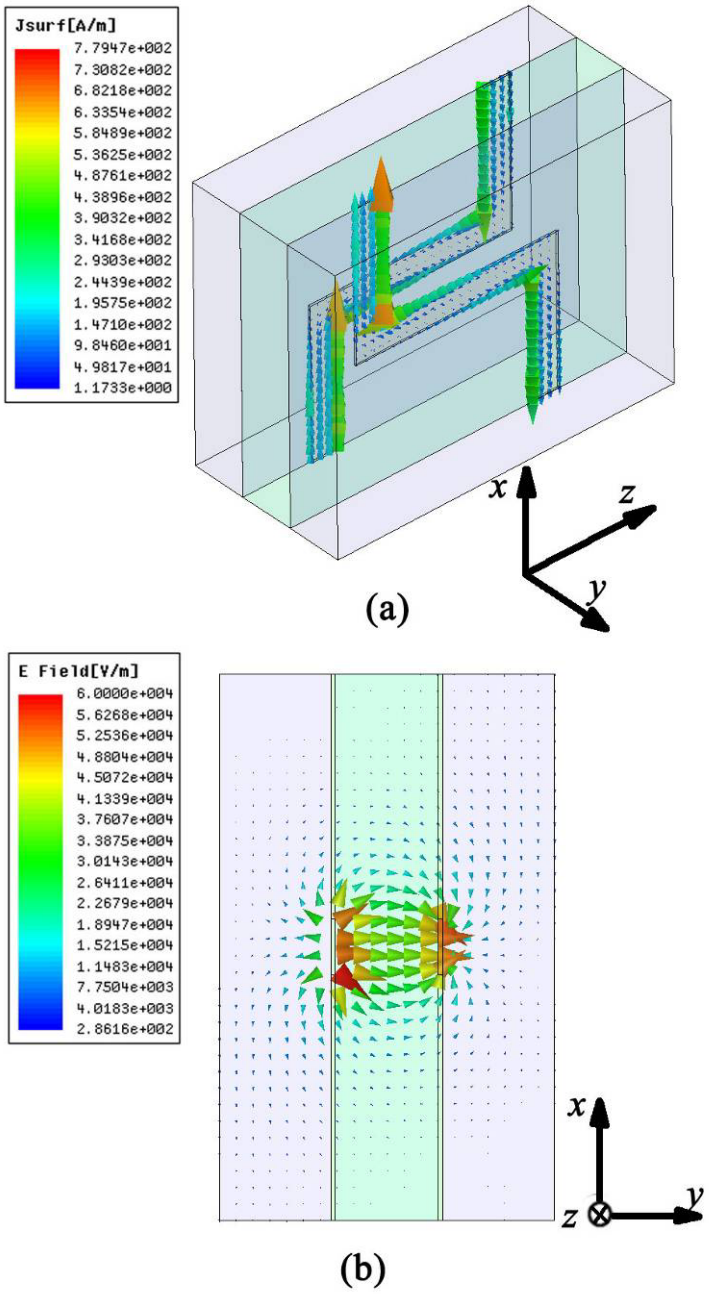

Fig. 4.3 Surface currents (a) and electric field distribution (b) for metamaterials incorporating LC with a director angle of 0° at magnetic resonance frequency (8.20 GHz) obtained under an isotropic treatment.

In Fig. 4.3, the surface currents and local electric field maps in the *x*-*y* plane were plotted at 8.20 GHz. This frequency corresponds to the magnetic resonance frequency ω_m of the S-type motif under the isotropic consideration of LC and director axis along the *x* ($\theta = 0°$). It can be noticed that circular currents were induced to flow around each loop, indicating a strong magnetic response. As shown

in Fig. 4.3(b), the local electric field, in the *x*-*y* plane, is concentrated between the face-to-face horizontal strips and along the *y* direction, which is no longer the electric polarization of the incident beam. Fringing field components contribute to the dielectric response along *x* but with a minor importance. Clearly here, the local scattered field distribution is completely different from that of the incident beam, hence, making an isotropic treatment unsuitable. Basically, the capacitance of the magnetic resonators formed by the two horizontal strips is mainly dependent on the permittivity along the *y* axis, as shown in Fig. 4.3(b), whereas the contribution of ε_x and ε_z , resulting from the fringing effects, are rather weak. Once the director is reoriented from a direction parallel the *x* to the *y* axis, ε_y is increased from $\varepsilon_{\perp}$to $\varepsilon_{//}$, resulting in a decrease of the magnetic resonance frequency.

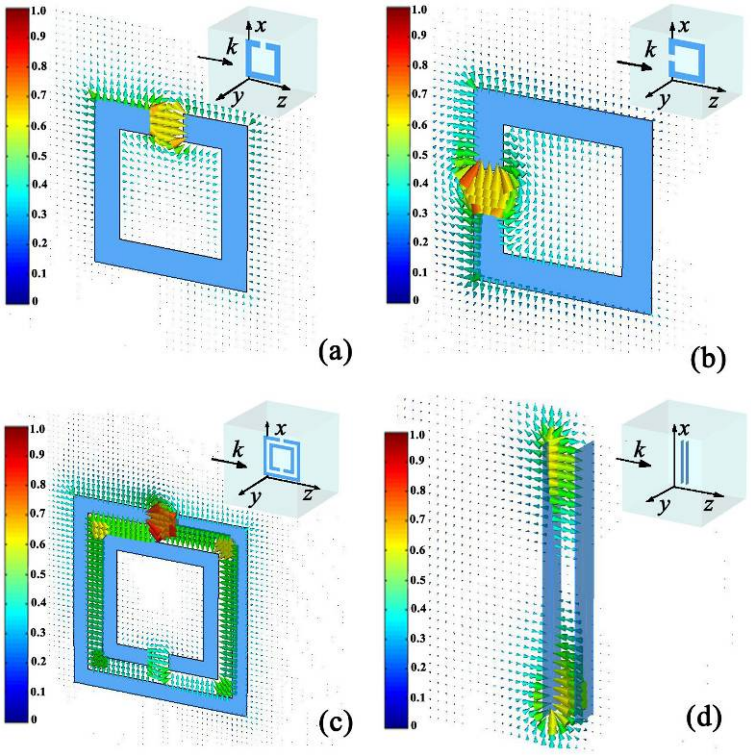

Fig. 4.4 Electric field distribution in different magnetic resonators at frequencies corresponding to a negative permeability. (a) Single SRR with the gap parallel to the incident. electric field, (b) single SRR with the gap perpendicular to the incident electric field, (c) double SRR, (d) short wire pair. In all cases, the electric fields in the *x*-*z* plane are shown, which have been normalized by the respective maximum values. The incident beam is illuminated with its electric field polarized along the *x* axis.

For a deeper understanding of the anisotropic effect pointed out above, we plotted in Fig. 4.4 the local electric field in the *x*-*y* plane, for various types of magnetic resonators (single SRR, double SRR, and short wire pair). Although the configurations of these magnetic resonators are different, in all cases, the polarization of scattered field is mainly determined by the capacitor orientation

rather than the incident electric field. On condition that LC is employed as the substrate for these magnetic resonators, we conclude that the isotropic treatment is not suitable for LC, according to our above reasoning. Even for the single SRR with local field around the gap mainly polarized parallel to the incident electric field (with gap perpendicular to the electric field of the incident beam in Fig. 4.4(b)), the isotropic treatment is not sufficient to obtain accurate frequency shift because of the lack of consideration of the behavior of LC molecules under the fringing effect of the gap.

4.2.3 Influence on the electric response

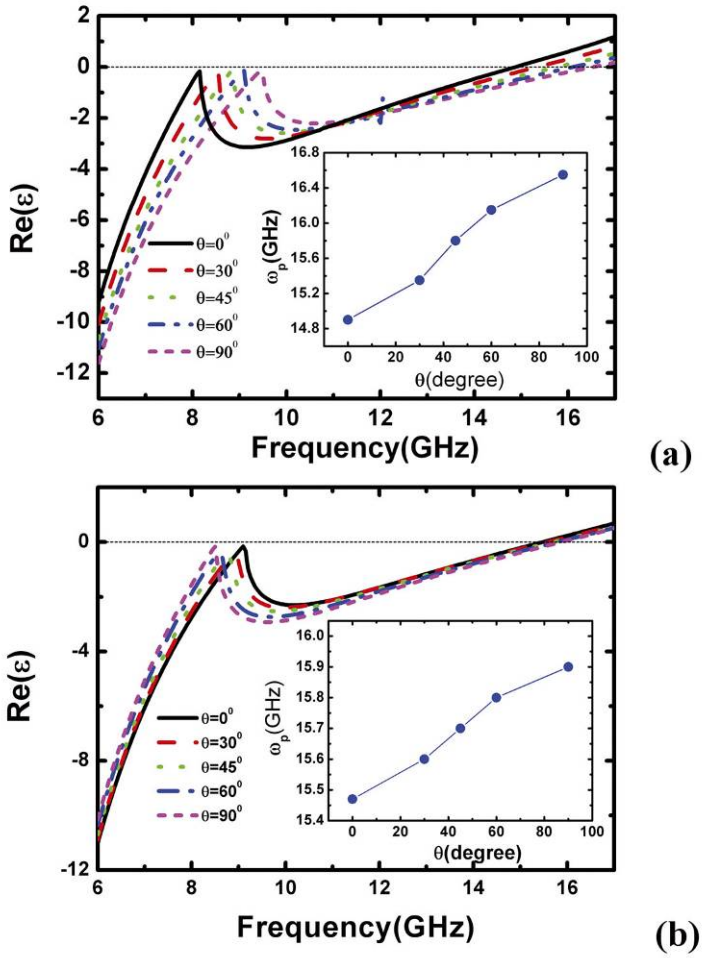

Fig. 4.5 The dependence of the real part of the effective permittivity ε′ of the metamaterial to the LC reorientation obtained from (a) an isotropic and (b) an anisotropic treatment. Inset: the plasma frequency ω_p as a function of the reorientation angle of LC.

The dependence of the LC reorientation to the real part of the effective permittivity ε′ as a function of frequency, is illustrated in Fig. 4.5. For an isotropic treatment (Fig. 4.5(a)), the effect of LC reorientation on the electric resonance is shifted towards a higher frequency as θ is increased. Concomitantly, the plasma frequency ω_p increases monotonically from 14.9 GHz to 16.65 GHz with thus an offset of 1.75 GHz, as shown in the inset of Fig. 4.5(a). For the anisotropic case (Fig. 4.5(b)), the plasma frequency ω_p is increased from 15.47 GHz to 15.90 GHz by thus a variation of 0.43 GHz. As a consequence, a quantitative difference of more than 1.0 GHz can be noticed for the plasma frequency shift between the two approaches, despite similar trends in the frequency shift with LC reorientation.

Figure 4.6 shows the surface currents and electric field distribution calculated at 14.9 GHz, which is the electric plasma frequency ω_p of the metamaterial by assuming isotropy of the EM characteristic and a director angle of 0°. As expected, the surface currents along the vertical strips are parallel to *x* axis, indicating the dominance of the electric field response. It is worthwhile mentioning that the anti-parallel current components along the horizontal strips are resulted from the back-to-back configuration of the S strips printed on the top and down sides of the dielectric substrates. In order to facilitate the analysis of the local electric field shown in Fig.4.6(b), we divided the whole cross-section into three parts: the area of the LC layer embedding the vertical strips (region I), the area of the LC layer around the horizontal strips (region Π) and the substrate layers (region ΙΙΙ). As seen in Fig. 4.6(b), most of the local field in the LC layer is polarized along the *x* direction, i.e., the same direction of the incident electric field (region I), while a considerable amount is excited along the *y* direction between the two horizontal strips (region Π). It should be noted that this transverse polarization is arising from the revised configuration of the double S strips rather than the magnetic field as depicted in Fig. 4.3(b).

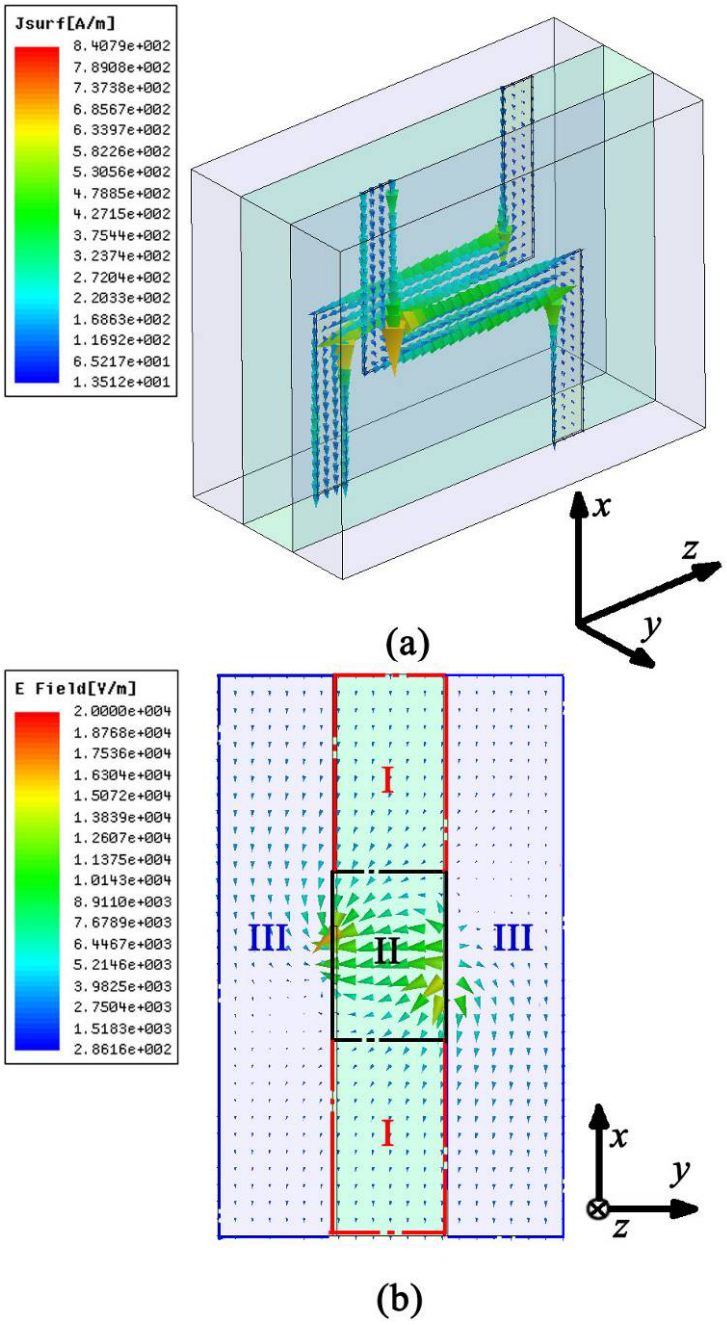

Fig. 4.6 Surface currents (a) and electric field distribution (b) for metamaterial incorporating LC with a director angle of 0º at plasma frequency of 14.9 GHz, which is predicted with an isotropic treatment.

At last, it is found that the electric resonance of the S-type metamaterial is comparable to the behavior of continuous wire arrays with a quasi Drude–like dispersion characteristic [45]. Previous studies have demonstrated that the electric plasma frequency of the wire array is proportional to $1/\sqrt{\varepsilon_r}$, where ε_r is the permittivity of background medium [11], which includes both the LC and dielectric

slabs in the present paper. Because the permittivity of the dielectric layers (region Ш) is independent of the polarization of the local field, the permittivity variation of the background medium is only determined by the LC layer. As shown in Fig. 6(b), when the LC director reoriented from 0° to 90°, the permittivity of the region I, which is dominated by ε_x, is decreased from $\varepsilon_{//}$ to $\varepsilon_{\perp}$, whereas the permittivity of region П, dominated by the y component, is increased from $\varepsilon_{\perp}$ to $\varepsilon_{//}$. Thus, the net effective permittivity of LC layer results from the opposite permittivity variations of regions I and П. In the present work, region I takes much larger room than region П, because the vertical strip length is much larger than the horizontal strip width. As a consequence, the average LC permittivity decreases as the permittivity variation of region I, resulting in an increase of the plasma frequency. Moreover, the variation of the mean permittivity is limited owing to the reversed permittivity variation in region П. Thereby, only a small increase of the plasma frequency should be observed as it can be assessed in the inset of Fig. 4.6(b).

4.3 Tunable negative permeability metamaterial

For common metamaterial cell SRR/wire, SRRs and related motifs behave as a negative permeability medium yielding the narrow band whereas continuous wire arrays display negative permittivity in a broad frequency window. As a consequence, special attention has to be paid on the dispersion characteristic tunability in SRRs.

Recently, Q. Zhao *et al.* showed experimentally that a negative permeability uniplanar SRR array infiltrated with LC can be reversibly controlled by an external electric field [24]. In this work, the periodicity of the uniplanar SRR array was of several millimetres at microwave frequencies. Nevertheless, a bias voltage as high as several thousand Volts was required, which somewhat limits potential applications.

In this section, we demonstrate a tunable negative permeability metamaterial based on the control of the birefringence in nematic LC through permanent magnets. A broadside coupled SRR was employed instead of a uniplanar scheme for improved tunability with moderate fields. Furthermore, a sub-millimeter–thick multi-layered structure was used in order to facilitate nematic LC director reorientation.

4.3.1 Tunable SRR prototype

The SRR pattern used in the present work consists of double C-shaped strips with a back-to-back orientation (Fig. 4.7(a)) to avoid a magneto-electric response [46] as described in previous chapter. Metal patterns were printed onto the surface of

Teflon fiberglass slabs with voids in between which were subsequently infiltrated with a nematic compound. An incident beam with the electric field polarized along the *x* direction and magnetic field polarized along the *y* direction was assumed to illuminate the structure along *z* direction.

In a first stage, we numerically predicted the resonant frequency shift resulting from the LC reorientation. Actually, we used the optical constants of a nematic compound 5CB fabricated at the Tsinghua University with birefringence Δn = 0.18 (n_0 = 1.50 and n_e = 1.68 at 589 nm) and positive magnetic anisotropy. Let us suppose the LC director lies in the *x*-*y* plane (Fig. 4.7(a)). For the LC slab with initial director of the molecules aligned along *x*, the director axis **n** can take all values $\{\cos\theta, \sin\theta, 0\}$ by applying a magneto-static field based on the Fréedericksz effect, where θ denotes the rotation angle of the molecular director with respect to the *x* axis.

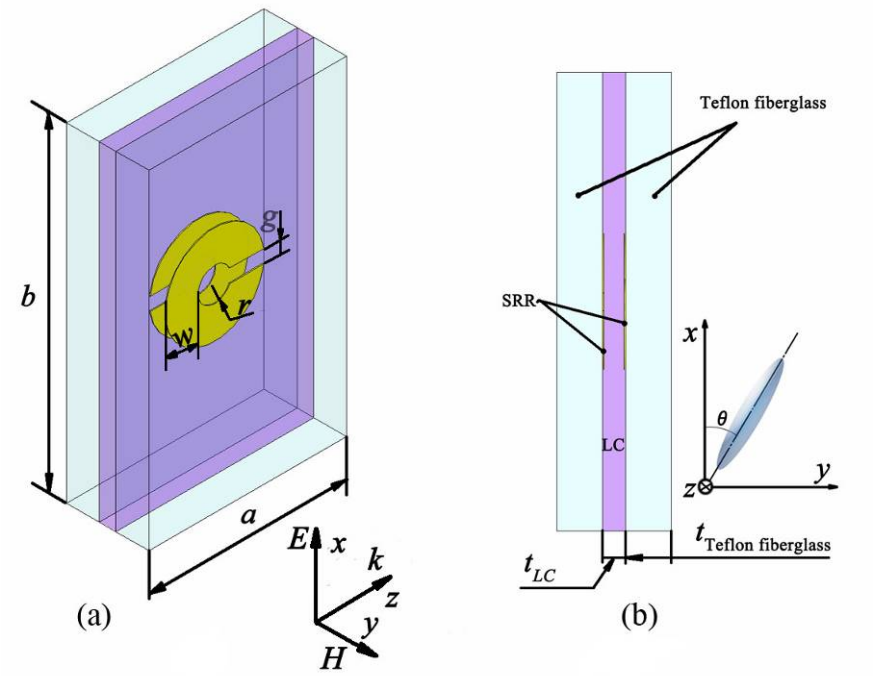

Fig. 4.7 Tunable broadside coupled SRR metamaterial based on anisotropic LC. (a) Schematic diagrams of basic unit cell. (b) Side view of unit cell and reorientation of LC molecule in *x*-*y* plane. The geometrical parameters of unit cell are as follows: r = 0.5, w = 1.0, $t_{Teflon\ fiberglass}$ = 1.0, t_{LC} = 0.5, a = 6.0, b = 10.0 (unit: mm). Teflon fiberglass (ε_r=2.65, tanδ=0.001) was chosen as host medium.

For the treatment of LC molecules, as aforementioned above, permittivity tensor is an imperative way to fully describe molecular reorientation. In the following analysis, $\varepsilon_{//} = n_e^2 = 2.82$ and $\varepsilon_{\perp} = n_o^2 = 2.25$ were used to describe the LC

medium, where $\varepsilon_{//}$ and $\varepsilon_{\perp}$ represent the respective permittivities for the polarized beam parallel and perpendicular to the director axis **n**. Using the finite element EM code HFSS by Ansoft, a full wave analysis was performed to determine the frequency dependence of the scattering parameters of a basic unit cell on which proper boundary conditions were applied. It has to be emphasized that the influence of LC reorientation on the metamaterial magnetic response was investigated rigorously by utilizing a permittivity tensor $\{\varepsilon_x, \varepsilon_y, \varepsilon_z\}$. For the initial case (θ = 0°), the LC permittivity can be given by $\{\varepsilon_{//}, \varepsilon_{\perp}, \varepsilon_{\perp}\} = \{2.82, 2.25, 2.25\}$. Once the LC director is oriented in the *x*-*y* plane, the values of the permittivity components ε_x and ε_y change whereas ε_z remains constant and equal to $\varepsilon_{\perp}$. In order to describe the reorientation of the LC director axis, we rotated the whole system around *z* including the metamaterial model and boundaries while maintaining the LC permittivity tensor of the initial case.

4.3.2 Simulation

Fig. 4.8(a) shows the frequency dependence of the metamaterial transmission response on the LC reorientation angle. For the initial case of θ = 0°, SRR exhibits a well-resolved transmission extinction around 11.32 GHz, corresponding to a negative effective permeability. When the director of LC is orientated from 0° to 90°, magnetic resonance dip of SRR is shifted to lower frequency. As seen in Fig. 4.8(b), the resonant frequency of SRR decreases gradually towards to 10.74 GHz, about 0.4 GHz variation, as LC director angle is increased. The dielectric loss of LC molecule was neglected in this initial simulation, however, this neither changes the resonance frequency nor the variation frequency range of SRR except for the dip strength.

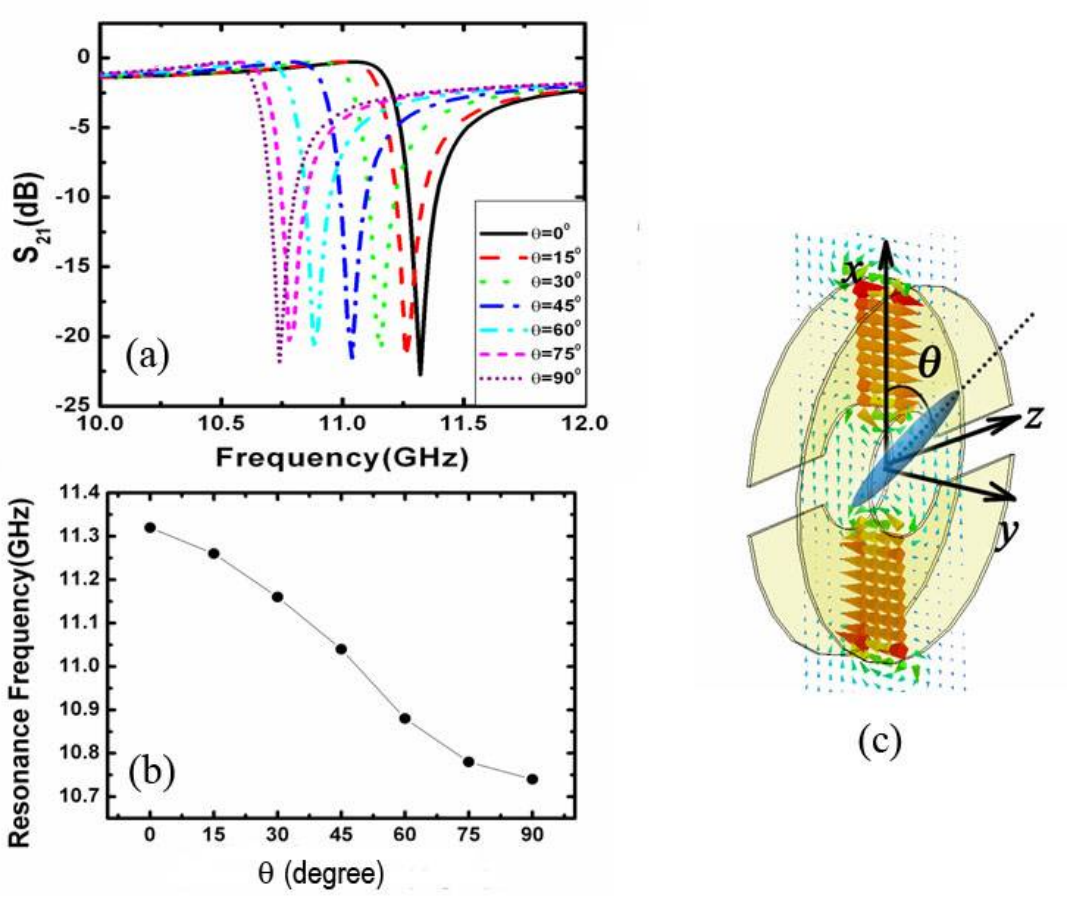

Fig. 4.8 (a) The transmission spectra and (b) magnetic resonance frequency of the basic unit cell as a function of the reorientation angle of the LC molecules. (c) Electric field distribution of SRR in the *x*-*y* plane when it is magnetically resonated.

In order to better understand the underlying mechanism, Fig. 4.8(b) shows the localized electric field distribution in the *x*-*y* plane at 11.32 GHz. It can be seen that the localized electric field is mostly concentrated between the two C strips and is polarized parallel to *y*, not along the *x* axis which is the polarization direction of the incident beam. Strictly speaking, the capacitance of the SRR is determined by the permittivity component of ε_x, ε_y, and ε_z, of which ε_y dominates as shown in Fig. 4.8(b). When an external field is applied to orientate the LC director from parallel to *x* to parallel to *y*, ε_y will be increased from ε_0 to ε_e, resulting in an increase of the capacitance and hence in a decrease of the resonant frequency.

4.3.3 Sample fabrication and experiment

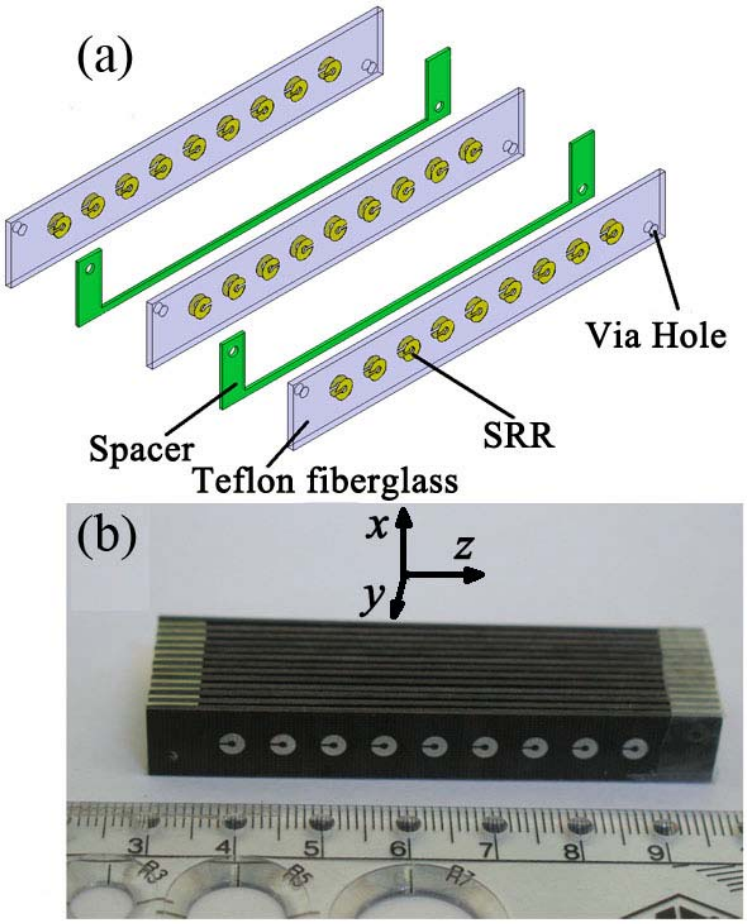

Fig. 4.9 (a) Schematic of assembly process of metamaterial. (b) Close-up view of the resulting SRR metamaterial.

To experimentally verify the numerical results, a SRR-based prototype infiltrated with a nematic LC compound with the aforementioned dielectric characteristics was fabricated and characterized. Fig. 4.9(a) and (b) illustrate the fabrication process and a photo of the device, respectively. At the beginning, C-shaped copper patterns were printed on both sides of a 1-mm-thick Teflon fiberglass board with the same orientation. Then, a 0.5-mm-thick U-shaped epoxy glass board was fabricated via using numerical controlled machine and used as a spacer between the Teflon fiberglass boards to offer a void spacing for LC infiltration. Finally, the Teflon fiberglass boards and spacers were alternatively stacked and aligned by means of via holes and plastic rods. SRRs on adjacent Teflon fiberglass boards were stacked in a back-to-back configuration to form broadside-coupled SRRs. It is no possible for magnetic resonance occurs between SRRs on both sides of one Teflon substrate as

they have the same orientation. Figure 4.10 offers various views of resulting bulk tunable SRR infiltrated by LC. It is noted that the width of the spacer bottom edge was set to 1.0 mm, thus leaving enough room for the LC infiltration. The nematic compound was infiltrated into the voids using a needle tube to fill-up the board interspacing via capillary forces.

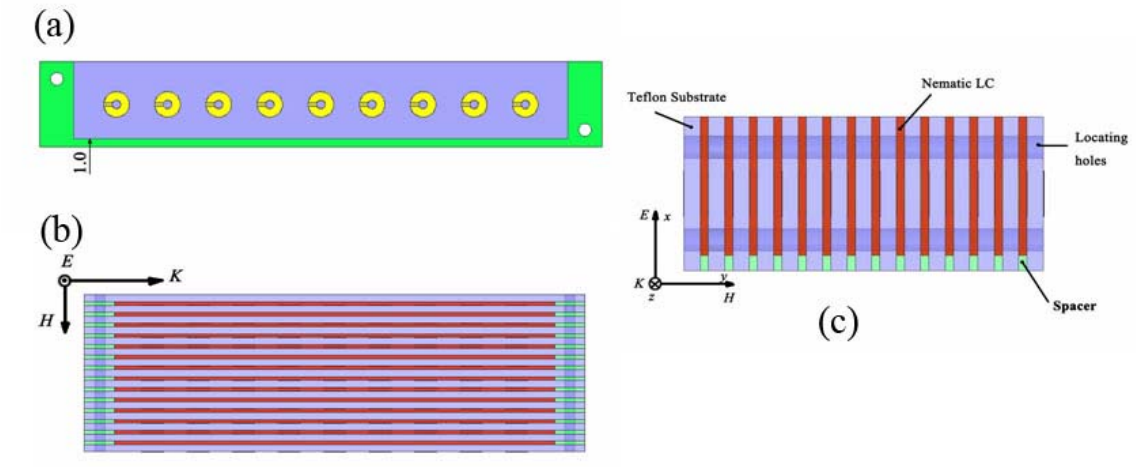

Fig. 4.10 Schematic front (a), top (b), and side (c) views of SRR metamaterial infiltrated by LC.

For the scattering parameters measurements, performed with an HP8720 ES Vectorial Network Analyzer, the SRR prototype was put between an X-band waveguide. As illustrated in Fig. 4.11, a pair of permanent magnets was mounted externally to align the LC director axis. Usually, the magnetic field threshold which is required to reorientate LC nematic molecules is of the order of 100 G. [36]. Using a digital magnetometer, we find that the magnetic field intensity in the waveguide is around 0.5 kG and is, hence, strong enough to correctly orientate the LC molecules.

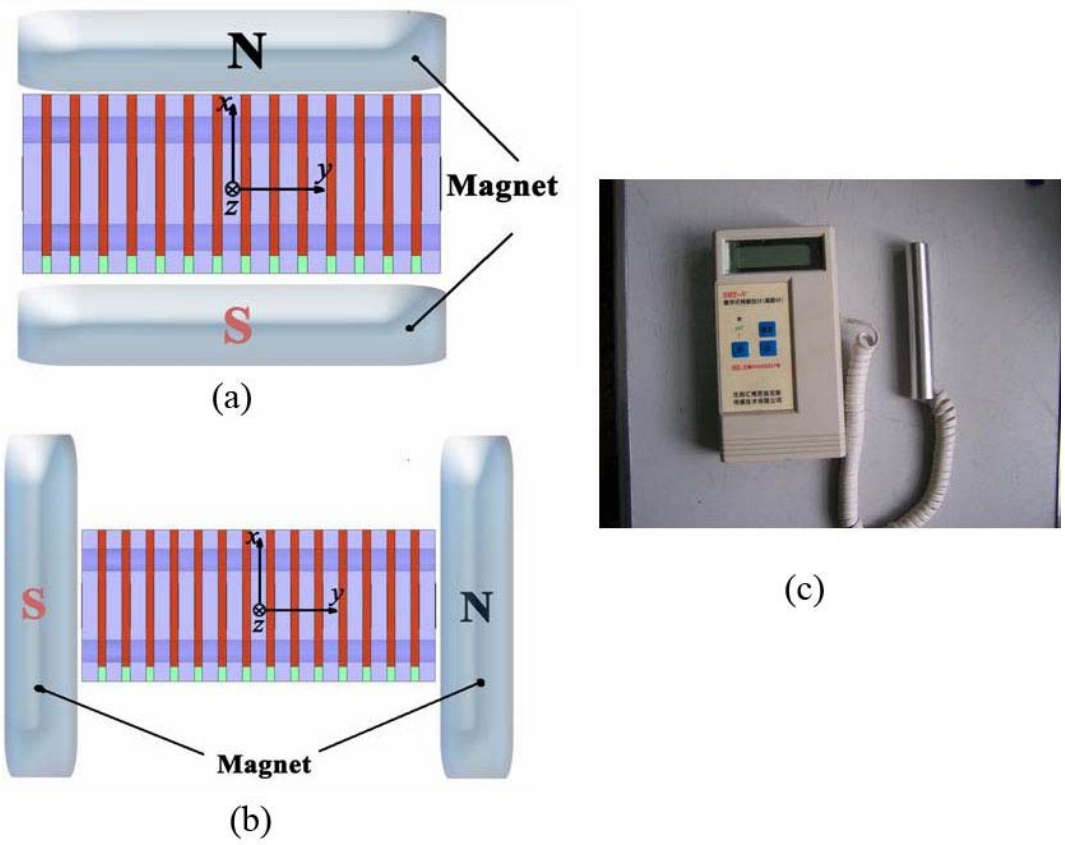

Fig. 4.11 Schematic diagram of the studied LC orientation obtained with a pair of permanent magnets (a) θ=0° and (b) θ=90°. (c) Digital magnetometer used to measure magnetic field intensity.

The transmission of the tunable SRR prototype were measured for three cases (i) the SRR without magnets (in this case the average permittivity of LC is 2.44 = (2 $\varepsilon_{\perp}$ + $\varepsilon_{//}$) / 3), (ii) with a magnetic field applied along *x* (θ = 0°) and (iii) along *y* (θ = 90°). Figure 4.12 shows the measured and calculated transmission spectra under these three conditions. The experimental results shown in Fig. 4.12(a) indicate that a pronounced dip occurs at 10.9 GHz for the case without the magnetic field. The resonant frequency shifts up to 11.0GHz when external magnetic field is applied parallel to *x* direction, whereas the resonance frequency moves down to 10.7 GHz as external magnetic field is imposed along the *y* direction. Totally, 300 MHz frequency shift was observed. It can be noted that the dependence of the resonant frequency to the LC director reorientation is in a good agreement with the results as displayed in Fig. 4.12 (b), calculated by including the description of the nematic substance permittivity tensor. On the other hand, this good agreement between the simulation and experiment results further demonstrates the validity of anisotropic description of LC via using permittivity tensor. For a better fit for experimental result, a dielectric loss tangent of 0.05 assumption for LC is used in the simulation.

Again, this definition has no influence on the resonance frequency position of SRR as aforementioned.

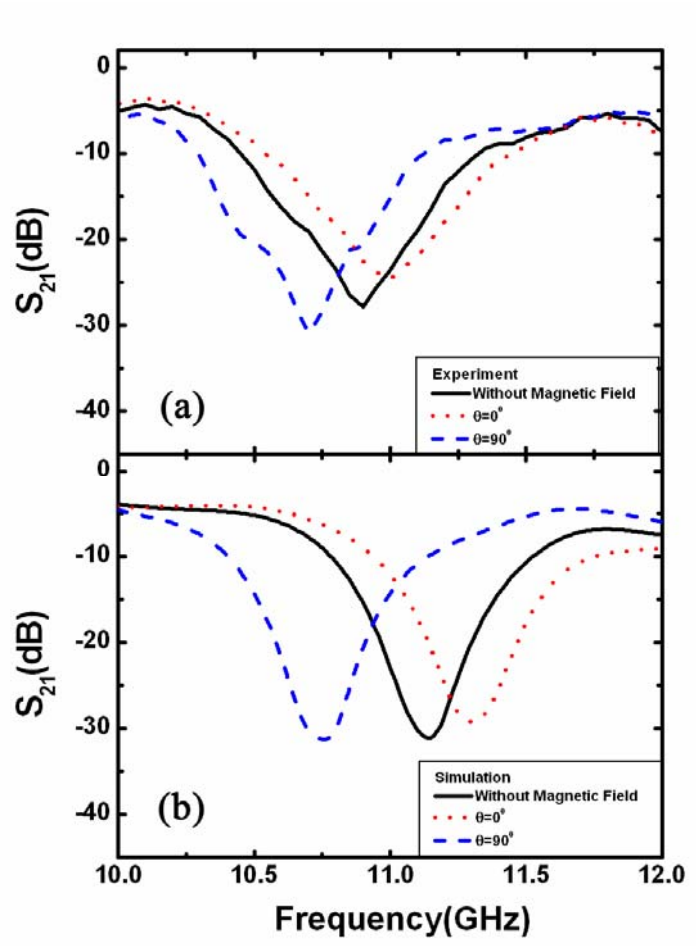

Fig. 4.12 Demonstration of the magnetically tunable negative permeability metamaterial. (a) Experimental results, (b) Simulations including the loss of LC (tanδ = 0.05).

A narrower variation in the resonant frequency shift can be noticed presumably due to a smaller birefringence in the microwave region compared to the optical regime. This assumption is confirmed by the property of 5CB whose birefringence is only 0.04 at microwave frequency as reported by Ref. [35].

4.4 Tunable double negative metamaterial

On the basis of successful realization of negative permeability metamaterial, the tuning of left handed metamaterial (LHM) properties, which can be realized by controlling LC molecular orientation, deserves much attention due to the prospect of tunable negative index. Up to now, although several numerical works have shown

that tunable LHM can be achieved by the infiltration of LC [21-23], the experimental verification has yet to be reported.

In this section, we report on the experimental results of a frequency-tunable LHM operating at microwave frequencies, which incorporated LC into sub-millimeter voids as multilayered substrate. By using an external magnetic field excitation on the alignment of LC, a frequency shift of the left handed pass-band was observed. In addition, the index variation of metamaterial was also assessed by both numerical retrieval effective parameters on the basic cell and a measurement of phase offset of a nine-cell prototype.

4.4.1. Tunable omega-like LHM prototype

Figure 4.13 (a) shows the schematic of the basic unit of the tunable metamaterial, which is composed of two omega patterns stacked in a reversed orientation. Under an illumination with *E*-polarized along the *x* and *H*-polarized along the *y* axis, the basic unit operates as a combination of broadside-coupled C-shaped-split right resonators (BCSRRs), providing negative permeability and wire arrays, yielding negative permittivity below the plasma frequency. As a consequence, the device exhibits negative index due to simultaneous negative permittivity and permeability in a frequency band between the resonant frequency and the magnetic plasma frequency of BC-SRR arrays. In the present work, the omega patterns are supported by Teflon fiberglass with infiltration of LC in between. Let us suppose that the LC director lies in the *x*-*y* plane (Fig. 4.13(a)). For the LC slab with the director of the molecules aligned along *x*, the director axis **n** can take all values $\{\cos\theta, \sin\theta, 0\}$ by applying a magneto-static field based on the Fréedericksz effect, where θ denotes the rotation angle of the molecular director with respect to the *x* axis. With the reorientation of the LC molecular director, we can control the effective permittivity of LC layer which influences the magnetic resonance of BC-SRR [25], as demonstrated in previous section, and consequently modifies the condition of the negative index regime.

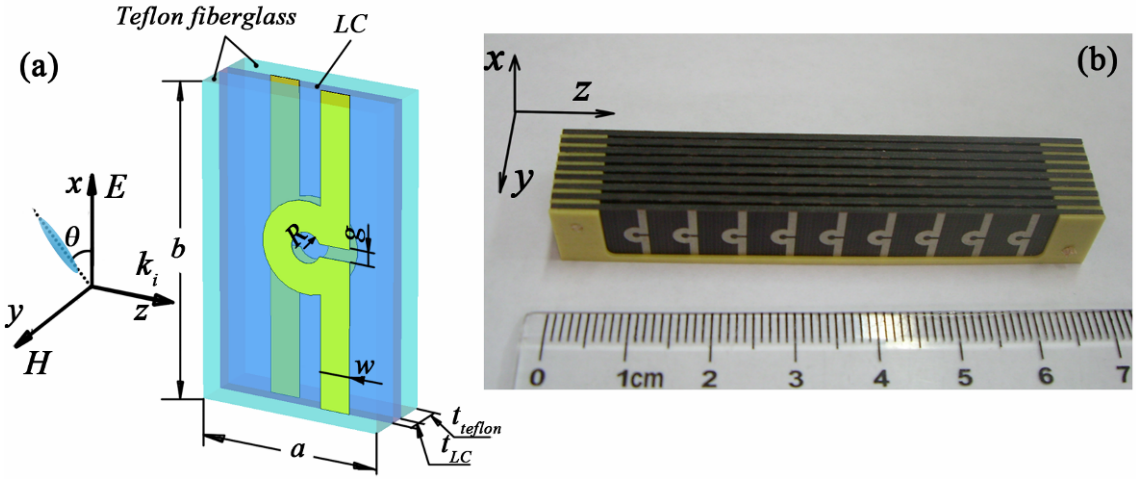

Fig. 4.13 (a) Schematic of the basic unit cell of the tunable negative index metamaterial as well as the reorientation of the LC molecule in the *x*-*y* plane. The geometry dimensions are as follows: R = 0.5, g = 0.4, w =1.0, t_{teflon} = 1.0, t_{LC} = 0.5 (unit: mm). The unit cell is stacked along the x and z directions with periodicities of 10.0 and 6.0 mm, respectively. (b) Close-up view of the mid-plane of the sample with the other part was removed to clarify the configuration of the voids.

Figure 4.13(b) shows a close-up view of the metamaterial sample, which was fabricated and assembly employing the similar method to tunable BCSRRs as describe above (Fig. 4.9). By using the standard print circuit board technology, two omega motifs with the same orientation were firstly patterned on both sides of a 1.0-mm-thick Teflon fiberglass board. In this way, there is no possibility for magnetic coupling occurring between omega patterns on both sides of one Teflon fiberglass board. By means of a numerically controlled machine, a U-shaped thin slice of epoxy fiberglass with a thickness of 0.5 mm was fabricated and then used as a spacer between Teflon fiberglass boards with voids for LC infiltration. The width of the spacer edge was set to 1.0 mm, thus leaving enough room for the LC infiltration. Finally, Teflon fiberglass boards and spacers were alternatively stacked and aligned by means of via holes and plastic rods. It is worth mentioning that omega patterns on adjacent Teflon fiberglass boards were stacked in a back-to-back configuration to form BC-SRRs as shown in Fig. 1(a).

4.4.2. Birefringence of LC mixture at microwave frequency

In previous section, it has been shown that the tunability range of metamaterial mainly depends on the birefringence of LC (Fig. 4.12). On the other hand, unlike SRR possessing a sharp resonance dip, LHM passband is usually much broader and not so visible for the same tunability range. As an attempt for large tunability of metamaterial, a type of LC mixture with an overall positive magnetic anisotropy and a large birefringence of 0.22 at optical regime was synthesized at Chemistry

department of Tsinghua University. However, as the birefringence of LC decreases at microwave or millimeter waves [35-37], it is necessary to measure the dielectric properties of LC at the specified frequencies of interest (X band).

By employing the method based on phase shift in LC slab of various lengths as proposed in Ref. [34], LC indexes were measured between 10 and 12 GHz. As shown in Fig. 4.14, wavelength λg of a propagated microwave inside a lossless dielectric loaded metal Transverse Electric (TE) rectangular waveguide is

$$\lambda_g = \frac{1}{\sqrt{\frac{n^2}{\lambda_0^{\,2}} - \frac{1}{4a^2}}} \tag{4.3}$$

where n is the refractive index of dielectric medium , λ_0 is the wavelength in free space, and a is the broadside dimension of the cross section of waveguide. The relative phase shifts with Φ for a length d of dielectric loaded waveguide with refractive index of n can be given by

$$\Phi = 360d\left(\sqrt{\frac{n^2}{\lambda_0^{\,2}} - \frac{1}{4a^2}} - \sqrt{\frac{1}{\lambda_0^{\,2}} - \frac{1}{4a^2}}\right) \tag{4.4}$$

Then, the phase shifts with $\Delta\Phi$ for dielectric loaded waveguide with various lengths of d_1, d_2 is rewritten by

$$\Delta\Phi = 360(\Delta d)\left(\sqrt{\frac{n^2}{\lambda_0^{\,2}} - \frac{1}{4a^2}} - \sqrt{\frac{1}{\lambda_0^{\,2}} - \frac{1}{4a^2}}\right) \tag{4.5}$$

where $\Delta d = \left|d_1 - d_2\right|$

Therefore, we can obtain effective index of LC from measuring the phase shift between two LC samples with different lengths using formula

$$n = \lambda_0 \sqrt{\left(360\frac{\Delta\Phi}{\Delta d} + \sqrt{\frac{1}{\lambda_0^{\,2}} - \frac{1}{4a^2}}\right)^2 + \frac{1}{4a^2}} \tag{4.6}$$

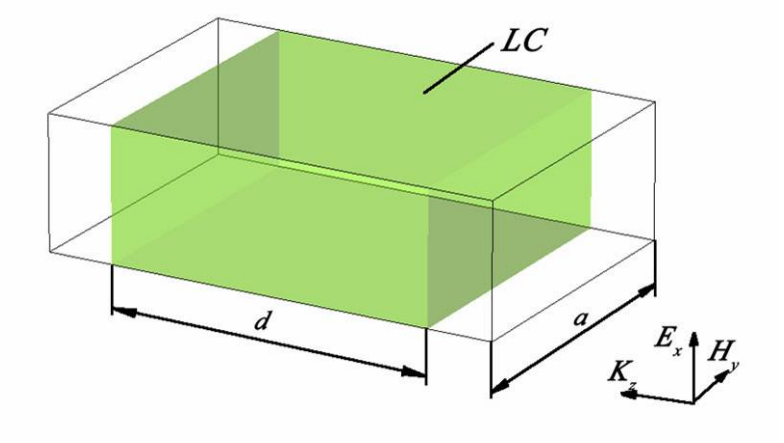

Fig. 4.14 Schematic of LC inside a waveguide.

The measurement consists of following steps:

- Fabricated two hollow plastic boxes with cross section dimensions (22.86×10.16 mm^2), which is the same as that of TE_{10} waveguide WR90 used for X band. The length difference of two boxes is Δd = 9.3mm. The thickness of plastic plate used to assembly box is around 0.5 mm, so that the influence on propagated phase is rather minor and neglected in the subsequent calculation.

- Average index n_r. LC was initially stirred mechanically prior to molecular random alignment measurement. The calibration was carried out as the sample box absent from waveguide. Then, LC was poured to fill the plastic boxes to form a liquid slab. The phase of each LC sample was measured and compared to calculate the average index n_r by using Eq. 4.5.

- Extraordinary index n_e. A pair of permanent magnets was mounted externally to waveguide to supply bias magnetic field along the incident electric field direction, see Fig. 4.14. In this case, under bias enough magnetic field, LC molecular director were reoriented along the magnetic fied, i.e, parallel to the incident electric field. Thus, the incident wave experienced the extraordinary index n_r. The phase shift between two LC slabs was also measured and to obtain extraordinary index n_r.

- Ordinary index n_0. The ordinary index of LC can be calculated by from n_r and n_e

$$n_r^{\,2} = \frac{n_e^{\,2} + 2n_0^{\,2}}{3} \tag{4.7}$$

Figure 4.15(a) shows the frequency dependence of the extraordinary n_e and ordinary n_o from 10 to 12 GHz. As shown in Fig. 4.15(a), LC compound exhibits a positive birefringence ($n_e > n_o$) in the frequency band of interest, in which n_e varies between 1.33 and 1.48 whereas n_o changes from 1.28 to 1.41. The birefringence Δn versus frequency is plotted in Fig. 4.15(b). Δn fluctuates around 0.05, which is only a little higher than the birefringence of some commercial nematic compound such as 5CB in the same frequency range [35].

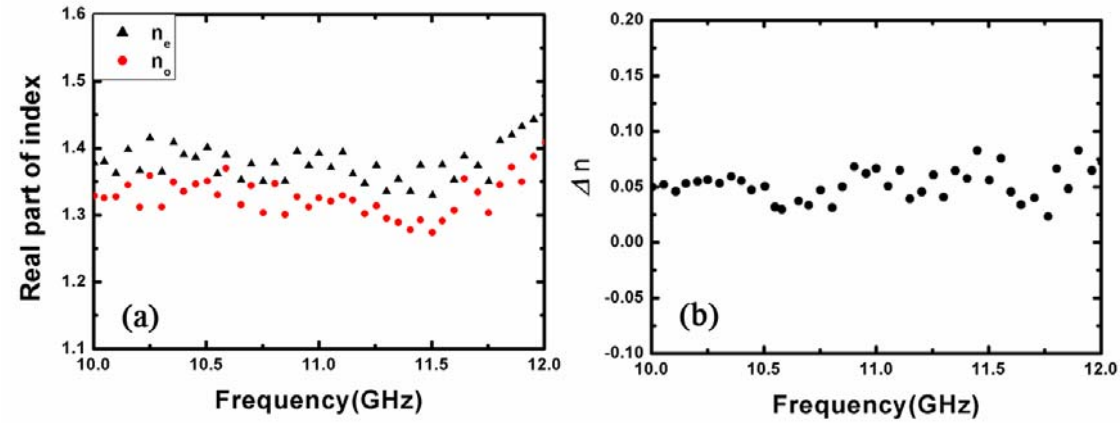

Fig. 4.15 (a) Extraordinary (black triangular) and ordinary (red circle) refractive indexes measured at room temperature as a function of frequency. (b) Birefringence of the nematic compound was deduced in the 10-12 GHz frequency band.

4.4.3. Transmission measurement of LHM

By using a needle tube, LC compound was infiltrated into the board interspacing via capillary forces. In order to orientate the LC molecules, a pair of permanent magnets with centimeter size was mounted externally to apply a uniform magnetic field in the *x-y* plane. As stated above, the external magnetic field of 500 G measured by a digital magnetometer enables a good alignment of the LC molecules as the threshold field is less than 100 G for thin cells [36]. The metamaterial sample was then inserted in an X-band hollow waveguide and the scattering parameters were measured by using a HP8720 ES Vectorial Network Analyzer.

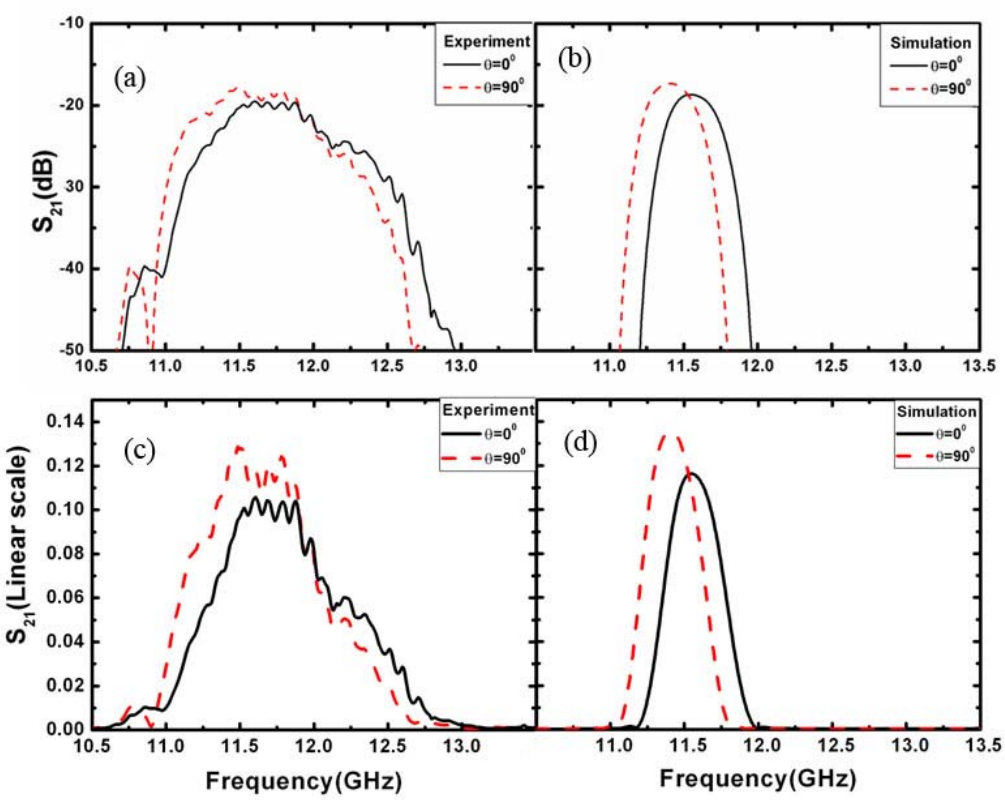

Fig. 4. 16 The experimental (a), (c) and simulation (b), (d) transmission responses of the metamaterial with infiltrated by LC under different molecules orientations: θ = 0° (solid black line) and 90° (dashed red line), respectively. The transmission spectra are plotted in dB ((a), (b)) and linear scale ((c), (d)), respectively.

The measurements of the transmission spectra were carried out (i) with the magnetic field applied along the *x* axis (θ = 0°) and (ii) along the *y* axis (θ = 90°). The results are reported in Figs. 4.16(a) and (c). When the magnetic field is applied along the *x* axis (θ = 0°), omega arrays exhibit a well-defined transmission pass-band, as expected with negative index property. The transmission maximum is at 11.72 GHz. For θ = 90° and hence for an orthogonal magnetic field excitation, a red-shift of the pass-band was observed with a maximum of transmission at 11.50 GHz. Although the pass-band shift of 220 MHz is not large compared to the relatively broad bandwidth, it can be measured visibly without any ambiguity, especially for the result plotted in linear scale (Fig. 4.16(c)), due to the fact that the overall form of the transmission band is relatively unchanged between the two LC reorientation states. In addition, it is also noted that the red-shift of passband occurs with an increasing transmittance.

For a better understanding of the tuning of the omega-type metamaterial based on LC orientation, simulations were performed by using the full wave software CST Microwave Studio. As tunability is not so large, it is no meaning to investigate the passband dependence on LC molecular reorientation angle with a parameter sweep requiring rotation of whole model as done for that of SRR stated above (Fig. 4.8). A permittivity tensor was used for a rigorous description of LC molecules, where $\varepsilon_e = n_e^2$ and $\varepsilon_o = n_o^2$ are the permittivities parallel and perpendicular to the molecular director, respectively. For these calculations, we employed the experimental data of LC indexes: n_o = 1.38, n_e = 1.43 and thus a birefringence of 0.05. The loss tangents of LC were set as $tan\ \delta_o$ = 0.020 for n_o and $tan\ \delta_e$ = 0.016 for n_e in order to fit the experimental transmittance level. A slightly larger $tan\ \delta_o$ compared to that of $tan\ \delta_e$ was chosen according to the previous report on the dielectric properties of some LC compounds at microwave frequencies [36]. Therefore in simulation, a LC layer is treated as $\{2.0449,1.9044,1.9044\}$ and $\{1.9044,2.0449,1.9044\}$ for the respective two reorientations: θ = 0° and 90°.

Figures 4.16(b) and (d) show the simulation results for the transmission response versus frequency. For the LC reorientation corresponding to θ = 0°, omega arrays exhibit a well-defined pass-band with a centre frequency at 11.55 GHz, which is in a fairly good agreement with the experimental results. However, the experimental result (Fig. 4.16(b)) shows a broader operating bandwidth. This is mainly due to the slightly variations of the voids interspacing as the Teflon fiberglass is not perfectly rigid. Further simulation results confirmed that the pass-band position is very sensitive to the void thickness variation. For instances, a 360 MHz frequency shift occurs when the thickness of voids changes 50 μm. The unwanted spacing differences result in different magnetic resonances between layers, causing multiple adjacent pass-bands and consequently a broader transmission window. Under the orthogonal excitation of external magnetic field (θ = 90°), the passband shifts down to 11.40 GHz, showing the same dependence on LC reorientation as the experimental results.

To provide an insight on the relation between the LHM passband shift and the reorientation of LC molecules, local electric field map was monitored at center frequency of passband and plotted in Fig. 4.17. It can be noticed that local electric field is polarized along the *y* axis rather than along the *x* axis which corresponds to the incident electric field polarization. This is a result of the broadside coupling between the omega patterns facing together as explained in previous section and Ref. [47]. In fact, the capacitance of the omega pattern is mainly determined by the

permittivity component ε_y along the y direction, which thus dominates the magnetic response as shown in Fig. 4.17(c). When an external magnetic field is applied to orientate the LC molecules from randomly alignment to parallel to x, ε_y is mainly experienced the ordinary permittivity of LC as ε_o. As the LC director is reorientated from θ = 0° to 90°, ε_y is increased from ε_o to ε_e, giving rise to an increase of the capacitance and therefore a redshift of the resonant frequency. Additionally, as the loss tangent of the molecule along the y axis is decreased from $tan\ \delta_o$ to $tan\ \delta_e$, the passband transmittance is increased to a higher level.

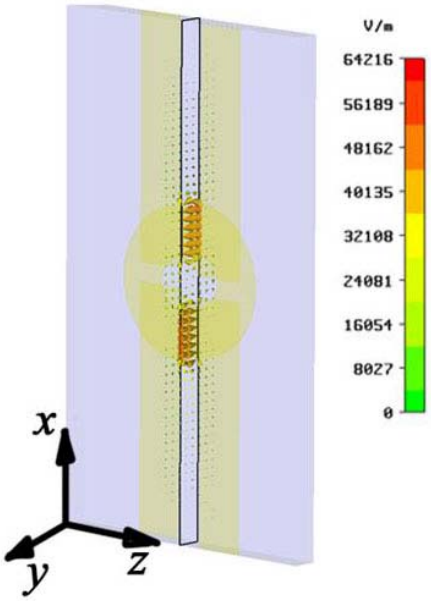

Fig. 4.17 The local electric field distribution is plotted in the x-y plane at the magnetic resonance of omega pattern. Teflon fiberglass boards were invisible for clarity.

4.4.4. Effective index variation

The frequency dependences of the index real parts were subsequently calculated from the scattering parameters of a basic unit cell by employing a well-established algorithm [41-43] (Fig .4.18). As shown in Fig. 4.18(a), negative values of index are observed from 11.0 to 13.0 GHz, verifying that the pass-bands correspond to a left handed dispersion branch. With the change of LC orientation by external magnetic field, a visible redshift of the index curve is noticed between 11.0 and 12.5 GHz. In the lower frequency band identified by shadowed region, the metamaterial transmission is very weak and dominated by the evanescent waves, so that the derivation of a refractive index value becomes questionable.

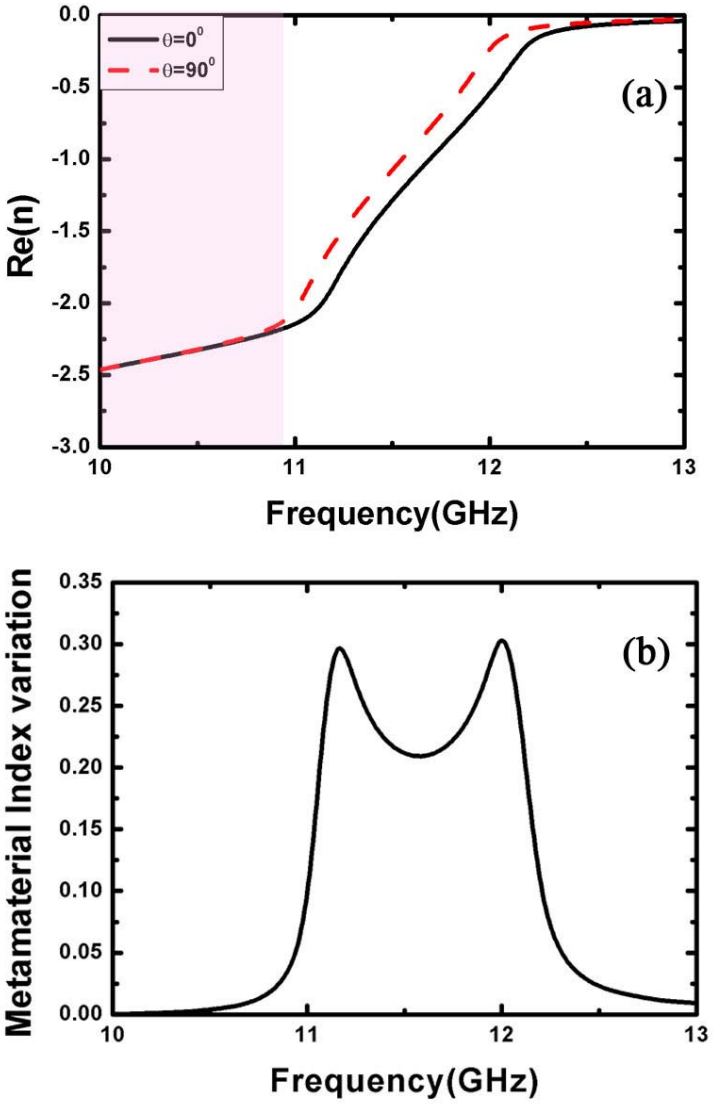

Fig. 4.18 (a) The real parts of retrieval indexes for metamaterial infiltrated by LC under different LC molecular reorientations: θ = 0° (solid black line) and 90° (dashed red line). (b) Index variation of metamaterial between LC molecular reorientation.

The variation of the real part of n is also calculated and plotted in Fig. 4.18(b). For the external magnetic field changing from parallel to perpendicular to incident E field, metamaterial index increases around the regime from 11.0-12.5 GHz with a w-like variation as a function of frequency. Beyond this regime, the index is nearly unchanged. In addition, a maximum index change of 0.29 at 11.17GHz and 12.0 GHz is observed under LC reorientation with a rather smaller birefringence of 0.05. However, further calculation demonstrated that frequency dependent index variation shape is not always symmetric, two peaks with the same maximum value, but suffers

from loss tangent definition of LC permittivity tensor in some sense. Anyway, in our numerous calculations, the frequency dependent index variation of metamaterial always shows two peaks at two cut-off frequency points of left-handed branch.

There are various methods such as prism refraction [2, 8], effective parameters retrieval [48] and phase shift [9] to measure effective index for metamaterial. With respect to our sample, in addition to difficulty to fabricate a prism sample, the application of powerful external field is another tricky as the sample size becomes much bigger requiring bigger magnets. The effective parameter approach needs scattering parameters measured in free space. On the contrary, it is very convenient to obtain the sample phase. Therefore, we attempted to obtain the index variation via phase shift. For a medium with a given length d loaded in a waveguide, phase delay Φ of traveling wave between input and output interfaces is given by

$$\phi = -nk_0 d \tag{4.8}$$

where k_0 is the wave number in hollow waveguide which has a slight difference from the wave number in free space according to Eq. 4.3, n is the effective index. It is seen that phase delay Φ is proportional to index. When index changes Δ n, phase shift can be calculated by

$$\Delta\phi = -\Delta n k_0 d \tag{4.9}$$

Therefore, we can obtain index change of metamaterial via the comparison of phase delays for metamaterial under LC molecular reorientation.

The measured phase shift of a nine-cell-long sample (Fig. 4.13), as a consequence of the index variation between the two orthogonal magnetic field excitations, is shown in Fig. 4.19. As the director of LC is reoriented from 0° to 90°, phase delay of metamaterial sample has a visible red shift, resulting in the peaks in frequency dependent phase shift as shown in Fig. 4.19(b). It is seen that phase shift reaches a maximum value of 174.5° at 10.93 GHz, corresponds to an approximate index variation peak of 0.25 for the 5.4-cm-long sample considered here, which is in a remarkable agreement with simulation results. However, second peak of phase shift occurring at 12.59 GHz is rather week, a large difference from effective index pointed by numerical calculation shown in Fig. 4.18. In fact, imperfect void spacing, which may lead to broader passband than simulation, also presumably deteriorates effective index relation frequency of metamaterial, hence, leads to different index variation of metamaterial as well as phase shift between LC reorientation in

comparison with simulation. It is noted the enhanced index variation 0.25 arising from a LC birefringence of 0.05 is mainly due to the intrinsic strong magnetic resonant character around 11.0 GHz.

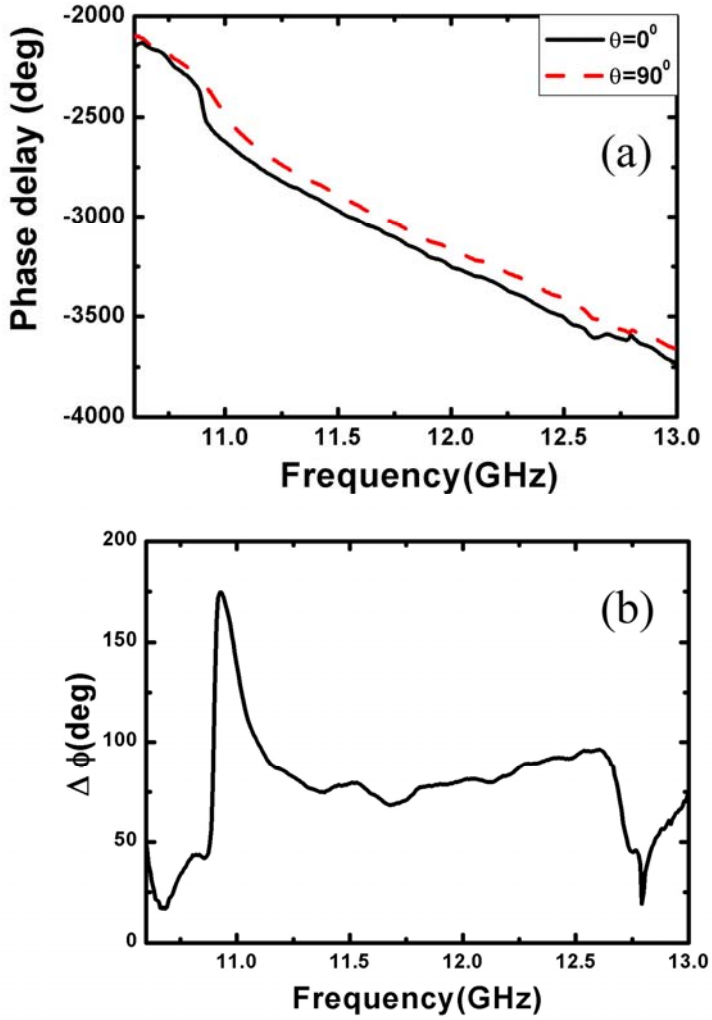

Fig. 4.19 (a) Phase delays for metamaterial under orientations of LC. (b)The measured phase shift for a nine-cell prototype when the LC molecules are reorientated from θ = 0° to 90°.

Both experimental and numerical results of omega array infiltrated by LC stated above show a relatively large index variation can be produced via LC molecular reorientation, indicating potential application in some devices such as phase shifter. However, nearly more than 2 dB/cell insertion loss is one main drawback. Hereafter, we attempt to optimize omega structure as well as corresponding reconfiguration results on LC reorientation.

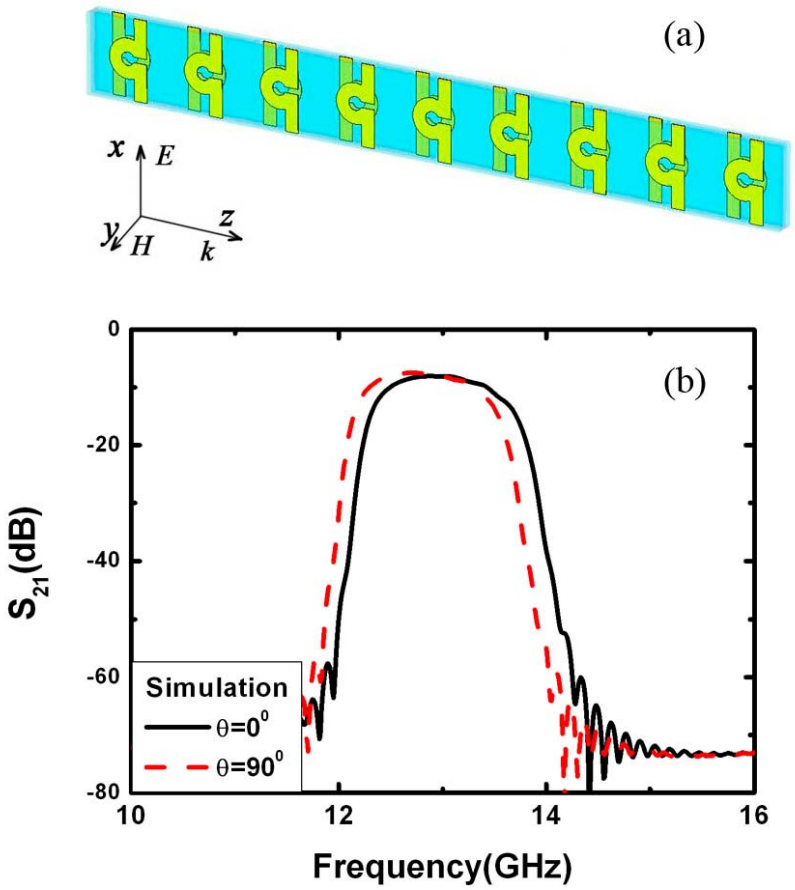

Fig. 4.20 (a) Optimized tunable omega metamaterial model. The geometrical parameters are nearly the same as the original one except for the periodicity along *x* direction reduces to 6.0 mm. (b) simulated transmission spectra of tunable omega metamaterial under LC reorientation.

For the original scheme, the periodicity is set as 10.0 mm along electric field direction to fit the cross section of X band waveguide and only one cell magnetic current loop is used in purpose to reduce the filling factor to the bandwidth of left handed passband, hence, to make the frequency shift much more visible. Therefore, the optimized structure has nearly the same geometrical dimensions but a smaller periodicity along *x* direction as shown in Fig. 4.20(a). The transmission spectra is shown in Fig. 4.20(b). When the periodicity along the incident electric polarization direction decreases from 10.0 to 6.0 mm, left handed passband shifts a littler higher toward 12.0 GHz, as the inductance of the basic unit cell *L* drops down. Additionally, please notice that the transmission level of the passband increases to -7.4 dB for nine cells. Since all scattering effects such as the reflection were taken into account for the transmittance calculation, the maximum insertion loss is around 0.8 dB per cell, which enables this prototype to be put into application. Under two orthogonal

magnetic field excitations applied for LC molecular alignment, a frequency tuning of 200 MHz, similar to that of the previous sample, is also observed. Due to the increase of filling factor of magnetic resonator, the frequency range of negative permeability becomes larger, extending the bandwidth of passband [8].

4.5. Summary

In this chapter, we are mainly involved in the tunability of metamaterial based on LC molecular reorientation in this chapter. Not only numerical analysis method of LC incorporated into metamaterial but also experimental demonstrations of tunability for single negative and double negative metamaterials were performed and some conclusions can be drawn as follows:

- We analyzed the magnetic and electric responses of S-type tunable LHMs via utilizing isotropic and anisotropic treatments for the LC, respectively. By comparing the results obtained by the two methods, it is shown that the dependence of the magnetic resonance on the LC molecule reorientation is completely reversed by assuming isotropic and anisotropic treatments respectively. For the magnetic resonance, the intrinsic inductor-capacitor resonance causing the local electric field polarized transverse to that of the incident beam. On the other hand, a large quantitative difference in the plasma frequency shift is pointed out. It is concluded that an isotropic description of the LC molecules is not sufficient to predict the tunability of highly anisotropic metamaterials incorporating LC. These numerical results are further confirmed by consequent experimental demonstration.

- A magnetically tunable negative permeability metamaterial is demonstrated at microwave frequencies. A multi-layer void structure was created for the infiltration of LC. The dependence of the magnetic resonant frequency to the LC reorientation, experimentally characterized by means of a prototype fabricated for X-band operation, satisfactorily agrees with the simulation employing a permittivity tensor approach. Based on LC molecular reorientation, 300 MHz frequency shift of magnetic resonance was observed.

- The left handed passband of an omega-type metamaterial infiltrated by LC was successfully controlled magnetically. Simulation and experimental results demonstrate unambiguously that the left handed passband can be tuned by an external dc magnetic field via the orientation of LC director. A maximum shift of 220 MHz was observed experimentally for a LC birefringence $\Delta n = 0.05$

measured at X band. These findings were further confirmed by phase shift measurements on a nine-cell prototype, as well as retrieval index variation retrieved from a one-cell device. As the birefringence of LC increases dramatically with frequency (For instance, 5CB LC exhibits a birefringence as large as 0.21 at 1 THz [49]), it is believed that the efficiency of the tunability via a LC approach could be enhanced by operating in the infrared spectral region. On the other hand, the omega-type motif used in the present experimental demonstration is a generic pattern of metamaterial technology with several related inclusions whose operation relies on the same principles. This is notably the case of S-type arrays, whose fabrication under self sustaining condition by means of a frame, were recently demonstrated and frequency assessed around 2 THz [50]. This free standing technology with natural voids between the staked arrays appears very promising for the extent of LC controlled metamaterials in the Terahertz spectral range.

References

[1]. V. G. Veselago, Sov. Phys. Usp. **10**, 509 (1968).

[2]. R. Shelby, D. R. Smith, and S. Schultz, Science **292**, 77 (2001).

[3]. D. R. Smith, W. J. Padilla, D. C. Vier, S. C. Nemat-Nasser, and S. Schultz, Phys. Rev. Lett. **84**, 4184 (2000).

[4]. H. Chen, L. Ran, J. Huangfu, X. Zhang, K. Chen, T. M. Grzegorczyk, and J. A. Kong, Phys. Rev. E **70**, 057605 (2004).

[5]. H. Chen, L. Ran, J. Huangfu, X. Zhang, K. Chen, T. M. Grzegorczyk, and J. A. Kong, Appl. Phys. Lett. **86**, 151909 (2005).

[6]. J. Huangfu, L. Ran, H. Chen, X. Zhang, K. Chen, T. M. Grzegorczyk, and J. A. Kong, Appl. Phys. Lett. **84**, 1537 (2004).

[7]. L. Ran, J. Huangfu, H. Chen, Y. Li, X. Zhang, K. Chen, and J. A. Kong, Phys. Rev. B **70,** 073102 (2004).

[8]. F. Zhang, G. Houzet, E. Lheurette, D. Lippens, M. Chaubet, and X. Zhao, J. Appl. Phys. **103**, 084312 (2008).

[9]. G. Dolling, C. Enkrich, M. Wegener, C. M. Soukoulis, and S. Linden, Science **312**, 892 (2006).

[10]. X. Zhou, Q. H. Fu, J. Zhao, Y. Yang, and X. P. Zhao, Opt. Express **14**, 7188 (2006).

[11]. P. Markos, and C. M. Soukoulis, Phys. Rev. B **65**, 033401 (2001).

[12]. W. J. Padilla, A. J. Taylor, C. Highstrete, M. Lee, and R. D. Averitt, Phys. Rev. Lett. **96**, 107401 (2006).

[13]. H.-T. Chen, W. J. Padilla, J. M. O. Zide, A. C. Gossard, A. J. Taylor, and R. D. Averitt, Nature **444** 597 (2006).

[14]. H.-T. Chen, J. F. O'Hara, A. K. Azad, A. J. Taylor, R. D. Averitt, D. B. Shrekenhamer,and W. J. Padilla, Nature Photonics **2**, 295 (2008).

[15]. A. Degiron, J. J. Mock, and D. R. Smith, Opt. Express **15**, 1115 (2007).

[16]. I. Gil, J. García-García, J. Bonache, F. Martín, M. Sorolla, and R. Marqués, Electron. Lett. **40**, 1347–1348 (2004).

[17]. I. V. Shadrivov, S. K. Morrison, and Y. S. Kivshar, Opt. Express. **14**, 9344-9349 (2006).

[18]. H. Chen, B.-I. Wu, L. Ran, T. M. Grzegorczyk, and J. A. Kong, Appl. Phys. Lett. **89**, 053509 (2006).

[19]. T. H. Hand and S. A. Cummer, J. Appl. Phys., **103**, 066105 (2008).

[20]. R. Wangberg, J. Elser, E. E. Narimanov, and V. A. Podolskiy, J. Opt. Soc. Am. B **23**, 498 (2006).

[21]. I. C. Khoo, D. H. Werner, X. Liang, A. Diaz, and B. Weiner, Opt. Lett. **31**, 2592 (2006).

[22]. D. H. Werner, D.-H. Kwon, I.-C. Khoo, A. V. Kildishev, and V. M. Shalaev, Opt. Express **15**, 3342 (2007).

[23]. X. Wang, D.-H. Kwon, D. H. Werner, I.-C. Khoo, A. V. Kildishev, and V. M. Shalaev, Appl. Phys. Lett. **91**, 143122 (2007).

[24]. Q. Zhao, L. Kang, B. Du, B. Li, J. Zhou, H. Tang, X. Liang, and B. Zhang, Appl. Phys. Lett. **90**, 011112 (2007).

[25]. F. Zhang, Q. Zhao, L. Kang, D. P. Gaillot, X. Zhao, J. Zhou, and D. Lippens, Appl. Phys. Lett. **92**, 193104 (2008).

[26]. L. Kang, Q. Zhao, H. Zhao, and J. Zhou, Opt. Express **16**, 8825 (2008).

[27]. L. Kang, Q. Zhao, H. Zhao, and J. Zhou, Opt. Express **16**, 17269 (2008).

[28]. L. Kang, Q. Zhao, H. Zhao, and J. Zhou, Appl. Phys. Lett. **93**, 171909 (2008).

[29]. A. Djermoun, A. de Lustrac, J.M. Lourtioz, F. Gadot, and E. Akmansoy, Electron. Lett. **42**, 223 (2006).

[30]. K. Busch and S. John, Phys. Rev. Lett. **83**, 967 (1999).

[31]. D. Kang, J. E. Maclennan, N. A. Clark, A. A. Zakhidov, and R. H. Baughman, Phys. Rev. Lett. **86**, 4052 (2001).

[32]. Y. Shimoda, M. Ozaki, and K. Yoshino, Appl. Phys. Lett. **79**, 3627 (2001).

[33]. E. Graugnard, J. S. King, S. Jain, C. J. Summers, Y. Zhang-Williams, and I. C. Koo, Phys. Rev. B **72**, 233105 (2005).

[34]. K. C. Lim, J. D. Margerum, and A. M. Lackner, Appl. Phys. Lett. **62**, 1065 (1993).

[35]. C. Weil, St. Müller, P. Scheele, P. Best, G. Lüssem, and R. Jakoby, Electron. Lett. **39**, 1732 (2003).

[36]. C.–Y. Chen, T.–R Tsai, C.-L. Pan, and R.-P. Pan, Appl. Phys. Lett. **83**, 4497 (2003).

[37]. F. Yang, and J. R. Sambles, Appl. Phys. Lett. **85**, 2041 (2004).

[38]. D. H. Werner, D.-H. Kwon, I.-C. Khoo, A. V. Kildishev, and V. M. Shalaev, Opt. Express **15**, 3342 (2007).

[39]. X. Wang, D.-H. Kwon, D. H. Werner, I.-C. Khoo, A. V. Kildishev, and V. M. Shalaev, Appl. Phys. Lett. **91**, 143122 (2007).

[40]. Q. Zhao, L. Kang, B. Du, B. Li, J. Zhou, H. Tang, X. Liang, and B. Zhang, Appl. Phys. Lett. **90**, 011112 (2007).

[41]. C. Croënne, B. Fabre, D. Gaillot, O. Vanbésien, and D. Lippens, Phys. Rev. B **77**, 125333 (2008).

[42]. D. R. Smith, S. Schultz, P. Markoš, and C M. Soukoulis, Phys. Rev. B **65**, 195104 (2002).

[43]. X. Chen, T. M. Grzegorczyk, B-I. Wu, J. Pacheco, and J. A. Kong, Phys. Rev. E **70**, 016608 (2004).

[44]. I. C. Koo, *Liquid Crystal: Physical Properties and Nonlinear Optical Phenomena* (Wiley, New York, NY, 1995).

[45]. J. Zhang, H. Chen, L. Ran, Y. Luo, B. W, and J. A. Kong, Appl. Phys. Lett. **92**, 084108 (2008).

[46]. R. Marques, F. Mesa, J. Martel and F. Medina, IEEE Trans. Antennas Propag. **51**, 2572 (2003).

[47]. F. Zhang, Q. Zhao, L. Kang, D. P. Gaillot, X. Zhao, J. Zhou, and D. Lippens, Appl. Phys. Lett. **92**, 193104 (2008).

[48]. J. Zhou, L. Zhang, G. Tuttle, T. Koschny, and C. M. Soukoulis, Phys. Rev. B 73, 041101 (2006).

[49]. T. R. Tsai, C.-Y. Chen, C.-L. Pan, R.-P. Pan, and X.-C. Zhang, Appl. Opt. **42**, 2372 (2003).

[50]. H. O. Moser, J. A. Kong, L. K. Jian, H. S. Chen, G. Liu, M. Bahou, S. M. P. Kalaiselvi, S. M. Maniam, X. X. Cheng, B. I. Wu, P. D. Gu, A. Chen, S. P. Heussler, S. B. Mahmood, and L. Wen, Opt. Express **16**, 13773 (2008)

Chapter 5 Full dielectric metamaterial and its application

5.1 Introduction

Since the first left-handed metamaterials (LHMs) with simultaneously negative permittivity and permeability have been fabricated by means of metallic split ring resonators (SRRs) and wires [1, 2], for tailoring the magnetic and electric responses respectively, many other related elements, such as Ω-shaped structures [3-5], *U*-shaped structures[6], staplelike structures [7], paired rods [8], dendritic [9] and fishnet structures [10], are also successfully used to fabricate LHMs. However, almost metamaterial schemes are made of metal, which inevitably suffers from conductive loss. In addition, the constitutive anisotropic property of unit cell make the realization of isotropic bulk structure difficult, although some efforts have been given to overcome this drawback [11].

Recently, another route based on the interaction between electromagnetic waves and dielectric particles [12, 13], namely Mie resonance, was proposed to achieve the electric or magnetic resonances The Mie resonances of dielectric inclusions provide a novel mechanism for the creation of magnetic and electric resonance based on displacement currents, and offers a simpler and more versatile route for the fabrication of isotropic metamaterials operating at higher frequencies. A recent experiment demonstration of a prism prototype composed of dielectric cylinders exhibits negative refraction [14]. Popa *et al.* have shown that a dielectric magnetic

resonator has the significant advantages of low-loss and simply geometry in comparison with a typical SRR [15]. Zhao *et al.* experimentally presented a negative permeability metamaterial based on $Ba_{0.5}Sr_{0.5}TiO_3$ (BST) cube and the resulting LHMs via adding wire array to provide negative permittivity [16]. In these works, high permittivity is the key issue to realize metamaterial otherwise, otherwise the ratio between the incident wavelength and periodicity can not satisfy effective medium theory.

Besides, Mie resonance mechanism was also considered as a feasible way to realize metamaterial at higher frequency notably visible frequency, where large constitutive loss of metal prevents the performance of typical metamaterial schemes as high as that of low frequencies. In this approach, high permittivity at visible frequency, which can not occurs at natural existing materials, arises from collective plasmon resonance frequency of densely packed metallic nanoparticles [17-19].

In this chapter, we focus on the scattering mechanisms based on magnetic Mie resonance in dielectric particles. Firstly, we presented a full dielectric negative permeability metamaterial based on $Ba_{0.5}Sr_{0.5}TiO_3$ (BST) cubes. A tilted incidence was performed to show isotropic property of cubic metamaterial. The potential application of dielectric magnetic resonator on antenna and invisible cloak were also investigated.

5.2 Dielectric negative permeability metamaterial

The Mie theory**,** developed by Gustav Mie in 1908, is a complete mathematical-physical theory of the scattering of electromagnetic radiation by spherical particles. In contrast to Rayleigh scattering, the Mie solution to the scattering problem is valid for all possible ratios of diameter to wavelength, although the technique results in numerical summation of infinite sums. In its original formulation it assumed an homogeneous, isotropic and optically linear material irradiated by an infinitely extending plane wave. However, solutions for layered spheres are also possible.

From the viewpoint of scattering theory, all scattering objects can be represented by effective electric and/or magnetic polarizability densities. Light scattering by small (relative to the incident light wavelength) spherical particles is a fundamental topic in classical electrodynamics [14], and is based upon the exact Mie solution of the diffraction problem [15]. The scattered field of a single isolated dielectric sphere

with radius r_0 and relative refractive index n can be decomposed into a multipole series with the 2^m-pole term of the scattered electric field proportional to

$$a_m = \frac{n\psi_m(nx)\psi_m'(x) - \psi_m(x)\psi_m'(nx)}{n\psi_m(nx)\xi_m'(x) - \xi_m(x)\psi_m'(nx)} \tag{5.1}$$

whereas the 2^m-pole term of the scattered magnetic field is proportional to

$$b_m = \frac{\psi_m(nx)\psi_m'(x) - n\psi_m(x)\psi_m'(nx)}{\psi_m(nx)\xi_m'(x) - n\xi_m(x)\psi_m'(nx)}. \tag{5.2}$$

where $x = k_0 r_0$, k_0 is the free-space wavenumber, and $\psi_m(x)$ and $\xi_m(x)$ are the Riccati-Bessel functions, and the primes indicate derivation with respect to the argument. The scattering coefficient a_m and b_m are related to the electric and magnetic responses of the sphere, respectively. Mie theory shows that only the values of a_1 and b_1 contribute to the effective permittivity and permeability of the particle composite.

5.2.1 Mie resonance in BST cubes

In this section, we will firstly numerically calculated basic order Mie resonance of dielectric cube with high permittivity. The basic unit cell of dielectric metamaterial, composed of $Ba_xSr_{1-x}TiO_3$ (BST) cube surrounded by a thin Teflon layer, is shown in Fig. 5.1(a). The effective permittivity property (ε_{bst} = 850, tan δ = 0.001) of the cube was employed as reported in [16]. A thin Teflon layer (ε_r = 2.1, tan δ = 0.001) is used to support the BST cube. An incident beam is excited along the *z* axis with electric field polarized along the *x* axis and magnetic field polarized along the *y* axis. The periodic boundaries (Perfect electric (PEC)/magnetic conductors (PMC)) were used so as to enable us to mimic a thin layer for the incident beam but with infinite dimensions along the transverse directions to the propagation. The region out of the basic unit cell is assumed to be vacuum.

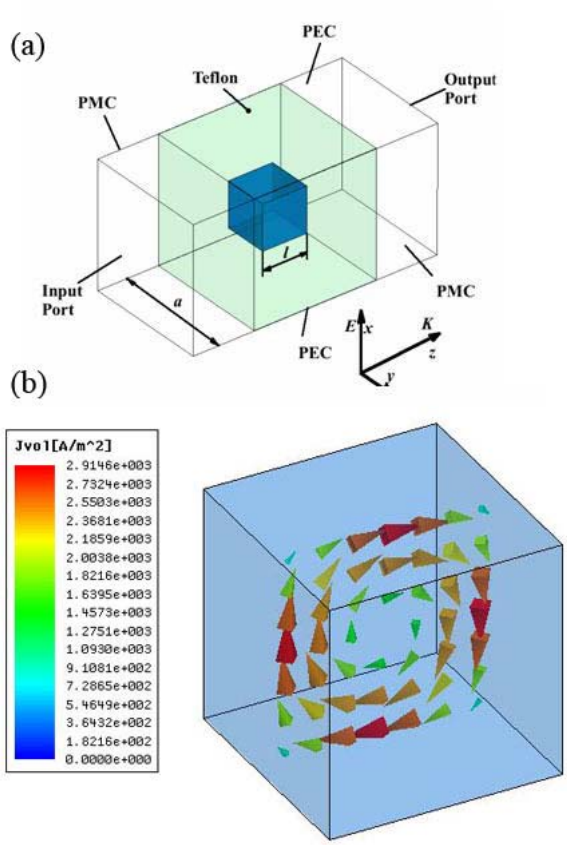

Fig. 5.1 (a) The schematic diagram of the basic unit cell of BST-based metamaterial. The geometry parameters are as follows: l = 0.9 a = 2.5 (unit: mm). (b) Zoom view of displacement currents inside BST cube excited by the incident magnetic field are shown in the x-z plane.

The lowest order resonant mode frequency, magnetic resonance, of a cubic dielectric resonator can be given by [20, 21]

$$f = \frac{c_0}{\sqrt{2}\sqrt{\varepsilon_r \mu_r} l} \tag{5.1}$$

where c_0 is the electromagnetic wave speed in free space, ε_r and μ_r are the respective relative permittivity and permeability of dielectric cube, l is the side length of the cube. Given relative permittivity of BST ε = 850, side length l = 0.9 mm, magnetic resonance frequency of BST cube can be given by 8.1 GHz.

Using commercial software package, HIGH FREQUENCY STRUCTURE SIMULATOR (HFSS), we can obtain the reflection parameters as well as the transmission. Fig. 5.2 plots the scattering parameters of elementary dielectric metamaterial cell. As shown in Fig. 5.2 (a), the basic unit cell exhibits a well-defined

dip with a magnitude of - 22.0 dB around 9.57 GHz in the transmission window, which is accompanied by a strong reflection. Compared to the magnetic resonance frequency predicted by Eq. 5.1, there is a modest discrepancy of the magnetic resonance frequency of BST cube. Unlike infinite cylinder rod discussed in Ref. [12], when a circular displacement loop is excited in a rectangular dielectric resonator, some local fields can break out of the square shape constraints [14], leading to a smaller effective permittivity ε_{eff} of BST cube than the original value, hence, a higher resonance frequency.

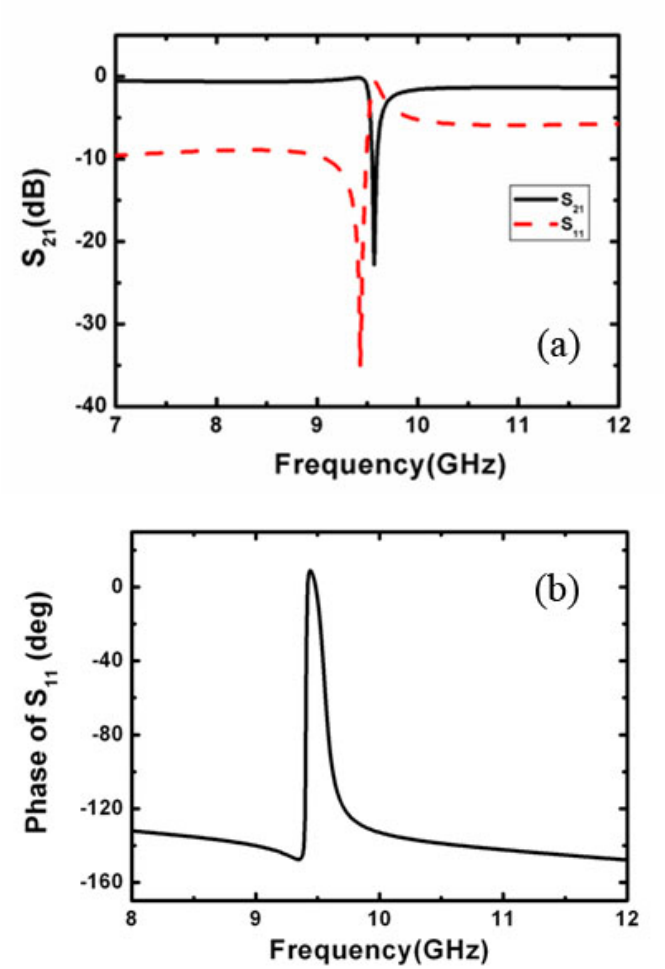

Fig. 5.2 (a) Scattering parameters of dielectric metamaterial based on BST. (b) Reflection phase of dielectric metamaterial based on BST.

The propagation constant, $\gamma = \alpha + j\beta$ where α and β depict the evanescence of the wave and the phase constant, calculated by using the method stated in previous chapter [22] was shown in Fig. 5.3. It can be seen that phase constant exhibits a bandgap ranging from 9.50 - 9.70 GHz, where the attenuation constant α becomes extremely large.

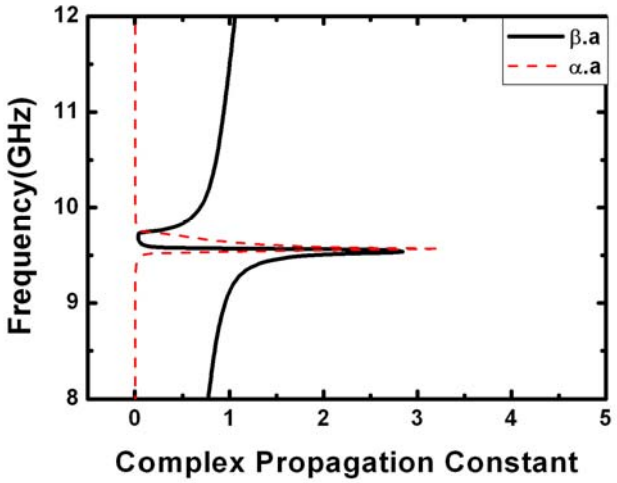

Fig. 5.3 Dispersion diagram of BST cube whose geometry dimensions are shown in Fig. 5.1.

In order to distinguish the mechanism underlying propagation bandgap, we retrieved the effective parameters from scattering parameters via well-established retrieval algorithm [23-25]. Figure 5.4 gives the calculated constitutive parameters of dielectric metamaterial. At low frequencies we have a primarily real refractive index which followed a large imaginary part as we approach the resonance frequency around 9.5 GHz. In the bandgap region, the strong imaginary part of effective index dominates the behavior of incident wave, implying the strong attenuation of the wave inside BST cube. Above the gap region, the refractive index is almost zero and as the frequency is increased further we return to the regime of linear dispersion, and turn to constant as the frequency far away from the resonance region. With respect to the impedance as plotted in Fig. 5.4 (b), the real part of impedance approaches large values as well as the imaginary part near the resonance frequency region. As the impedance is defined by

$$Zc = \frac{E_x}{H_y} \tag{5.2}$$

Thus, the large value of real part of impedance means that around the surface the magnetic field is rather small even the electric field is big. In this case, this type of dielectric cube can be referred as perfect magnetic conductor, or artificial magnetic conductor (AMC), whose surface has no phase change between the incident and reflected waves. The reflection phase of dielectric metamaterial is given in Fig. 5.2(b). The reflection phase curve jumps from – 147.0º at 9.37 GHz to 8.97º at 9.44 GHz, then decrease as frequency. . It is noted that the phase of S_{11} goes through

zero at 9.49 GHz, showing the in-phase reflection characteristic, indicating this dielectric material can function as an AMC. Around this regime, The reflected beam would not have destructive interferences with the incident wave. The property of this type of AMC and potential application on antenna will be investigated in details in latter section.

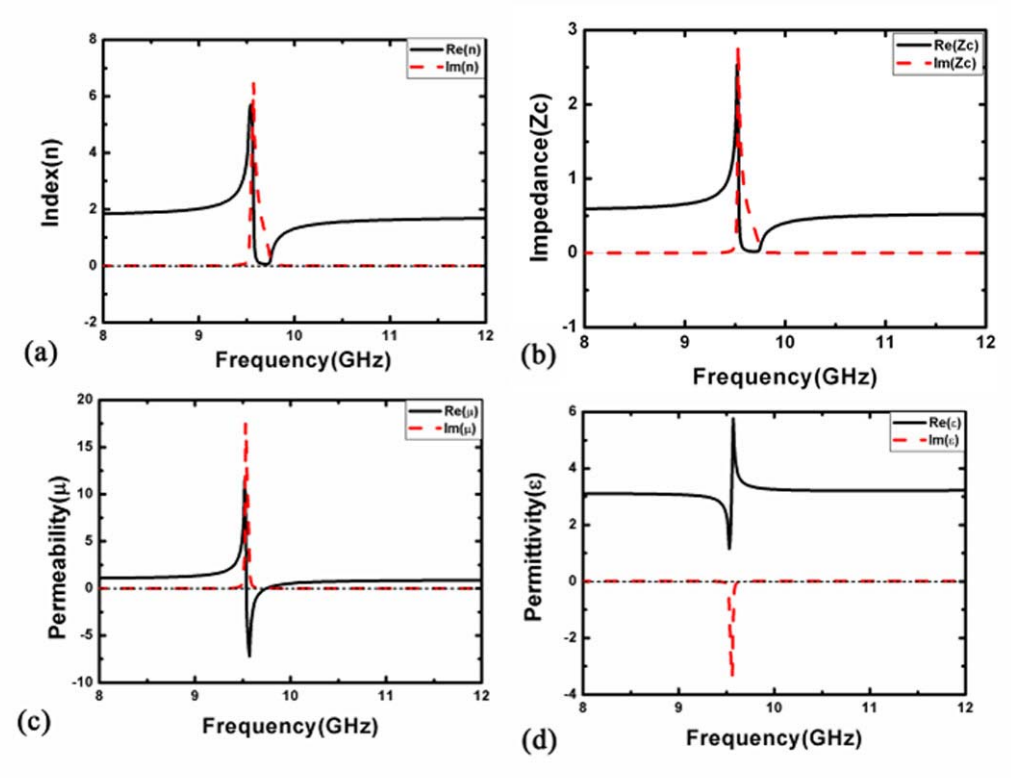

Fig. 5.4 The effective parameters of BST based dielectric metamaterial. (a) Index n; (b) Impedance Zc; (c) Permeability μ; (d) Permittivity ε. The real and imaginary parts are presented by solid black and dashed red line, respectively. Another dotted line is added to distinguish the positive and negative values of effective parameters.

The effective permeability and permittivity are given in Figs. 5.4 (c) and (d). At low frequency, the effective permeability is close to unity, implying no magnetic polarization occurs. However, the effective permeability is strongly dispersive near the Mie resonance. As the frequency close to the resonance region, the effective permeability becomes large with a comparable imaginary part. At the resonance region, the effective permeability is negative and primarily real. As the frequency further increases, the effective permeability turns positive with linear dispersive characteristics, followed by constant value in the frequency regime far away from the resonance region. In Fig. 5.4 (d), the effective permittivity almost is unchanged in addition to an anti-resonance behavior around the Mie resonance arising from

finite length of cell [26]. Note that the periodicity is only 2.5 mm, less than 10 times smaller than the wavelength at frequency of interest, allows homogenous treatment of elementary cell.

From the effective parameters especially effective permeability shown above, we see that the band gap arising from Mie resonance is due to negative value of permeability. The induced displacement currents inside BST cube is given in Fig. 5.1 (b). Near Mie resonance incident magnetic field can induce an circular displacement currents, which in turn, produces an opposite magnetic component to external magnetic field, hence, may result in negative value of permeability. The local magnetic field at the resonance frequency is given in Fig. 5.5. The local magnetic field inside BST cube is greatly enhanced along with opposite sign to the incident magnetic field, leading to negative effective permeability.

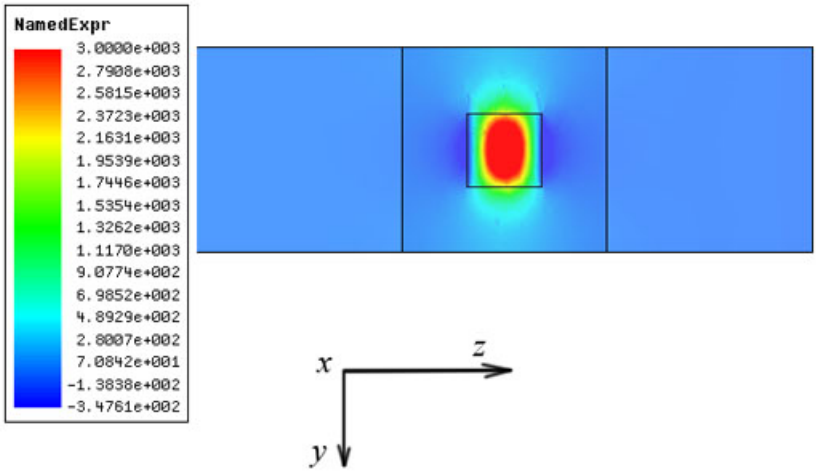

Fig. 5.5 The local magnetic field component H*y* in the *y*-*z* plane.

5.2.2 Loss tangent influence

In fact, all the natural occurring materials have constitutive loss representing the damping effect of the response for the external field. The influence of material loss on the behaviour of Mie resonance based metamaterial is of interest, notably for the potential application. The effect of loss of BST on the scattering parameters is given in Fig. 5.6. As the loss tangent of BST increases, the transmission dip becomes weaker. Especially, it changes from - 22.0 dB to – 7.0 dB when loss tangent of BST increases one order from 0.001 to 0.01. Importantly, when loss tangent becomes 0.05, the transmission level is less than -2 dB, nearly damping out, indicating the intuitive material loss plays an important role on the resonance behaviour of Mie resonance. In addition, reflection property changes as the loss of BST. For instance, reflection

phase fails to reach zero degree around Mie resonance for loss tangent of 0.03. In this case, BST based AMC can not be realized due to the fact that BST is too lossy.

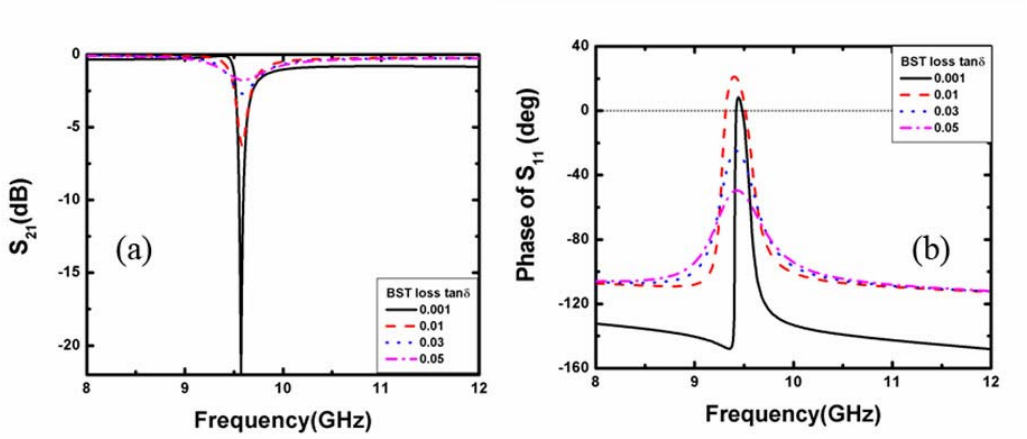

Fig. 5.6 The influence on the scattering parameters of Mie resonance based metamaterial. The geometrical dimension as well as the relative permittivity is used the same as stated above (l=0.9 a=2.5, ε=850).

5.2.3 Periodicity influence

The periodicity influence of elementary cell on first order Mie resonance, i.e., magnetic resonance, is also calculated and given in Fig. 5.7. Here, we set the periodicity of elementary cell increases from 1.2 to 5.0 mm while keeping the other parameters of BST cubes including the dimensions and dielectric property. It can be seen that Mie resonance frequency increases monotonically with periodicity. When periodicity increases gradually from 1.2 to 5.0 mm, magnetic Mie resonance frequency shifts up from 9.07 to 9.62 GHz. From the transmission dip variation, the resonance strength decreases as periodicity becomes larger. However, when periodicity is not very small, little influence arising from periodicity change can be observed. For example, magnetic Mie resonance frequency only changes from 9.52 to 9.62 GHz as periodicity increases from 2.0 to 5.0 mm. This frequency variation is so minor that sometimes it can be neglected in some sense. The high permittivity of BST, which is a key issue to realize Mie resonance based metamaterial as stated above, ensures that most of displacement currents rotate inside cube, thus, periodicity has minor influence on magnetic Mie resonance frequency, which is similar to that reported in Ref. [14]. Even though, coupling effect between neighbouring cells can not be ignored when periodicity is comparable to that of BST cube.

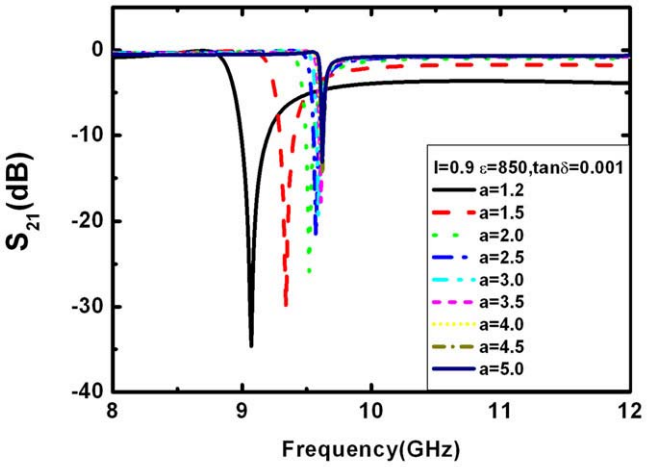

Fig. 5.7 The influence of periodicity of elementary cell for dielectric metamaterial on the Mie resonance. The size as well as dielectric property of BST is fixed as constant.

5.2.4 Experimental demonstration of Mie resonance metamaterial

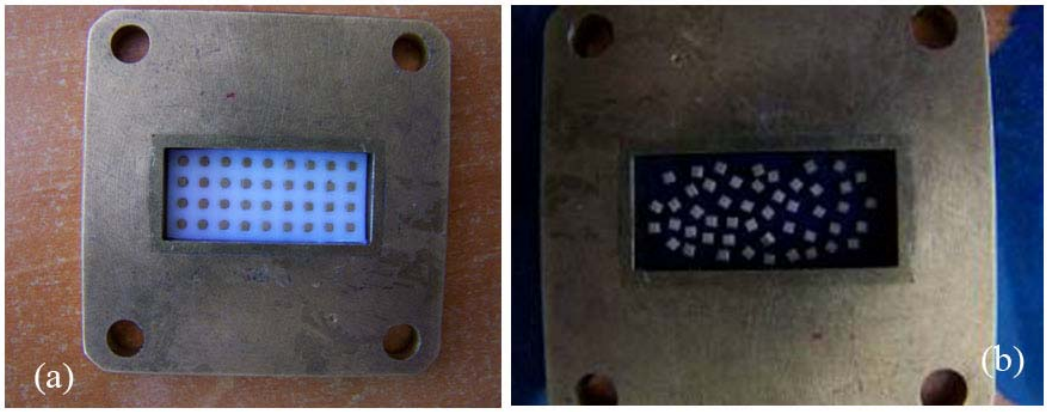

Fig. 5.8 (Close-up view of BST cubes arranged periodically (a) and randomly (b) inside a Teflon template, which is placed into an X band waveguide flange.

Recently, University of Tsinghua succeeded in fabricating BST ceramic cubes, which were subsequently characterized over a wide temperature range around the Curie temperature [27]. One can find in the Ref. [27] further details of the fabrication techniques and the temperature dependence of the material properties. In present section, special attention will be given to the experimental transmission characteristic at room temperature as well as the reflection property. To achieve this aim, BST ceramic cubes were arranged in a square lattice into a Teflon film as shown in the photograph in Fig. 5.8. The size length of BST cube is 0.9 mm. The lattice periodicity is 2.5 mm.

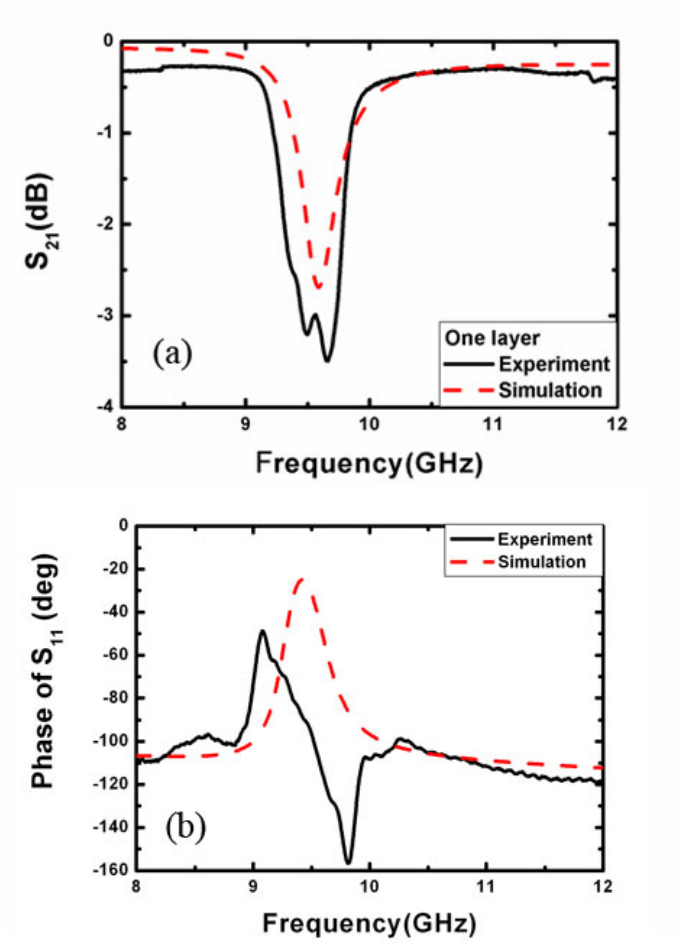

Fig. 5.9 The experimental (solid line) and simulated (dashed line) results of transmission spectra (a) and reflection phase (b) of BST cubes. The BST cube has a side length of 0.9mm and is arranged in square array of periodicity of 2.5 mm. The simulation is performed by presuming BST with a relative permittivity $\varepsilon = 850$, $\tan\delta = 0.03$.

The experimental and simulation results for BST cubes are given in Fig. 5.9. The scattering parameters of BST cubes were measured in an X band waveguide by HP 85107A Vector Network Analyzer. Calibration was carried out when the BST sample was removed. As shown in Fig. 5.9(a), BST cube array exhibits a relative broad transmission gap centered at 9.5 GHz, which is in a good agreement with previous simulation result with respect of resonance frequency. However, for one layer of BST cubes array stacked along the propagation direction, the observed -3.5 dB of transmission level is much weaker than simulated results with an assumption of dielectric loss tangent 10^{-3} for BST as stated above (Fig. 5.2). In order to fit experimental result, a new set of full wave calculation for BST cubes was performed by changing the definition of dielectric loss of BST. It is found that a good agreement between simulation and experimental results can be achieved when loss tangent of BST is set to 0.03, which is much larger than that used in previous

calculation. As aforementioned before, the reflection property notably the reflection phase, as well as transmission response of BST is mainly determined by the dielectric loss. A much lossy material will fail to reach an in-phase property of AMC. One can see this conclusion from Fig. 5.9 (b), in which only – 50º degree, far away from zero degree around Mie resonance, of the reflected phase was obtained as a consequence of higher dielectric loss. Besides, in comparison with simulation, broader bandwidth and lower reflection phase in experiment curves are presumably due to the fact that a slight variation of BST cube size.

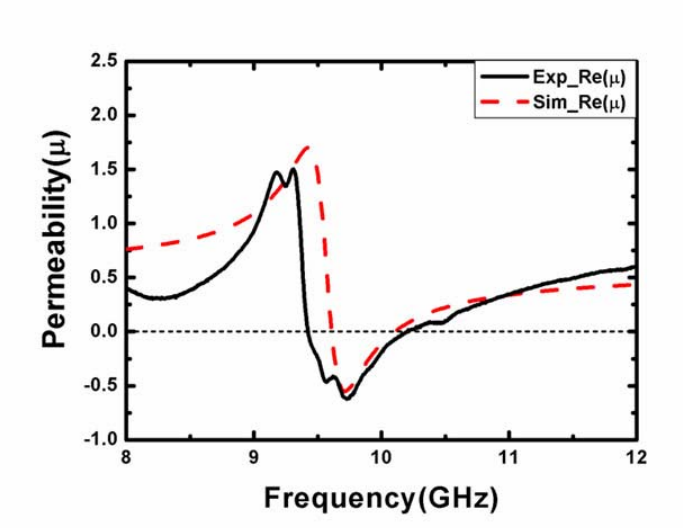

Fig. 5.10 Experimental and simulated retrieval effective permeability of BST cube based metamaterial. The dimension and periodicity are the same as shown in Fig. 5.1.

Using well-established algorithm [23-25], effective permeability of BST cube based metamaterial is retrieved and plotted in Fig. 5.10. Even though dielectric loss of BST is increased by one order, negative permeability still exists around resonance regime ranging from 9.42 to 10.42 GHz, indicating the feasibility of dielectric negative permeability based on BST cube presented here. Experimental result agrees well with simulation based on new assumption for BST dielectric property.

The periodicity influence on magnetic Mie resonance of BST cubes was also experimentally investigated. At a first stage, we compared transmission response of periodically and randomly arranged BST cube arrays, as shown in Fig. 5.8. For the random case, BST cubes were stuck to a thin film and dispersed randomly in transverse plane of propagation direction. For both case, BST cube has a side length of 0.9 mm. The transmission spectra were measured and given in Fig. 5.11. It is seen that an excellent agreement of the transmission response between periodical and random cases was obtained except for a little bit larger bandwidth of transmittance

gap for random array of BST cubes. It is noticed, as predicted by simulation, that supporting material has no influence on magnetic resonance frequency of BST cubes, as its dielectric property is greatly different from that of BST. In Fig. 5.8, random arrangement of BST cubes is incompact, leaving modest periodicity of each cube at least. In this case, periodicity has minor influence on magnetic Mie resonance frequency, as pointed by numerical analyzed before. That is to say, magnetic resonance frequency of BST cube is independent of periodicity somewhat.

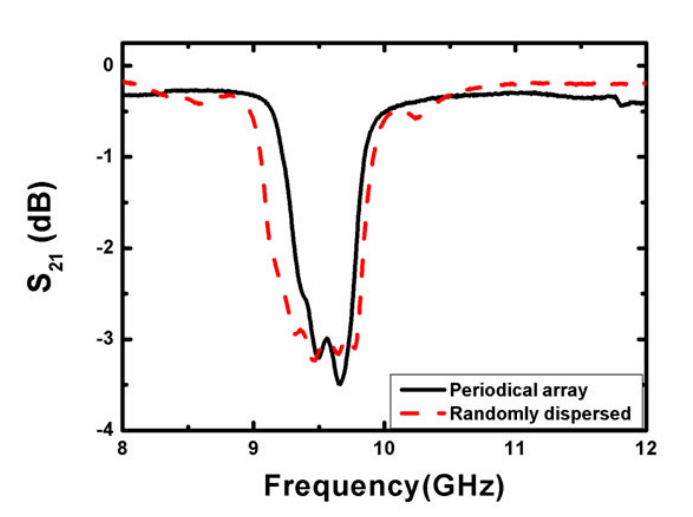

Fig. 5.11 Transmission spectra comparison between periodically and randomly arranged BST cubes. The photographs for these two prototype are shown in Fig. 5.8.

To further check the relation between magnetic resonance and periodicity of BST cubes, we studied experimentally transmission spectra of BST cubes with various periodicities. However, as shown previous, one layer of BST cubes exhibits a weak but broad dip due to large dielectric loss, which is not easy for the observation of center frequency change, here we stacked three unit cell along the incident beam propagation direction so as to enhance magnetic resonance strength of BST cubes. In the experiment, BST cubes were placed in various periodicities and the corresponding transmission spectra were recorded and given in Fig. 5.12. For the case of periodicity a = 2.5mm, three layers of BST cubes have the same resonance frequency but a much more profound transmittance of -9 dB in comparison with that of one layer. When periodicity increases from 2.0 to 6.0 mm gradually, transmittance dip becomes weaker from -13.8 to -3.5 dB. Nevertheless, magnetic resonance of BST cubes remains unchanged from both experimental and simulated results. It is also noticed that an excellent quantitative agreement between experiment and simulation is achieved. Therefore, in some sense, we can conclude that magnetic resonance of BST cubes is only determined by size length, i.e., minor independent of

periodicity.

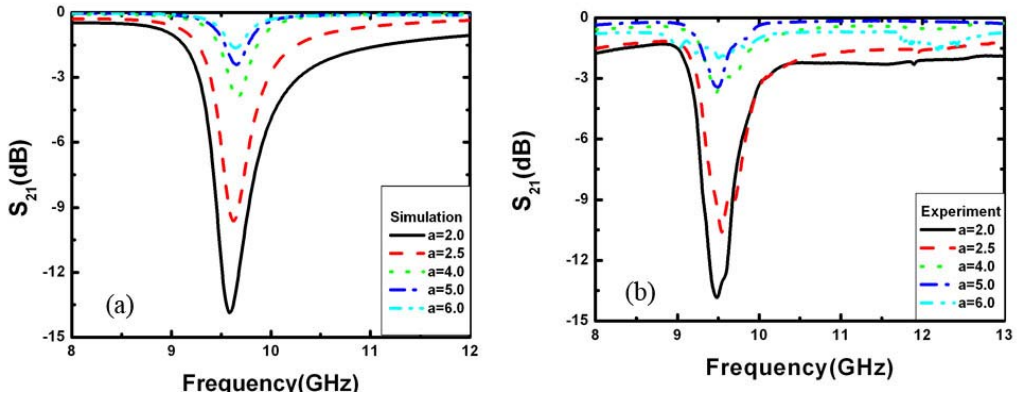

Fig. 5.12 Simulated (a) and experimental (b) transmission spectra of BST cubes with various periodicity. The side length of BST cube is 0.9 mm. Three cubes are stacked along the propagation direction.

5.2.5 Isotropic property of BST cube via tilted transmission

Since left-handed metamaterial with simultaneous negative permittivity and permeability was demonstrated experimentally by using the combination scheme of split-ring resonator (SRR) and wire [1] providing the respective negative permeability and negative permittivity, the realization of the isotropic metamaterial has attracted much attention especially in view of the potential application such as the perfect lens [28]. Shelby *et al.* have investigated a 2D isotropic LHM by arranging SRR/wire in an orthogonal lattice [29]. Koschny *et al.* numerically studied the transmission property of an isotropic LHM composed of a multi-gap symmetric SRR and crossing wire [11]. However, the complex design and intrinsic anisotropic property of SRR due to the asymmetric configuration have restricted greatly the realization of a true isotropic metamaterial. An alternative way to devise metamaterial, which avoids using metallic inclusions, is to employ high dielectric constant materials. Despites some previous works [14-16], stated in the introduction part of this chapter, paved the way to a dielectric metamaterial, a detailed isotropic property demonstration of this type metamaterial has yet to be reported. In this section, we proposed a thin single layer of the metamaterial composed of BST cube. From the transmission property, especially for the response of oblique incidence, the dielectric resonator shows isotropic property for various incident angles and polarizations as shown in Fig. 5.13. A good agreement between the simulation and experiment was observed.

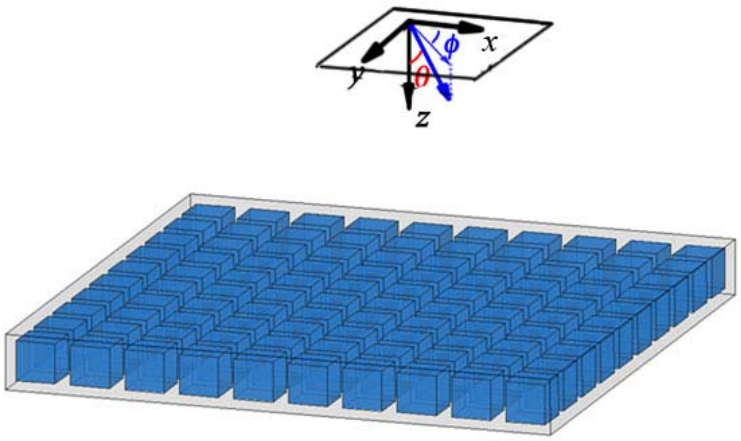

Fig. 5.13 Schematic diagram of oblique incidence on one thin layer of BST cube array.

5.2.5.1 Numerical simulation of Isotropic property of BST cube

In this section, we chose a type of BST with a relative permittivity of 850 + 25i, which is doped by 5 wt % mgo [17]. We used HFSS version 11, a latest commercial finite element package to simulate electromagnetic response of the single layer of dielectric metamaterial. In this version, a new type of excitation port, namely Floquet port, can facilitate greatly the calculations of the phase shift or oblique incidence/reflectance for periodic array. As shown in Fig. 5.13 and 5.14, incident electromagnetic plane can be characterized by two angles: the incidence angle θ between the wave vactor **k** and the surface normanl of the slab, and the angle Φ between the projection of **k** and the some chosen edge of the sample.

In order to facilitate observation of BST cube resonance frequency variation, the periodicity is reduced to 1.25 mm, which leads to higher resonance strength as stated in previous sections. Please also note that the periodicity of the basic unit cell of 1.25 mm, approximate 25 times smaller than the incident wavelength in free space at the frequency of interest, enabling us to consider this dielectric structure as a homogenous material by using effective medium theory. The scattering parameters of the basic cell under the normal incidence were calculated, and then converted into the effective parameters by using a well-established algorithm [23 - 25].

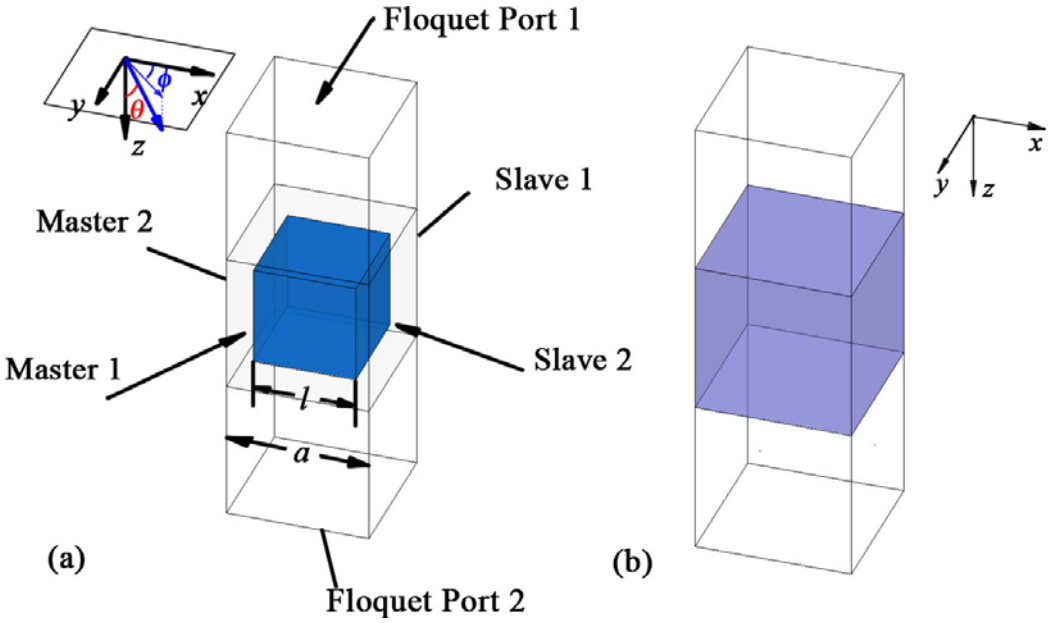

Fig. 5.14 (a) HFSS model of dielectric metamaterial consisting of BST cube under oblique incidence. The geometry dimensions of the elementary cell are: l = 0.9, a = 1.25 mm. Teflon (ε = 2.1 tan δ = 0.001) was chosen to support the BST dielectric cube. Two pairs of Master and Slave periodic boundaries are used to vary phase shift so as to control the incident angle. (b) Schematic of HFSS model for the homogenous dielectric metamaterial, whose dielectric and magnetic material properties are defined by using effective permittivity and permeability depicted in Fig. 5.15.

Figure 5.15 shows the retrieved effective $\mu(\omega)$ and $\varepsilon(\omega)$ for the basic cubic cell of metamaterial. Similar to the typical SRR, effective permeability $\mu(\omega)$ for the BST based metamaterial exhibits a Lorentz-like resonance around 9.0 GHz, followed by negative values until the magnetic plasma frequency, ω_{mp}, at 9.67 GHz. Compared to magnetic resonance frequency of the same BST cube but with large periodicity, there is a clear frequency redshift. On the other hand, an anti-resonance behavior for the real part as well as the negative imaginary part of $\varepsilon(\omega)$ is artifact arising from the periodicity effect [26].

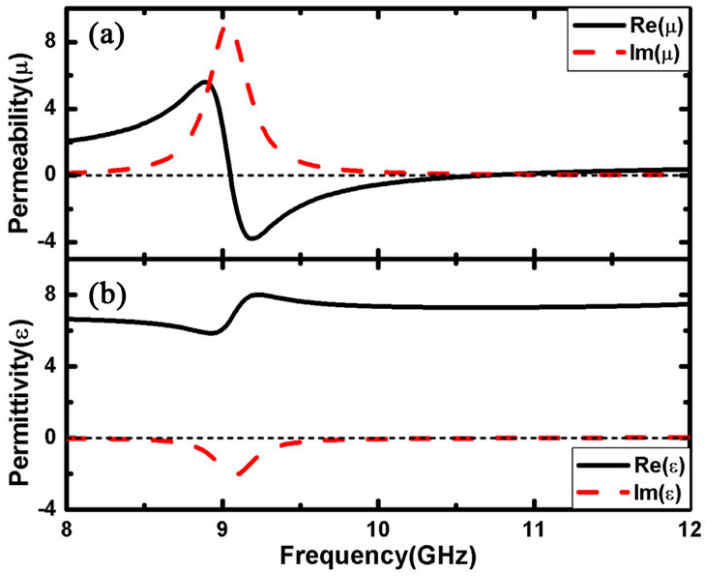

Fig. 5.15 Effective constitutive parameters (a) permeability and (b) permittivity of the dielectric metamaterial under normal incidence.

To calculate the response of the proposed dielectric metamaterial layer to an arbitrary incidence angle and polarization in free space, two fundamental modes, TE_{00} (Electric field parallel to the dielectric layer surface) and TM_{00} (Magnetic field parallel to the dielectric layer surface), together with various phase shifts between the two pairs of periodic boundaries (See Fig. 5.14) were employed. Fig. 5.16 shows the calculated transmission spectra for the dielectric metamaterial layer to various incidence angles and polarizations. For the normal incidence a dip occurs at 9.1 GHz, corresponding to the magnetic resonance as shown in Fig. 5.16. When the incidence beam is off to the surface normal, magnetic resonance dip position is unchanged, revealing the independent property of both the incident angle. Furthermore, although the basic cell only has a square surface, we see an absolutely constant scattering amplitude on the changing Φ of the incidence plane for TE and TM modes and arbitrary θ, which in an accordance with numerical results of cubic lattice of SRRs reported in Ref. [11]. The transmittance variation at the lower and higher frequency sides of the resonance dip is arising from the finite thickness of the slab along the propagation direction in comparison with the infinite large on the transverse directions. For the off-normal incidence spectra of TE mode, however, there is an extra dip occurs at 9.7 GHz. Additionally, the dip strength is increased with the angle off to the metamaterial surface normal.

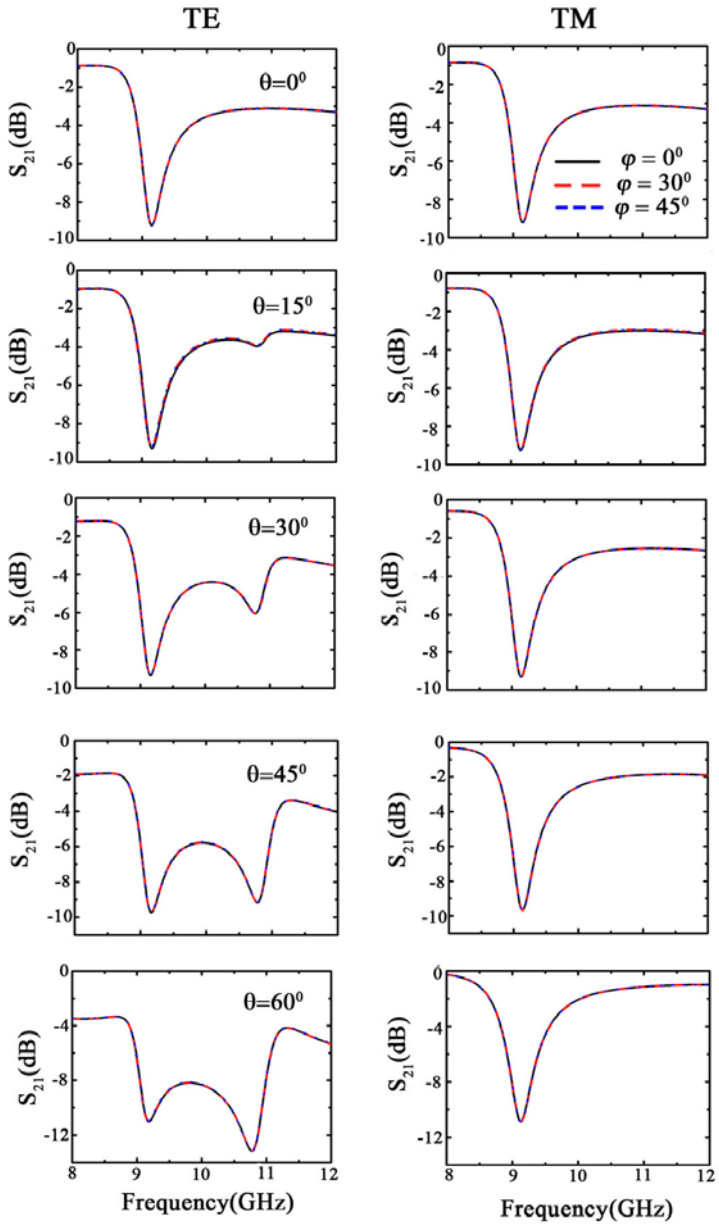

Fig. 5.16 Transmission spectra for a single layer of dielectric negative permeability metamaterial under various incidences angles (θ, Φ) and modes (TE and TM).

In order to show that this extra-zero of transmission is quite general and is independent on the structuring technique, we simulated the transmission spectra for a homogenous slab characterized by using the effective permeability and permittivity reported in Fig. 5.15. The transmission results of homogenous and microstructured cases were plotted by a solid line and hollow circles in Fig. 3, respectively. A very good agreement was obtained showing the possibility to treat the microstructured array as a homogenous one. More importantly, an extra dip is also apparent around 10.7 GHz giving some evidence that this extra transmission

feature results from the intrinsic dispersion of the effective parameters rather than structuring. The slight discrepancy (blue shift of the characteristic frequency of the second dip for the microstructure) stems from the invariance of the permeability dispersion characteristic for a homogenous layer contrary to a composite device [11].

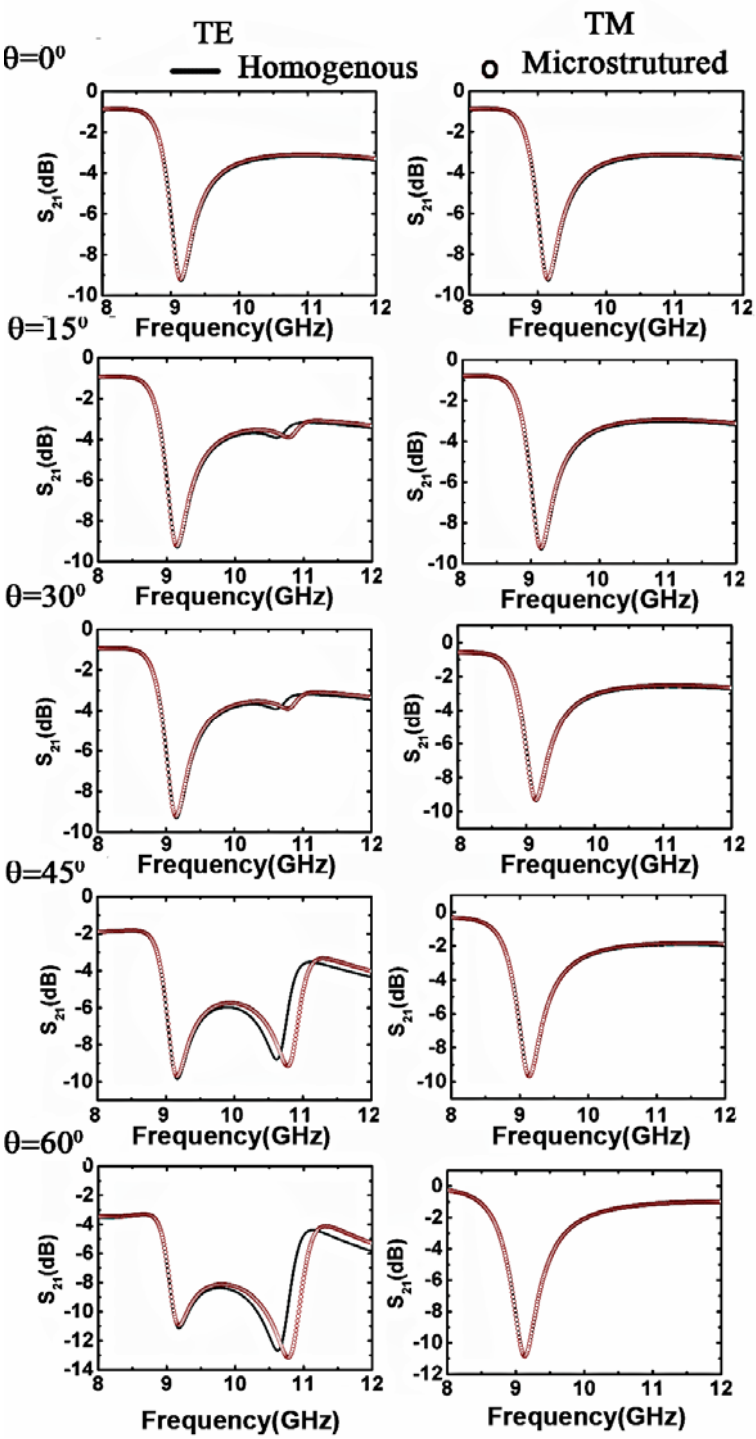

Fig. 5.17 Transmission spectra comparison for microstructured and homogenous single layer of dielectric negative permeability metamaterial under various incidence angles θ ($\phi = 45°$) and modes

(TE and TM).

A similar dip in the transmittance was already predicted theoretically in the literature by numerically studying the frequency response of negative magnetic artificial media. It was thus shown that this phenomenon is due to a zero in the permeability dispersion $\mu(\omega)$ around magnetic plasma frequency [11]. For a homogenous slab with permittivity ε and permeability μ, the dispersion relation is

$$k_{\perp}^{2} + k_{//}^{2} = k_{0}^{2}\varepsilon\mu \tag{5.3}$$

where k_0 is the wave vector in vacuum, $k\perp$ and $k_{//}$ are the wave vector components perpendicular and parallel to the surface of the slab, respectively. The analytical transmission amplitude T can be expressed:

$$T^{-1} = \cos k_{\perp} d - (i/2)(\zeta + 1/\zeta)\sin k_{\perp} d \tag{5.4}$$

where d is slab thickness, and $\zeta = \mu k / k_{\perp}$ for TE mode and $\zeta = \varepsilon k / k_{\perp}$ for TM mode. Given the $\mu(\omega)$ for TE mode or $\varepsilon(\omega)$ for TM equals zero, the prefactor of the second term in Eq. 5.4 diverges, which leads to a vanishing transmission except for the case of normal incidence where this divergence can be compensated by the vanishing $k_{\perp}^{2} = k_{0}^{2}\varepsilon\mu$. The observed second dip in the TE transmission spectra is exactly the magnetic plasma frequency, ω_{mp}, where the dielectric resonator exhibits zero permeability (Fig. 5.15).

Before considering the experimental verification of the dispersion effects pointed out above, it seems interesting to study the lattice conditions of insensitivity to incidence and polarization. Toward this goal, Fig. 5.18 compares the transmission spectra along three principal axes of the cube, namely [100] (θ = 0, ϕ = 0), [101] (θ = 0, ϕ = 45°) and [111] (θ = 45° ϕ = 45°) for two values of lattice constants, 1.25 mm and 2.00 mm, respectively. By comparing the transmission spectra it can be noticed that the two dips are much closer for the TE polarization when the lattice is increased 2.00 mm, thus starting the formation of a gap at increasing incidence angle. Importantly, for each lattice, the magnetic resonance frequency of dielectric resonator is independent of the incidence angle and polarization.

According to the aforementioned interpretation, the frequency corresponding to

the second zero-transmission is related to the magnetic plasma frequency, $\omega_{mp,}$ that depends on the filling factor and on the resonance frequency ω_m by the relation [15].

$$\omega_{mp} = \frac{1}{\sqrt{1-F}}\omega_m \tag{5.5}$$

where $F = \frac{S}{a^2}$ is the area filling factor of the magnetic resonator. On this basis, it is expected that the second dip in the transmission spectra of TE mode changes with the periodicity. By decreasing the filling factor via a change of the periodicity (2.00 mm rather than 1.25 mm), the second dip is dramatically decreases to 9.86 GHz for TE mode so that a bandgap appears. This further confirms our assumption that the second dip is arising from the vanishing permeability at magnetic plasma frequency and shows the importance of the lattice constant.

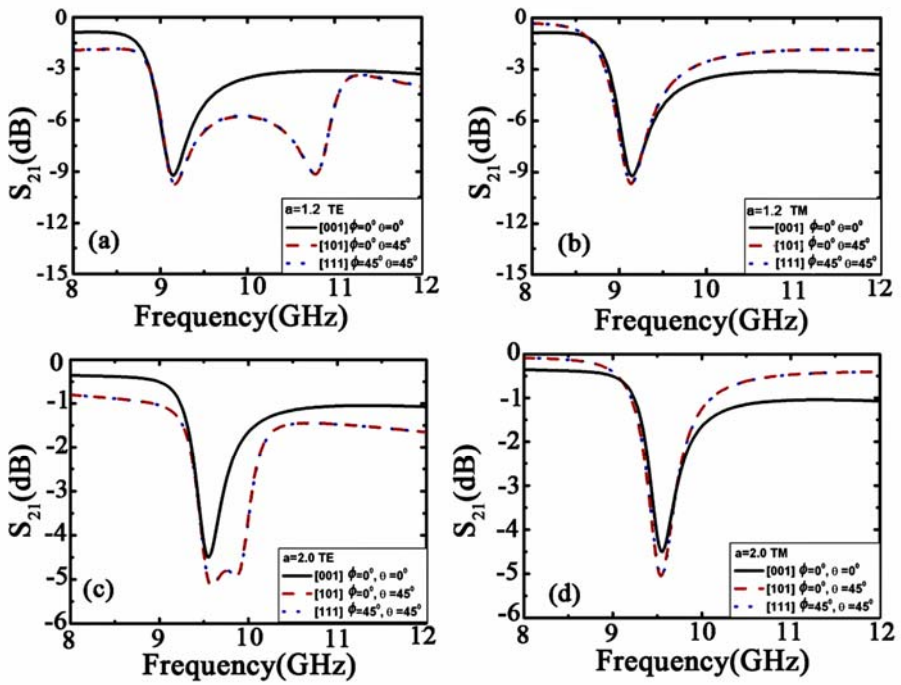

Fig. 5.18 Transmission spectra for a layer of dielectric negative permeability metamaterial along three principal directions [*x, y, z*] of a cube cell by considering TE and TM (b) modes with lattice *a* = 1.25 (a, b) and a = 2.0 mm (c, d), respectively.

5.2. Experiments of oblique incidence response of BST cube

As the simulations results shown above, the frequency positions of the first and

second dips for TE mode will be much closer when the elementary cell periodicity becomes larger. This may somewhat bring difficulties in distinguishing experimentally the two dips. Thus, we chose a periodicity of 1.25 mm for the experimental prototype (See Fig. 5.19). The ideal measurement is to be carried out in free space, but this requires the total sample as large as the order of the wavelength and consequently more than several thousand dielectric cubes required, which can not be affordable actually. In the experiment, we performed the measurement in a parallel plate setup, which has been extensively used in the characterizations of metamaterial [2, 29]. We used two pieces of copper clad PCB board to form up and bottom plates of parallel plate step, as shown in Figs. 5.20 and 5.21. A single layer of dielectric metamaterial, composed of BST cubes embedded into Teflon template, is clad by two absorbers on the sides in order to eliminate the unwanted scattering influences. The incident beam is excited by a microwave adapter and guided by the absorber layers (Fig. 5.20).

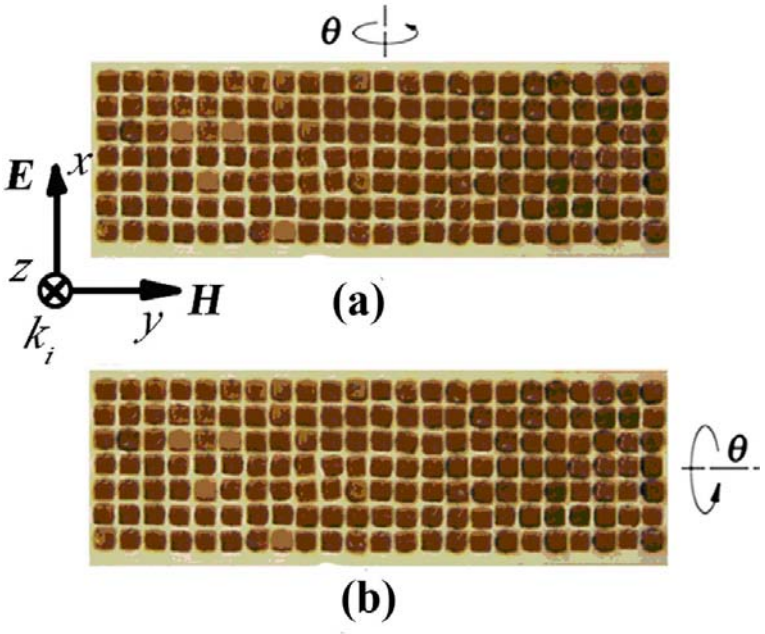

Fig. 5.19 The front view of dielectric metamaterial sample consisting of BST resonator in a dense arrangement. The single layer is rotated around the *x* and *y* axes to measure the transmittance for TE (a) and TM (b) modes with various incidence angles, respectively.

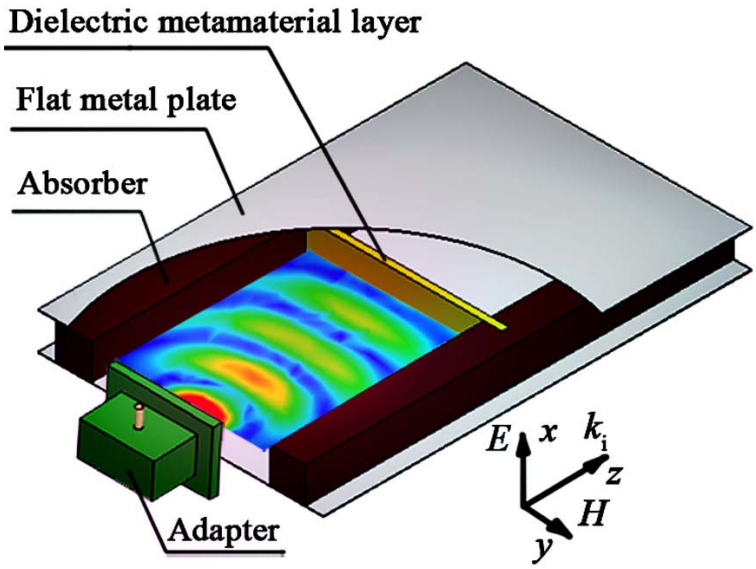

Fig. 5.20 Schematic parallel plate system used for oblique incidence measurement of thin layer of BST cubes.

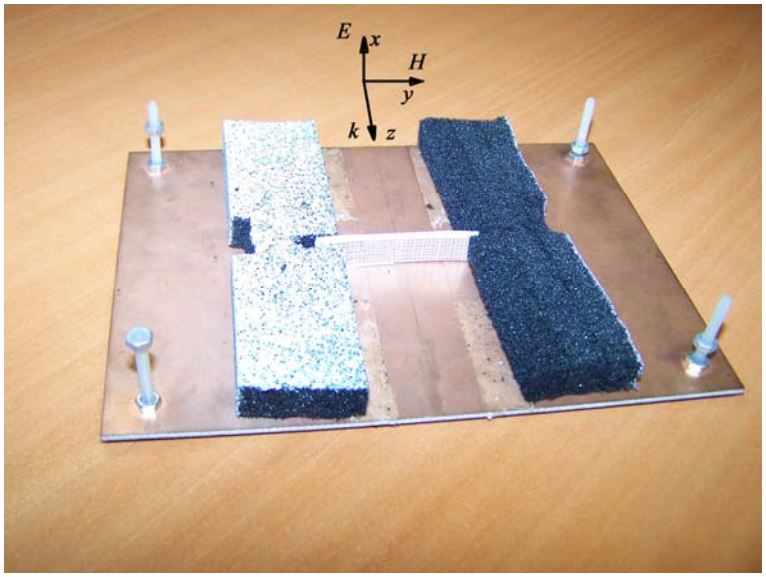

Fig. 5.21 Parallel plate step used for oblique incidence measurement of thin layer of BST cubes.

From the simulation results stated above, the scattering amplitude of the cubic dielectric resonator is independent on the angle Φ between the incidence plane and cube edge, making the experimental measurement more simplified, and hence only the case of Φ = 0º is considered. To perform the oblique incidence, we rotated the metamaterial layer along the *x* (the direction of **E** field) and *y* axes (the direction of **H** field) for the transmission spectra of TE and TM modes, respectively, as shown in Fig. 5.19. The measured data were recorded by using a HP8720 ES Vectorial

Network Analyzer.

Figure 5.22 shows the experimental and calculated transmission spectra for the single layer of dielectric metamaterial. For the normal incidence the dielectric metamaterial shows a transmission dip at 8.6 GHz, having a modest discrepancy with the simulated result. This can be understandable that the actual periodicity of dense arrangement of BST cubes is slightly smaller than the value used for simulation, resulting in a lower magnetic resonance frequency. For instances, the resonance frequency is shifted below 9.0 GHz when the periodicity decreases to 1.1 mm from the simulation results which are not shown here. In addition, an unexpected minor dip occurs at 10.7 GHz, which is not found in the simulation for normal incidence. In fact, the propagation channel formed by absorber layers has much large width than that of the microwave adapter used to offer signals, consequently a normal incidence of plane wave is only preserved in the middle region of the channel whereas tilted incidences occurrence can not be avoided in the side area. Therefore, a week dip appears at the frequency point with zero permeability. When the metamaterial layer is rotated along the *x* axis, the electric field of the incidence beam is always parallel to the layer surface, equaling to the oblique incidence of TE mode. As seen in Fig. 5.22(b), the second dip becomes visible and its strength increases with the tilted angle θ, becoming comparable to that of the first dip when θ = 45º. In contrast, the minor dip shape is unchanged for the measurement of TM mode, confirming this is a setup system error. Nevertheless, the first dip does not change with the varying incidence angle, θ, for either TE or TM mode. From the good agreement between the simulation and experiment, we can conclude that the dielectric metamaterial based on BST cube indeed shows isotropic property behavior, even though it is not formed by the sphere, ideal symmetry, particles.

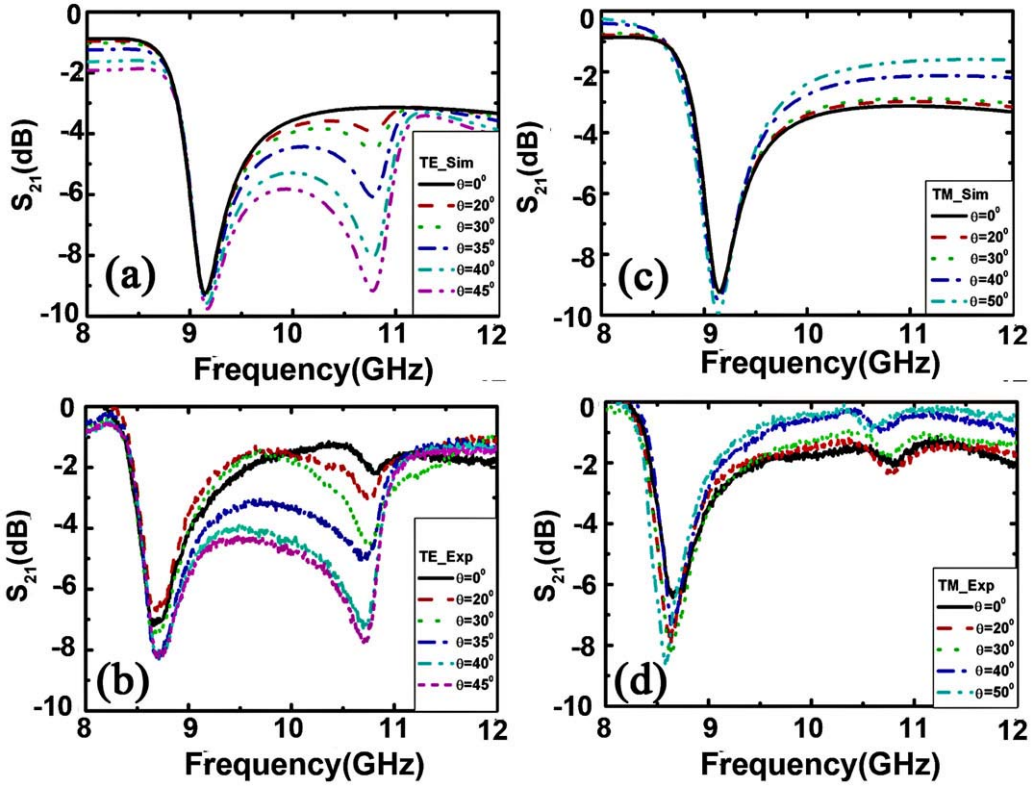

Fig. 5.22 The simulated ((a), (c)) and experimental ((b), (d)) oblique transmission spectra for the single layer of dielectric metamaterial with TE and TM modes.

To our knowledge, the effect of polarization on magnetic single negative media was predicted theoretically for a SRR technology but not experimentally assessed. Compared to the SRR approach whose fabrication for an isotropic metamaterial is very challenging, the full dielectric approach has the advantage of a simpler geometry and no requiring a patterning stage. It is also worth-mentioning that the achievement of a magnetic Mie resonance does not require an additional structuring stage such as a split which is commonly used starting from a closed ring in a metal dielectric technology. The latter thus requires balancing the anisotropy induced by the slot by patterning for instance omega–type metal inclusion in a back-to-back configuration [5].

5.3 Application of dielectric artificial magnetic resonator (AMC)

As aforementioned above, dielectric resonator based on BST cube has been demonstrated as a promising substitute for conventional magnetic metamaterial

particles especially SRR. During the transition from basic research to the application of magnetic metamaterial, various attempts have been performed such as AMC based antenna reflector [31-35], bandpass filter [37, 38], invisible cloaks [39, 40] and so on. In this section, we are concentrated on the possibility of application of dielectric AMC on antenna, as well as full dielectric cloak.

5.3.1 Dielectric AMC application on dipole antenna

Over past few years, artificial magnetic conductors (AMC) has attracted much attention, since it can exhibit an in-phase reflection property via high impedance around the resonance frequency [31]. In comparison with the common reflector offered by perfect electric conductor (PEC), AMC can reflect the incident beam without phase loss, which overcomes the limitation of necessary required distance between the reflector and radiation elements, hence, enabling the possibility of the compact communication structure and devices. The proof-in-principle prototype was proposed and assessed by taking benefit of the mushroom with via hole connected to the ground plane [31-33]. T. Itoh *et al.* proposed a uniplanar compact photonic bandgap (UC-PBC) structure, which is composed of periodically distributed conducting elements on a grounded dielectric substrate [34, 35]. Recently, a new emerging material, namely, metamaterial, which possesses the unique characteristics can not be found in naturally occurring materials, has promoted further the development of AMC [36]. Using split ring resonator (SRR), A. Erentok *et al.* realized a compact AMC with high impedance, which is arising from the extremely large permeability along with a zero permittivity at the resonance frequency [42, 43]. S.-S. Oh *et al.* found SRR can still work as an AMC only through the electric field excitation [44]. In this case, a zero permittivity could be obtained via a Lorentz-like electric resonance of SRR. Nevertheless, the anisotropic property of SRR and specified requirement of the incident beam polarization have limited the potential application of SRR on antenna.

In previous investigation on magnetic Mie resonance of BST cube, we have shown some results of dielectric AMC. Here we present a systematical analysis on full dielectric metamaterial, which exhibits the similar property of SRR-type AMC. The interaction between dielectric AMC and antenna is also investigated by using a dipole and a thin layer of dielectric resonators. Numerically results reveal that a front-to-back ratio as high as 35 dB and more than two-fold enhancement of the refracted electric field are obtained.

5.3.1.1 Dielectric AMC elementary cell

The basic unit cell of dielectric AMC, composed of BST cube surrounded by a thin Teflon layer, is shown in Fig. 5.23(a). In view of application at microwave frequency notably X band, we set the working frequency of interest around 10.0 GHz. To this aim, side length of BST cube is set to 0.8mm after full-wave simulation. The periodicity is further decreased to 1.5 mm so as to strengthen resonance in the following numerical investigation. The dielectric property of BST is set to ε = 850, tan δ = 0.001. It is noted that low dielectric loss tangent plays an important role on the realization of in-phase reflection, as demonstrated before.

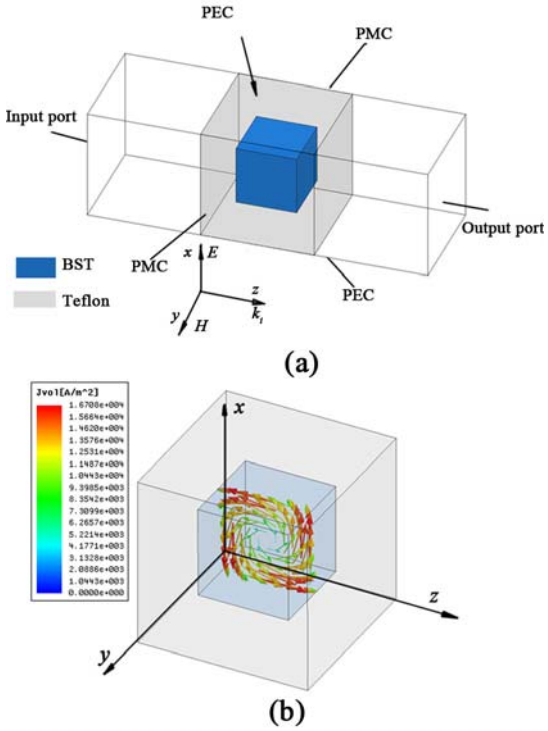

Fig. 5.23 (a) The schematic diagram of the basic unit cell of BST-based AMC. The geometry parameters are as follows: l = 0.8 a =1.5 (unit: mm). (b) The displacement currents excited by the incident magnetic field are shown in the x-z plane.

As shown in Fig. 5.24, the basic unit cell exhibits a well-defined dip with a magnitude of - 29.0 dB around 10.6 GHz in the transmission window, which is accompanied by a strong reflection. Furthermore, the reflection phase of S_{11} shows an abrupt change around this narrow regime, which jumps to 15.2° at 10.33 GHz from negative values at lower frequencies and then turns to the decreasing variation as a function of frequencies. It is noted that the phase of S_{11} goes through zero at 10.45 GHz, showing the in-phase reflection characteristic, indicating this dielectric

material can function as an AMC. By using the ± 90° phase definition of bandwidth [31], an effective working frequency range of 400 MHz is observed (grey region), in which the reflected beam would not have destructive interferences with the incident wave.

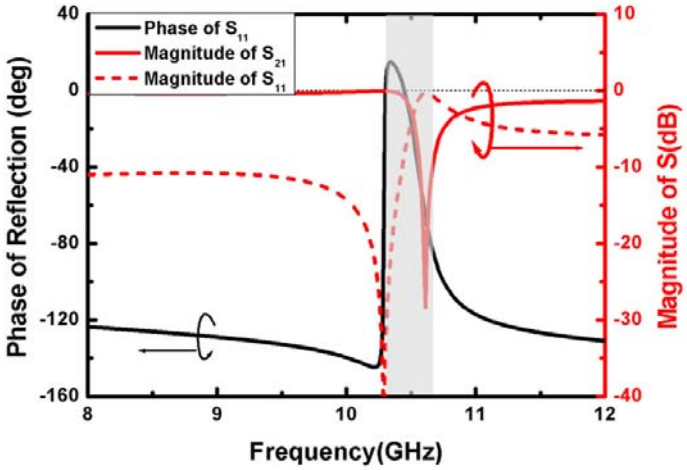

Fig. 5.24 (Left axis) The phase of reflection S_{11} (dotted red line). The magnitude of the S_{21} (solid red line) and S_{11} (dashed red line). The bandwidth of dielectric AMC is colored in grey.

The displacement currents was also monitored at 10.60 GHz and plotted in Fig. 5.23(b). Similar to the results of Fig. 5.1, a circular displacement current was also excited inside BST cube around the *y* axis, which produced a magnetic component opposed to the incident magnetic field and thereby resulting an negative value of permeability.

After obtaining the full matrix of the S parameters, the effective parameters can be calculated by using a well-established retrieval algorithm [23-25]. In Fig. 5.25, the real part of the effective permeability shows a Lorentz resonance response around 10.6 GHz. This magnetic resonance of BST cube results in a large positive value of permeability just above the resonance frequency, thereby leading to a large value of impedance Z. This high impedance characteristic leads to the in-phase reflection directly. In Ref. [42], the extremely high impedance of SRR is obtained not only by the magnetic resonance but also the co-occurrence of the electric resonance with zero permittivity at the same frequency, which is due to the magneto-electric effect on condition that SRR has the configuration with the gap perpendicular to the electric field [45, 46]. This has somewhat differences in comparison with our work, which only makes use of magnetic resonance, i.e., the large permeability, to produce high impedance. Thus, this approach may fail

especially when the effective permeability is not large enough. Here, this is directly related to the loss tangent of the cube, as pointed out in previous section of loss tangent influence. However, as the dielectric unit considered here exhibits highly-isotropic property due to the geometrical symmetry, it is a great advantage for the uniform response to the radiation elements especially for the application on antenna, which is discussed in the following section.

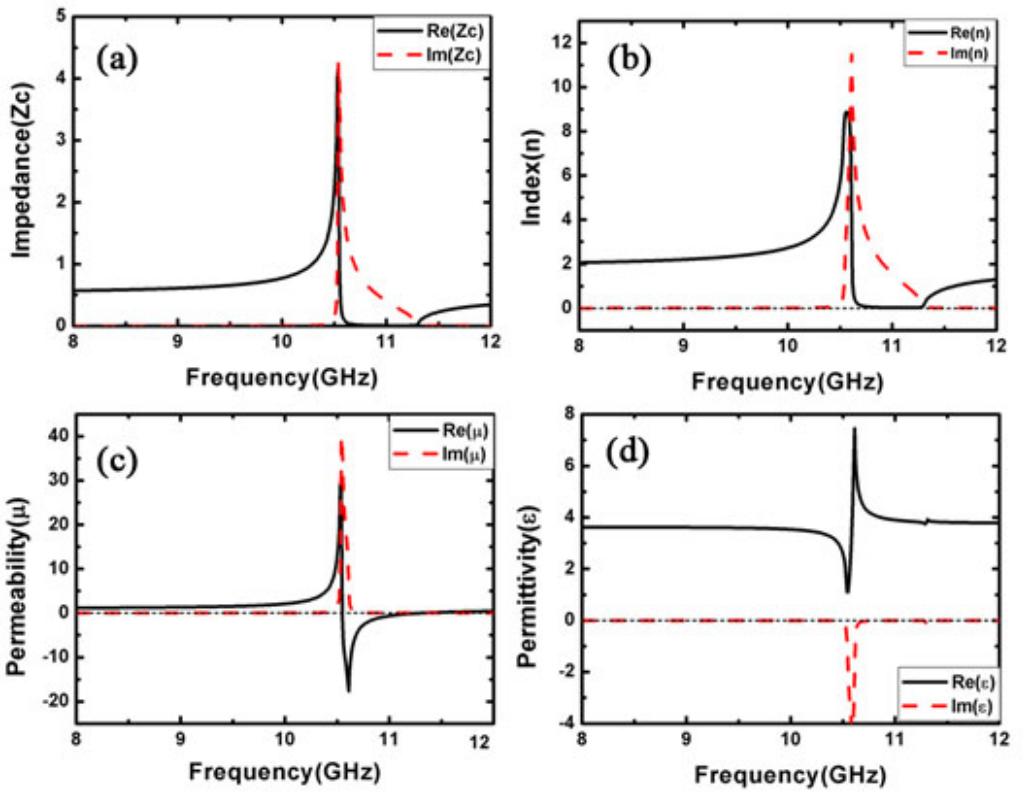

Fig. 5.25 The effective parameters of the BST-based AMC. (a) Impedance, (b) index, (c) permeability, and (d) permittivity. The real and imaginary parts are presented by solid black and dashed red lines, respectively.

5.3.1.2 Application of dielectric based metamaterial on ideal dipole antenna

In this section, the interaction between the antenna and dielectric AMC is studied. For simplicity, an ideal electrically small dipole antenna was employed, which is positioned symmetrically at the origin of the coordinate system and oriented along the *x* axis (Fig. 5.26).

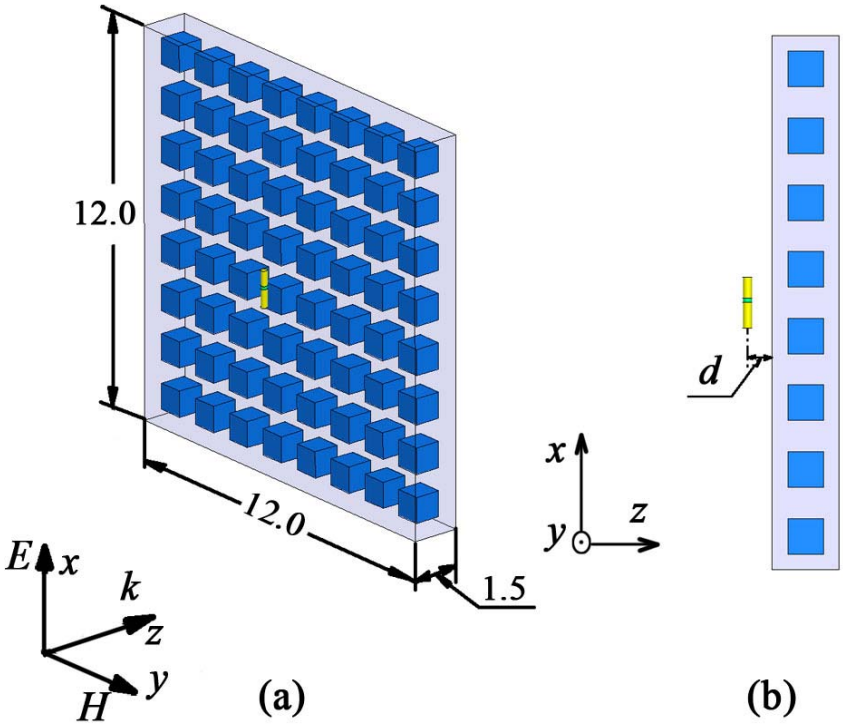

Fig. 5.26 (a) Close-up and (b) side views of the model for AMC based on dielectric metamaterial working as reflector for electrically small antenna.

The dipole antenna is composed of two identical cylinders of perfect electric conductors with the radius of 0.1 mm separated by a short cylinder of vacuum, which is assumed as the current source with a constant current of 1A along the axis of cylinder. The total length of the dipole is 1.1428 mm, corresponding approximately 0.04 λ_0 (λ_0 is the wavelength of 10.5 GHz). For the AMC layer, 64 units are stacked in an 8×8 array in the *x*-*y* plane, forming a thin slab with the dimensions: 12.0 mm×12.0 mm×1.5 mm. This metamaterial slab is placed symmetrically about the *x*-*z* and *y*-*z* planes. The distance between the center of dipole and the surface of Teflon substrate is 0.5714 mm, which is determined through the optimization for parameter sweep with respect to the front-to-back ratio of the far field radiation pattern of the antenna. A cubic free space radiation box with side length of 40.0 mm, which ensures the enough distance away the slab, was created and centered at the origin. For the sake of modeling purpose, PMC and PEC symmetry boundaries were introduced along the *x*-*z* and *y*-*z* planes, respectively. The mesh of air box was optimized with a maximum length of initial mesh of 3 mm, approximately one tenth of the operating wavelength, in order to make sure an accurate calculation of the field distribution.

The electric field values in far field range were calculated for the dipole

antenna alone and with dielectric metamaterial layer, respectively. Fig. 5.27 presents the frequency dependent front-to-back of the dipole antenna with the dielectric metamaterial. A significantly enhancement of the front-to-back ratio with a peak value of 34.48 dB occurs at 10.612 GHz, which is in consistent with the in-phase frequency band (Fig. 5.27).

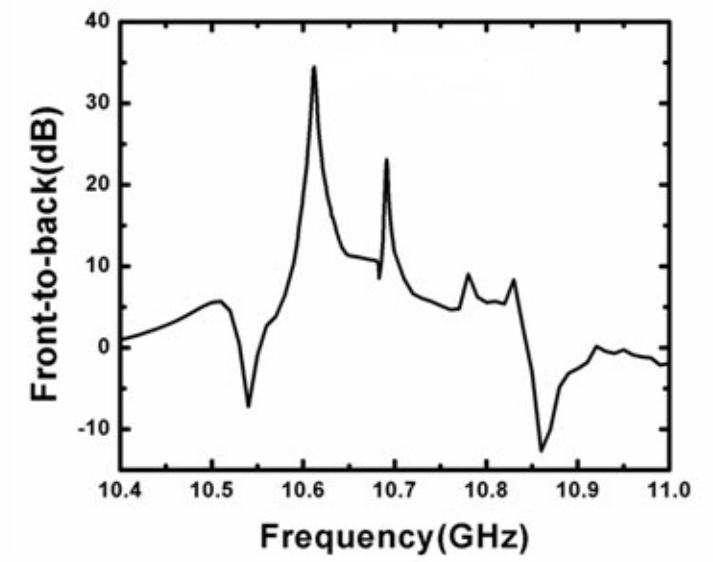

Fig. 5.27 The frequency dependent front-to-back ratio of far field pattern of the dipole working with dielectric metamaterial layer.

Figure 5.28 shows the comparisons of E- and H-plane far field patterns of the electric field for the dipole antenna alone and with the dielectric AMC layer present, respectively. The electric field values are normalized with their respective E_{max}. With the presence of the dielectric AMC layer, radiation patterns have a deep null in the back direction, which leading to the large front-to-back ratio. Besides, the reflected field of dipole positioned in front of the AMC layer is increased by a factor 2.11 times, slightly more than 2-fold enhancement, as compared to that of the dipole in the free space, indicating that the dielectric metamaterial performs as an efficient reflector.

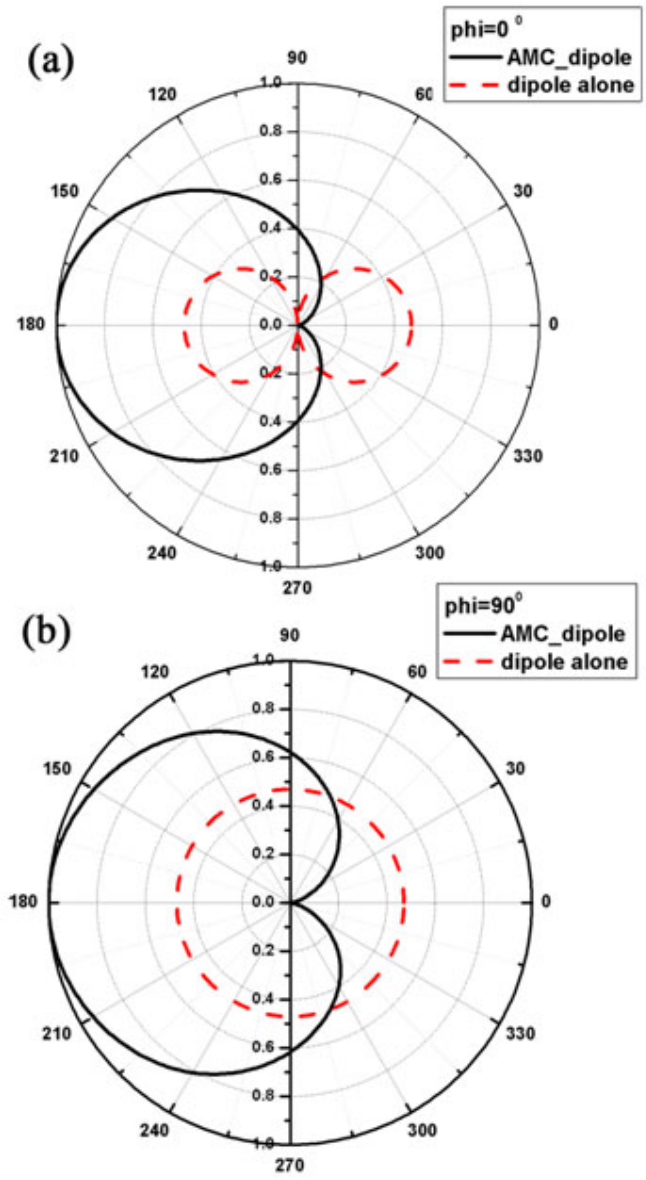

Fig. 5.28 The far field pattern of the dipole antenna alone in the free space and with AMC based on dielectric metamaterial layer at 10.612 GHz: (a) Normalized E plane; (b) Normalized H plane.

Figure 5.29 presents the electric field for the dipole antenna with dielectric AMC layer at 10.612 GHz at near-field in the *x*-*z* and *y*-*z* planes, respectively. A strong reflected field around the AMC interface can be clearly observed, resulting in a rather week energy propagates through AMC layer although there is only one layer of BST cubes. Few fields pass around is due to the limited side length of AMC layer, which is expected to be improved with a larger and thicker model. Nevertheless, this dielectric metamaterial AMC is demonstrated to provide a highly efficient isolation

between its front and back sides, which is very promising for some communication applications especially for the health consideration of mobile phone holder requiring low-profile and low backlobe radiation.

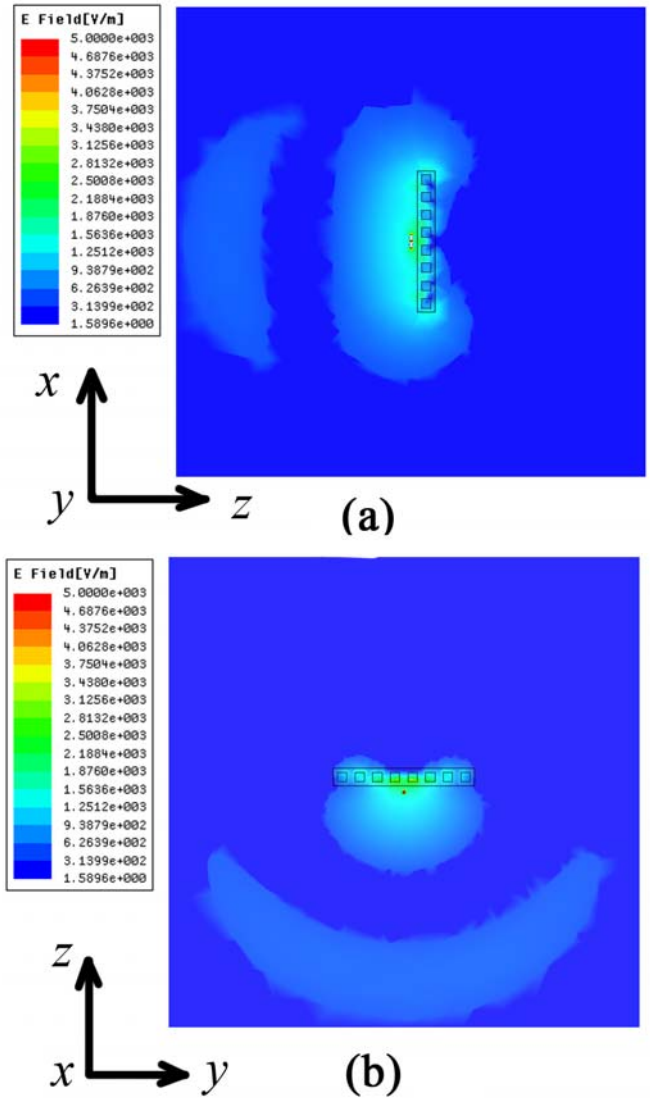

Fig. 5.29 The electric field distribution in the near field for the dipole antenna working with dielectric metamaterial: (a) the *x*-*z* plane; (b) the *y*-*z* plane.

5.3.1.3 Application of dielectric AMC on printed dipole antenna

Hereafter, we present how dielectric AMC interact with a true antenna. BST property is set to ε = 194, tan δ = 0.005, according to latest dielectric property of new BST sample fabricated at Tsinghua University. This permittivity around 200 allows bigger sample to working at the same frequency as that realized by cube with permittivity of 850. As the permittivity lower, the resonance frequency is less sensitive to the size

variation, thus, this could alleviate high dicing requirement for required cube, especially for the realization of full dielectric cloak, which needs a minor size variation along the radius at microwave.

The side length of and periodicity of BST cube are 1.75 and 3.0 mm, respectively. The corresponding magnetic Mie resonance occurs at 10.0 GHz, resulting in narrow dip accompanied by strong reflection as shown in Fig. 5.30. Effective impedance and index are given in Fig. 5.31. Due to strong Mie resonance, both impedance and index shows extreme value around 10.0 GHz.

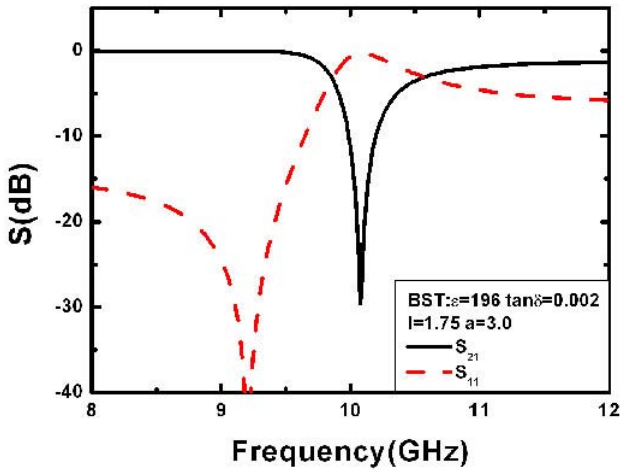

Fig. 5.30 Scattering parameters of BST cube array. The permittivity of BST: ε=196, tan δ = 0.005, The side length and cubic periodicity are 1.75 and 3.0 mm, respectively.

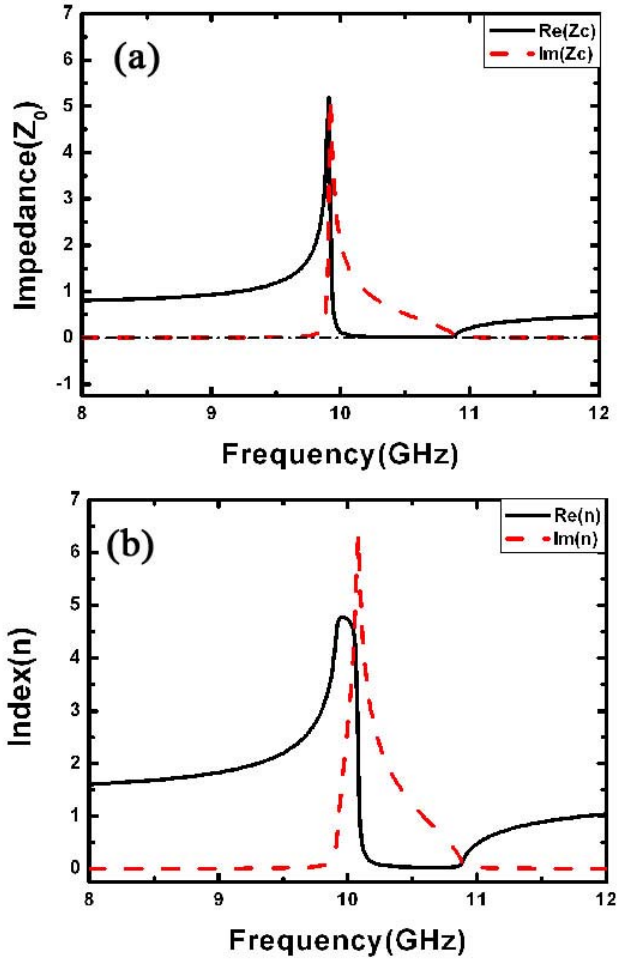

Fig. 5.31 Effective impedance (a) and index of BST cube array.

As shown in Fig. 5.32, a printed dipole antenna, which is embedded inside between two layers of Rogers RT/Duroid 5880 (ε_r =2.2, tan δ = 0.0004), is selected due to its dipole antenna performance and planar configuration. The geometrical dimensions are given in detail in the caption of Fig. 5.32. A waveguide port is used to excite incident signal.

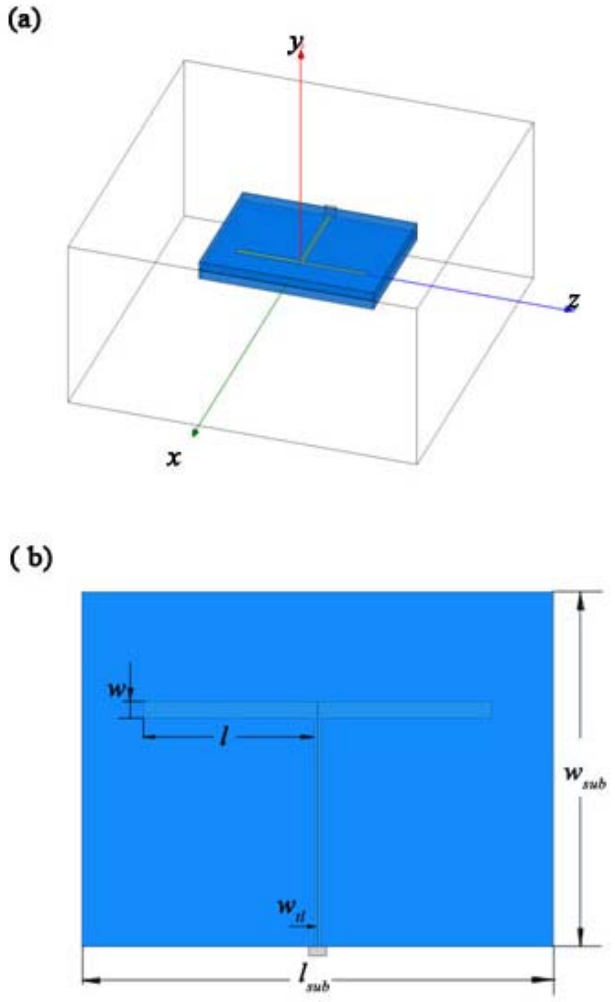

Fig. 5.32 Printed dipole antenna: (a) 3d and (b) top view of antenna model in HFSS. Dipole antenna geometry dimensions are as follows: L_{sub} = 10.5 w_{sub} = 11.25 w_{tl} = 0.1, l = 5.1 w = 0.508 the gap between transmission lines is g = 0.0015 (unit: mm). Roger 5080(ε_r =2.2 tan δ=0.0004) is chosen for the substrate and the thickness of each substrate is t_{sub} =0.508. The dipole and transmission line are made of copper whose thickness is 0.030 mm.

The return loss of printed dipole alone is given in Fig. 5.33. The return loss exhibits a dip at 10.0 GHz, indicating the position of central working frequency of printed dipole antenna. The directivity is also given for the printed dipole antenna at 10.0 GHz (See Fig. 5.34). An maximum of the directivity is seen as 2.26 dBi (1.68), which is very close to the reference's value 2.15 dBi, whereas the gain is 1.92 dBi (1.56) (not shown here), accounting for a total radiation efficiency of 92.8 %.

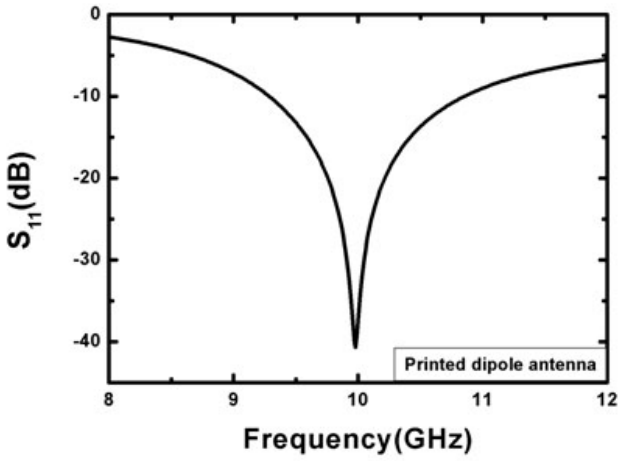

Fig. 5.33 Return loss of printed dipole antenna.

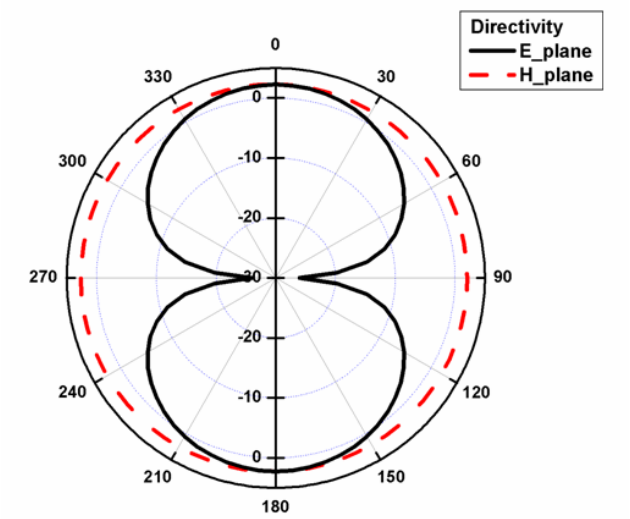

Fig. 5.34 Directivity pattern of printed dipole antenna

The schematic view of HFSS model of printed dipole antenna integrated with BST based dielectric AMC array is plotted in Fig. 5.35. We stacked 2×9×8 cells along the *x*, *y* and *z* directions, respectively, in order to form an AMC block. This means only two BST cubes used along the *x* direction, similar to that employed for ideal dipole antenna. In the *y*-*z* plane, middle row of BST cube array, 5th row, was removed to fit antenna substrate. The distance between dielectric AMC block to dipole antenna is represented by lowercase *h*. In this initial calculation, *h* is set as 0.5 mm, indicating AMC is very close to radiative element. For the sake of model simplicity, two symmetry boundaries, perfect E for *x*-*y* plane and perfect H for *x*-*z* plane, were set to enhance calculation efficiency. Therefore, HFSS model depicted in

Fig. 5.35 is only one quarter of actual configuration of antenna and dielectric AMC. To obtain a high simulation accuracy of radiated field especially for the far field calculation, the simulation domain, air box side length, along the *y* and *z* axes were both extended to 60 mm to make sure enough distance between dielectric AMC block surface and radiation boundary, which requires at least one quarter of wavelength of specified frequency.

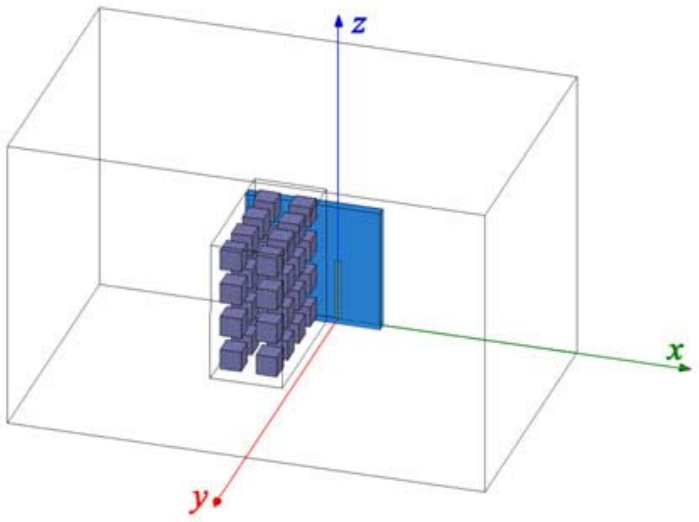

Fig. 5.35 HFSS model for printed dipole antenna integrated with BST based dielectric AMC array.

The return loss of dipole antenna along with dielectric AMC is given in Fig. 5.36. With presence of dielectric AMC, dipole antenna return loss has a big difference in comparison with that of dipole antenna alone. From the comparison, we see that, after introducing the dielectric AMC block, return loss of the dipole antenna fluctuates around -12 dB below 10 GHz, followed by an increase to -5.6 dB at 10.04 GHz, which is the original central working frequency of dipole antenna alone. Instead, it exhibits a narrow reflection coefficient dip at 10.14 GHz.

The antenna resonance frequency of dipole antenna is mainly determined by the permittivity and permeability properties of the surrounding materials, as well as the geometry dimensions of the radiation elements. The relation can be expressed simplified as

$$f \propto \frac{1}{\sqrt{\varepsilon_r \mu_r}} = \frac{1}{n_r} \tag{5.6}$$

where ε_r, μ_r, and n_r are the respective average permittivity, permeability and index of the surrounding materials including the substrate and the air. Clearly, the antenna resonance changes with some variations of n_r. When dielectric AMC block was introduced into the antenna system, local effective index around the AMC block varied. As shown in the effective parameters diagram, the effective index increases abruptly to 4.73 at 9.92 GHz (Fig. 5.31), leading to a large increase of the average index of the surrounding materials for dipole antenna, thereby, shifting center operating frequency of the antenna to lower frequencies and leaving a poor return loss value at original frequency regime. Please note that it is exactly the frequency in which AMC possesses the maximum impedance, great enhancement of directivity but lower radiation efficiency can be expected, which will be described in detail later. On the other hand, the return loss with a minimum value of -33 dB occurs at 10.14 GHz, which is due to the fact that the effective index of AMC passes unity during the sharp decrease from maximum to zero above 10.0 GHz, as shown in Fig. 5.31.

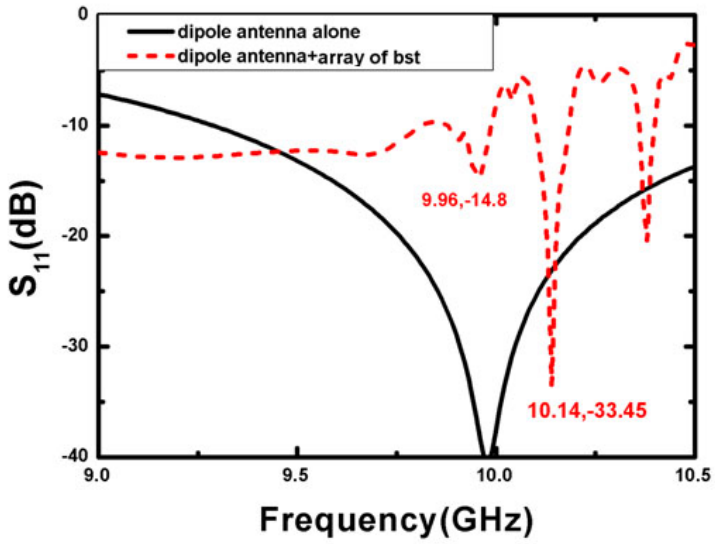

Fig. 5.36 The comparison of return loss for dipole antenna alone and dipole antenna interacted with dielectric AMC.

We chose observed resonance frequency point of 9.97 GHz which is in the regime of high impedance of AMC (Fig. 5.31) and modest return loss. The corresponding far field radiation pattern is given in Fig. 5.37. For the presence of AMC block, the radiation along the back side (- *y* direction) is decreased significantly, thus a high directivity of 5.37 (7.38 dBi), more than three times (3.25) the value of the dipole antenna alone, was obtained. The relative gain 3.71(5.7 dBi) is observed, revealing a radiation efficiency of 69.1%. The presence of AMC

enhanced the gain more than two times the value of the dipole antenna alone, demonstrating that this approach is feasible to enhance antenna radiation efficiency greatly even though the impedance match of the antenna is not so favorable.

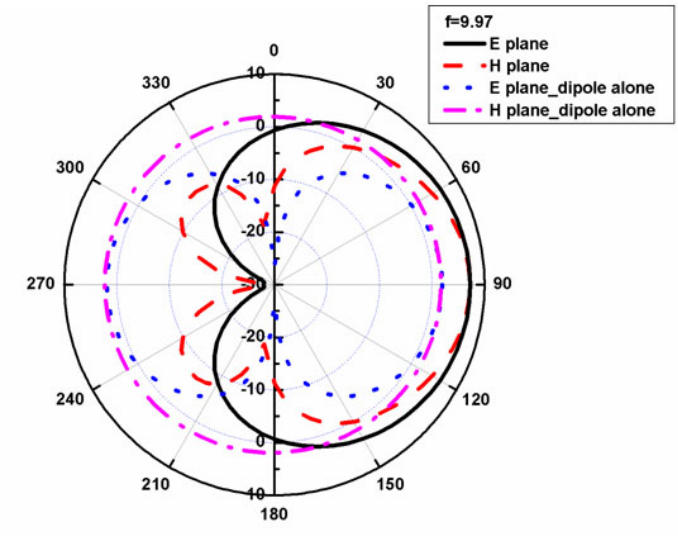

Fig. 5.37 The far field pattern comparison between dipole antenna alone and dipole antenna along with dielectric AMC at 9.97 GHz.

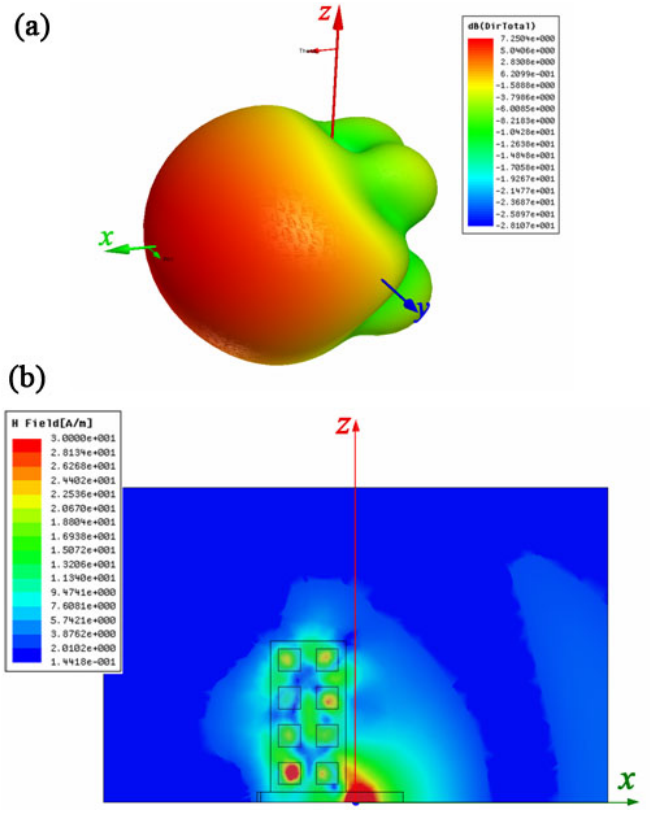

Fig. 5.38 (a) 3d view and (b) *x*-*z* plane of far field radiation pattern at 9.97 GHz.

It is also noted that a high front-to-back ratio, more than 35 dB, resulted from in-phase reflection from dielectric AMC, can be observed from the radiation pattern. This is also demonstrated by the magnetic filed in the *x-z* plane (Fig. 3.38). Similar to the case of AMC application on ideal dipole antenna, most of radiated energy is propagated forwards whereas minor energy can be penetrated through dielectric BST layer, leading high front-to-back ratio, as well as high directivity and gain.

The radiation pattern at 10.14 for both dipole antenna alone and with the presence of dielectric AMC is given in Fig. 5.39. From the return loss diagram shown before, we see an optimal value of return loss less than -30 dB occurs at 10.14 GHz, meaning there is out of problem for the impedance match. However, the radiation pattern for the dipole antenna with AMC block is almost omnidirectional The front-to-back ratio is only 7 dB, indicating that AMC losses its in-phase reflection at this frequency point, which is consistent with impedance dispersion of BST as shown in Fig. 5.31.

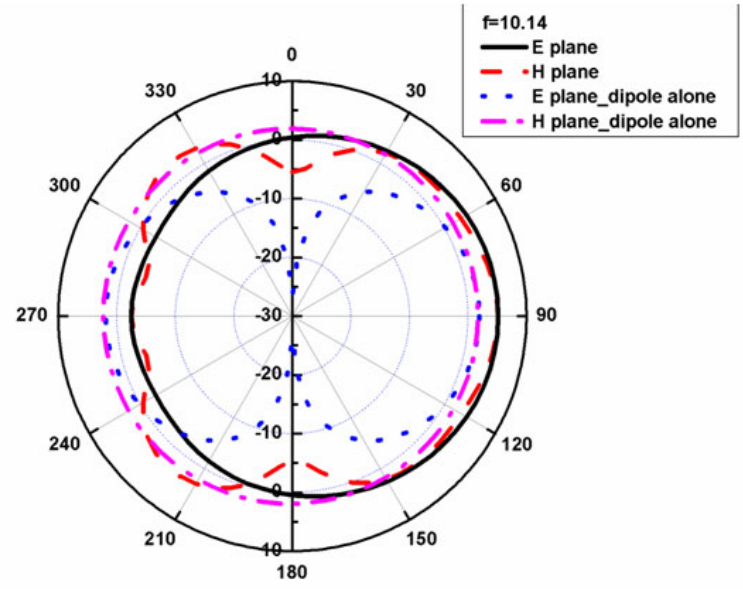

Fig. 5.39 Far field pattern for dipole and dipole along with AMC at 10.14 GHz.

5.3.2 Full dielectric cloak.

Conformal transformation of electromagnetic domains has been proposed as an exciting approach to control the flow of propagating waves [39]. It enables the design of objects displaying unprecedented functionalities [47] with the requirement of space gradients and anisotropy of the constitutive parameters (permittivity and permeability). The magnetic cloak of invisibility demonstrated at microwave

frequencies was the first experimental breakthrough under these guidelines [40]. Since then, many other groups have lighted a great of enthusiasm [48-51]. In our group, D. P. Gaillot *et al.* have successfully demonstrated a full dielectric cloak at 0.5 THz by using finite long BST rod with gradient variation of permeability [52, 53].

In view of actual realization notably fabrication process, a rectangular building block is much easier to be fabricated compared to cylinder rod. On the other hand, higher frequency such as THz causes another challenge for experimental measurement as well as the sample dicing. Therefore, in this section, we present a full dielectric cloak based on BST rectangular block at microwave frequency.

For an annular cloak defined by its inner radius *a* and outer radius *b*, as shown in Fig. 5.40(a), the effective parameters of the cloak shell (permittivity and permeability) must be independently engineered to satisfy a set of equations derived from the conformal transformation theory [47]. However, it was shown that this design burden can be overcome by using a reduced set of equations [54]. This allows one parameter only (permittivity or permeability) to be varied with the cloak radius. Here we will follow the varied permeability along the radius approach. Under this configuration, a transverse-electric (TE) polarized plane wave (H_r, H_θ, E_z in cylindrical coordinates) has to be employed to illuminate the magnetic cloak and the original set of equations can be reduced to:

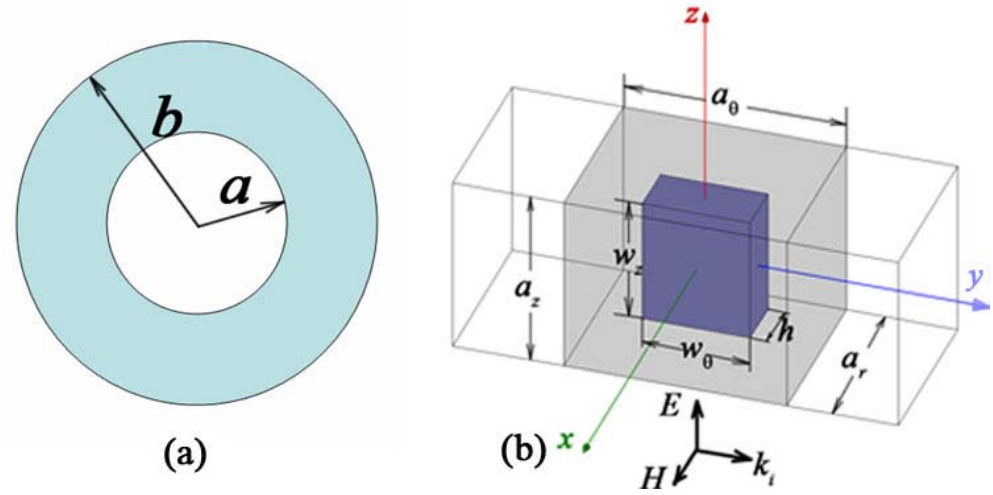

Fig. 5.40 (a) Schematic view of homogenous cloak. (b) HFSS Mode for elementary cell used for cloak. The fixed dimension of elementary are as follows: w_θ =2.0, h_{bst} = 1.0 , a_r = 3.32, a_θ=4.14, a_z = 3.4 mm. w_z is varied to tailor the magnetic permeability. BST has a relative dielectric ε = 194, tan δ= 0.005.

$$\mu_r(r) = \left(\frac{r-a}{r}\right)^2 \tag{5.7}$$

$$\mu_\theta(r) = 1 \tag{5.8}$$

$$\varepsilon_z(r) = \left(\frac{b}{b-a}\right)^2 \tag{5.9}$$

Similarly, we use BST rectangular building block, as depicted in Fig. 5.40(b), to replace cylinder rod employed in our group previous work [52, 53]. In a quasi arbitrary configuration where b = 2a = 60 mm, the radial component in the permeability is zero at the inner surface of the cloak where $r = a$. On the other hand, permittivity components ε_z is a constant as 4.

After setting whole size for cloak, there are still some issues to be noted for microstructured cloak design.

Radius of each ring $$r_i = a + \frac{2i-1}{2} a_r \tag{5.10}$$

Circumference of each rings $$C_i = 2\pi r_i \tag{5.11}$$

The total number of rings: $$n_rings = \frac{b-a}{a_r} \in N \tag{5.12}$$

Number of cubes in each rings $$n_{cubes} = \frac{C_i}{a_\theta} \in N \tag{5.13}$$

Cell number variation between adjacent rings $$\Delta n_{cubes} = \frac{2\pi}{a_\theta} a_r \in N \tag{5.14}$$

Based on the restriction of above formula, the periodicity a_r and a_θ should be carefully selected to make sure the other parameters fulfil requirement of Eqs 5.12-14. With this first assumption of the total sizes a and b, we set a preliminary number of rings as 9, then a_r and a_θ were calculated as 3.32 and 4.14 mm, respectively. The number of cells in the first ring is n_1 = 48. For two adjacent rings, the BST cell number Δn varies by 5. Totally, 612 unit cells are needed for the whole cloak device.

As shown in Fig. 5.40(b), BST rectangular brick is embedded into Teflon layer. In the calculation, we fixed most of geometry dimensions except for w_z, which was

varied to engineer magnetic permeability of elementary cell.

For the case of BST rectangular brick with following parameters: w_θ =2.0, w_z = 2.19, h_{bst} = 1.0 , a_r = 3.32, a_θ = 4.14, a_z = 3.4 mm, it exhibits a first order of magnetic Mie resonance frequency at 9.92 GHz under a grazing incidence with electric field polarized along z axis. At 10.554 GHz, permeability component μ_r = 0.00126, so close to the theoretical value that it was considered as elementary cell for the first inner layer of cloak. Then, w_z was varied with a step of 0.01 mm from 2.19 to 2.40 to change permeability component value μ_r. The corresponding complex permeability and permittivity components were retrieved by using Field summation method [55, 56] and compared to theoretical value calculated from Eqs. 5.7-5.9, so as to determine suitable size of BST elementary cell for cloak.

TABLE 5-1 Effective parameters of elementary cloak cell

Ring	w_z	μ_r	μ_θ	ε_z	μ_r	μ_θ	ε_z
					Theoretical value		
1	2.19	0.00126+0.04i	1.16	3.6263+0.002i	0.00275	1	4.0
2	2.20	0.017802+0.04i	1.16	3.637+0.002i	0.02027	1	4.0
3	2.22	0.051703+0.03i	1.16	3.680+0.002i	0.04696	1	4.0
4	2.24	0.08132+0.03i	1.16	3.697+0.002i	0.07795	1	4.0
5	2.26	0.10727+0.03i	1.16	3.772+0.002i	0.11052	1	4.0
6	2.29	0.14346+0.03i	1.16	3.833+0.001i	0.14316	1	4.0
7	2.32	0.17271+0.024i	1.16	3.900+0.003i	0.17504	1	4.0
8	2.36	0.20607+0.022i	1.16	4.0305+0.003i	0.20571	1	4.0
9	2.40	0.23502+0.020i	1.16	4.1345+0.003i	0.23495	1	4.0

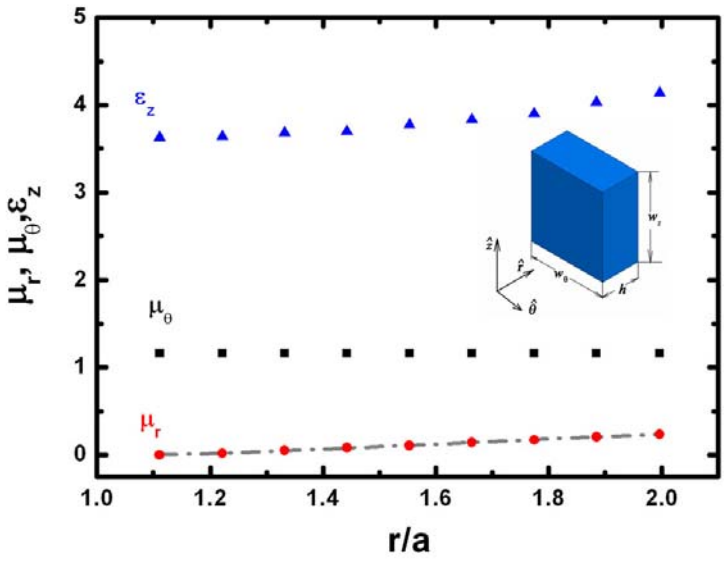

Fig. 5.41 Effective parameters of elementary cell for cloak at 10.554 GHz. μ_θ, μ_r, and ε_z are represented by square, circular and triangular symbols, respectively. The theoretical value for μ_r is also plotted by dashed dotted line.

The calculated complex permeability and permittivity for 10.554 GHz are given in Table 5-1 and Fig. 5.41. To satisfy the required value of permeability μ_r, the side length w_z of BST building brick is increased from 2.19 to 2.40 mm but without linear variation. The resulting permeability component μ_r has a remarkable agreement with that pointed by Eqs. 5.7. Instead of constant values, the permittivity ε_z and permeability component μ_θ of elementary cloak cell have slight differences from that of theoretical ones. However, in the following section, we will see these mismatches do not disturb the fundamental function of cloak.

In order to check whether the retrieval complex permeability and permittivity of BST cube with varied side length can be used for cloak, two approaches of full wave simulation are employed. In the first stage, COMSOL Multiphysics finite element-based electromagnetics solver is used for simulations because of the flexibility it allows in specifying material anisotropy and continuous inhomogeneity.

The cloak is consisting of nine layers and the effective parameters of each layers are used from the retrieval results as shown in the Table 5-1. In the first initial simulation, the electric and magnetic loss components are not considered. The resulting electric field distribution in the vicinity of the cloaked metallic cylinder is given in Fig. 5.42. As the waves propagates through the cloak, the center section of the wave front begins to lag to as it approaches the inner radius, then separates to

pass around the cloaked cylinder and reforms on the opposite side. This suggests the reduced cloak with the effective parameters from the elementary cell of BST brick can preserve the functionality of cloak, even though there are some discrepancies of permittivity and permeability components compared to that of theoretical values [54]. As the loss tangent parts are neglected in the simulation, it is expected that actual forward scattering would be worse than the present results

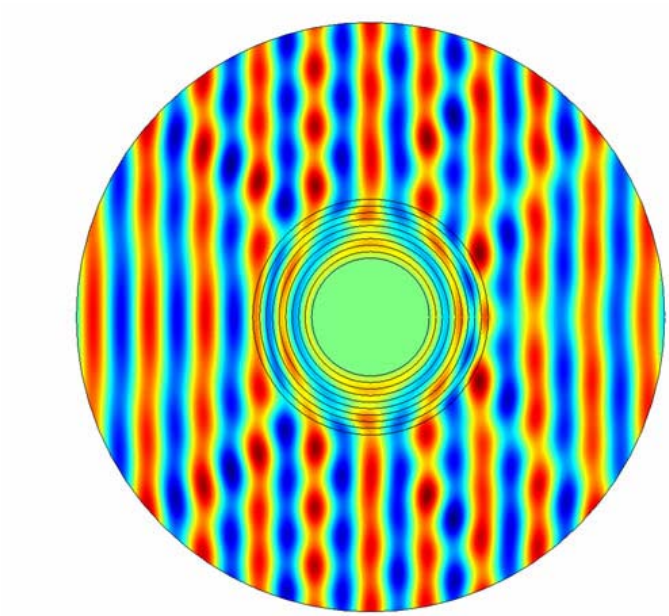

Fig. 5.42 Field mapping for homogenous cloak with effective parameters of BST elementary cell with varied sidelength.

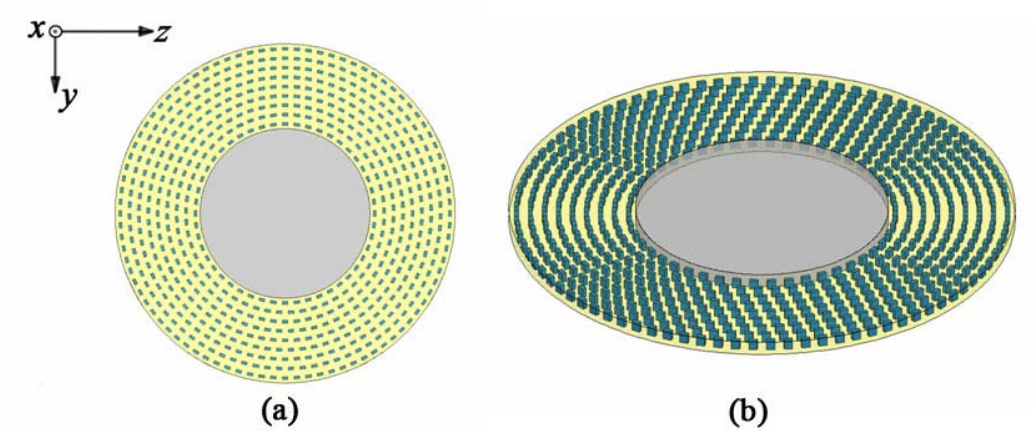

Fig. 5.43 Top view (a) and close-up view of full dielectric cloak consisting of BST rectangular bricks.

For a second stage, we will build a microstructured cloak, consisting of elementary cell of BST brick in HFSS, as shown in Fig. 5.43. There are 612 BST rectangular bricks positioned radially to form a circular cloak. A perfect electric cylinder is centered inside this dielectric cloak. We set the top and bottom layers as PEC whereas the lateral directions of incident wave as radiation boundary. The right and left sides were defined as the input and output waveports. Thus, this configuration can mimic the actual scattering field distribution carried out in a parallel-plate system. The cross section of calculation domain is set as 120 mm, four times of the incident wavelength in free space at the frequency of interest. As the calculation is so huge that a Dell Precision 690 working station with eight CPUs and 8 GB RAM were used. The corresponding field mapping is monitored and given in Fig. 5.44.

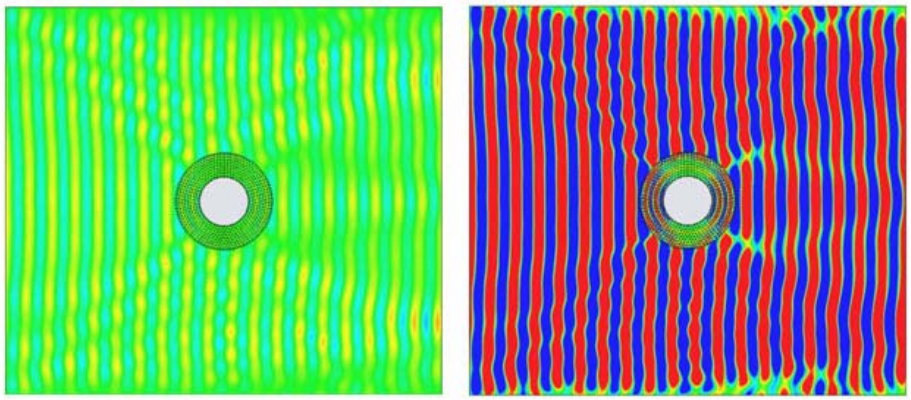

Fig. 5.44 Electric field mapping for micro-structure cloak surrounding a radius 30 mm metallic rod at 10.60 GHz (a) Maximum magnitude 2000 (b) 250 for field intensity.

From the electric field distribution around the cloaking device, we observed clearly that the wave fronts pass around the surrounded metal cylinder and reform outside the cloak, demonstrating the feasibility of a full dielectric cloak composed of BST rectangular brick. The attenuated field on the exit side of the cloak is arising from the intrinsic loss of the elementary metamaterial cell. The optimal working frequency for cloak shifts slightly to 10.60 GHz because of the unavoidable mesh intensity decrease in large calculation domain.

5.4 Summary

In this chapter, we are concentrated on magnetic Mie resonance of BST cube and its potential application on antenna as well as cloak. Some conclusions can be given as follows:

- From numerical and experimental analysis of Mie resonance of high permittivity block, it is demonstrated BST cube exhibits negative permeability around magnetic Mie resonance. Magnetic Mie resonance of BST cube is almost independent of periodicity for the modest values whereas is greatly influenced by the dielectric loss which can even deteriorate Mie resonance. From a tilted incidence response of BST cubes, it is seen that the magnetic resonance is independent of incidence angle, demonstrating isotropic property of BST cube.

- The numerical results show that BST cubes exhibit the similar behavior as AMC around its magnetic resonance, in which the effective impedance is extremely large. The interaction between dipole antenna, including electrically small and printed dipoles, and dielectric AMC layer was also studied. It is shown that a thin layer of BST cubes can perform as a highly efficient AMC reflector and improve the front-back-ratio of far field pattern as high as 35 dB. The reflected field is enhanced more than two times in comparison with that of the dipole alone in free space.

- A full dielectric cloak composed of BST rectangular block at microwave frequency is investigated. By carefully change side length of BST block, the corresponding effective parameters can be tailored and used for construction of cloak. Through both a homogenous model with piecewises and microstructured cloaks, it is shown that incident wave fronts can be transformed after passing through cloak without any phase distortion, demonstrating the feasibility of full dielectric approach to realize invisible cloak.

References

[1]. R. Shelby, D. R. Smith, and S. Schultz, Science **292**, 77 (2001).

[2]. D. R. Smith, W. J. Padilla, D. C. Vier, S. C. Nemat-Nasser, and S. Schultz, Phys. Rev. Lett. **84**, 4184 (2000).

[3]. J. Huangfu, L. Ran, H. Chen, X. Zhang, K. Chen, T. M. Grzegorczyk, and J. A. Kong, Appl. Phys. Lett. **84**, 1537 (2004).

[4]. L. Ran, J. Huangfu, H. Chen, Y. Li, X. Zhang, K. Chen, and J. A. Kong, Phys. Rev. B **70,** 073102 (2004).

[5]. F. Zhang, G. Houzet, E. Lheurette, D. Lippens, M. Chaubet, and X. Zhao, J. Appl. Phys. **103**, 084312 (2008).

[6]. C. Enkrich, M. Wegener,S. Linden, S. Burger, L. Zschiedrich, F. Schmidt, and J. F. Zhou, Th. Koschny, and C. M. Soukoulis, Phys. Rev. Lett. **95,** 203901 (2005).

[7]. S. Zhang, W. Fan, B. K. Minhas, A. Frauenglass, K. J. Malloy, and S. R. J. Brueck, Phys. Rev. Lett. **94**, 203901 (2005).

[8]. V. M. Shalaev, W. Cai, U. K. Chettiar, H. – K. Yuan, A. K. Sarychev, V. P. Drachev, and A.V. Kildishev, Opt. Lett. **30**, 3356 (2005).

[9]. X. Zhou, Q. H. Fu, J. Zhao, Y. Yang, and X. P. Zhao, Opt. Express **14**, 7188 (2006).

[10]. G. Dolling, C. Enkrich, M. Wegener, C. M. Soukoulis, and S. Linden, Science **312**, 892 (2006).

[11]. Th. Koschny, L. Zhang , and C. M. Soukoulis, Phys. Rev. B **71**, 121103 (R) (2005).

[12]. S. O'Brien, and J. B.Pendry, J. Phys.: Condens. Matter **14**, 4035 (2002).

[13]. C. L. Holloway, E. F. Kuester, J. Baker-Jarvis, and P. Kabos , IEEE Trans. Antennas Propag. **51**, 2596 (2003).

[14]. L. Peng, L. Ran, H. Chen, H. Zhang, J. A. Kong, and T. M. Grzegorczyk, Phys. Rev. Lett. **98**, 157403 (2007).

[15]. B.-I. Popa, and S. A. Cummer, Phys. Rev. Lett. **100**, 207401 (2008).

[16]. Q. Zhao, L. Kang, B. Du, H. Zhao, Q. Xie, X. Huang, B. Li, J. Zhou, and L. Li, Phys. Rev. Lett. **101,** 027402 (2008).

[17]. C. Rockstuhl, F. Lederer, C. Etrich, T. Pertsch, and T. Scharf, Phys. Rev. Lett. **99**, 017401 (2007).

[18]. W. Park, and Q. Wu, Solid State Commun. **146**, 221 (2008).

[19]. J. H. Lee, Q. Wu, and W. Park, Opt. Lett. **34**, 443 (2009).

[20]. J. Kim and A. Gopinath, Phys. Rev. B **76**, 115126 (2007).

[21]. D. K. Cheng, Field and wave electromagnetics, 2nd edition (Addison-Wesley, New York, 1989).

[22]. T. Decoopman, O. Vanbesien, D. Lippens, IEEE Microwave Wireless Components Lett. **14**, 507 (2004).

[23]. C. Croënne, B. Fabre, D. Gaillot, O. Vanbésien, and D. Lippens, Phys. Rev. B, **77**, 125333 (2008).

[24]. D. R. Smith, D. C. Vier, T. Koschny, and C M. Soukoulis, Phys. Rev. E **71**, 036617 (2004).

[25]. X. Chen, T. M. Grzegorczyk, B.-I. Wu, J. Pacheco, and J. A. Kong, Phys. Rev. E **70**, 016608 (2004).

[26]. T. Koschny, M. Kafesaki, E. N. Economou, and C. M. Soukoulis, Phys. Rev. Lett. **93**, 107402 (2004).

[27]. Q. Zhao, B. Du, L. Kang, H. Zhao, Q. Xie, B. Li, X. Zhang, J. Zhou, L. Li, and Y. Meng, Appl. Phys. Lett. **92**, 051106 (2008).

[28]. J. B. Pendry, Phys. Rev. Lett. **85**, 3966 (2000).

[29]. R. A. Shelby, D. R. Smith, S. C. Nemat-Nasser, and S. Schultz, Appl. Phys. Lett. **78**, 489 (2001).

[30]. L. Lewin, Proc. Inst. Electr. Eng. **94**, 65 (1947).

[31]. D. Sievenpiper, IEEE Trans. Microw. Theory Tech. **47**, 2059 (1999).

[32]. D. Sievenpiper, H.-P. Hsu, J. Schaffner, G. Tangonan, R. Garcia, and S. Ontiveros, Elect. Lett. **36**, 1343 (2000).

[33]. D. Sievenpiper, J. Schaffner, R. Loo, G. Tangonan, S. Ontiveros, and R. Harold, IEEE Trans. Antennas Propag. **50**, 384 (2002).

[34]. F.-R. Yang, K.-P. Ma, Y. Qian, and T. Itoh, IEEE Trans. Microw. Theory Tech., **47**, 2123 (1999).

[35]. R. Coccioli, F.-R. Yang, K.-P. Ma, and T. Itoh, IEEE Trans. Microw. Theory Tech. **47**, 2092 (1999).

[36]. A. L. Borja, J. Carbonell, V. E. Boria, and D. Lippens, Appl. Phys. Lett. **93**, 203505 (2008).

[37]. F. Martín, F. Falcone, J. Bonache, T. Lopetegi, R. Marqués, and M. Sorolla, IEEE Microwave Wirel. Comp. Lett., **13**, 511 (2004).

[38]. J. García-García, J. Bonache, I. Gil, F. Martín, R. Marqués, F. Falcone, T. Lopetgi, M. A. G. Laso, and M. Sorolla, Microwave Opt. Tech. Lett., **44**, 376 (2005).

[39]. J. B. Pendry, D. Shurig, and D. R. Smith, Science **312**, 1780 (2006).

[40]. D. Schurig, J. J. Mock, B. J. Justice, S. A. Cummer, J. B. Pendry, A. F. Starr, and D. R. Smith, Science **314**, 977 (2006).

[41]. J. B. Pendry, A. J. Holden, D. J. Robbins, and W. J. Stewart, IEEE Trans. Microw. Theory Tech. **47**, 2075 (1999).

[42]. A. Erentok, P. Luljak, and R. W. Ziolkowski, IEEE Trans. Antennas Prog. **53**, 160 (2005).

[43]. A. Erentok, D. Lee, and R. W. Ziolkowski, IEEE Antennas Wirel. Propag. Lett. **6**, 134 (2007).

[44]. S.-S. Oh and L. Shafai, Microwave Opt. Tech. Lett. **48**, 329 (2006).

[45]. N. Katsarakis, T. Koschny, M. Kafesaki, E. N. Economou, and C. M. Soukoulis, Appl. Phys. Lett. **84**, 2943 (2004).

[46]. D. R. Smith, J. Gollub, J. J. Mock, W. J. Padilla, and D. Schurig, J. Appl. Phys. **100**, 024507 (2006).

[47]. D. Schurig, J. B. Pendry, and D. R. Smith, Opt. Express **14,** 9794 (2006).

[48]. B. Kanté, A. D. Lustrac, J. –M. Lourtioz, and S. N. Burokur, Opt. Express **16**, 9191 (2008).

[49]. S. A. Cummer and D. Schurig, New J. Phys. **9**, 37675 (2007).

[50]. W. Cai, U. K. Chettiar, A. V. Kildishev, and V. M. Shalaev, Opt. Express **16**, 5444 (2008).

[51]. R. Liu, C. Ji, J. J. Mock, J. Y. Chin,T. J. Cui, and D. R. Smith, Science **323**, 366 (2009).

[52]. D. P. Gaillot, C. Croënne, and D. Lippens, Opt. Express 16, 3986 (2008).

[53]. D. P. Gaillot, C. Croenne, F. Zhang, and D. Lippens, New J. Phys. **10**, 115039 (2008).

[54]. S. A. Cummer, B. I. Popa, D. Schurig, D. R. Smith, and J. Pendry, Phys. Rev. E **74**, 36621 (2006).

[55]. O. Acher, J.- M. Lerat, and N. Malléjac, Opt. Express **15**, 1096 (2007).

[56]. D. R. Smith and J. B. Pendry, J. Opt. Soc. Am. B **23**, 391 (2006).

Chapter 6 Conclusions and future direction

In this chapter, we would like to present a short summary of previous chapters and the results of this thesis. In addition, we will briefly mention the new questions and possible future work that our results have led us to.

In the second chapter, we gave an analysis description in detail for the design of balanced bulk metamaterial, which requires the equality of magnetic and electric plasmas frequencies. Following this guideline, we designed and fabricated an omega pattern based balanced metamaterial. Then, we experimentally and numerically demonstrated that this structure exhibits a broad transmission window from 8.3 GHz to 16.0 GHz without any gap in between. In addition, it was found that the proposed structure shows a negative-zero-positive property with a seamless transition frequency at 13.605 GHz, around which the group velocity is not vanishing.

In the third chapter, a low-loss omega-like metamaterial was successfully fabricated on BCB substrate via optical photolithography technology at millimeter waves. The left-handedness of the transmission window was confirmed by phase delay measurement under normal incidence and by the sensitivity of transmission levels of oblique incidence. An insertion loss below -0.5 dB per unit cell was observed.

In the forth chapter, we are mainly involved in the investigation of tunable metamaterial based on nematic liquid crystal. From numerical comparative analysis, we found that it is imperative to treat liquid crystal with permittivity tensor to give an accurate predication for electric or magnetic resonance frequency dependency of metamaterial on the reorientation of LC. A tunable broadside coupling split ring resonator infiltrated by liquid crystal was proposed and experimentally demonstrated by 300 MHz shift of magnetic resonance. Then, a reconfigurable left handed metamaterial based on liquid crystal is also designed and an index variation of 0.25 in the negative index regime was observed experimentally.

In the fifth chapter, we studied the mechanism of Mie resonance of dielectric resonator as well as its application on antenna and invisible cloak. BST cube exhibits negative permeability around the magnetic Mie resonance. Constitutive dielectric loss of BST plays an important role for Mie resonance, i.e., large loss tangent can destroy Mie resonance. It is shown that a thin layer of BST cubes can perform as a highly efficient AMC reflector, arising from in-phase reflection around magnetic resonance, and improve the front-back-ratio of far field pattern as high as 35 dB. The directivity and gain are enhanced more than two times in comparison with that of the dipole alone in free space. In addition, a full dielectric cloak designed to make objects inside invisible is also demonstrated successfully at microwave by radically positioning BST rectangular bricks.

Since left–handed materials is a hot topic in the scientific community these years, there are several discussions questioning the problems of the left-handed materials. For us, three focuses in the next research stages are as follows:

Firstly, high insertion loss is a critical drawback prevents practical application for metamaterial. For metallic elements such as SRR and wire and other relative shapes, metal, structure design should be given much attention, in addition to Ohmic and dielectric attenuations as pointed in this thesis. Recently, our group have designed, fabricated and demonstrated a low loss metamaterial at THz frequency by using multi-layer subwavelength hole as elementary cell [1]. We will continue more works on this motif and attempt to push it to higher frequency. Another alternative way is to employ dielectric resonator since metallic attenuation does not exit. However, the dielectric loss should be at a rather small scope, approximately 10^{-3} as pointed in chapter 5. We will checked the possibility of Mie resonance based on low permittivity dielectric resonator, which is not so sensitive to that as BST.

Second, tunability is another point deserves attention. With respect to our group work, tunability is realized by controlling the anisotropic substrate notably liquid crystal at present. As mechanism as well as numerical analysis of liquid crystal reorientation influence has been studied well, we will shift the aim to experimental realization of tunable metamaterial at higher frequency especially for THz frequency where liquid crystal exhibits large birefringence. Based on numerical simulation, optical lithography technology will be employed for the fabrication of metamaterial. Various control methods, such as electric, magnetic field and both of them, can be options to excite the reorientation of liquid crystal.

The last one is about invisible cloak based on optics transform technology,

which has increasing interests around the whole scientific world in the development of metamaterial. On the basis of numerical full wave demonstration of dielectric cloak as described in this thesis, how to realize it practically is up to the top agenda of our future work. Up to now, we have Teflon template which is used to hold dielectric resonators made to order. After obtaining BST rectangular bricks with carefully dicing, we will try to see the electromagnetic scattering phenomena around proposed dielectric cloak.

List of Publications

Papers

1. Q. Zhao, J. Zhou, **F. Zhang,** and D. Lippens, "Mie resonance-based dielectric metamaterial," **Mater. Today** (To be published).
2. **F. Zhang**, Q. Zhao, L. Kang, J. Zhou, and D. Lippens, " Experimental verification of isotropic and polarization properties of high permittivity-based metamaterial," **Phys. Rev. B** (To be published)
3. **F. Zhang**, L. Kang, Q. Zhao, J. Zhou, X. Zhao, and D. Lippens, "Magnetically tunable left handed metamaterials by liquid crystal orientation," **Opt. Express** 17, 4360 (2009)
4. **F. Zhang**, S. Potet, J. Carbonell, , E. Lheurette, O. Vanbésien, X. Zhao, and D. Lippens, "Negative-zero-positive refractive index in a prism-like omega-type metamaterial," **IEEE Trans. Microwave Theory Tech**. 56, 2566 (2008).
5. **F. Zhang**, Q. Zhao, D. P. Gaillot, X. Zhao, and D. Lippens, "Numerical Investigation of Metamaterials Infiltrated by Liquid Crystal," **J. Opt. Soc. Am. B** 25, 1920 (2008).
6. **F. Zhang**, D. P. Gaillot, C. Croënne, E. Lheurette, X. Mélique, and D. Lippens, "Low-loss left-handed metamaterials at millimeter waves," **Appl. Phys. Lett.** 93, 083104 (2008).
7. **F. Zhang**, Q. Zhao, L. Kang, D. P. Gaillot, X. Zhao, J. Zhou, and D. Lippens, "Magnetic control of negative permeability metamaterials based on liquid crystals," **Appl. Phys. Lett.** 92, 193104 (2008).
8. **F. Zhang**, G. Houzet, E. Lheurette, D. Lippens, M. Chaubet, and X. Zhao, "Negative-zero-positive metamaterial with omega-type metal inclusions," **J. Appl. Phys.** 103, 084312 (2008).
9. D. P. Gaillot, C. Croenne, **F. Zhang**, and D. Lippens, "Transformation optics for the full dielectric electromagnetic cloak and metal–dielectric planar hyperlens," **New J. Phys.** 10, 115039 (2008).
10. E. Lheurette, G. Houzet, J. Carbonell, **F. Zhang**, O.Vanbésien, and D. Lippens, "Omega-type balanced composite negative refractive index materials," **IEEE Trans. Antennas Propag.** 56, 3462 (2008).

International Conferences

11. **F. Zhang**, Q. Zhao, L. Kang, D. P. Gaillot, X. Zhao, J. Zhou, and D. Lippens, "Magnetic control of negative permeability metamaterials based on liquid crystals," 38th European Microwave Conference, October 2008, Amsterdam, Netherlands.
12. **F. Zhang**, G. Houzet, S. Potet, E. Lheurette, M. Chaubet, and D. Lippens, "Metamaterials-based routing devices for space applications," International Symposium on Signals, Systems and Electronics (ISSSE '07), August 2007, Montreal, Canada.
13. **F. Zhang,** S. Potet, J. Carbonell, E. Lheurette, O. Vanbésien, X. Zhao, and D. Lippens, "Application of Omega-Type and Related Metamaterials for Beam Steering in X-Ku " 37th European Microwave Conference, October 2007, Munich.